Numerical Studies on Effects of Leading-Edge Manufacturing Defects on Marine Propeller Cavitation Performance

by

© *Shanqin Jin*

A thesis submitted to the

School of Graduate Studies

in partial fulfilment of the

requirements for the degree of

Doctor of Philosophy

Faculty of Engineering and Applied Science

Memorial University of Newfoundland

March 2024

St. John's Newfoundland

Abstract

During the propeller manufacturing process, grinding of propeller surfaces can introduce imperfections and deviations from the desired geometry. These defects could lead to degradation of propeller performance in terms of efficiency, cavitation, vibration and noise. However, there is a lack of scientific literature available that specifically addresses the subject of manufacturing tolerances of propellers.

In this dissertation, numerical simulations were conducted for foils with constant DTMB modified NACA-66 $a = 0.8$ sections using the steady Reynolds-Averaged Navier-Stokes (RANS) solvers in Star-CCM+ to investigate the effects of manufacturing tolerances. 2-D simulations were first performed for the modified NACA-66 ($a = 0.8$, $t/c = 0.0416$ and $f/c = 0.014$) foils without and with the leading-edge (LE) defects in infinite flow. Convergence studies were carried out to examine the effects of domain size, grid distribution, grid resolution, and turbulence model on the solution. Using the best-practice settings for 2-D simulation, verification studies were carried out for the cavitation buckets of NACA-66 ($a = 0.8$, $t/c = 0.2$ and $f/c = 0.02$) foils without defect. CFD simulations with best-practice settings were then extended to the modified NACA-66 ($a = 0.8$, $t/c = 0.0416$ and $f/c = 0.014$) foils with three different sizes of LE defects, representing three levels of manufacturing tolerances within International Standards Organization (ISO) 484 Class S. The results showed that the LE defects have significant effects on the cavitation performance of 2-D foils in terms of reduced cavitation inception speed in the typical design range of angle of attack.

To investigate the differences in 2-D and 3-D simulations and further quantify the effect of LE defect in future validation studies, 3-D simulations were carried out for

the modified NACA-66 ($a = 0.8$, $t/c = 0.0416$ and $f/c = 0.014$) foils in 1.0 m and 0.525 m spans with and without LE defects in cavitation tunnel. Effects of RANS modelling parameters, such as domain size, grid aspect ratio, first-grid spacing, y^+, and turbulence model, on the solutions were carefully examined. Using the corresponding recommended settings, the cavitation buckets, the reduction of cavitation inception speed and the efficiency due to LE defect were predicted. Additionally, preliminary validation studies were performed on two sections of 0.525 m span with no and 0.5 mm defects.

Furthermore, this dissertation extended 3-D RANS studies on the foils in cavitation tunnel to full-scale propellers, based on the geometry of David Taylor Model Basin (DTMB) 5168 propeller, with and without LE defects. Effects of simulation parameters, including domain size, grid size, stretch ratio, first-grid spacing, y^+, and turbulence model on the solutions were carefully examined and the best modelling practices for the full-scale propeller was developed. Since there is no full-scale data available, convergence studies were performed for the model-scale propeller followed by validation studies in order to develop the best-modelling practices for model-scale propellers. The wake field, open-water and cavitation performance were presented and compared with the experimental data. The best-practice settings for the model-scale and full-scale propellers were compared. Using the best-practice modelling settings for full-scale propellers, simulations were carried out to full-scale propellers without and with 0.10 mm, 0.25 mm, and 0.50 mm LE defects. The results showed that the LE defects within Class S tolerances narrow the cavitation buckets. As a consequence, such LE defects can result in more than 40% reduction in cavitation inception speed, which is similar to the conclusions drawn from earlier 2-D studies.

General Summary

In this dissertation, a novel and comprehensive study was carried to investigate the effects of leading-edge (LE) defect on propeller cavitation performance using the steady RANS solver.

Small geometric variations relative to the dimensions of the propeller suggest that much could be learned from less computationally intensive simulations based on 2-D sections before full-scale 3-D propeller simulations. 2-D simulations were first performed for the modified NACA-66 ($a = 0.8$, $t/c = 0.0416$ and $f/c = 0.014$) foils without and with the LE defects. To investigate the differences in 2-D and 3-D simulations and further quantify the effects of LE defect in future validation studies, 3-D simulations were then carried out for the foils of 1 m span in a cavitation tunnel. The reason for choosing 1 m span was that the foils with and without LE defect were intended to be tested in a cavitation tunnel with 1 m by 1 m test section. However, due to the limitation of the foil support mechanism in cavitation tunnel, the span of 0.525 m was applied to minimize the force and moment on the foil. Simulations were also conducted for the foils in 0.525 m spans with and without LE defects in cavitation tunnel. Finally, this dissertation extended 3-D RANS studies on the foils in cavitation tunnel to full-scale propellers, based on the geometry of David Taylor Model Basin (DTMB) 5168 propeller, with and without LE defects.

Extensive convergence studies were carried out to examine the effects of domain size, grid aspect ratio, first-grid spacing, y^+, and turbulence model on the solutions of 2-D and 3-D simulations. The best-practice settings could be useful for the simulations of foils and further study of other manufacturing tolerances.

Acknowledgements

Firstly, I would like to express my greatest gratitude to my supervisor, Dr. Heather Peng, for her academic and financial support throughout my Ph.D. studies and research. I truly appreciate her patience and kindness. Not only has her guidance consistently helped me throughout conducting my research, but also her continuous encouragement has helped me overcome the challenges I encountered.

My gratitude also goes to Dr. Wei Qiu for his invaluable guidance and perceptive insights. I am truly appreciative of the opportunities he offered me to participate in research projects and undergraduate course teaching, from which I have gained priceless knowledge and skills.

I would like to extend my gratitude to Dr. Lorenzo Moro for his supervision and insightful comments. Without his precious support, it would not have been possible to conduct this research. I would also like to show my gratitude to my colleagues, Dr. Dexin Zhan, Dr. Peng Wen, Dr. Md. Ashim Ali, Dr. Wei Meng, Dr. Ruosi Zha, Meng Chen, Saeed Barzegar Valikchali, Emre Cilkaya, Adwaith Nath, Alexandria Major, Liam Gregory and other faculty members and laboratory technicians at Memorial University, for the helpful discussions and assistance in all the stages of my research.

I would like to express my sincere appreciation to Slobodan Gospodnetic for his help and support during my research.

Last but not the least, I would like to thank my family. I would like to owe my deepest gratitude to my parents, C.Y. Jin and X.Y. Xiong, and my sister, H.Y. Jin. During my years of pursuing a Ph.D., they consistently support me and believe in me. I appreciate their love all the time.

Contents

List of Tables

List of Figures

Chapter 1

Introduction

1.1 Background

Underwater radiated noise (URN) from ships is being recognized as a world-wide problem since underwater noise from shipping is increasingly being considered as a significant and omnipresent pollutant with the potential to impact marine ecosystems on a global scale. Continued growth in the number of ships will significantly increase the total volume of noise generated by the global shipping fleet. Projections suggest that URN level could increase by as much as a factor of 1.9 of the current level by the year 2030 (Southall et al., 2017). The URN of a ship is primarily caused by the propeller and the main machinery. The European Union's collaborative research project Achieve QUieter Oceans has provided valuable insight into the relative contribution of each source of noise generated by different types of ships (Salinas, 2015). A significant conclusion of the study is that propeller cavitation is the most important source of noise for ferries and cruise vessels at normal operating speeds. The noise levels

from a ship jump substantially when propeller cavitation begins.

The majority of propellers manufactured today are hand or robotic finished from castings which are rough machined using computer numerical control (CNC). Blade edges and tips, the most sensitive parts of the geometry of a propeller, are made to conform to templates of their required form using manual grinding (Janssen and Leever, 2017; Van Beek and Janssen, 2000). Manual grinding of propeller surfaces introduces inaccuracies and deviations from design, which could lead to degradation of propeller performance in terms of efficiency, cavitation and noise.

Manufacturing tolerances for new ship propellers are specified by organizations, such as International Standards Organization (ISO), which defines the manufacturing standards for propeller construction, and the Naval Sea Systems Command, USA (NAVSEA), which provides manufacturing standards for US Navy's ship construction (NAVSEA, 2004). The ISO 484-1 and ISO 484-2 standards (ISO, 2005a,b) for manufacturing tolerances of ship propellers were established in 1981 by adopting an ISO Recommendation of 1966. ISO 484-1 standard (ISO, 2005a) is applicable to propellers with diameters greater than 2.5 m, while ISO 484-2 standard (ISO, 2005b) is applicable to propellers with diameters from 0.8 m to 2.5 m. There are four classes of tolerances in each standard. Each tolerance class is intended for a certain type of vessels. Among the four classes, Class S denotes the smallest tolerance and hence the highest precision.

Manufacturers could take various measures to finish machining propellers. Dominis Engineering, for example, uses a CNC milling process which eliminates manual grinding of blade edges and tips (Gospodnetic and Gospodnetic, 1996; Gospodnetic, 2013). This process has put possible manufacturing tolerances in a new and more ac-

curate era (Gospodnetic, 2015; Tremblay and Gospodnetic, 2017), which better complements today's sophisticated propeller design tools. In light of these changes, it is necessary to better understand the sensitivity of propeller performance to manufacturing defects.

Many studies have been carried out to investigate effects of design parameters on cavitation and efficiency performance of a propeller with an objective to avoid or control vortex cavitation and to improve its efficiency. A review of experimental and numerical studies on cavitation performance of marine propeller is given in the next section.

1.2 Literature Review

Cavitation is a phase change phenomenon that occurs in high-speed flows when the local absolute pressure equals or drops below the vapor pressure at the ambient temperature (Breslin and Andersen, 1994). One of the earliest references for the cavitation on marine propeller dated back to 1875 when Osborne Reynolds discussed the effect of propeller racing, as noted in Newton (1961). This phenomenon was first fully recorded by Barnaby (1897), in the trails of the British high-speed destroyer Daring, and was further observed by Parsons (1897) when building the first marine steam turbine-driven vessel, Turbinia. To understand the mechanism of the cavitation and reduce the effects of cavitation on the marine propeller, numerous experimental and numerical studies have been carried out on the cavitation performance of marine propeller.

1.2.1 Experimental Studies

The prediction of cavitation inception on marine propellers heavily relies on physical model tests in cavitation tunnels. In 1897, Parsons conducted a series of tests using 5 cm diameter propellers in the world's first cavitation tunnel, aiming to address the issues associated with Turbinia. Although Parsons did not publish the detailed experimental results, his achievements were mentioned in the memorial lecture of Burrill (1951).

In the model tests, the propeller models are operated at low Reynolds numbers, leading to a large laminar boundary layer and a strong tendency for laminar separation. This is in contrast to the observations of full-scale propellers, which work in almost fully developed turbulent flows. The effects of turbulence level on cavitation inception have been investigated by many researchers. For example, Arndt and George (1979) studied cavitation inception in turbulent shear flow. Their results indicated that the transition of the boundary layer had a significant impact on cavitation inception, primarily due to the complex interaction between an unsteady pressure field and the distribution of free stream nuclei. Huang (1986) conducted an investigation into the effects of turbulence stimulators on cavitation inception in the David Taylor Naval Ship Research and Development Center (DTNSRDC) 36-inch water tunnel. The study showed that the measured cavitation inception numbers were notably smaller than the computed negative minimum pressure coefficients, and the predicted transition locations occurred at positions considerably aft of the minimum pressure locations.

To reduce the viscous scale effect on the cavitation inception and simulate the tur-

bulent flow in the experiments, the leading-edge roughness technique was employed in cavitation tests. Holl (1960) carried out a series of cavitation tests in the water tunnel of the Ordnanace Research Laboratory on roughness elements ranging from 0.002 to 0.5 inch. The results demonstrated that the cavitation inception depended on the relative height of roughness, the boundary-layer shape and the velocity. For the circular arcs, the negative minimum pressure coefficient, determined by the frozen-streamline theory, was about 25% greater than the measured negative minimum pressure coefficient and was as much as 40% greater than the incipient cavitation number. Kuiper (1978) applied sand grain roughnesses of 30 and 60 μm carborundum on four model propellers with an average chord length of 102 mm at 0.7 radius. Test results showed that the critical radius associated with laminar separation was effectively removed and that high Reynolds number conditions were simulated. Based on the experimental results of Jones (1980), spherical glass beads with a nominal diameter of 94 μm were used in the experiment of Shen (1985) to simulate high Reynolds number conditions. It was found that the application of surface roughness could lower the cavitation inception number. Although the leading-edge roughness technique has been widely used, the level of turbulence generated by the roughened leading edge cannot be easily quantified. The size and type of the roughness element, as well as the location of the roughness area should be carefully considered. These parameters can significantly influence the outcomes of cavitation tests and the accuracy of predictions related to cavitation inception.

In order to address the limitations of the leading-edge roughness method, a turbulent free-stream method was introduced by Korkut et al. (1999). Free-stream turbulence was generated using wire mesh screens and measured using a laser doppler

anemometry (LDA) system. Cavitation tests were systematically conducted for a relatively large rectangular NACA-66 foil and a Meridian-type propeller model to investigate the effects of free-stream turbulence and artificial roughness on the inception of tip vortex and sheet cavitation. Further details of the test results were discussed in the work of Korkut and Atlar (2002). Their findings indicated that the leading-edge roughness technique could be replaced with a more controlled method of altering the free-stream turbulence. In a recent study, Kethanur Balasubramaniam et al. (2023) investigated the impact of free-stream turbulence on cavitation inception using a wire mesh fence. It was found that the turbulence has a delaying effect on cavitation inception, and it tends to occur primarily at higher flow rates.

As experimental techniques continue to advance, researchers have the capability to collect more detailed flow information, i.e., the velocity in the tip vortex core region, as well as downstream pressure and Reynolds shear-stress, during cavitation tests. A comprehensive velocity measurements were made for the downstream of DTMB 5168 propeller model by Chesnakas and Jessup (1998) in the Carderock Division Naval Surface Warfare Center (CDNSWC) 36-inch water tunnel. Their findings indicated that the measurements obtained with the coincident laser doppler velocimeter (LDV) system exhibited higher accuracy in both velocity and Reynolds shear-stress terms when compared to the results from the non-coincident sets. Using the LDV system, Bertetta et al. (2012) measured the complex wake behind an unconventional contracted loaded tip (CLT) propeller to analyze the dynamics of generated tip vortices. Their research revealed that the vortices generated by the propeller and the end plate had different pitches, with the blade tip vortex showed a higher pitch than the other. Compared to LDA system, which provides single-point measurements, particle image

velocimetry (PIV) has the ability to capture data across a plane or even a volume with just one measurement (Lee et al., 2009). Many studies (Foeth et al., 2006; Li et al., 2020; Pereira et al., 2004; Salvatore et al., 2006) had been carried out for the predictions of cavitation performance on marine propellers with the PIV system. Most recently, D'Agostino et al. (2023) investigated the underlying mechanisms governing the evolution of tip vortices in the far field of a naval propeller wake. Phase-locked PIV snapshots recorded throughout the transitional and far fields of a propeller wake were used in the clustering analysis. The clustering results suggested that the wake instability and subsequent progression of tip vortices were governed by deterministic chaos.

Most of the cavitation tests for propeller model were carried out with the uniform incoming flow in cavitation tunnel. However, in real-world scenarios, the inflow is typically non-uniform due to the presence of the ship's wake, which can significantly impact cavitation performance. Moreover, the interaction between the propeller and rudder is another crucial factor affecting propeller cavitation. Over the past two decades, the effects of non-uniform inflow on the cavitation performance of marine propellers were investigated experimentally by many researchers (Alves Pereira et al., 2016; Felli and Falchi, 2018; Kinnas et al., 2015; Lloyd et al., 2015; Lubke, 2015). Recently, Abbasi et al. (2023) measured the flow field around a propeller with an inclined shaft using LDV system. The effects of non-uniform inflow conditions caused by the oblique shaft were analyzed focusing on the dynamics of vortices. Their findings revealed that significant variations can be observed in the pitch of the vortices during rotation.

Nowadays, there has been a notable increase in experimental efforts focused on

propeller cavitation to provide valuable reference data for the validation of CFD simulations. For example, comprehensive model test results including the open-water performance, the propeller-induced flow field and cavitation patterns of the Italian National Institute for Naval Architecture Studies and Testing (INSEAN) E779A propeller were summarized in Salvatore et al. (2006). To enhance the accuracy and quality of numerical methods used in the calculation of marine propellers under both cavitating and non-cavitating conditions, an experimental benchmark was established at the propeller workshop of the Second International Symposium on Marine Propulsors 2011 (Barkmann et al., 2011). A series of model tests were conducted for a controllable pitch propeller, SVA-VP1304, and corresponding measurements (Heinke, 2011; Heinke and Kröger, 2013; Lubke, 2015; Mach, 2011) were collected to serve as benchmark data. Considering the underwater radiated noise resulting from propeller cavitation, a thorough examination of the Princess Royal propeller was conducted by eight major cavitation tunnels and wave basin facilities around the world (Yilmaz et al., 2020). Extensive cavitation test results along with the noise measurements have been published. Furthermore, the Princess Royal propeller has also been recommended by the International Towing Tank Conference (ITTC) as a recommended benchmark propeller for a wide range of tests (ITTC, 2021).

Experiments continue to be important to predict the inception of cavitation, reveal the flow characteristics, and offering benchmark data for validating numerical simulations. However, experimental studies are costly and limited to model scale.

1.2.2 Numerical Simulations

In terms of numerical methods to predict the cavitation performance of marine propeller, methods based on the potential-flow theory and the computational fluid dynamics (CFD) have been developed over years.

The initial simulations of marine propeller cavitation primarily relied on methods based on potential-flow theory. One notable advancement in this field was the introduction of a lifting-surface method by Kerwin and Lee (1978), aimed at predicting the performance of marine propellers. In their work, the blades were assumed to operate at a small angle of attack, and the spatial variation of the ship wake was assumed small accordingly. The blade boundary layer and shed vortex wake thickness were assumed to be thin so that the fluid rotation due to the propeller was confined in a thin layer. Lee (1979) further developed this method, and applied it to predict sheet cavitation on the suction side of the propeller blade. The theoretical predictions were compared with experimental data, and it was found that this method could effectively predict the performance of a propeller model in both uniform flow and flow generated by screens. But the prediction of the cavity extent for a full-scale propeller was not satisfactory, indicating that the extrapolation from the wake measured behind the model ship to the full-scale wake was important for the prediction of the cavity. Furthermore, the lifting-surface method (Lee, 1979) with the leading-edge correction was incorporated into a code named PUF-3A by Kerwin et al. (1986). A similar lifting-surface method was employed by Van Gent (1994) to predict pressure fluctuations induced by a propeller flow, taking into account unsteady sheet cavitation.

One of the limitations in the lifting-surface method is the neglecting of the blade

thickness. This omission makes it challenging to capture the details of the flow near the leading and trailing edges of the blade. To address this problem and account for the displacement effects, Lee (1987) developed a potential based panel method to analyze the marine propeller the steady flow. Viscous effects were also taken into account by incorporating a tangential friction force on each panel. A reliable pressure distribution around a marine propeller, especially near the leading-edge of the blade was obtained. The calculated thrust and torque were in close agreement with the experimental data, even under off-design conditions. A efficient and robust panel method was developed by Fine (1992) to predict the extent and shape of sheet cavities on propellers in unsteady flow. In this approach, unsteady cavitating flow was treated in nonlinear theory by employing a low order potential based boundary element method (BEM). Comprehensive validation studies were carried out for various scenarios, including 2-D and 3-D hydrofoils in steady flow, propellers in steady flow, and propellers in unsteady flow. The results showed that the conventional linear theory overpredicted the cavity planform in both spanwise and chordwise directions.

The method introduced by Fine (1992) was further extended to examine both steady and unsteady sheet cavitation on hydrofoils and propellers. For example, Fine and Kinnas (1993) investigated the the cavity extent and shape for 3-D partially and supercavitating hydrofoils of arbitrary geometry by employing a low-order potential-based boundary element method. Their results showed that the predicted cavity surfaces were in good agreement with the corresponding reference data for the cavitation number ranging from 0.2 to 1.6. This method was also applied for the prediction of time-dependent sheet cavitation for propellers by Kinnas and Fine (1992).

Note that the fluid was assumed to be inviscid and irrotational in the method of Fine (1992). The influence of viscosity, however, on cavitation performance can not be neglected, as mentioned by Franc and Michel (1985). To solve the flow in the boundary layer, Brewer and Kinnas (1997) introduced a numerical approach that coupled a nonlinear panel method with a boundary layer solver. Both numerical and experimental studies using a foil based on the geometry of the NACA0012-64, which had a zero camber and symmetrical cross section, were carried out in their work. The numerical method accurately predicted velocity fields away from the foil and inside the boundary layer with fully wetted conditions. However, under cavitating conditions, it was found that the displacement and momentum thickness loss at the trailing edge were not well simulated. In addition, Sun and Kinnas (2006) developed a viscous/inviscid interactive (VII) BEM model to study the cavitating flow around a marine propeller. The more details of the VII BEM model was further presented in the work of Pan (2009). Compared with the results from a commercial RANS software (Fluent), the pressure was well predicted with the BEM inviscid theory. However, it's worth noting that the calculated pressure was increased with the coupled method considering the viscous effect. In a recent study conducted by Kim and Kinnas (2022), a semi-empirical criterion was introduced into a lower-order panel method to simulate the viscous core of tip vortex. Their results demonstrated that the modified boundary element method was able to predict sheet cavity patterns, as well as the trajectories and shapes of developed tip vortex, in reasonable agreement with experimental observations. Importantly, the BEM method successfully captured the higher-order harmonics in hull pressure fluctuations.

The potential-flow based methods have difficulties in dealing with highly non-

linear problems, such as the significant flow separation near the trailing edge and breaking free surface. Another disadvantage associated with BEM is its susceptibility to numerical instability and ill-conditioning. With the development of computer technology, many CFD methods have been developed to predict the cavitation performance of marine propeller.

Numerical methods for predicting cavitation based on Reynolds Averaged Navier-Stokes (RANS) model have been developed and widely used in marine industry. Abdel-Maksoud (2003) employed the cavitation model in the commercial CFD software package (CFX-TASCflow) to predict the flow characteristics on a marine propeller. The investigation covered a wide range of cavitation numbers, spanning from 1.36 to 10.22. The standard k - ε turbulence model (Jones and Launder, 1972) was applied in combination with a scalable wall function. It was recommended that the applied cavitation model was able to predict most types of cavitation which take place in the propeller flow. In the work of Watanabe et al. (2003), RANS simulations of two conventional propellers, namely MP017 and Seiun-maru, were carried out using the "full cavitation model" proposed by Singhal et al. (2002). The k - ω turbulence model (Wilcox, 1998) in a commercial CFD code, Fluent Version 6.1, was implemented. Their results showed that the cavitating flow around the Seiun-maru propeller was well simulated, and there was a good agreement in the cavity shape at the advance ratio of $J = 0.2$. In summary, these findings suggested that the RANS approach proved to be a suitable method for simulating propeller flow in both cavitating and non-cavitating conditions.

However, the tip vortices were not captured in the work of Abdel-Maksoud (2003) and Watanabe et al. (2003) due to limitations of mesh resolution in the tip region.

The tip vortices generated by marine propellers exhibit a higher degree of concentration and have a more compact structure, which require a finer grid within the tip vortex core. Numerical efforts (Ali et al., 2017; Hsiao and Chahine, 2005, 2008; Hsiao and Pauley, 1999; Peng et al., 2013; Shen et al., 2009) have been made to address this challenge and gain a deeper understanding of the tip vortex dynamics within propeller flows. Most recently, Duan et al. (2023) conducted a numerical study to assess the tip vortex inception for PPTC propeller. In this study, three types of feasible cavitation initiation prediction methods, including the minimum pressure coefficient method, the tip vortex model method and the minimum vapor volume method, were investigated. Based on their CFD predictions, the tip vortex model was recommended to predict cavitation initiation. It was also found that the turbulence model has little effect on propeller cavitation inception prediction.

As mentioned earlier, full-scale ship propellers are generally installed at the stern of the vessels. The effects of no-uniform wake field and propeller-hull-rudder interactions should be considered when predicting cavitation performance. For example, Li et al. (2012) studied the impact of incoming flow on a four-bladed propeller, INSEAN E779A, cavitation inception properties. The numerical simulations were performed using both uniform inflow conditions and non-uniform wake conditions, the latter were obtained from experiments. Their numerical results with the uniform incoming flow revealed that the predicted sheet cavities were stable and had similar patterns as observed in experiments. The calculated thrust and torque coefficients showed minimal differences of less than 5% compared to the measured data, while the cavitation area was over-estimated by more than 30%. In contrast, for the predictions at the cavitation number of 4.455 in the non-uniform wake, vapor structures

were shed from the tail of cavity and become cloudy when exiting the wake.

The effect on sheet cavitation due to the different wake distributions was examined for a typical full-scale ship by Regener et al. (2018). Their results showed that the propeller designed with the full-scale effective wake distribution exhibited better cavitation performance compared to the propeller designed with the nominal wake field in model scale. Therefore, if only the measured nominal wake field was available, a conservative design was required. They predicted the roughness effects of typical coatings and different fouling conditions on propeller performance for various advance coefficients. Their results demonstrated that as propeller surface fouling increases, the thrust coefficient magnitude decreases while the torque coefficient magnitude increases, resulting in a net decrease in open water efficiency of up to 30% at the highest simulated fouling level. The effects of biofouling-related roughness on propeller's hydrodynamic and URN performance were investigated by Sezen et al. (2021a). Different roughness configurations were represented using roughness functions implemented in the wall function model of the CFD solver. The results showed that the propeller's thrust decreases while the torque increases with increasing severity of roughness. The efficiency loss of the propeller at the most severe roughness condition can be as high as 30% and 25% at $J = 0.795$ and $J = 0.71$, respectively.

In order to mitigating tip vortex cavitation, the possibility and effectiveness of roughness application to mitigate tip vortex flows are evaluated by many researchers. For example, Sezen et al. (2021b)conducted simulations for the Princess Royal propeller under uniform, inclined, and non-uniform flow conditions. The Schneer-Sauer cavitation model (Sauer and Schnerr, 2001) was used to model the sheet and tip vortex cavitation along with the detached eddy simulation (DES) approach. With the

application of roughness inside the tip region, the velocity was reduced, leading to a pressure increase and tip vortex cavitation mitigation. The maximum cavitation volume reductions due to the tip vortex for the full-scale propeller in the uniform and non-uniform flows were 10% and 5%, respectively. Asnaghi et al. (2019) employed implicit large eddy simulation (ILES) of OpenFOAM, incorporating a wall-function to account for roughness effects in simulating propeller tip vortex flow. Their results suggested that a roughness size of 250 μm is sufficient to mitigate the tip vortex. Furthermore, they found that applying roughness on the leading edge and trailing edge of the suction side is effective not only in mitigating the tip vortex but also in limiting performance degradation.

It is noted that the surface roughness at the leading-edge (LE) also has significant effect on the marine propeller cavitation performance. The presence of LE roughness generates very small cavitating vortical structures which interact with the main sheet cavity developing over the foil to later form a cloud cavity. These interactions create a streaky sheet cavity interface which cannot be captured in the smooth condition, influencing both the richness of structures in the detached cloudy cavitation as well as the extent and transport of vapour (Asnaghi and Bensow, 2020). In the work of Johnsson and Rutgersson (1991), leading-edge roughness applied on the pressure side near the leading edge was found to have a delaying effect on tip vortex cavitation, even when the planform of the hydrofoil (or the propeller blade) is highly swept. The increase in drag caused by the roughness ranged from 1% to 10%, corresponding to a maximum decrease in efficiency for the propeller of about 2%. Additionally, Asnaghi et al. (2021) evaluated the application of surface roughness on model and full-scale marine propellers to mitigate tip vortex cavitation. The effect of rough-

ness was simulated using modified wall functions. Their findings suggested that the combination of roughness on the blade tip and a limited area on the leading edge is the optimum roughness pattern, achieving a reasonable balance between tip vortex cavitation mitigation and performance degradation. For model-scale propeller, this pattern led to an average tip vortex cavitation (TVC) mitigation of 37% with an average performance degradation of 1.8%, while an average TVC mitigation of 22% and performance degradation of 1.4% were obtained in full-scale condition.

Regarding the influence of ship's wake on marine propeller cavitation performance, Rizk et al. (2023) calculated the performance of the INSEAN E779A propeller behind a generic hull at the self-propulsion point. The open-water simulations were first carried out using a RANS based method. Grid sensitivity studies were also conducted to accurately model the cavitating flow around the propeller. An interesting observation from their research was that cavitation had an unexpected effect of enhancing the propulsion efficiency. Specifically, the propeller rotation rate was lower, while higher thrust and torque coefficients were obtained at the cavitation number of $\sigma = 1.5$.

With computational capabilities and methods continuing to advance in recent years, the Large Eddy Simulation (LES) has been widely used in aerospace (Heinz, 2020; Spalart and Venkatakrishnan, 2016; Tucker and Tyacke, 2016) and combustion (Brito Lopes et al., 2022a, 2020, 2022b; Rutland, 2011). Owing to the high Reynolds numbers encountered in ship hydrodynamics, the application of the LES method is limited in practical design projects, as highlighted by Liefvendahl et al. (2010) and the International Towing Tank Conference (ITTC, 2017). Early LES simulation of the propeller can be found in work of Di Felice et al. (2009). They compared the velocity fields measured by Laser Doppler Velocimetry (LDV) and pre-

dictions of LES. However, the simulation encountered challenges in capturing the wake due to limitations in grid resolution and distribution. Recognizing this, they recommended an increased grid number of over 10 million to more accurately simulate the wake structure in future LES simulations. Alin et al. (2010) extended the LES investigation of the Italian National Institute for Naval Architecture Studies and Testing (INSEAN) E1619 propeller by employing finer grids, up to 13 million cells. Despite the grid refinement, the constrained resolution of the computational mesh continued to limit the analysis to the downstream wake flow. The self-propulsion of a notional submarine model equipped with an INSEAN E1619 propeller was simulated by Posa and Balaras (2018) using LES method. To capture the dominant hub vortex in the downstream wake, they utilized an extensive grid number of more than 3 billion. Subsequently, Posa et al. (2019) employed an immersed boundary methodology coupled with LES to investigate propeller-rudder interaction. They simulated three configurations using 1024 Central Processing Unit (CPU) cores, utilizing approximately 1.7 billion grids for each case. The total computational time for each simulation was about 6 million CPU hours. Due to the high computational costs, the majority of LES studies focused on simulating propellers in model scale. The RANS method, applied in present work, remains a valuable tool for studying the flow characteristics and performance of full-scale marine propellers due to its computational efficiency.

The national and international organizations, as well as the classification societies and IMO have emphasized the importance of underwater radiated noise (URN). For instance, Det Norske Veritas Germanisher Lloyd (DNV GL) issued SILENT class notations in 2010, highlighted the noise-related issues and encouraged ship owners to

take measures to reduce URN emissions (DNV, 2010). Subsequently, International Maritime Organisation (IMO) published a non-mandatory guideline in 2014 aimed at providing advice to ship owners and designers on reducing URN generated by commercial ships (IMO, 2014). In response to these concerns, numerous numerical simulations have been carried out to explore the influence of cavitation on propeller-generated URN. Recently, a series numerical and experimental studies have been conducted by Sezen and Atlar (2022, 2023a,b) to investigate the hydroacoustic performance of the benchmark Princess Royal propeller. The effects of various factors, including incoming flow conditions, scale ratios, turbulence models and hydroacoustic models, on the predictions were carefully examined. The cavitation on and off the blades was modelled successfully in comparison with the experimental data. It was observed that due to the lack of cavitation dynamics, especially tip vortex cavitation, the the propeller URN was under-predicted at certain frequencies compared to the model scale test campaigns and full-scale measurements.

1.3 Problem Statement

From the literature review, it becomes evident that little effort has been made to understand the effects of propeller manufacturing tolerances or defects on the propeller performance, and no study in the public literature was found to address this issue. A preliminary CFD study of Hally (2018) indicates that the manufacturing defects potentially have large impact on propeller cavitation performance. It is also well know that the propeller cavitation can result in load variation and lead to reductions in propulsive and hydroacoustic performance. A better understanding of the influences

of manufacturing tolerances on the propeller performance can help to mitigate these undesirable effects.

Canadian propeller manufacturer, Dominis Engineering, has been at the forefront of propeller manufacturing since its formation in 1985. Over years the company has developed state-of-the-art technologies for manufacturing of propellers and propeller blades. The precision routinely achieved using Dominis's technology is significantly better than Class S of ISO 484 (ISO, 2005a,b). In light of this technological excellence, it is necessary to better understand the sensitivity of propeller performance to manufacturing defects within Class S so that manufacturers can develop appropriate, cost-effective processes; naval architects can better specify tolerances to their needs; and owners and regulators can rest assured that vessels will meet their requirements.

In real-world scenarios, marine propellers operate in harsh, corrosive environments characterized by biofouling. The cleaning and polishing of propeller blades to remove fouling may also introduce tolerances.

Blade edges and tips are the most sensitive parts of the geometry of a propeller. Robotic and hand grinding of blade edges could easily introduces inaccuracies and deviations from design. This thesis uses CFD to gain a comprehensive understanding of the effects of leading-edge defects on propeller cavitation performance.

1.4 Leading-Edge Manufacturing Tolerances

Manufacturing tolerances for new ship propellers are specified by the International Standards Organization (ISO), which defines the manufacturing standards for propeller construction. The ISO 484 standards (ISO, 2005a,b) for manufacturing toler-

ances of ship propellers were established in 1981 by adopting an ISO Recommendation of 1966. ISO 484-1 can be applied to propellers with diameters greater than 2.5 m, while ISO 484-2 is applicable to propellers with diameters from 0.8 m to 2.5 m. Table 1.1 presents a list of vessel types and their intended ISO manufacturing tolerance classes. As shown in Table 1.1, four classes of tolerances were defined in each standard.

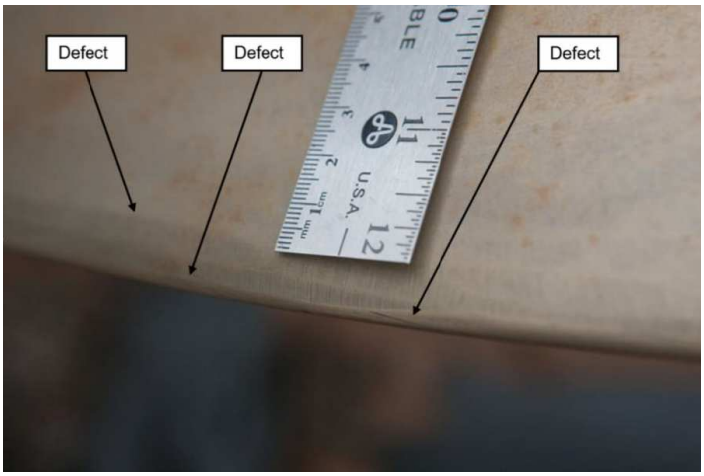

Figure 1.1: Real leading-edge defects on a propeller blade in service (Gospodnetic, 2022)

There exists an extensive types of potential defects that can be subject to examination. The tightest dimensional tolerances on ISO 484 standards are applied for the geometry of the leading edge, clearly demonstrating the propeller manufacturers' awareness of the critical characteristic of this region. Real leading-edge (LE) defects on a propeller blade from DRDC-Atlantic (Gospodnetic, 2022) is shown in Fig. 1.1. These tolerances could potentially be attributed to the manual grinding process conducted during the manufacturing phase. It can be seen that the size of real defect is small and varies at different blade sections. The start points of these defects do not

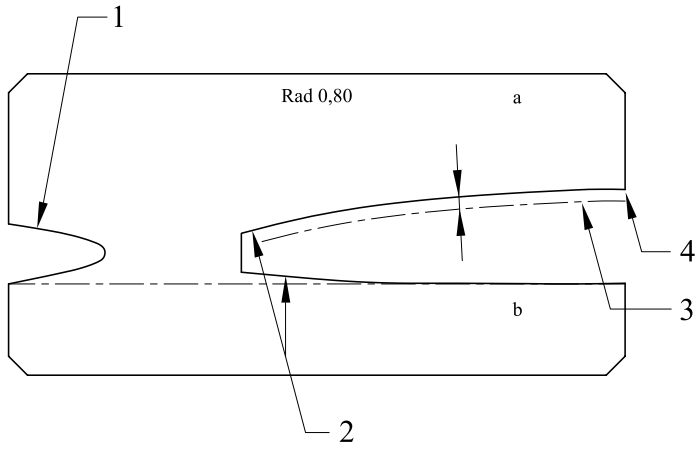

1: Short nose template made to size + max tolerance;
2: Form templates for pressure and suction sides separated by 6 mm for independent application;
3: Theoretical suction side profile;
4: Contact surface for suction side.

Figure 1.2: 3-Part template (ISO, 2005a,b)

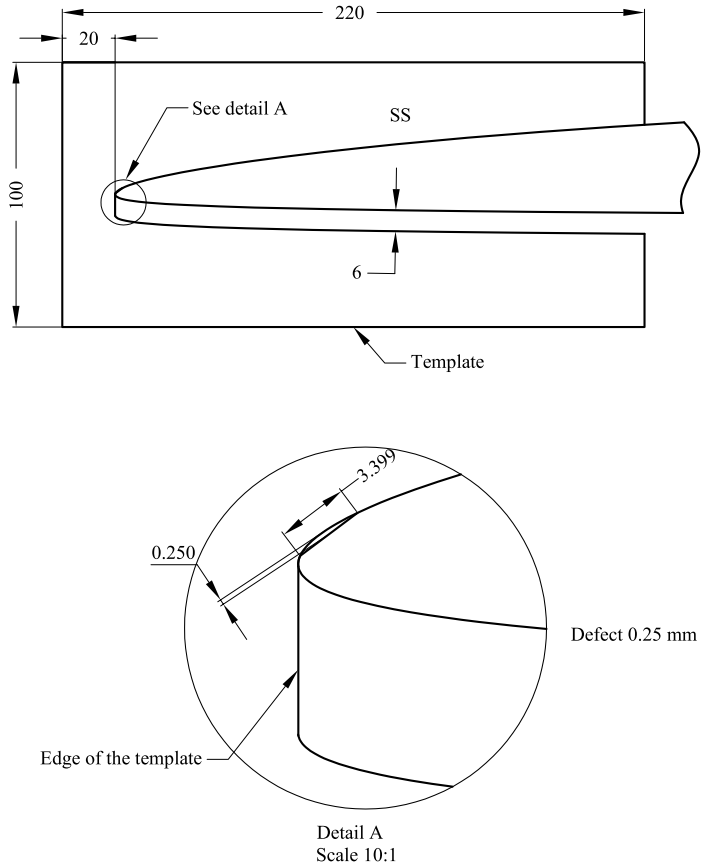

Figure 1.3: Template and the foil section with 0.25 mm deviation (Jin et al., 2020)

Table 1.1: The accurate class for manufacturing tolerance

Class	Manufacturing accuracy	Ship type
S	Very high accuracy	Naval vessels such as frigates and destroyers
		Cruise vessels
		High speed ferries
		Research vessels
		Special purpose merchant vessels
I	High accuracy	General merchant ships
		Deep sea trawler
		Tugs
		Ferries
		Naval auxiliary vessels
II	Medium accuracy	Low-power craft
		Low-speed craft
		Inshore finishing vessels
		Work boats
III	Wide tolerances	Similar types as Class II

align precisely with the leading edge. For geometric simplification in this thesis, the flat sections, resembling the real defects, with the constant deviations at leading edge are intended to represent the defects caused by grinding.

A LE defect is determined by measuring the difference between the template and the manufactured blade section. According to ISO 484 standards (ISO, 2005a,b), Class S tolerances for LE deviations are defined as ± 0.5 mm for a 1-part template or

± 0.25 mm for the 3-part template (see Fig. 1.2). For example, Fig. 1.3 shows how a foil with 0.25 mm LE defect is measured using a 3 part template (note that the short nose template was omitted here for clarity). In Detail A, the straight line on the upper surface is used to represent the defect at leading edge.

1.5 Research Aims and Objectives

The present research aims to investigate the effects of leading-edge manufacturing defects on cavitation performance of marine propeller. The main objectives and contributions of this thesis are summarized as follows:

- Calculating cavitation performance of foils in infinite flow. The cavitation buckets of DTMB modified NACA-66 $a = 0.8$ foil had been predicted with potential flow based method in Brockett (1966). Hally (2008) conducted a preliminary investigation on the impact of leading-edge defects on cavitation performance for 2-D foils using three RANS solvers, ANASYS CFX, OpenFOAM and TRANSOM. Small geometric variations relative to the dimensions of the propeller suggest that much could be learned from less computationally intensive simulations based on 2-D sections before full-scale 3-D propeller simulations. In present work, the effect of simulation parameters, such as domain size, grid resolution, grid distribution, grid stretching ratio, grid aspect ratio, first-grid spacing, y^+, and turbulence model, on the solution were carefully examined. Based on the results of convergence studies, the best-practice settings for 2-D simulations with the steady RANS solver in Star-CCM+ were proposed. Furthermore, using the best-practice settings, the cavitation buckets for the mod-

ified NACA-66 sections (a=0.8, t/c=0.0416, f/c=0.014) with three different sizes of defects near LE, representing three levels of manufacturing tolerances within ISO 484 Class S, were compared at various angles of attack.

- Calculating cavitation performance of foils in cavitation tunnel. The foils with and without LE defects were intended to be tested in a cavitation tunnel with 1 m by 1 m test section. It was important to investigate the differences in 2-D and 3-D solutions and to further quantify the effect of LE defect in future validation studies. Effects of RANS modelling parameters, such as domain size, span, grid aspect ratio, first-grid spacing, y^+, and turbulence model, on the solutions were carefully examined. Based on the results of convergence studies, the best-practice settings for 3-D simulations with the steady RANS solver in Star-CCM+ were proposed. Using the best practices, studies were then carried out for the foils with no defect, 0.10 mm defect, 0.25 mm defect and 0.50 mm defect at various angles of attack. Furthermore, the preliminary validation studies for the foils of 0.525 m span with no defect and 0.50 mm defect were also carried out on the cavitation buckets.

- Calculating cavitation performance of a full-scale propeller. There is a need to investigate the effects of LE defects on cavitation performance of a full-scale marine propeller. In this study, the simulations were carried out with full-scale propellers, based on the geometry of DTMB 5168 propeller. Convergence studies were first carried out for the open-water simulation to examine the effects of domain size, grid size, y^+ and turbulence model on the solutions. Based on the findings from these convergence studies, the best-practice settings

were proposed. Using the recommended settings, CFD simulations were then extended to the same propeller with three different sizes of LE defects.

1.6 Outline of the Thesis

This dissertation is organized into seven chapters as follows.

In Chapter 1, the research background of manufacturing tolerances problems on marine propeller performance is briefly described. A literature review on predicting cavitation performance of propeller by using experimental studies and numerical approaches is detailed. The objectives and the scope of this research are also presented.

Chapter 2 shows the details of the research methodologies. The governing equations for various turbulence models used in this thesis are presented. The description of the least square root (LSR) method, introduced by Eça and Hoekstra (2014), for uncertainty analysis is also included in this chapter.

Chapter 3 studied the effects of manufacturing defects on the cavitation performance of a propeller blade section in infinite flow. DTMB modified NACA-66 $a = 0.8$ sections without and with LE defects were investigated at various angles of attack using 2-D steady RANS solvers on structured grids. Numerical results were compared with potential-flow solutions by Brockett (1966) and the RANS solutions with ANSYS CFX and TRANSOM by Hally (2008).

Chapter 4 shows the 3-D CFD simulations for the foils of 1 m span in a cavitation tunnel with 1 m by 1 m test section. Convergence studies on RANS modelling parameters, such as domain size, grid aspect ratio, first-grid spacing, y^+, and turbulence model were conducted. The best-practice settings were then summarized and

recommended for the 3-D simulations of intended cavitation tunnel tests. The results of predicted cavitation buckets in terms of minimum pressure coefficient for foils of 1 m span were discussed and compared with those from 2-D simulations.

Due to the limitation of the foil support mechanism of cavitation tunnel, the span of 0.525 m was applied to minimize the force and moment on the foil. The 3-D numerical simulations for the foils of 0.525 m span in a cavitation tunnel were carried out in Chapter 5. Convergence studies were also performed to examine the sensitivity of solutions to domain size, grid aspect ratio, first-grid spacing, y^+, and turbulence model. Furthermore, the preliminary validation studies for the foils of 0.525 m span with no defect and 0.5 mm defect were also carried out on the cavitation buckets.

The objective of Chapter 6 is to investigate the effects of LE defect on a full-scale marine propeller. Validation studies were carried out for the model-scale propeller, the wake field, open-water and cavitation performance were presented and compared with the experimental data (Chesnakas and Jessup, 1998). The best-practice settings for the model-scale propeller were extended and verified for the full-scale propellers with no and 0.5 mm defects. Using the best-practice modelling settings for full-scale propellers, simulations were carried out to full-scale propellers without and with 0.10 mm, 0.25 mm, and 0.50 mm LE defects. The influences of LE defect on open-water and cavitation performance are presented and discussed.

In Chapter 7, this thesis ends with conclusions and some future perspectives.

1.7 List of Publications

1.7.1 Journal Articles

- Jin, S., Peng, H., Qiu, W., Oldfield, C., and Stockdill, B. (2023). Development of best modelling practices for RANS simulations of propeller-hull interaction in model scale. *Physics of Fluids*, 35(10): 105129.

- Jin, S., Peng, H., Qiu, W., Hunter, R., and Thompson, S. (2023). Numerical simulation of planing hull motions in calm water and waves with overset grid. *Ocean Engineering*, (287): 115858.

- Jin, S., Zha, R., Peng, H., Qiu, W., and McTaggart, K. Determination of manoeuvring force coefficients for a destroyer model with OpenFOAM. *Journal of Ship Research*. (Accepted)

- Jin, S., Peng, H., Qiu, W., and Gospodnetic, S. Numerical studies on effects of leading-edge propeller manufacturing defects on cavitation performance. *Journal of Marine Systems and Ocean Technology*. (Submitted)

- Jin, S., Peng, H., and Qiu, W. Numerical Study on Effects of Leading-Edge Manufacturing Defects on Cavitation Performance of a Full-Scale Propeller - Part I: Simulation for the Model- and Full-Scale Propellers without Defect. *Ocean Engineering*. (To be submitted)

- Jin, S., Peng, H., and Qiu, W. Numerical Study on Effects of Leading-Edge Manufacturing Defects on Cavitation Performance of a Full-Scale Propeller -

Part II: Simulation for the Full-Scale Propeller with Defect. *Ocean Engineering*. (To be submitted)

1.7.2 Conference Papers

- Jin, S., Peng, H., and Qiu, W. (2024). Effects of thickness manufacturing tolerance on cavitation performance of a full-scale propeller. In *Proceedings of the 8th International Symposium on Marine Propulsors*. (Accepted)

- Jin, S., Peng, H., and Qiu, W. (2023). RANS simulations of propeller-hull interaction in model scale with the best-practice settings. In *Proceedings of the 42nd International Conference on Ocean, Offshore and Arctic Engineering*.

- Jin, S., Zha, R., Peng, H., and Qiu, W. (2021). Comparison of 2-D and 3-D RANS studies on effects of leading-edge propeller manufacturing defects on cavitation performance. In *Proceedings of the 29th Annual Conference of the Computational Fluid Dynamics Society of Canada*.

- Jin, S., Peng, H., Qiu, W., Hunter, R., and Thompson, S. (2021). Simulation of planing hull motions in calmwater and waves with overset grid. In *Proceedings of the 29th Annual Conference of the Computational Fluid Dynamics Society of Canada*.

- Jin, S., Zha, R., Peng, H., and Qiu, W. (2021). Uncertainty analysis for CFD simulations of flow over flat plate and foil with OpenFOAM. In *Proceedings of the 29th Annual Conference of the Computational Fluid Dynamics Society of Canada*.

- Jin, S., Zha, R., Peng, H., Qiu, W., and Gospodnetic, S. (2020). 2D CFD studies on effects of leading-edge propeller manufacturing defects on cavitation performance. In *SNAME Transaction*.

- Zha, R., Jin, S., Peng, H., and Qiu, W. (2021). Comparable studies on effects of leading-edge propeller manufacturing defects on cavitation performance. In *Proceedings of the 29th Annual Conference of the Computational Fluid Dynamics Society of Canada*.

- Zha, R., Zhan, D., Jin, S., Peng, H., Qiu, W., Oldfield, C., and Stockdill, B. (2021). Developing best modelling practices for RANS simulations of propeller-hull interaction. In *Proceedings of the 29th Annual Conference of the Computational Fluid Dynamics Society of Canada*.

- Jin, S., Peng, H., Qiu, W., Hally, D., Gauthier, M., and Gospodnetic, B. (2019). Numerical investigation of the impact of manufacturing tolerances on marine propeller performance. In *Proceedings of the Joint Canadian Society for Mechanical Engineering and CFD Society of Canada International Congress 2019*.

Chapter 2

Research Methodology

2.1 Governing Equations

The governing RANS equations for the incompressible viscous flow are:

$$\frac{\partial \overline{u}_i}{\partial x_i} = 0 \tag{2.1}$$

$$\rho \frac{\partial \overline{u}_i}{\partial t} + \rho \frac{\partial}{\partial x_j} \left(\overline{u}_i \overline{u}_j + \overline{u'_i u'_j} \right) = -\frac{\partial \overline{p}}{\partial x_i} + \frac{\partial \overline{\tau}_{ij}}{\partial x_j} + \rho g_i \tag{2.2}$$

where $\overline{u}_{i,\ i=1,\ 2 \text{ and } 3}$, denotes the mean velocity components along x-, y- and z-axis, respectively, for a three-dimensional flow, $\overline{p}$ is the mean pressure, ρ is the density of water, g_i represents the acceleration of gravity, and $-\rho\overline{u'_i u'_j}$ are the Reynolds stresses. The mean viscous stress tensor $\overline{\tau}_{ij}$ is defined by:

$$\overline{\tau}_{ij} = \mu \left(\frac{\partial \overline{u}_i}{\partial x_j} + \frac{\partial \overline{u}_j}{\partial x_i} \right) \tag{2.3}$$

where μ is the dynamic viscosity of water.

2.2 Turbulence Modeling

The Reynolds stresses can be solved based on the Boussinesq hypothesis using the eddy viscosity turbulence models, or be solved from the transport equation based on Reynolds stress models. In the present studies, one-equation and two-equation eddy viscosity models as well as Reynolds stress models were employed to solve the RANS equations.

In the eddy viscosity turbulence models, it is assumed that the Reynolds stresses are related to the mean velocity gradients, the turbulence kinetic energy and the eddy viscosity, i.e.,

$$-\rho\overline{u_i'u_j'} = \mu_t\left(\frac{\partial\overline{u}_i}{\partial x_j} + \frac{\partial\overline{u}_j}{\partial x_i}\right) - \frac{2}{3}\rho k\delta_{ij} \tag{2.4}$$

where μ_t represents the eddy viscosity, δ_{ij} is the Kronecker delta, $k = \frac{1}{2}\overline{u_i'u_j'}$ is the turbulent kinetic energy that can be solved from the transport equations. The Reynolds stress tensor is linearly proportional to the mean strain rate.

Six turbulence models, including the Spalart-Allmaras (SA) model, the standard $k-\varepsilon$ model, the standard $k-\omega$ model, the shear stress transport (SST) $k-\omega$ model, the linear pressure strain Reynolds stress model (LPS-RSM) and the elliptic blending Reynolds stress model (EB-RSM), were applied in this thesis.

The one-equation turbulence model, Spalart-Allmaras (SA) (Spalart and Allmaras, 1992), used by Star-CCM+ solves a transport equation for the modified turbulence viscosity, $\tilde{\nu}$, to determine the turbulence eddy viscosity, μ_t, i.e.,

$$\mu_t = \rho f_{\nu 1}\tilde{\nu} \tag{2.5}$$

where $f_{\nu 1} = \chi^3/\left(\chi^3 + C_{v1}^3\right)$ is the damping function and $\chi = \widetilde{\nu}/\nu$. The transport

equation for the modified turbulence viscosity is:

$$\begin{aligned}\frac{\partial\tilde{\nu}}{\partial t}+\overline{u}_i\frac{\partial\tilde{\nu}}{\partial x_i}=&C_{b1}\left[1-f_{t2}\right]\tilde{S}\tilde{\nu}-\left[C_{w1}f_w-\frac{C_{b1}}{\kappa^2}f_{t2}\right]\left(\frac{\tilde{\nu}}{d}\right)^2\\&+\frac{1}{\sigma_{\tilde{\nu}}}\left[\frac{\partial}{\partial x_i}\left((\nu+\tilde{\nu})\frac{\partial\tilde{\nu}}{\partial x_i}\right)+c_{b2}\frac{\partial\tilde{\nu}}{\partial x_j}\frac{\partial\tilde{\nu}}{\partial x_j}\right]\end{aligned}\tag{2.6}$$

where d is the distance to wall, while the other model parameters, $\tilde{S}$, f_w, f_{t2} and C_{w1}, are defined as,

$$\tilde{S}=\sqrt{2\overline{\Omega}_{ij}\overline{\Omega}_{ij}}+\frac{\tilde{\nu}}{\kappa^2d^2}f_{v2},\quad f_{v2}=1-\frac{\chi}{1+\chi f_{v1}}\tag{2.7}$$

$$f_w=g_{\tilde{\nu}}\left[\frac{1+C_{w3}^6}{g_{\tilde{\nu}}^6+C_{w3}^6}\right]^{1/6},\quad g_{\tilde{\nu}}=r_{\tilde{\nu}}+C_{w2}\left(r_{\tilde{\nu}}^6-r_{\tilde{\nu}}\right)\tag{2.8}$$

$$r_{\tilde{\nu}}=\min\left(\frac{\tilde{v}}{\tilde{S}\kappa^2d^2},10\right)\tag{2.9}$$

$$f_{t2}=C_{t3}\exp\left(-C_{t4}\chi^2\right)\tag{2.10}$$

$$C_{w1}=C_{b1}/\kappa^2+\left(1+C_{b2}\right)/\sigma_{\tilde{\nu}}\tag{2.11}$$

where $\overline{\Omega}_{ij}=\frac{1}{2}\left(\partial\overline{u}_i/\partial x_j-\partial\overline{u}_j/\partial x_i\right)$ is the mean rotation tensor. The default model coefficients are summarized in Table 2.1. The details of SA model can be found in the work of Spalart and Allmaras (1992). The SA model has good convergence and robustness for specific flows. However, the turbulence length and time scales are not well defined as they are in other two-equation models.

Table 2.1: The default coefficients used in Spalart-Allmaras model

$\sigma_{\tilde{\nu}}$	C_{b1}	C_{b2}	κ	$C_{\omega2}$	$C_{\omega3}$	C_{t1}	C_{t2}	C_{t3}	C_{t4}
2/3	0.1355	0.622	0.41	0.3	2.0	1.0	1.0	1.1	2.0

Two-equation models are widely used to solve the RANS equations, in which both the velocity and length scale are solved using separate transport equations. The turbulence length scale is estimated from the kinetic energy and its dissipation rate. The standard $k-\varepsilon$ model, the standard $k-\omega$ model and the SST $k-\omega$ models were investigated in the present work.

In the standard $k-\varepsilon$ model (Launder and Spalding, 1974), the turbulent eddy viscosity is calculated as:

$$\mu_t = \rho C_\mu f_\mu k T \tag{2.12}$$

where C_μ is a model coefficient, f_μ is defined as 1.0, and T is the turbulent time scale determined by:

$$T = \max(T_e, C_t\sqrt{\frac{\nu}{\varepsilon}}) \tag{2.13}$$

where $T_e = k/\varepsilon$ is the large-eddy time scale, C_t is a model coefficient, ν is the kinematic viscosity. The transport equations for the turbulent kinetic energy, k, and the turbulence dissipation rate, ε, are given as,

$$\frac{\partial(\rho k)}{\partial t} + \frac{\partial\left(\rho k \overline{u}_i\right)}{\partial x_i} = \frac{\partial}{\partial x_i}\left[\left(\mu + \frac{\mu_t}{\sigma_k}\right)\frac{\partial k}{\partial x_i}\right] + P_k + S_k - \rho(\varepsilon - \varepsilon_0) \tag{2.14}$$

$$\frac{\partial(\rho \varepsilon)}{\partial t} + \frac{\partial\left(\rho \varepsilon \overline{u}_i\right)}{\partial x_i} = \frac{\partial}{\partial x_i}\left[\left(\mu + \frac{\mu_t}{\sigma_\epsilon}\right)\frac{\partial \epsilon}{\partial x_i}\right] + \frac{1}{T_e}C_{\varepsilon 1}P_\varepsilon - C_{\varepsilon 2}f_2\rho(\frac{\varepsilon}{T_e} - \frac{\varepsilon_0}{T_0}) + S_\varepsilon \tag{2.15}$$

where σ_k, σ_ε, $C_{\varepsilon 1}$ and $C_{\varepsilon 2}$ are the model coefficients, P_k and P_ε are the production terms, $f_2 = 1$ is applied for the standard $k-\varepsilon$ model, S_k and S_ε are the source terms. k_0 and ε_0 are the ambient turbulence values in the source terms that counteracts turbulence decay (Spalart and Rumsey, 2007). The possibility to impose an ambient source term also leads to the definition of a specific time-scale T_0 that is defined as:

$$T_0 = \max\left(\frac{k_0}{\varepsilon_0}, C_t\sqrt{\frac{v}{\varepsilon_0}}\right) \tag{2.16}$$

where constant coefficient, C_t, can be found in the Table 2.2.

Table 2.2: The default coefficients used in the standard $k-\varepsilon$ model

σ_k	σ_ε	C_M [1]	C_t	$C_{\varepsilon 1}$	$C_{\varepsilon 2}$	C_μ
1.0	1.3	2.0	1.0	1.44	1.92	0.09

For the standard $k-\omega$ model (Wilcox, 2008), the turbulent eddy viscosity is related to the turbulence kinetic energy, k, and the specific turbulence dissipation rate, ω, which is also referred to the mean frequency of the turbulence. The turbulent eddy viscosity is calculated as:

$$\mu_t = \rho k T \tag{2.17}$$

where $T = \alpha^*/\omega$ is the turbulence time scale in the standard $k-\omega$ model and α^* is a model coefficient. The transport equations for the turbulent kinetic energy, k, and the specific dissipation rate, ω, are written as:

$$\begin{aligned}\frac{\partial(\rho k)}{\partial t} + \frac{\partial\left(\rho k \overline{u}_i\right)}{\partial x_i} =& \frac{\partial}{\partial x_i}\left[\left(\mu + \sigma_k \mu_t\right)\frac{\partial k}{\partial x_i}\right] + G_k + G_b \\ & -\rho\beta^* f_{\beta^*}(\omega k - \omega_0 k_0) + S_k\end{aligned} \tag{2.18}$$

$$\frac{\partial(\rho\omega)}{\partial t} + \frac{\partial\left(\rho\omega \overline{u}_i\right)}{\partial x_i} = \frac{\partial}{\partial x_i}\left[\left(\mu + \sigma_\omega \mu_t\right)\frac{\partial \omega}{\partial x_i}\right] + G_\omega + S_\omega - \rho\beta f_\beta(\omega^2 - \omega_0^2) \tag{2.19}$$

where σ_k and σ_ω are turbulence model coefficients, G_k, G_b and G_ω are the production terms of turbulent, buoyancy and specific dissipation, respectively, and f_{β^*} is the free-shear modification factor or the vortex-stretching modification factor, k_0 and ω_0 are the ambient turbulence values that counteract turbulence decay (Spalart and Rumsey, 2007), S_k and S_ω are the source terms. The $k-\omega$ model demonstrates superior ac-

curacy in predicting strong vortices and near-wall interactions compared to the $k-\varepsilon$ models. The standard $k-\omega$ model and its variations have shown to be able to give accurate predictions and are by far the most widely applied turbulence models in the field of ship hydrodynamics. For example, 80% of the submissions for the Gothenburg 2010 Workshop were simulated with the $k-\omega$ model (ITTC, 2017).

Table 2.3 presents the values of default parameters for standard $k-\omega$ model. More detailed description of the standard $k-\omega$ model can be found in the study of Wilcox (2008).

Table 2.3: The default coefficients used in the standard $k-\omega$ model

α^*	β	β^*	σ_k	σ_ω
1.0	0.072	0.09	0.5	0.5

The SST $k-\omega$ model (Menter, 1994) introduces the cross-diffusion term, D_ω, and improves the prediction of the onset and the flow separation under adverse pressure gradients. The transport equations are the same as those of the standard $k-\omega$ model when setting D_ω as zero in the near field. Furthermore, the non-linear production, G_{nl}, is included in the transport equation of turbulence kinetic energy. Then, the transport equations can be expressed as

$$\begin{aligned}\frac{\partial(\rho k)}{\partial t}+\frac{\partial\left(\rho k\overline{u}_i\right)}{\partial x_i}=&\frac{\partial}{\partial x_i}\left[\left(\mu+\sigma_k\mu_t\right)\frac{\partial k}{\partial x_i}\right]+G_k+G_b+G_{nl}\\&-\rho\beta^* f_{\beta^*}(\omega k-\omega_0 k_0)+S_k\end{aligned} \tag{2.20}$$

$$\begin{aligned}\frac{\partial(\rho\omega)}{\partial t}+\frac{\partial\left(\rho\omega\overline{u}_i\right)}{\partial x_i}=&\frac{\partial}{\partial x_i}\left[\left(\mu+\sigma_\omega\mu_t\right)\frac{\partial\omega}{\partial x_i}\right]+G_\omega+S_\omega\\&+2\left(1-F_1\right)\frac{\rho\sigma_{\omega2}}{\omega}\frac{\partial k}{\partial x_i}\frac{\partial\omega}{\partial x_i}-\rho\beta f_\beta(\omega^2-\omega_0^2)\end{aligned}\tag{2.21}$$

where $\sigma_k=F_1\sigma_{k1}+\left(1-F_1\right)\sigma_{k2}$, $\sigma_\omega=F_1\sigma_{\omega1}+\left(1-F_1\right)\sigma_{\omega2}$, $\beta=F_1\beta_1+\left(1-F_1\right)\beta_2$, and the turbulent eddy viscosity, μ_t, is computed with

$$\begin{aligned}\mu_t=&\rho kT\\T=&\min\left(\frac{\alpha^*}{\omega},\frac{a_1}{SF_2}\right)\\F_2=&\tanh\left[\left(\max\left(\frac{2\sqrt{k}}{\beta^*\omega d},\frac{500v}{d^2\omega}\right)\right)^2\right]\\\beta^*=&F_1\beta_1^*+\left(1-F_1\right)\beta_2^*\end{aligned}\tag{2.22}$$

in which, d represents the distance to the wall, S is the modulus of the mean strain rate tensor, the specific values of a_1, β_1^* and β_2^* are 0.31, 0.09 and 0.09, respectively.

The blending function F_1, which combines the near-wall contribution of a coefficient with its value far away from the wall, is defined as

$$\begin{aligned}F_1=&\tanh\left(F_{\omega1}^4\right)\\F_{\omega1}=&\min\left[\max\left(\frac{\sqrt{k}}{0.09\omega d},\frac{500v}{d^2\omega}\right),\frac{2k}{d^2\mathrm{CD}_{k\omega}}\right]\\\mathrm{CD}_{k\omega}=&\max\left(2\rho\sigma_{\omega2}\frac{1}{\omega}\frac{\partial k}{\partial x_i}\frac{\partial\omega}{\partial x_i},10^{-20}\right)\end{aligned}\tag{2.23}$$

Detailed formulations can be found in the work by Menter (1994). The modelling coefficients of SST $k-\omega$ model are summarized in Table 2.4.

In the Reynolds stress models (RSM), the transport equations are solved for all the components of the Reynolds stress tensor and the turbulence dissipation rate,

$$\frac{\partial\left(\rho\overline{u_i'u_j'}\right)}{\partial t}+\frac{\partial\left(\rho\overline{u}_m\overline{u_i'u_j'}\right)}{\partial x_m}=D_{ij}+P_{ij}+F_{ij}+\varphi_{ij}-\varepsilon_{ij}\tag{2.24}$$

Table 2.4: The default coefficients used in the SST $k-\omega$ model

a_1	α^*	β_1	β_2	β_1^*	β_2^*	σ_{k1}	σ_{k2}	$\sigma_{\omega1}$	$\sigma_{\omega2}$
0.31	1.0	0.075	0.0828	0.09	0.09	0.85	1.0	0.5	0.856

where D_{ij} is the turbulent diffusion term, P_{ij} is the turbulent production term, F_{ij} is the rotation term, φ_{ij} is the pressure-strain correlation term, and ε_{ij} is the dissipation rate tensor.

The modelling of diffusion term D_{ij} is based on the assumption that the rate of transport of Reynolds stresses by diffusion is proportional to the gradients of Reynolds stresses. Following the study of Lien and Leschziner (1994), a simple isotropic form of D_{ij} is

$$D_{ij} = \frac{\partial}{\partial x_m}\left[\left(\mu + \frac{\mu_t}{\sigma_k}\right)\frac{\partial \overline{u_i' u_j'}}{\partial x_m}\right] \tag{2.25}$$

where the turbulent viscosity μ_t in the elliptic blending model is determined by

$$\begin{aligned} \mu_t =& \rho C_\mu k T \\ T =& \max\left(\frac{k}{\varepsilon}, C_t\sqrt{\frac{v}{\varepsilon}}\right) \end{aligned} \tag{2.26}$$

in which C_t is the modelling coefficient.

The production term P_{ij} in Eq. (2.24) is closed, which does not require modelling, and it can be calculated with

$$P_{ij} = -\left(\overline{u_m' u_i'}\frac{\partial \overline{u}_j}{\partial x_m} + \overline{u_m' u_j'}\frac{\partial \overline{u_i}}{\partial x_m}\right) \tag{2.27}$$

In the study of Versteeg and Malalasekera (2007), the rotating term F_{ij} is given as

$$F_{ij} = -2\omega_k\left(\overline{u_m' u_i'}e_{jkm} + \overline{u_m' u_j'}e_{ikm}\right) \tag{2.28}$$

where ω_k is the rotation vector, $e_{ijk} = 1$ if i, j, k are in cyclic order and are distinct, $e_{ijk} = -1$ when i, j, k are in anti-cyclic order and are different and $e_{ijk} = 0$ in case any two indices are same.

In the elliptic blending Reynolds stress model (Manceau and Hanjalić, 2002), the pressure-strain model is based on a blending of near-wall and quadratic pressure-strain models for the pressure-strain and dissipation:

$$\varphi_{ij} - \varepsilon_{ij} = \left(1 - \alpha^3\right)\left(\varphi_{ij}^w - \varepsilon_{ij}^w\right) + \alpha^3\left(\varphi_{ij}^h - \varepsilon_{ij}^h\right) \tag{2.29}$$

where the superscripts, w and h, denote the near-wall layer and outer region, respectively. The blending parameter α is the solution of the elliptic equation,

$$\alpha - L^2\nabla^2\alpha = 1 \tag{2.30}$$

where the turbulent length-scale L is defied as

$$L = C_l \max\left(\frac{k^{3/2}}{\varepsilon}, C_\eta \frac{v^{3/4}}{\varepsilon^{1/4}}\right) \tag{2.31}$$

The traditional modelling of the dissipation rate tensor ε_{ij} is based on the assumption that the small dissipative eddies are isotropic. The dissipation can then be simply compute by

$$\varepsilon_{ij} = \frac{2}{3}\varepsilon\delta_{ij} \tag{2.32}$$

where ε is dissipation rate of turbulent kinetic energy. The isotropic turbulent dissipation rate is solved from a transport equation analogous to the $k - \varepsilon$ model with various model coefficients.

$$\begin{aligned}\frac{\partial(\rho\varepsilon)}{\partial t} + \frac{\partial\left(\rho\varepsilon\overline{u}_m\right)}{\partial x_m} =& \frac{\partial}{\partial x_m}\left[\left(\mu + \frac{\mu_t}{\sigma_\epsilon}\right)\frac{\partial\epsilon}{\partial x_m}\right] - \frac{\varepsilon^2 C_{\varepsilon 2}\rho}{k} \\ &+ C_{\varepsilon 1}\frac{\varepsilon}{k}\left[\frac{1}{2}\operatorname{tr}(\mathbf{P}) + \frac{1}{2}C_{\varepsilon 3}\operatorname{tr}(\mathbf{G})\right]\end{aligned} \tag{2.33}$$

In general, the Reynolds stress models can predict complex flows with swirl rotation and high strain rates more accurately than eddy viscosity models. The elliptic blending Reynolds stress model of Manceau and Hanjalić (2002) was employed in both 2-D simulations and 3-D simulations for the model- and full-scale propellers. While the LPS-RSM (Gibson and Launder, 1978) was only applied in the 2-D simulations for the foil sections with and without LE defect. Furthermore, the values of modelling parameters for EB-RSM are presented in Table 2.5.

Table 2.5: The default coefficients used in the elliptic blending Reynolds stress model

σ_k	σ_ε	C_M	C_s	$C_{\varepsilon 1}$	$C_{\varepsilon 2}$	$C_{\varepsilon 3}$	C_μ	C_l	C_t	C_η
1.0	1.15	2.0	0.21	1.44	1.83	0.50	0.07	0.133	6.0	80

2.3 Uncertainty Analysis

In this thesis, the least square root (LSR) method, introduced by Eça and Hoekstra (2014), was employed to estimate the numerical uncertainty resulting from the spatial discretization. This method assumed that the iterative and round-off errors are insignificant when compared to the discretization error, which is considered the primary source of numerical uncertainty.

The discretization error can be estimated using the generalized Richardson extrapolation method, as proposed by Richardson (1911) in 1911.

$$\varepsilon_\Phi \simeq \delta_{RE} = \Phi_i - \Phi_{\text{exact}} = \alpha h_i^\gamma \tag{2.34}$$

where Φ_i represents the flow quantity Φ on the i-th grid, γ is the observed order of grid convergence, and h_i denotes the corresponding representative grid size. The representative grid size h_i can be determined by

$$h_i = \left[\frac{1}{N_i}\sum_{j=1}^{N_i}(\Delta V_j)\right]^{1/3} \tag{2.35}$$

where ΔV_j is the volume of cell j, and N_i is the total number of cells. For field variables, the local cell size can be used.

In the LSR method, three discretization error estimators are considered as alternatives:

$$\varepsilon_\Phi \simeq \delta_1 = \Phi_i - \Phi_{\text{exact}} = \alpha h_i \tag{2.36}$$

$$\varepsilon_\Phi \simeq \delta_2 = \Phi_i - \Phi_{\text{exact}} = \alpha h_i^2 \tag{2.37}$$

$$\varepsilon_\Phi \simeq \delta_{12} = \Phi_i - \Phi_{\text{exact}} = \alpha_1 h_i + \alpha_2 h_i^2 \tag{2.38}$$

where α_1 and α_2 are coefficients. The estimators defined in Eqs. (2.36), (2.37) and (2.38), are only applicable if the estimation with Eq. (2.34) is impossible or not reliable, i.e., the observed order of grid convergence, γ, is either too small or too large.

Steps to obtain U_{Φ_i} with the LSR method are summarized as follows:

- Determine the discretization error ε_Φ, the standard deviation,

  $\sigma_d = \min(\sigma_{RE}, \sigma_1, \sigma_2, \sigma_{12})$, and corresponding Φ_{fit}, where

$$\begin{aligned} \sigma_{RE} =& \sqrt{\frac{\sum_{i=1}^{n_g} n w_i (\Phi_i - \Phi_{\text{fit}})^2}{n_g - 3}} \\ \Phi_{\text{fit}} =& \Phi_0 + \alpha h_i^\gamma \end{aligned} \tag{2.39}$$

$$\begin{aligned}\sigma_1 =& \sqrt{\frac{\sum_{i=1}^{n_g} nw_i(\Phi_i - \Phi_{\text{fit}})^2}{n_g - 2}} \\ \Phi_{\text{fit}} =& \Phi_0 + \alpha h_i\end{aligned} \tag{2.40}$$

$$\begin{aligned}\sigma_2 =& \sqrt{\frac{\sum_{i=1}^{n_g} nw_i(\Phi_i - \Phi_{\text{fit}})^2}{n_g - 2}} \\ \Phi_{\text{fit}} =& \Phi_0 + \alpha h_i^2\end{aligned} \tag{2.41}$$

$$\begin{aligned}\sigma_{12} =& \sqrt{\frac{\sum_{i=1}^{n_g} nw_i(\Phi_i - \Phi_{\text{fit}})^2}{n_g - 3}} \\ \Phi_{\text{fit}} =& \Phi_0 + \alpha_1 h_i + \alpha_2 h_i^2\end{aligned} \tag{2.42}$$

In the equations above, w_i is the weight, n_g is the number of grids, and Φ_0 is the solution with $h_i = 0$.

- Determine a data range parameter, D_Φ, to assess the quality of the fit for ε_Φ.

$$D_\Phi = \frac{(\Phi_i)_{\max} - (\Phi_i)_{\min}}{n_g - 1} \tag{2.43}$$

where $(\Phi_i)_{\max}$ and $(\Phi_i)_{\min}$ are the maximum and the minimum values of Φ_i, respectively.

- Determine the factor of safety, F_s, from γ, σ_d and D_Φ. If $0.5 \leq \gamma \leq 2.1$ and $\sigma_d < D_\Phi$, $F_s = 1.25$. Otherwise, the value of F_s is set as 3.

- Obtain the uncertainty from Φ_0 and the factor of safety F_s.

$$\begin{aligned}U_{\Phi_i} =& F_s(\Phi_i - \Phi_0) + \sigma_d + |\Phi_i - \Phi_{\text{fit}}| \qquad \sigma_d \leq D_\Phi \\ U_{\Phi_i} =& 3\frac{\sigma_d}{D_\Phi}(\Phi_i - \Phi_0 + \sigma_d + |\Phi_i - \Phi_{\text{fit}}|) \quad \sigma_d > D_\Phi\end{aligned} \tag{2.44}$$

Furthermore, the detailed procedure can be found in the work of Eça and Hoekstra (2014).

Chapter 3

2-D Simulations of the Foils in Infinite Flow

Small geometric variations relative to the dimensions of the propeller suggest that much could be learned from less computationally intensive simulations based on 2-D sections before full-scale propeller simulations. The investigation into propeller manufacturing tolerances was carried out for 2-D modified NACA-66 foils using the steady RANS solver on structured grids.

Convergence studies were first carried out for foils without and with defects using circular computational domains. Effects of simulation parameters, such as domain size, grid stretching ratio, grid aspect ratio, first-grid spacing, y^+, and turbulence model, on the solution were carefully examined. Turbulence models considered in this work include four eddy viscosity models: Spalart-Allmaras, $k-\varepsilon$, $k-\omega$, and SST $k-\omega$ models, and two Reynolds stress models: the elliptic bending model, EB-RSM, and the linear pressure-strain model, LPS-RSM. Based on the results of convergence

studies, the best-practice settings for 2-D simulations with the steady RANS solver in Star-CCM+ were proposed.

Using the best-practice settings, verification studies were carried out for the cavitation buckets of a DTMB modified NACA-66 (a=0.8, t/c=0.2, f/c=0.02) foil without defect by comparing the RANS results with the potential-flow solutions by Brockett (1966) and the RANS solutions with ANSYS CFX and TRANSOM (Hally, 2008). Note that t, f and c denote the maximum thickness, the maximum camber and the chord length of a foil section, respectively. Furthermore, the minimum pressure coefficients for the modified NACA-66 (a=0.8, t/c=0.0416, f/c=0.014) foils with three different sizes of defects near leading edge (LE), representing three levels of manufacturing tolerances within Class S, were compared at various angles of attack.

3.1 Coordinate System

The coordinate system for all 2-D simulations is presented in Fig. 3.1. The origin, O, is at the leading edge of the foil. The OX axis is from the leading edge to the trailing edge (TE) along the chord line and the OY axis is perpendicular to the chord line.

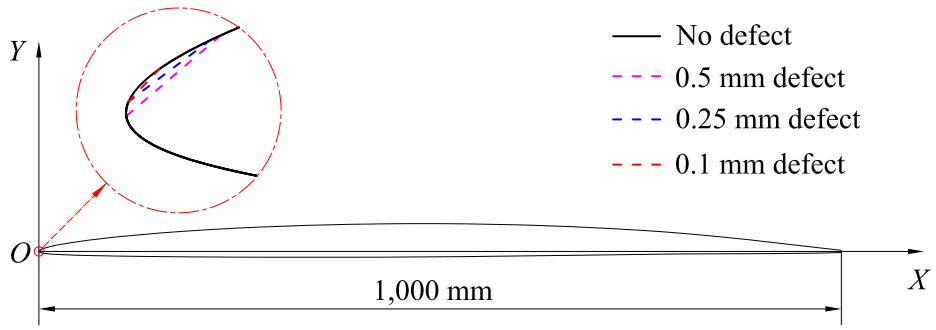

Figure 3.1: Modified NACA-66 (a = 0.8, t/c = 0.0416, f/c = 0.014) foils without and with LE defects

3.2 Geometry of LE Manufacturing Defects

Details of LE geometry for the foils ($a = 0.8$, $t/c = 0.0416$, $f/c = 0.014$) with and without defects are shown in Fig. 3.1. Dimensions of LE defects are given in Table 3.2. It can be found that the sizes of LE defects are relatively small when compared to the chord length of the foils. Note that all the defects are within Class S.

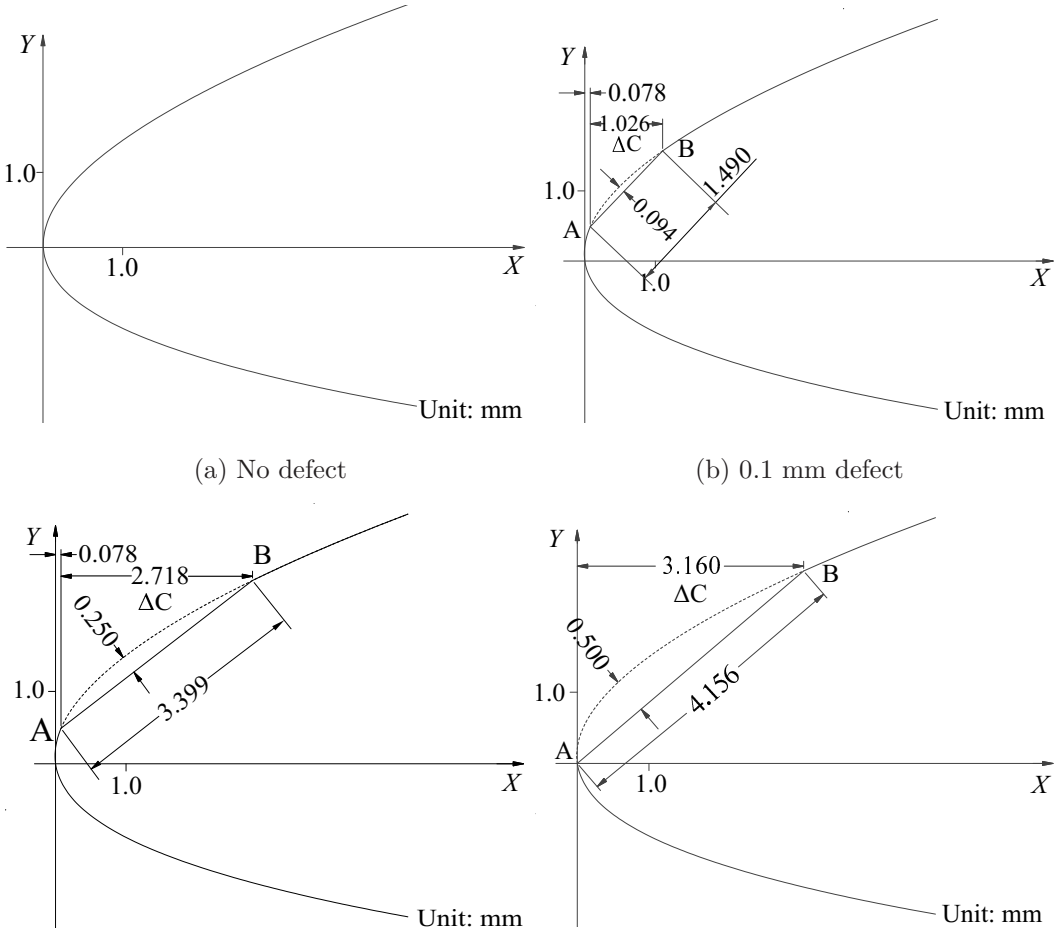

(a) No defect

(b) 0.1 mm defect

(c) 0.25 mm defect

(d) 0.5 mm defect

Figure 3.2: LE geometries for the foils with and without defects

Table 3.1: Dimensions of LE defects

Defect (mm)	Point A		Point B		Length (mm)	ΔC (mm)
	x (mm)	y (mm)	x (mm)	y (mm)		
0.094	0.078	0.490	1.104	1.571	1.490	1.026
0.250	0.078	0.490	2.796	2.531	3.399	2.718
0.500	0.000	0.000	3.160	2.700	4.156	3.160

3.3 Computational Domain

The computational domain must be sufficiently large to represent the infinite fluid domain. It is preferable to use structured grids for simulations to achieve greater accuracy. The geometry of the domain should be chosen in such a way that generated structured grids are of high quality. To generate the grids for foils with defects, adequate grids must be distributed on the foil surface, especially near LE defects, to resolve the flow details. On the other hand, since a large computational domain is required, the grid spacing needs to be increased when approaching to the domain boundaries for the purpose of computing efficiency. These lead to some challenges in generating structured grids.

The circular computational domain could provide high quality grids and hence leading to greater accuracy in solutions. Therefore, the circular domain with the O-type topology as shown in Fig. 3.3 was employed. Six domain sizes with radii (R) of 6, 12, 18, 24, 30 and 36 chord length were investigated in the present work.

Boundary conditions are also presented in Fig. 3.3. Note that the hydrostatic pressure was not taken into account in the 2-D simulations. The pressure boundary

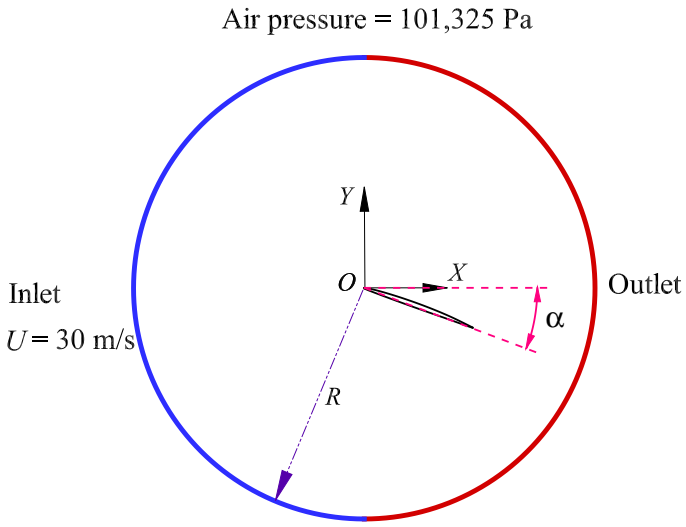

Figure 3.3: Circular computational domain

condition with $p = p_a$ was specified on the outlet. A no-slip wall boundary condition was imposed on the surface of the foil section. The Reynolds number for all cases was Re $= 3.0 \times 10^7$. At the inlet boundary, a uniform velocity of $U = 30$ m/s was specified.

3.4 Grid Generation

The generation of structured grids is dependent on the specified y^+, the grid aspect ratio (AR), and the grid stretching ratio (SR). The height of the first grid near the wall, ΔS, is calculated by:

$$\Delta S = \sqrt{\frac{2Re^{1/7}}{0.026U^2}} \frac{y^+ \mu}{\rho} \tag{3.1}$$

where y^+ is the non-dimensional first-grid spacing. Note that ΔS is measured from the center of the grid cell in Star-CCM+.

The grid aspect ratio (AR) is defined as the maximum ratio of grid width to height

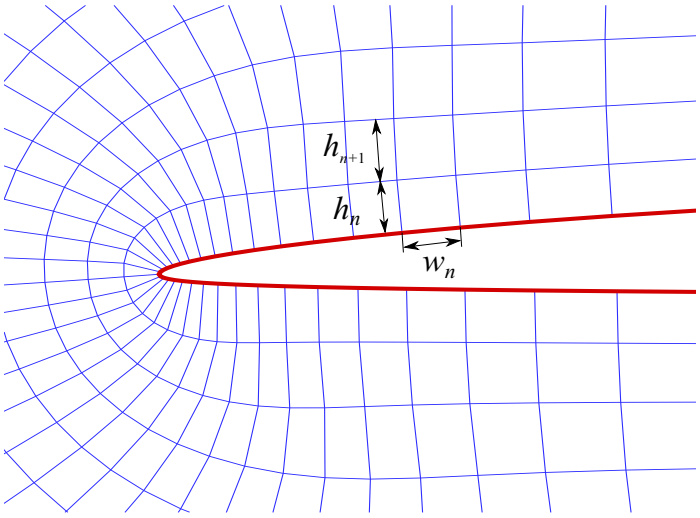

Figure 3.4: Definition of aspect ratio and stretching ratio

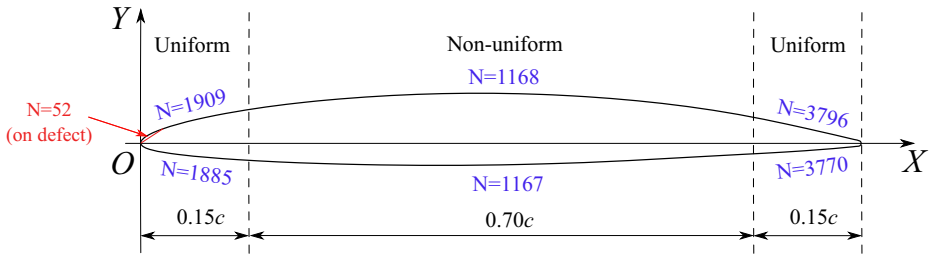

Figure 3.5: Grid distribution on the surface of the foil with 0.5 mm defect

for 2-D grids. As shown in Fig. 3.4, the AR of the n^{th} grid is determined as:

$$\text{AR} = h_n/w_n \tag{3.2}$$

where w_n and h_n are the grid width and the grid height, respectively.

The grid stretching ratio (SR) is defined as the ratio of the heights of adjacent cells. As shown in Fig. 3.4, the SR of the n^{th} grid is given as:

$$\text{SR} = h_{n+1}/h_n \tag{3.3}$$

where h_n and h_{n+1} are the heights of the n^{th} and the $(n+1)^{\text{th}}$ grids, respectively.

As shown in Fig. 3.5, both face and back of the foil are divided into three segments.

Uniform grids are distributed on the leading and the trailing edge segments while non-uniform grids are on the middle segment.

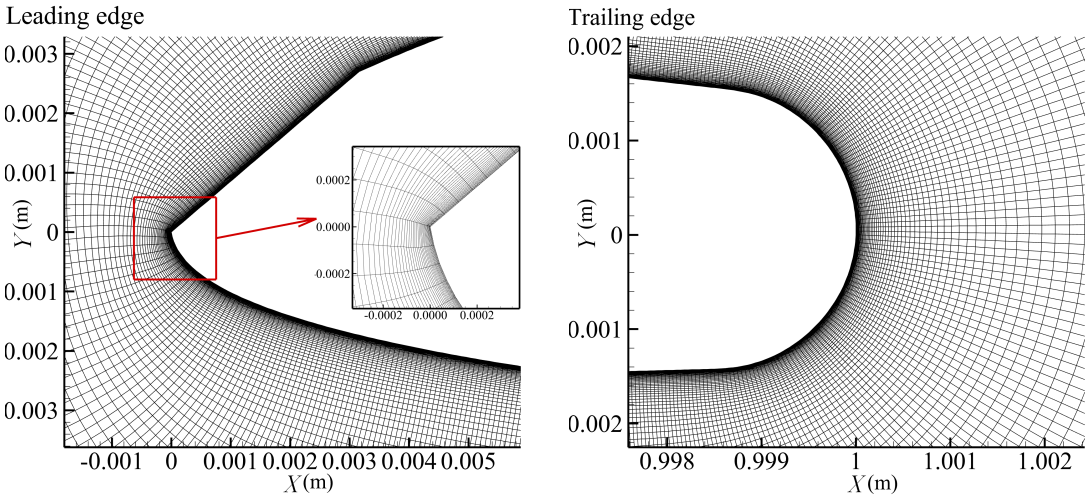

Figure 3.6: Grids near the leading edge and the trailing edge

As an example, grids near the leading edge and the tailing edge for the foil with 0.5 mm LE defect are shown in Fig. 3.6. For this case, the first grid spacing, y^+, is 1.0. The total number of grids on the foil surface is 13,695. The corresponding numbers of grids on the back/the face of the LE segment, on the trailing edge segment, and on the middle segment are shown in Fig. 3.5. The corresponding grid aspect ratios on the leading edge, the trailing edge and the middle segments are 40, 20 and 300, respectively. Note that 52 grids were distributed over the 0.5 mm defect to resolve the flow details.

3.5 Convergence Criteria

Two levels of convergence criteria were applied in the present 2-D studies, including:

- Residuals, defined as normalized root-mean-squared values in Star-CCM+, are used as the first convergence criterion. Three orders of magnitude reduction in residuals are considered as an acceptable level. Note that residuals are not the only measure for convergence. The initial values strongly influence the residuals. If the initial solution satisfies the discretized equations very well, the residuals would not reduce significantly. Therefore, it is necessary to examine the convergence of lift, drag and pressure coefficients.

- For the convergence of lift, drag and pressure coefficients, the changes between their values at the present and previous iterations are used as indicators after the residual criteria are satisfied. For the lift and drag coefficients, it is considered acceptable if the changes between two iterations are in the order of 10^{-6}. For the minimum pressure coefficient, the acceptable value is in the order of 10^{-5}.

The maximum number of iterations was set as 40,000 for all simulations. Residuals and changes in lift, drag and minimum pressure coefficients were then checked against the convergence criteria described above.

3.6 Simulation Parameters and Cases

The air pressure is set as $p_a = 101,325$ Pa. The density of water is $\rho = 1.0 \times 10^3$ kg/m^3 and the kinematic viscosity of water is 1.0×10^{-6} m^2/s. Extensive cases were simulated with different turbulence models, first-grid spacings, grid stretching ratios and grid aspect ratios.

A summary of simulation cases using the circular computational domain is pro-

vided below:

- Domain sizes in term of radius of domain (R): 6 m, 12 m, 18 m, 24 m, 30 m and 36 m.
- Grid stretching ratios: 1.1 and 1.2.
- Grid aspect ratios at LE, AR_L: 10.0, 20.0, 40.0, 56.56, 80.0, 113.12, 160.0 and 320.0.
- Grid aspect ratios at TE, AR_T: 20.0, 40.0, 60.0, 80.0, 120.0 and 160.0.
- First-grid spacing, y^+: 0.5, 0.707, 1.0, 1.414, 2.0, 2.828, 4.0, 5.0, 10.0, 15.0, 30.0, 60.0, 90.0 and 120.0.
- Turbulence models: Spalart-Allmaras, $k-\varepsilon$, $k-\omega$, SST $k-\omega$, elliptic blending and linear pressure-strain Reynolds stress models.

In these convergence studies, the number of grids ranges from 791,415 to 2,013,312. The best-practice settings are then summarized and recommended for the 2-D simulations. Using the recommended best practices, studies were then carried out for the foil ($a = 0.8$, $t/c = 0.2$, $f/c = 0.02$) without defect and the foils ($a = 0.8$, $f/c = 0.014$, $t/c = 0.0416$) with no defect, 0.1 mm defect, 0.25 mm defect and 0.5 mm defect at various angles of attack. The chord length, maximum thickness and maximum camber are 1 m, 41.6 mm and 14.0 mm, respectively. The 1 m chord length represents the chord length of a full-scale propeller at its 0.7 R section.

3.7 Computing Resources

Most of the simulations have been conducted using a high-performance computer cluster equipped with CPU 2x Intel Xeon Gold 6248. Each node has available memory of up to 186 GB, with 40 cores per node. For example, approximately 24 hours were required to complete 40,000 iterations for the 2-D case utilizing 80 cores.

3.8 Simulation Results

In the following results, the drag and lift coefficients, C_d and C_L, are defined as:

$$C_d = \frac{F_D}{0.5\rho U^2 S} \tag{3.4}$$

$$C_l = \frac{F_L}{0.5\rho U^2 S} \tag{3.5}$$

where ρ is the density of water, S is the reference area, F_D and F_L denote the drag and lift forces on the foil, respectively.

The pressure coefficient is defined as:

$$C_p = \frac{p - p_0}{0.5\rho U^2} \tag{3.6}$$

where p is the absolute pressure, and p_0 is the reference pressure, which can be calculated by

$$p_0 = p_a + \rho g h \tag{3.7}$$

where p_a denotes the air pressure, and $h = 0.5$ m is used for the hydrostatic pressure, $\rho g h$. Note that the hydrostatic pressure is 0 due to the gravity is not considered in the 2-D simulations. Then, the minimum pressure coefficient can be calculated with

$$C_{p_{\min}} = \frac{p_{\min} - p_0}{0.5\rho U^2} \tag{3.8}$$

In which, $p_{\min}$ is the the minimum pressure on the foil.

The cavitation number, σ, is defined as:

$$\sigma = \frac{p_0 - p_v}{0.5\rho U^2} \tag{3.9}$$

where p_v is the vapour pressure of water. Cavitation occurs if $-C_{p_{\min}} \geq \sigma$. The condition for cavitation inception is therefore $-C_{p_{\min}} = \sigma$.

Introducing the cavitation inception speeds for the sections without defect and with defect

$$U_0 = \sqrt{\frac{2(p_v - p_0)}{\rho C_{p_{\min}}}} \tag{3.10}$$

$$U' = \sqrt{\frac{2(p_v - p_0)}{\rho C'_{p_{\min}}}} \tag{3.11}$$

The cavitation inception speed ratio, ISR, is then defined as

$$\text{ISR} = \frac{U'}{U_0} = \sqrt{\frac{C_{p_{\min}}}{C'_{p_{\min}}}} \tag{3.12}$$

where $C_{p_{\min}}$ and $C'_{p_{\min}}$ are the minimum pressure coefficients for the sections without and with defect, respectively.

As all sections herein are DTMB modified NACA-66 ($a = 0.8$) foils, they will be referred to only by their (t/c, f/c) and by the size of their defect (if any) in the following sections.

3.8.1 Results of Convergence Studies

The foils ($f/c = 0.014$, $t/c = 0.0416$) without defect and with 0.5 mm defect were employed in the present 2-D convergence studies. Simulations were performed at the angles of attack $\alpha = 0°$ and $\alpha = 4°$ using steady RANS solver.

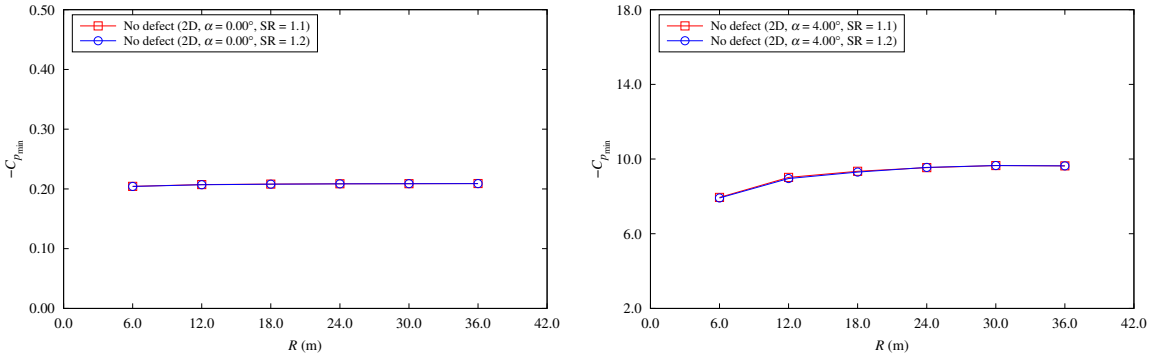

(a) $\alpha = 0.0°$ (b) $\alpha = 4.0°$

Figure 3.7: Convergence of $-C_{p_{\min}}$ to domain size and SR for the foils ($f/c = 0.014$, $t/c = 0.0416$) with no defect

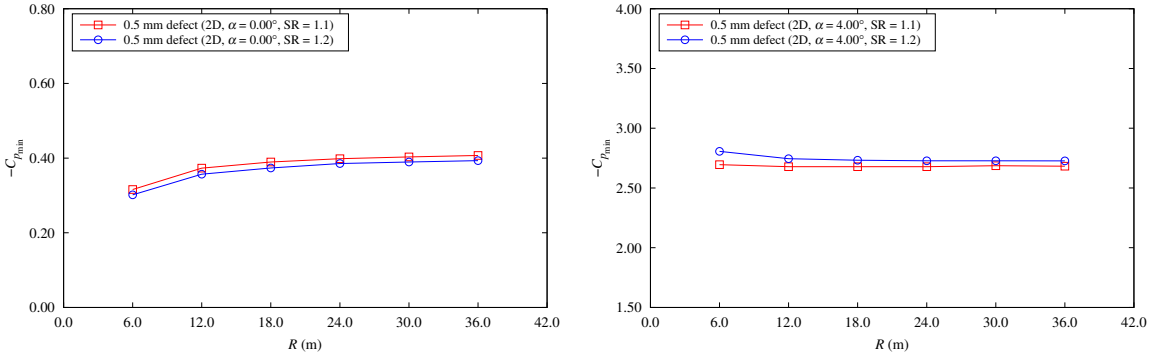

(a) $\alpha = 0.0°$ (b) $\alpha = 4.0°$

Figure 3.8: Convergence of $-C_{p_{\min}}$ to domain size and SR for the foils ($f/c = 0.014$, $t/c = 0.0416$) with 0.5 mm defects

Six domain sizes with $R = 6, 12, 18, 24, 30$ and 36 m were carried out with $y^+ = 1.0$ and $k - \omega$ model. The sensitivity of solution to the grid stretching ratio (SR) was investigated using SR = 1.1 and SR = 1.2. It was found that numerical results converged with the increase of R. For the foils ($f/c = 0.014$, $t/c = 0.0416$) with no and 0.5 mm defects, the convergence of negative minimum pressure coefficient to R and SR is shown in Figs. 3.7 and 3.8. The results indicated that the $-C_{p_{\min}}$ was

Table 3.2: Differences between $-C_{p_{\min}}$ of SR = 1.1 and 1.2 using various domain sizes for the foil ($f/c = 0.014$, $t/c = 0.0416$) with 0.5 mm defect

α (°)	R (m)	$-C_{p_{\min}}$		Difference	Relative error (%)
		SR = 1.1	SR = 1.2		
0	6	0.23335	0.21809	0.01526	6.54
	12	0.28366	0.27318	0.01048	3.70
	18	0.30402	0.29026	0.01377	4.53
	24	0.31443	0.30354	0.01089	3.46
	30	0.31875	0.30822	0.01053	3.30
	36	0.32328	0.31077	0.01251	3.87
4	6	2.69495	2.80656	0.11161	4.14
	12	2.67834	2.74471	0.06637	2.48
	18	2.67810	2.73198	0.05388	2.01
	24	2.67805	2.72718	0.04912	1.83
	30	2.68625	2.72769	0.04145	1.54
	36	2.68203	2.72666	0.04463	1.66

independent on the grid stretching ratio for the foil without defect at $\alpha = 0.0°$ and 4.0°. Table 3.2 presents the differences between $-C_{p_{\min}}$ of SR = 1.1 and 1.2 using various domain sizes for the foil with 0.5 mm defect. The relative errors with respect to the predictions of SR = 1.1 were also included. It can be seen that the relative error is less than 4.00% when R is greater than 24 m. In the following studies, $R = 24.0$ m with SR = 1.1 was applied.

In order to resolve the flow field near the defects, eight sets of grids with aspect

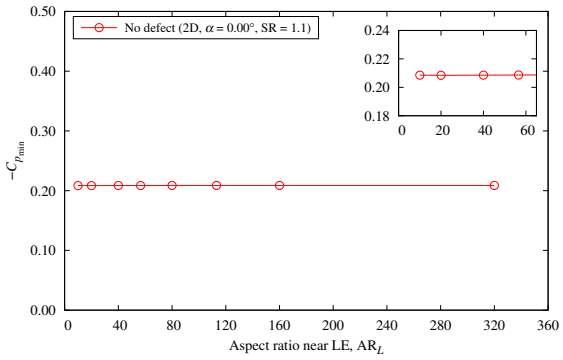

(a) $\alpha = 0.0°$

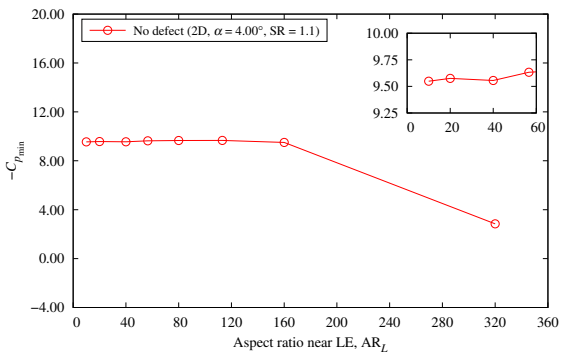

(b) $\alpha = 4.0°$

Figure 3.9: Convergence of $-C_{p_{\min}}$ to AR_L for the foils ($f/c = 0.014$, $t/c = 0.0416$) with no defect

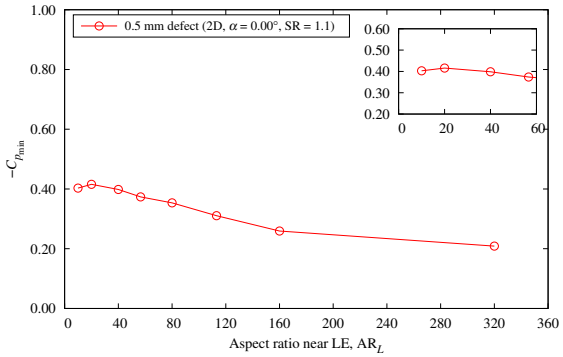

(a) $\alpha = 0.0°$

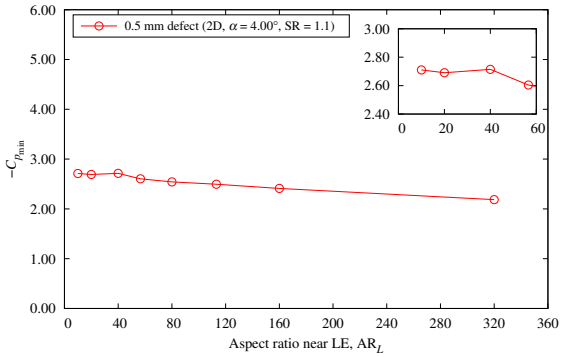

(b) $\alpha = 4.0°$

Figure 3.10: Convergence of $-C_{p_{\min}}$ to AR_L for the foils ($f/c = 0.014$, $t/c = 0.0416$) with 0.5 mm defect

ratios (AR) at LE of 320, 160, 113.12, 80, 56.56, 40, 20 and 10 with $y^+ = 1.0$ were used. The corresponding results at $\alpha = 0°$ and 4° for the foils ($f/c = 0.014$, $t/c = 0.0416$) without defect and with 0.5 mm defect are presented in Figs. 3.9 and 3.10, respectively. The results showed that numerical solutions were insensitive to the AR_L when the aspect ratio was less than 120 for the foil without defect. As shown in Fig. 3.10, the predictions with 0.5 mm defect converged as AR_L was refined.

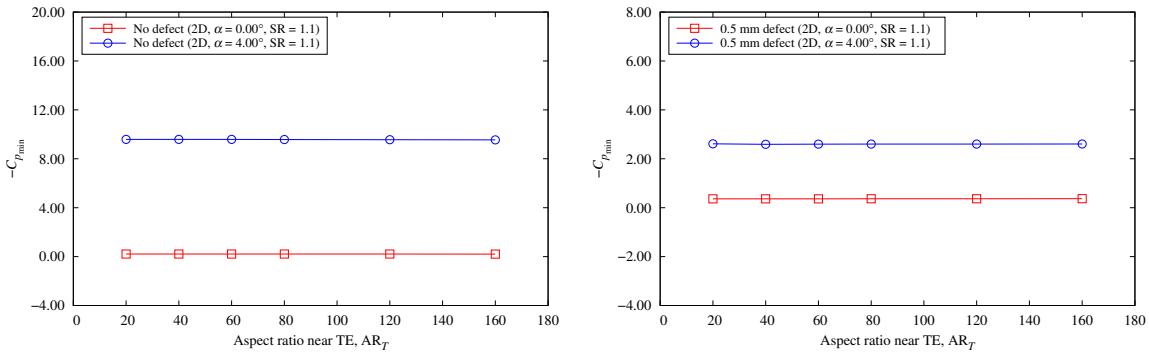

(a) No defect

(b) 0.5 mm defect

Figure 3.11: Convergence of $-C_{p_{\min}}$ to AR_T for the foils ($f/c = 0.014$, $t/c = 0.0416$) with no and 0.5 mm defects

In the following 2-D simulations, the aspect ratio of 40 over the defect was used.

The trailing-edge is another sensitive part of the foil. Investigations were also carried out with six aspect ratios at the TE of 160, 120, 80, 60, 40 and 20 for the foils ($f/c = 0.014$, $t/c = 0.0416$) with no and 0.5 mm defects. The value of y^+ was set to 1.0, and the $k-\omega$ model was employed. Figure 3.11 shows the convergence of predicted $-C_{p_{\min}}$ to AR_T for the foils with no and 0.5 mm defects. The results demonstrate that the predictions are independent of the aspect ratio near TE. A value of 120 for AR_T was selected for the subsequent studies.

Furthermore, 168 cases were carried out with different values of $y^+ = 0.5$, 0.707, 1.0, 1.414, 2.0, 2.828, 4.0, 5.0, 10.0, 15.0, 30.0, 60.0, 90.0 and 120.0. Various turbulence models, including the Spalart-Allmaras, $k-\varepsilon$, $k-\omega$, SST $k-\omega$, elliptic blending and linear pressure-strain Reynolds stress models, were employed to examine their effects on the prediction of the minimum pressure coefficients at the selected angles of attack. Note that no wall function was applied for the wall treatment for the small y^+ ($y^+ \leq 5.0$) cases, while the all y^+ wall treatment was applied for the other cases.

The aspect ratio of 40 over leading edge and the grid stretching ratio of SR = 1.1 were used.

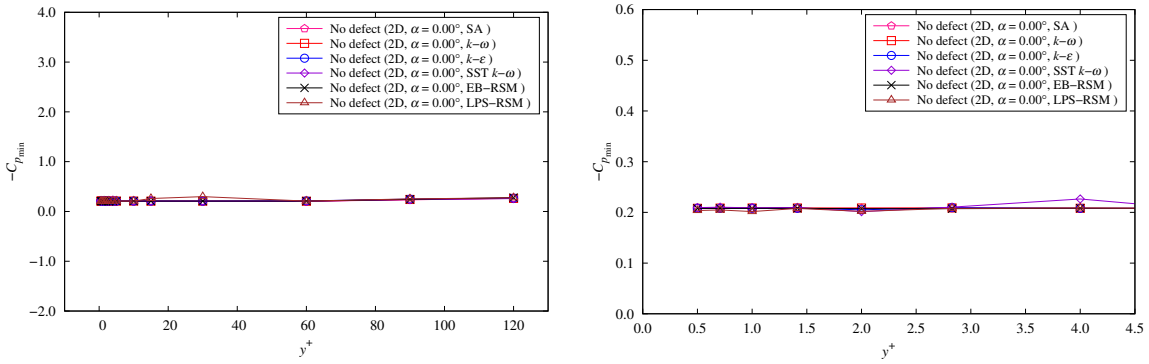

(a) $0.5 \leq y^+ \leq 120.0$ (b) $0.5 \leq y^+ \leq 4.0$

Figure 3.12: Convergence of $-C_{p_{\min}}$ to y^+ using different turbulence models for the foil ($f/c = 0.014$, $t/c = 0.0416$) with no defect at $\alpha = 0°$

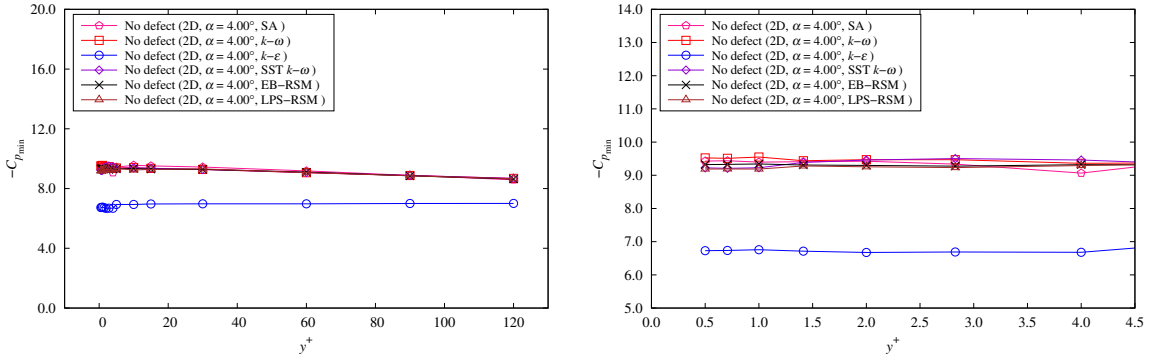

(a) $0.5 \leq y^+ \leq 120.0$ (b) $0.5 \leq y^+ \leq 4.0$

Figure 3.13: Convergence of $-C_{p_{\min}}$ to y^+ using different turbulence models for the foil ($f/c = 0.014$, $t/c = 0.0416$) with no defect at $\alpha = 4°$

The results of various turbulence models and y^+ for the foils ($f/c = 0.014$, $t/c = 0.0416$) with no and 0.5 mm defects are shown in Figs. 3.12 to 3.15. It can be observed that results converge with the decrease of y^+ for the foil without defect. In general,

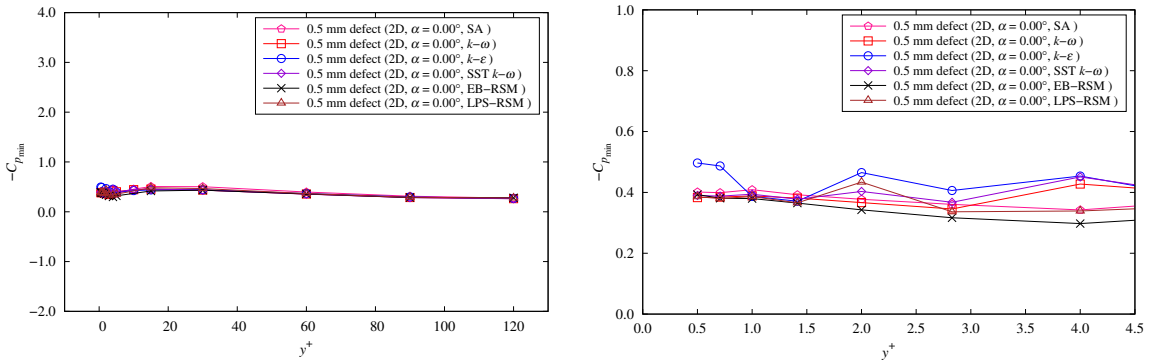

(a) $0.5 \leq y^+ \leq 120.0$ (b) $0.5 \leq y^+ \leq 4.0$

Figure 3.14: Convergence of $-C_{p_{\min}}$ to y^+ using different turbulence models for the foil ($f/c = 0.014$, $t/c = 0.0416$) with 0.5 mm defect at $\alpha = 0°$

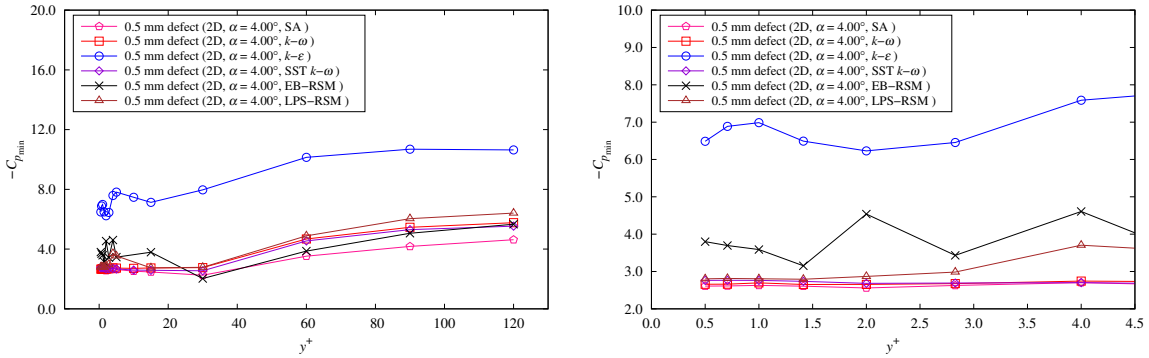

(a) $0.5 \leq y^+ \leq 120.0$ (b) $0.5 \leq y^+ \leq 4.0$

Figure 3.15: Convergence of $-C_{p_{\min}}$ to y^+ using different turbulence models for the foil ($f/c = 0.014$, $t/c = 0.0416$) with 0.5 mm defect at $\alpha = 4°$

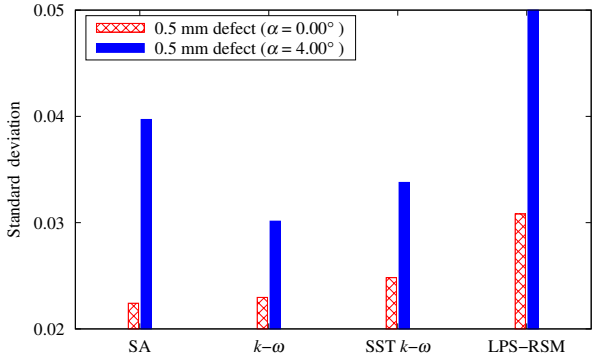

Figure 3.16: The standard deviations of $-C_{p_{\min}}$ using different turbulence models for the foil ($f/c = 0.014$, $t/c = 0.0416$) with 0.5 mm defect

the magnitude of oscillations in the predictions is small when y^+ is less than 1.414. However, for the foil with 0.5 mm defect, the results were diverged in the simulations using $k-\varepsilon$ model and elliptic blending Reynolds stress model (EB-RSM) at the largest angle of attack ($\alpha = 4°$). It is primarily due to flow separation. The prediction of flow near the stalling point remains a challenging issue in CFD simulations. Consequently, it is recommended that the value of y^+ should be in the range of [0.5, 1.414].

The standard deviations and differences between consecutive results using various y^+ and turbulence models for the foil ($f/c = 0.014$, $t/c = 0.0416$) with 0.5 mm defect at $\alpha = 0°$ and $\alpha = 4°$ are presented in Tables 3.3 and 3.4, respectively. In addition, Fig. 3.16 shows the standard deviations of $-C_{p_{\min}}$ using different turbulence models for the foil ($f/c = 0.014$, $t/c = 0.0416$) with 0.5 mm defect. At the angle of attack $\alpha = 4°$, the LSP-RSM model yielded the largest standard deviation (0.30723), while the minimum standard deviation (0.3014) was calculated with the $k-\omega$ model. For the results obtained at $\alpha = 0°$, the standard deviations of SA, $k-\omega$ and SST $k-\omega$ models were at similar magnitudes. The standard $k-\omega$ model was then employed in the following computations.

Based on extensive convergence studies, the best-practice settings for 2-D simulations with the Star-CCM+ steady RANS solver are determined and presented in Table 3.5. The specific values used for full-scale propellers are also provided in Table 3.5. Other default settings for the solver are summarized in Table 3.6.

Table 3.3: The standard deviations and differences between consecutive results using various y^+ and turbulence models for the foil ($f/c = 0.014$, $t/c = 0.0416$) with 0.5 mm defect at $\alpha = 0°$

Turbulence model	y^+	$-C_{p_{\min}}$	Differences in consecutive results	standard deviation
	0.500	0.40111	0.00204	
	0.707	0.39907	0.00983	
	1.000	0.40890	0.01677	
SA	1.414	0.39213	0.01479	0.02242
	2.000	0.37734	0.01673	
	2.828	0.36061	0.01819	
	4.000	0.34242	-	
	0.500	0.38286	0.00154	
	0.707	0.38440	0.00412	
	1.000	0.38853	0.00722	
$k-\omega$	1.414	0.38130	0.01493	0.02297
	2.000	0.36638	0.02094	
	2.828	0.34544	0.08198	
	4.000	0.42742	-	
	0.500	0.39018	0.00250	
	0.707	0.38768	0.00650	
	1.000	0.39418	0.01650	
SST $k-\omega$	1.414	0.37768	0.02552	0.02482
	2.000	0.40320	0.03562	
	2.828	0.36758	0.08329	
	4.000	0.45087	-	
	0.500	0.38579	0.00613	
	0.707	0.37965	0.00667	
	1.000	0.38633	0.02077	
LPS-RSM	1.414	0.36556	0.06839	0.03082
	2.000	0.43395	0.09780	
	2.828	0.33615	0.00268	
	4.000	0.33883	-	

Table 3.4: The standard deviations and differences between consecutive results using various y^+ and turbulence models for the foil ($f/c = 0.014$, $t/c = 0.0416$) with 0.5 mm defect at $\alpha = 4^\circ$

Turbulence model	y^+	$-C_{p_{\min}}$	Differences in consecutive results	standard deviation
SA	0.500	2.60893	0.00474	0.03971
	0.707	2.61367	0.01534	
	1.000	2.62900	0.02223	
	1.414	2.60678	0.04814	
	2.000	2.55864	0.06732	
	2.828	2.62596	0.07663	
	4.000	2.70259	-	
$k-\omega$	0.500	2.65949	0.00137	0.03014
	0.707	2.66086	0.03389	
	1.000	2.69475	0.04238	
	1.414	2.65237	0.00227	
	2.000	2.65464	0.02164	
	2.828	2.67627	0.06685	
	4.000	2.74312	-	
SST $k-\omega$	0.500	2.76304	0.00165	0.03379
	0.707	2.76468	0.00232	
	1.000	2.76236	0.02475	
	1.414	2.73762	0.05546	
	2.000	2.68216	0.00883	
	2.828	2.69098	0.01092	
	4.000	2.70190	-	
LPS-RSM	0.500	2.80463	0.00900	0.30723
	0.707	2.81363	0.00811	
	1.000	2.80552	0.01234	
	1.414	2.79318	0.07510	
	2.000	2.86828	0.11691	
	2.828	2.98518	0.71970	
	4.000	3.70489	-	

Table 3.5: Best-practice settings for 2-D simulations with the Star-CCM+ steady RANS solver

Items	Variable	Recommended setting	Value
Domain size	R	≥ 24 m	24 m
First-grid spacing	y^+	[0.5, 1.414]	1.0
Grid stretching ratio	SR	[1.1, 1.2]	1.1
Grid aspect ratio near LE	AR_L	≤ 40	40
Grid aspect ratio near TE	AR_T	≤ 120	120
Turbulence model		$k-\omega$ SST $k-\omega$	$k-\omega$

Table 3.6: Default settings used in the present simulations with Star-CCM+

Simulation Parameters	Default Settings
Convection scheme	2^{nd}-order upwind
Gradient method	Hybrid Gauss-Least squares method
Limiter method	Venkatakrishnan method
Custom accuracy level selector	2^{nd}-order
Initial turbulence intensity, I	1%
Initial turbulent viscosity ratio, μ_t/μ	10.0
Linear solver	Algebraic multigrid methods (AMG)
Relaxation scheme	Gauss-Seidel
Under-relaxation factor for velocity	0.4
Under-relaxation factor for pressure	0.1
Under-relaxation factor for turbulence	0.7

3.8.2 Results with Best-Practice Settings

With the best-practice settings summarized in the previous section, numerical simulations were carried out for the foil ($t/c = 0.2$, $f/c = 0.02$) without defect and the foils ($t/c = 0.0416$, $f/c = 0.014$) without and with LE defects in an infinite domain. The simulation results of cavitation buckets, pressure, residuals, lifting and drag coefficients are presented in this section and the effect of LE defect on cavitation inception speed and efficiency are discussed.

3.8.2.1 Cavitation Buckets for the Foil ($t/c = 0.2$, $f/c = 0.02$) without Defect

The predicted cavitation buckets of the foil ($t/c = 0.2$, $f/c = 0.02$) without defect in terms of the cavitation number at angles of attack from $-5°$ to $6°$ are presented in Fig. 3.17 and compared with the potential-flow solutions (Brockett, 1966) and the numerical results with ANSYS CFX and TRANSOM (Hally, 2018). The agreement is in general good.

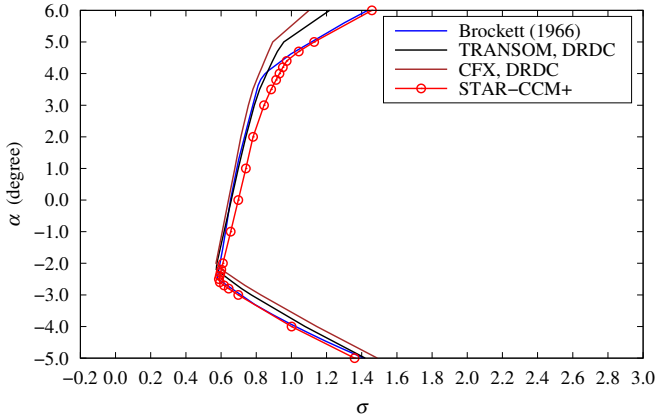

Figure 3.17: Cavitation buckets for the foil ($t/c = 0.2$, $f/c = 0.02$) without defect

3.8.2.2 Cavitation Buckets for the Foils ($t/c = 0.0416$, $f/c = 0.014$) without and with LE Defects

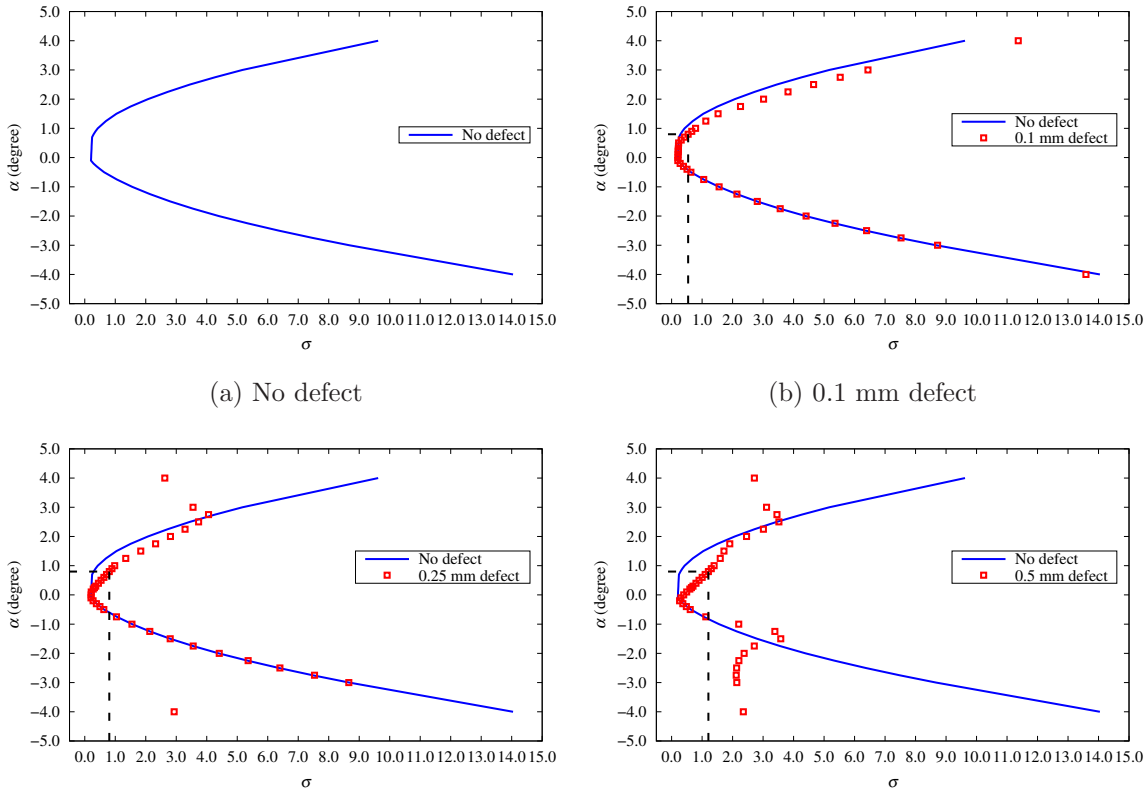

(a) No defect

(b) 0.1 mm defect

(c) 0.25 mm defect

(d) 0.5 mm defect

Figure 3.18: Cavitation buckets for the foils ($t/c = 0.0416$, $f/c = 0.014$) without and with LE defects

Cavitation buckets were compared for the foils ($t/c = 0.0416$, $f/c = 0.014$) without defect and with three different LE defects (0.5 mm, 0.25 mm and 0.1 mm) at a number of angles of attack (see Table 3.7). As shown in Fig. 3.18, the cavitation buckets are narrowed by the defects at the LE in the region of typical propeller design. In other words, the incipient cavitation speed is reduced by the LE defect. Note that dashed lines denote one example in the typical design range.

Table 3.7: Angles of attack for the foils ($t/c = 0.0416$, $f/c = 0.014$) with and without LE defects in 2-D simulation

Parameter	Values
Angle of attack, α (°)	-4.00, -3.00, -2.75, -2.50, -2.25, -2.00, -1.75, -1.50, -1.25, -1.00, -0.75, -0.50, -0.40, -0.30, -0.20, -0.10, 0.00, 0.10, 0.20, 0.25, 0.30, 0.40, 0.50, 0.60, 0.70, 0.80, 0.90, 1.00, 1.25, 1.50, 1.75, 2.00, 2.25, 2.50, 2.75, 3.00, 4.00

Minimum pressure coefficients and their locations on the foil surface, residuals of simulations, and the convergence of drag and lift coefficients (C_d and C_l) are provided in the following subsections.

3.8.2.3 Pressure Contours and Streamlines

As one example in the typical propeller design range, the contours of pressure coefficient and streamlines near the LE at $\alpha = 0.8°$ for the foils ($t/c = 0.0416$, $f/c = 0.014$) with no defect, 0.5 mm defect, 0.25 mm defect and 0.1 mm defect are presented in Fig. 3.19. It can be observed that the defect led to lower pressure near the LE. Although locations of the minimum pressure depend on the size of a defect, they are all located close to the upper end of the flat defect. For example, the upper end point of the 0.5 mm defect is (0.00316 m, 0.0027 m) and the location of the minimum pressure is at (0.00323 m, 0.00267 m).

Table 3.8 presents negative minimum pressure coefficients and their locations for the foils with no defect, 0.5 mm defect, 0.25 mm defect and 0.1 mm defect at $\alpha = 0.8°$. The cavitation inception speed ratios and their reduction percentages with respect to

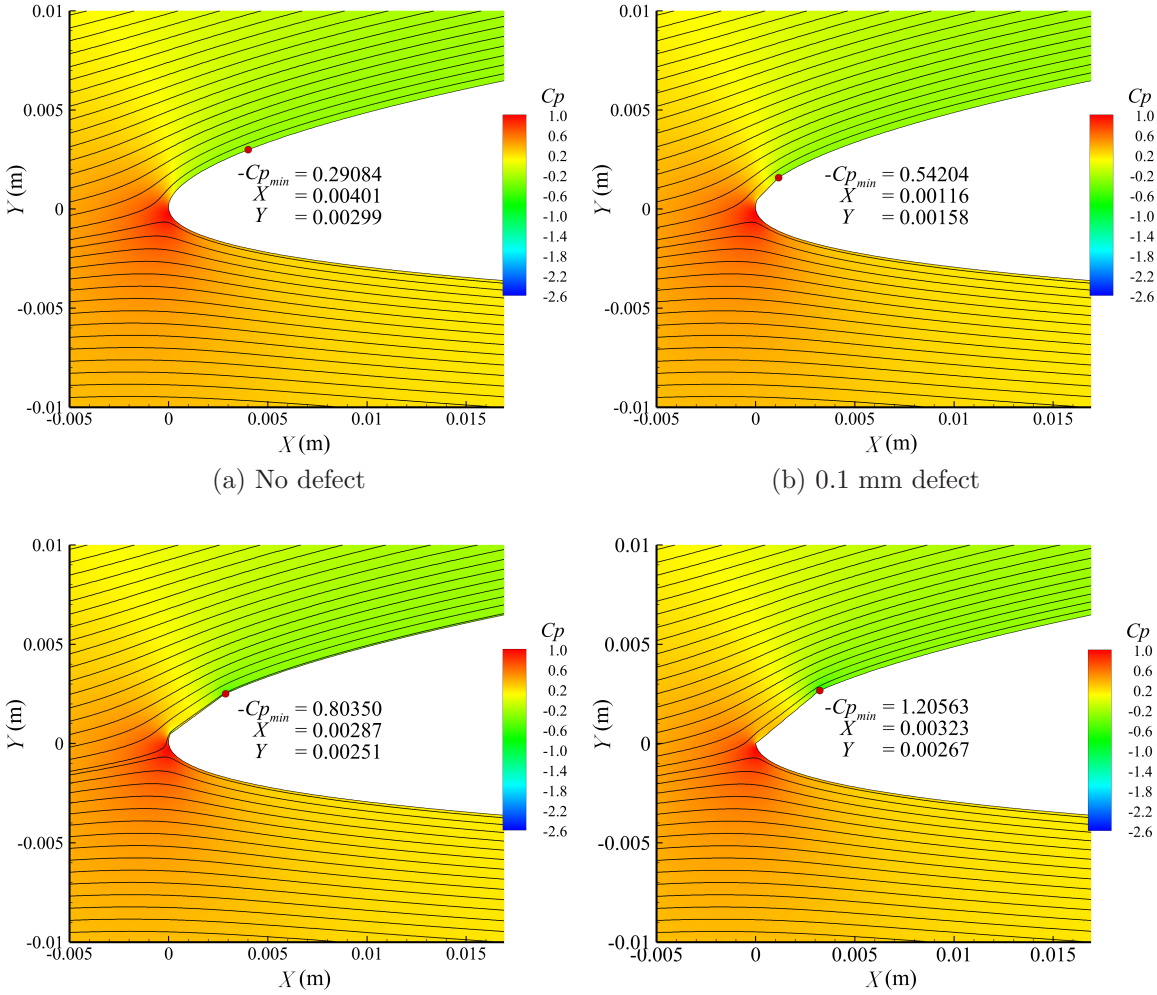

(a) No defect

(b) 0.1 mm defect

(c) 0.25 mm defect

(d) 0.5 mm defect

Figure 3.19: Pressure coefficient contours and streamlines for the foils ($t/c = 0.0416$, $f/c = 0.014$) without and with LE defects at $\alpha = 0.8°$

the foil without defect (as designed) are also included in the table. It can be observed that even the smallest defect leads to a significant reduction in the cavitation inception speed (over 25% reduction for 0.1 mm defect) at angle of attack $\alpha = 0.8°$.

Table 3.8: Cavitation inception speed variations with defects for the foils (t/c = 0.0416, $f/c = 0.014$) without and with LE defects at $\alpha = 0.8°$

Item	No defect	0.5 mm defect	0.25 mm defect	0.1 mm defect
$C_{p_{\min}}$	-0.29084	-1.20563	-0.8035	-0.54204
Location (X,Y) (m)	(0.00401, 0.00299)	(0.00323, 0.00267)	(0.00287, 0.00251)	(0.00116, 0.00158)
Inception Speed (m/s)	26.173	12.855	15.753	19.179
ISR	1	0.491	0.602	0.733
Inception Speed Reduction Percentage	-	50.9%	39.8%	26.7%

3.8.2.4 Pressure Plots

Continuing with the above example, the pressure distributions near the LE at $\alpha = 0.8°$ for the four foils, i.e., with no defect, 0.5 mm defect, 0.25 mm defect and 0.1 mm defect, are shown in Fig. 3.20. It was found that the pressures on the back were significantly changed by the defect near LE.

3.8.2.5 Results of Residuals, $-C_{p_{\min}}$, C_d and C_l

In Star-CCM+, the normalized Root Mean Squared value of residual for all cells is used to monitor the behavior of the solvers at each iteration. Residuals of simulations for the four foils with no defect, 0.5 mm defect, 0.25 mm defect and 0.1 mm defect at $\alpha = 0.8°$ are shown in Fig. 3.21 as one example. Three order-of-magnitude reduction in residuals were achieved. In these figures, the legend of "Continuity" denotes the residual for the continuity equation, "X-momentum" is the residual for the momentum

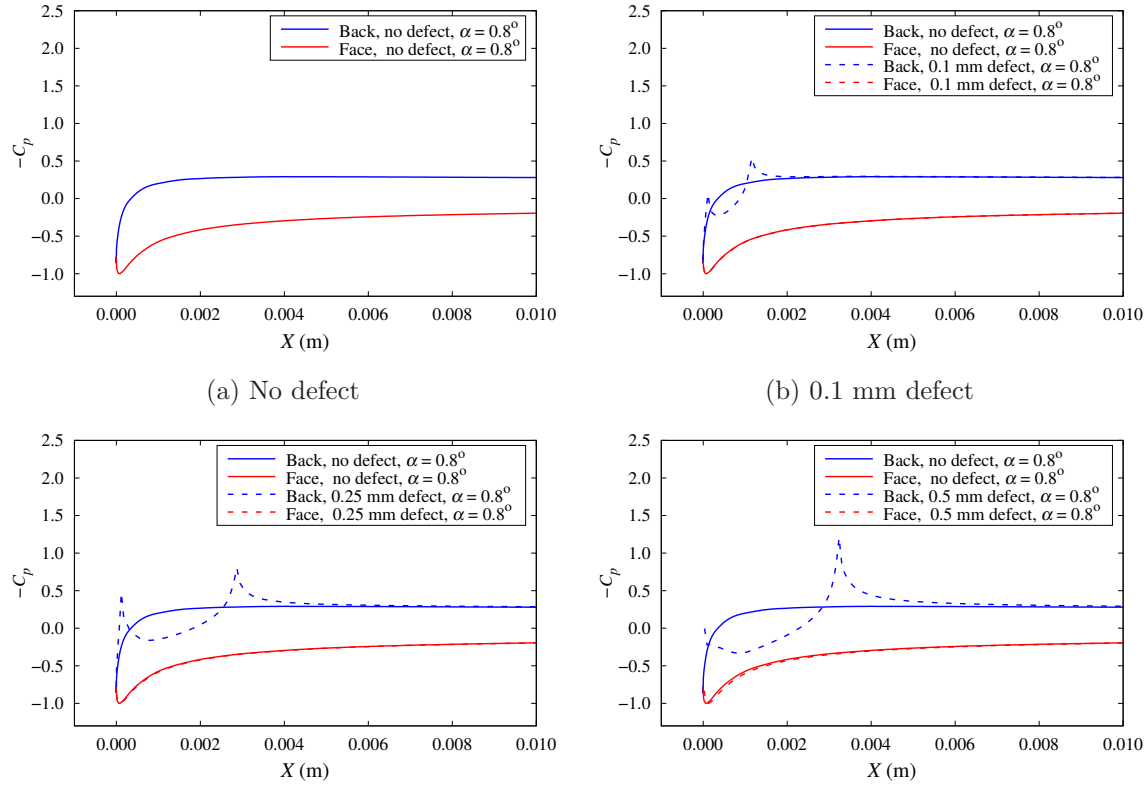

(a) No defect

(b) 0.1 mm defect

(c) 0.25 mm defect

(d) 0.5 mm defect

Figure 3.20: Pressure distributions on the face and back of the foils ($t/c = 0.0416$, $f/c = 0.014$) without and with LE defects at $\alpha = 0.8°$

equation (X-component), "Y-momentum" is the residual for the momentum equation (Y-component), "Tke" represents the residual for the transport equation of turbulence kinetic energy (k), and "Sdr" denotes the residual for the transport equation of specific dissipation rate (ω).

The corresponding iteration histories for the drag and lift coefficients (C_d and C_l) are shown in Fig. 3.22, respectively. The negative minimum pressure coefficient, $-C_{p_{\min}}$, the drag and lift coefficients and their changes between the last two iterations are summarized in Table 3.9.

Table 3.9: Numerical results of $-C_{p_{\min}}$, C_d and C_l for the foils ($t/c = 0.0416$, $f/c = 0.014$) without and with LE defects at $\alpha = 0.8°$

Item	No defect	0.5 mm defect	0.25 mm defect	0.1 mm defect
$-C_{p_{\min}}$	0.290840	1.205630	0.803500	0.542040
C_d	0.005468	0.005475	0.005474	0.005468
C_l	0.254443	0.254402	0.254437	0.254473
Changes in $-C_{p_{\min}}$ between the last two iterations	6×10^{-7}	6×10^{-7}	6×10^{-7}	6×10^{-7}
Changes in C_d between the last two iterations	5×10^{-9}	0	0	0
Changes in C_l between the last two iterations	2×10^{-7}	0	0	0

3.8.2.6 Effect of LE Defect on Cavitation Inception Speed

Based on the cavitation buckets for the foil ($t/c = 0.0416$, $f/c = 0.014$) as shown in Fig. 3.18, the reduction percentages in inception speed due to LE defects are presented in Fig. 3.23 for the foils with defects. In the typical design range of angle of attack ($-1.5° < \alpha < 2°$) for a moderately loaded propeller, the reduction in inception speed can reach to 60% for the 0.5 mm defect around $\alpha = 0.75°$. Between 0° and 1.5°, the reduction increases with the size of LE defect. At $-1.5° < \alpha < 2°$, the reductions for the three defects are around 15% to 20%.

In summary, the LE defects significantly reduce the cavitation inception speeds at the normal range of angle of attack.

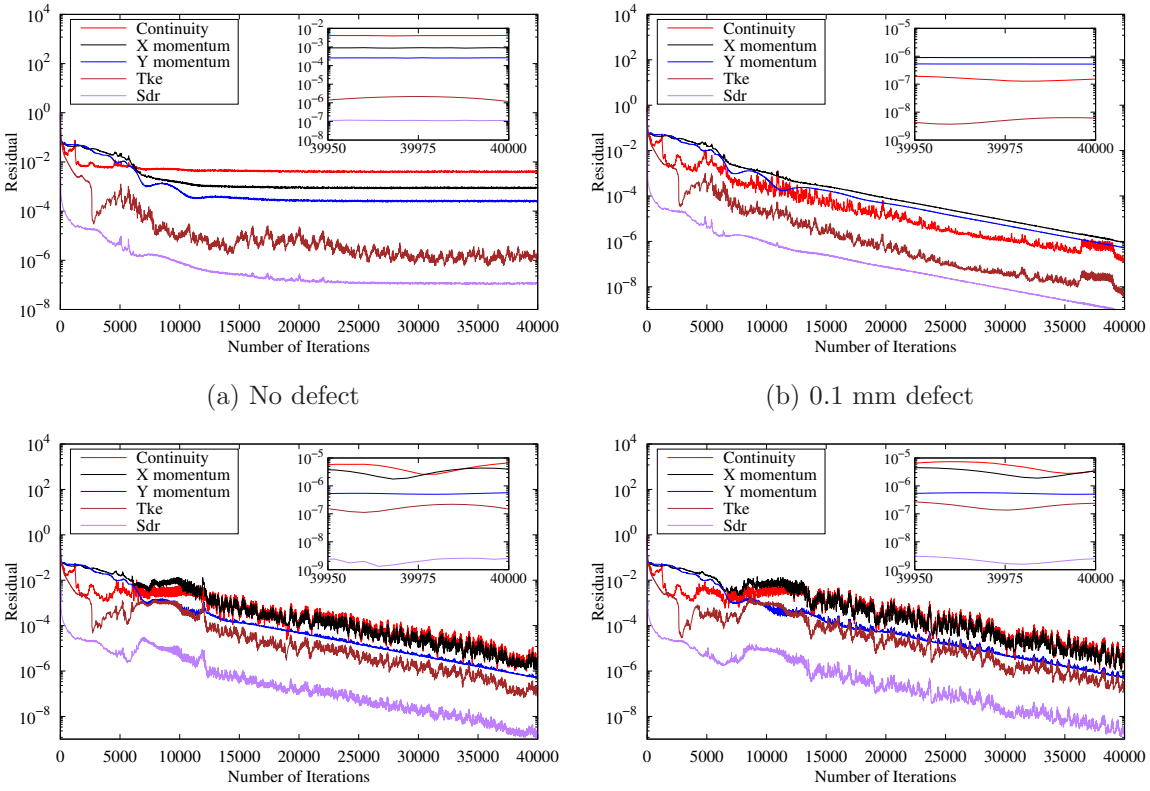

(a) No defect

(b) 0.1 mm defect

(c) 0.25 mm defect

(d) 0.5 mm defect

Figure 3.21: Residuals for the foils ($t/c = 0.0416$, $f/c = 0.014$) without and with LE defects at $\alpha = 0.8°$

3.8.2.7 Effect of LE Defect on Efficiency

The ratio of lift to drag, i.e., C_l/C_d of a 2-D section provides an indicator of the hydrodynamic efficiency of the propeller which incorporates it. The effect of a defect on C_l/C_d is shown in Fig. 3.24. In the normal range of angle of attack for a moderately loaded propeller, the LE defect has little on the efficiency. However, at larger angles of attack, for example, a heavily loaded propeller or a propeller operating in a highly uneven wake pattern, a LE defect reduces the efficiency more significantly. A larger LE defect leads to a greater decrease in efficiency.

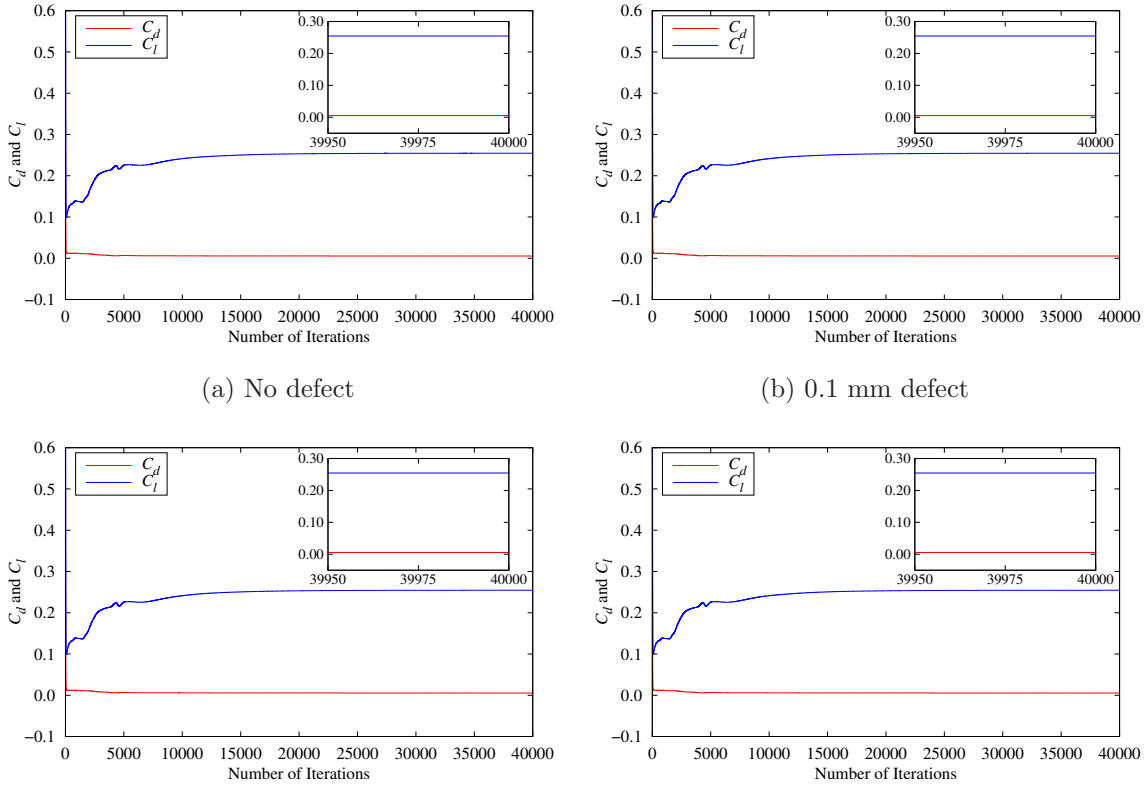

(a) No defect

(b) 0.1 mm defect

(c) 0.25 mm defect

(d) 0.5 mm defect

Figure 3.22: C_d and C_l for the foils ($t/c = 0.0416$, $f/c = 0.014$) without and with LE defects at $\alpha = 0.8°$

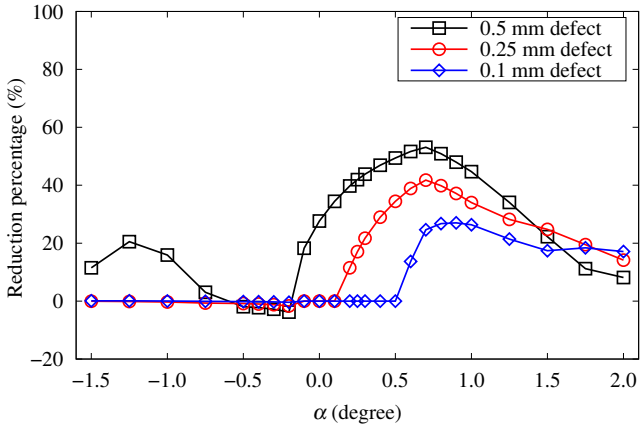

Figure 3.23: Reduction percentage in cavitation inception speed for the foils ($t/c = 0.0416$, $f/c = 0.014$) with LE defects

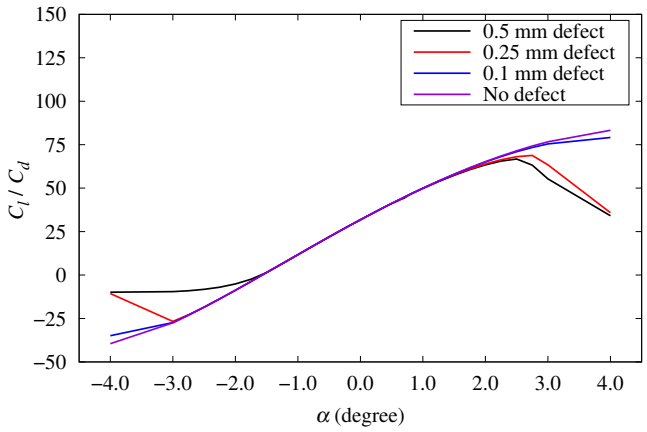

Figure 3.24: Effect of LE defect on lift-to-drag ratio

Chapter 4

3-D Simulations for the Foils of 1 m Span

This chapter focuses on 3-D RANS studies on foils ($a = 0.8$, $t/c = 0.0416$, $f/c = 0.014$) of 1 m span with and without LE defect to understand the 3-D effect in simulations by comparing the solutions with those from 2-D RANS computations. The reason for choosing 1 m span is that the foils with and without LE defect were intended to be tested in a cavitation tunnel with 1 m by 1 m test section. It is important to investigate the differences in 2-D and 3-D solutions and to further quantify the effect of LE defect in future validation studies.

In present work, convergence studies were carried out on angles of attack $\alpha = 0$ and 1.25 degrees. Effects of RANS modelling parameters, such as domain size, grid aspect ratio, first-grid spacing, y^+, and turbulence model, on the solutions were carefully examined. Impact of foil span on solution at the mid-span section was also investigated. The 3-D CFD simulations were performed with the steady RANS solver

in Star-CCM+ on structured grids. Based on the results of convergence studies, the best-practice settings for 3-D simulations with the steady RANS solver in Star-CCM+ were proposed.

Using the best-practice settings, 3-D simulations were carried out for the foils in a cavitation tunnel without and with LE defects and at various angles of attack. The cavitation buckets were presented and compared with those from 2-D RANS simulations.

4.1 Geometry and Computational Domain

3-D RANS simulations were carried out for foils with constant DTMB modified NACA-66 ($a = 0.8$, $t/c = 0.0416$, $f/c = 0.014$) sections, where t, f and c denote the maximum thickness, the maximum camber and the chord length of a foil section, respectively. Details on the definitions of LE defects and their sizes can be found in Section 3.2.

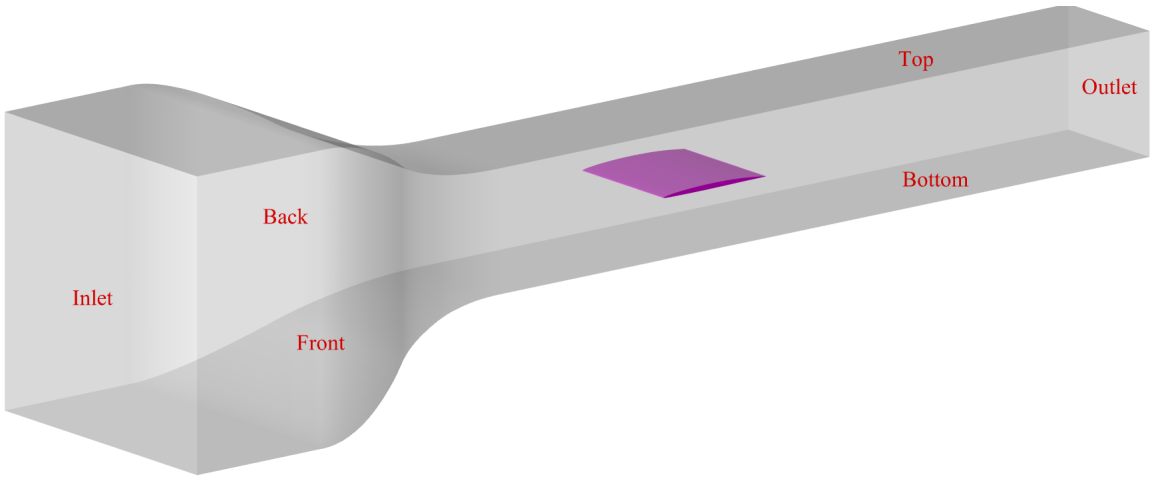

Figure 4.1: Geometry and computational domain for the foils of 1 m span

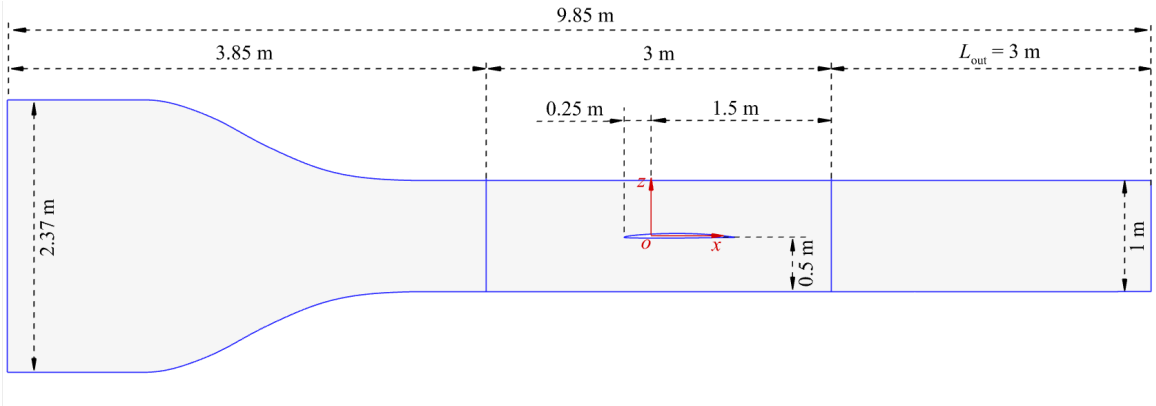

Figure 4.2: Domain sizes for the simulation of foils with 1 m span and $L_{\text{out}} = 3.0$ m

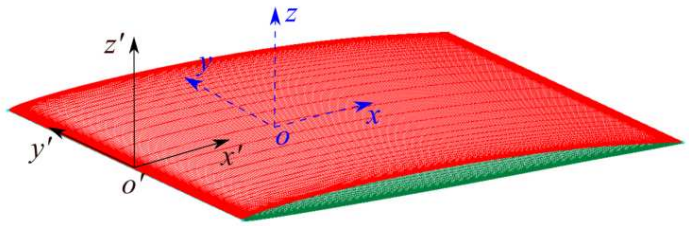

Figure 4.3: Coordinate system for 3-D simulations

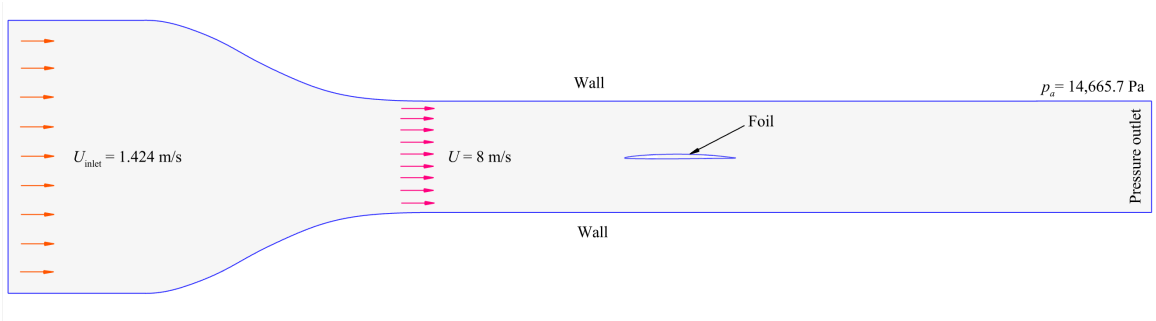

Figure 4.4: Boundary conditions for the simulation of foils with 1 m span

As shown in Fig. 4.1, the computational domain covers a segment of the cavitation tunnel with square inlet and outlet sections. Figure 4.2 presents the domain size and the location of the foil inside the tunnel with the length of downstream $L_{\text{out}} = 3.0$ m. The origin is located at the center of the support shaft. The oy-axis is along the span direction. The origin of the coordinate system, $o - xyz$, used in the present 3-D

simulations was shifted to o' (-0.25 m, 0, -0.01107 m), as shown in Fig. 4.3. In this way, $o'x'z'$ is consistent with the coordinate system in 2-D studies, which allows for direct comparison of 2-D and 3-D results.

The boundary conditions, as an example, for the foil with no defect at the angle of attack $\alpha = 0°$ are presented in Fig. 4.4. The pressure boundary condition with $p = p_a$ was specified on the outlet. A no-slip wall boundary condition was imposed on the surface of the foil. The maximum water velocity can be achieved in the tunnel is 8.6 m/s. At the inlet boundary, a uniform velocity of $U_{\text{Inlet}} = 1.424$ m/s was then specified. This leads to the inflow velocity of $U = 8.0$ m/s on the inlet of the test segment. The Reynolds number in terms of the chord length of foil for all cases was $Re = 8.0 \times 10^6$.

4.2 Grid Generation

To achieve greater accuracy, the computational domain is discretized into structured grid. The generation of grid around the foil is dependent on the non-dimensional first-grid spacing, y^+, the grid aspect ratio, and the grid stretching ratio. Based on the recommended settings of 2-D cases, the stretching ratio was set as 1.2 in present 3-D simulation. To reduce the total number of grid, the meshing topology of Gauthier and Hally (2019) was applied, the foil surface was divided into three segments. As shown in Fig. 4.5, uniform grids are distributed on the LE defect (red part), while non-uniform grids are applied on the pressure side (blue part) and the segment of suction side without defect (green part). In this case, the corresponding grid aspect ratios on the leading edge defect, AR_L, and the cell at the end of trailing

edge, AR_T, are 16 and 32, respectively.

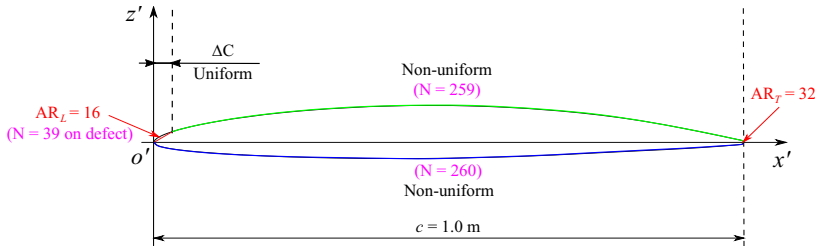

Figure 4.5: Example of grid distribution on the surface of the foil with 0.5 mm defect

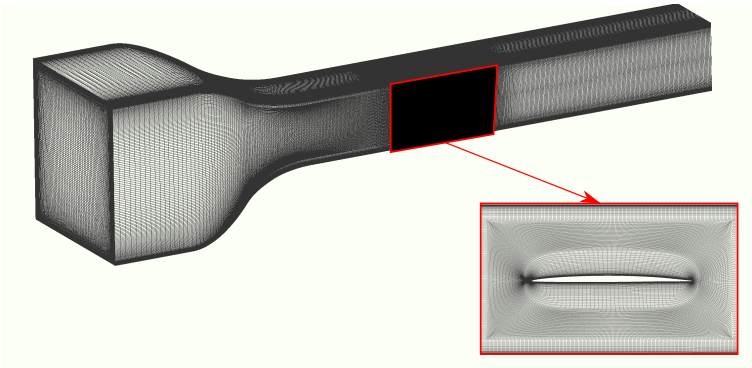

Figure 4.6: A representative grid for 0.5 mm defect at the angle of attack $\alpha = 0°$

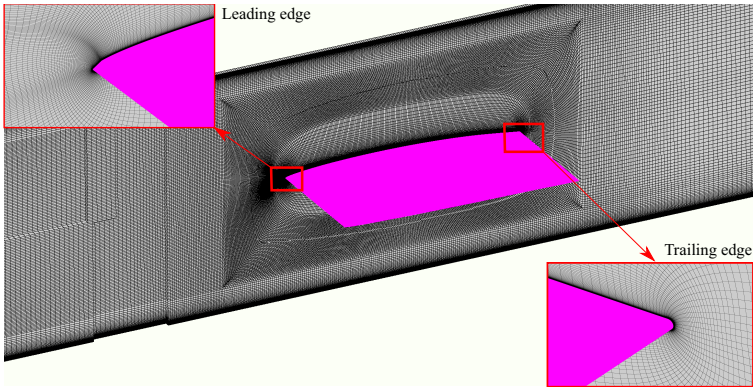

Figure 4.7: The grid of mid-span section $y' = 0$ m

A representative numerical grid for 0.5 mm defect at the angle of attack $\alpha = 0°$, as an example, is shown in Fig. 4.6. For this case, the first-grid spacing, y^+, is 1.0 and the length between the end of test segment and outlet, L_{out}, is 3 m. The total number of grids is 35,897,600. Note that 39 cells were distributed over the 0.5 mm defect to resolve the flow details. Figure 4.7 shows the grids on the mid-span section $y' = 0$ m as well as near the leading and trailing edges . In present work, the number of grids in convergence studies ranges from 22,319,600 to 140,422,800.

4.3 Convergence Criteria

The convergence criteria in previous 2-D simulations were also applied in the present 3-D studies, including the residuals and lift, drag, and pressure coefficients. Details can be found in Section 3.5. For the minimum pressure coefficient, the acceptable value for the changes between two iterations is in the order of 10^{-4}. The maximum number of iterations was set as 40,000 for all simulations. Residuals and changes in lift, drag and minimum pressure coefficients were then checked against the convergence criteria.

4.4 Simulation Parameters

Convergence studies on the domain size, span of foil, grid aspect ratio, first-grid spacing, y^+, and turbulence model were first carried out. The foils with and without defect at angles of attack $\alpha = 0°$ and $1.25°$ were investigated. A summary of simulation parameters in convergence studies is provided below:

- Domain size in terms of L_{out} (m): 3.0, 4.0, 5.0 and 6.0.
- Span of foil (m): 1.0, 2.0 and 3.0.
- Grid aspect ratio at LE, AR_L: 8.0, 16.0 and 32.0.
- First-grid spacing, y^+: 0.5, 0.707, 1.0, 1.414, 2.0, 2.828 and 4.
- Turbulence model: $k - \varepsilon$, $k - \omega$, SST $k - \omega$ and Spalart-Allmaras

The best-practice settings are then summarized and recommended for the 3-D simulations of intended cavitation tunnel tests. Using recommended best practices, further studies were carried out for the foils with no defect, 0.1 mm defect, 0.25 mm defect and 0.5 mm defect at angles of attack between -4.00 and 4.75 degrees (see Table 4.1). Other default settings used in the 3-D simulations with the steady RANS solver are same as those of 2-D simulations, as shown in Table 3.6.

Table 4.1: Angles of attack for the foils of 1 m span with and without LE defects in cavitation tunnel

Parameter	Values
Angle of attack, α (°)	-4.00, -3.50, -3.00, -2.50, -2.34, -2.00, -1.50, -1.25, -1.00, -0.80, -0.75, 0.00, 0.80, 1.25, 2.00, 2.50, 3.75, 4.00, 4.25, 4.75

4.5 Simulation Results

4.5.1 Results of Convergence Studies

A total of 84 cases were carried out in the convergence studies for the foils with 0.5 mm defect and no defect at angles of attack $\alpha = 0$ and 1.25 degrees. Results on the mid-span sections of foils are presented in this dissertation.

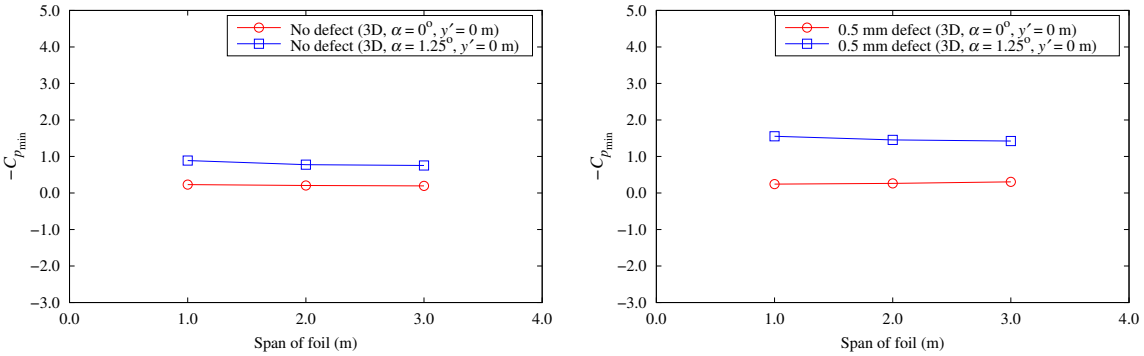

(a) No defect (b) 0.5 mm defect

Figure 4.8: Convergence of $-C_{p_{\min}}$ to span for the foils with no and 0.5 mm defects

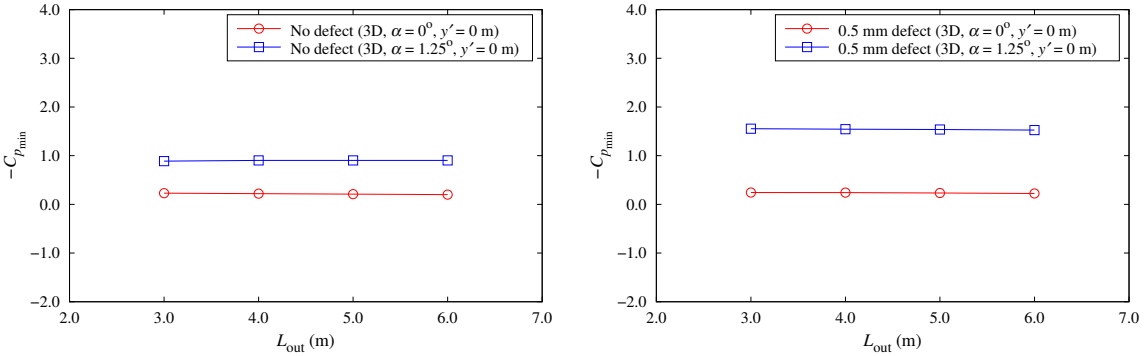

(a) No defect (b) 0.5 mm defect

Figure 4.9: Convergence of $-C_{p_{\min}}$ to L_{out} for the foils with no and 0.5 mm defects

Effect of span on the results for the mid-span section were carried out using foil aspect ratios (span/chord length) of 1.0, 2.0 and 3.0, for the foils with no defect and 0.5 mm defect, i.e., the corresponding foil spans are 1.0, 2.0 and 3.0 m, respectively. This led to simulations of three different tunnels of 1 m, 2 m and 3 m square test sections. The corresponding velocities on the inlet boundary were adjusted to 1.424, 2.818 and 3.770 m/s to maintain the same Reynolds number of the foil $Re = 8.0 \times 10^6$. Figure 4.8 presents the corresponding negative minimum pressure coefficients on the mid-span section for the foils with and without LE defect. It can be seen that the effect of span on the negative minimum pressure coefficient at the mid-span section was insignificant. In other words, 1 m span is adequate to avoid the tunnel wall effect. The span of 1 m was then employed in the following studies.

Four domain sizes in terms of $L_{\text{out}} = 3$, 4, 5 and 6 m were investigated. The convergence of negative minimum pressure coefficient to L_{out} is shown in Fig. 4.9. It can be seen that numerical results converged with the increase of the length of downstream. The negative minimum pressure coefficient is insensitive to L_{out} at both angles of attack $\alpha = 0$ and 1.25 degrees. In the following studies, $L_{\text{out}} = 3$ m was used.

The influence of the first-grid spacing, y^+, on the foils with no defect and 0.5 mm defect was also investigated with $y^+ = 0.5$, 0.707, 1.0, 1.414, 2.0, 2.828 and 4.0. The negative minimum pressure coefficients with the $k - \omega$ model at angles of attack, $\alpha = 0^\circ$ and 1.25°, are presented in Fig. 4.10. It can be observed that results are converged with the decrease of y^+. The first-grid spacing, $y^+ = 1.0$, was then employed.

In order to resolve the flow field near the defect, three aspect ratios for the near

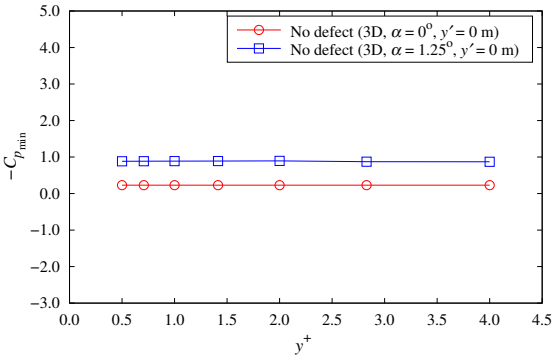

(a) No defect

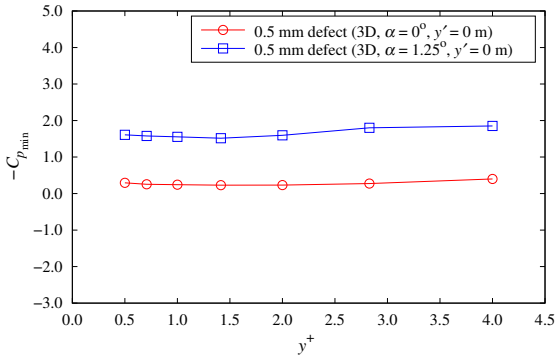

(b) 0.5 mm defect

Figure 4.10: Convergence of $-C_{p_{\min}}$ to y^+ for the foils with no and 0.5 mm defects

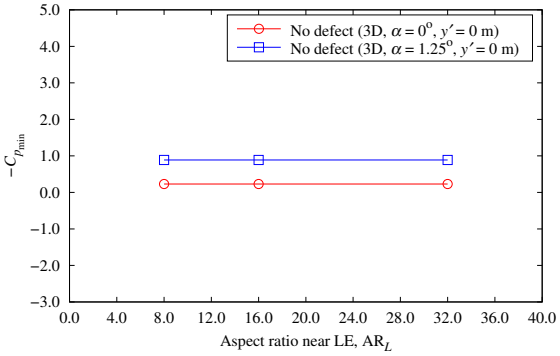

(a) No defect

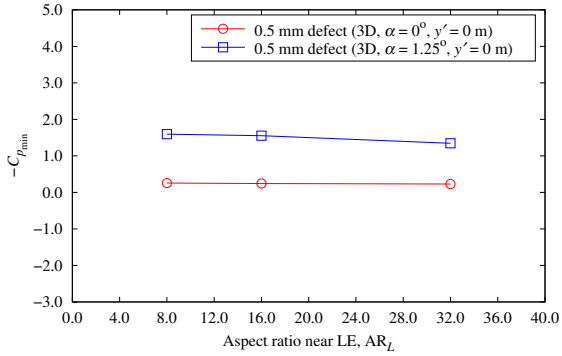

(b) 0.5 mm defect

Figure 4.11: Convergence of $-C_{p_{\min}}$ to AR_L for the foils with no and 0.5 mm defects

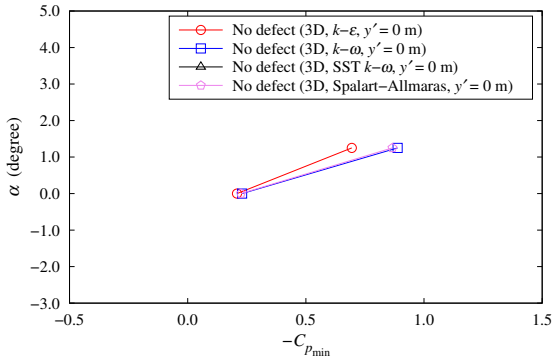

(a) No defect

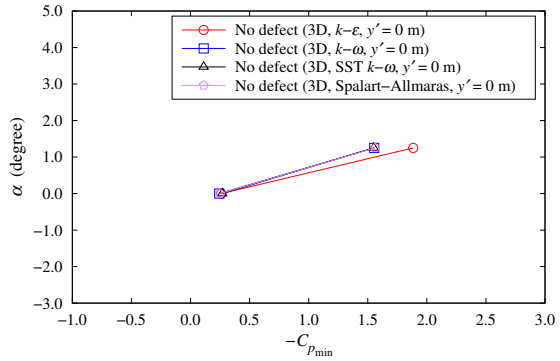

(b) 0.5 mm defect

Figure 4.12: Convergence of $-C_{p_{\min}}$ to turbulence model for the foils with no and 0.5 mm defects

LE, 8, 16, and 32, were used with $y^+ = 1.0$. The corresponding results at $\alpha = 0°$ and 1.25° are presented in Fig. 4.11. The results indicated that the effect of grid aspect ratio on solutions with the $k - \omega$ was insignificant. The grid aspect ratio of 16 over the defect was then chosen.

Furthermore, various turbulence models, including the $k - \varepsilon$, $k - \omega$, SST $k - \omega$, and Spalart-Allmaras models, were employed to examine their effects on the prediction of the minimum pressure coefficient at selected angles of attack. The aspect ratio of 16 over leading edge was employed. In the near-wall layers, the first-grid spacing was set as $y^+ = 1.0$. Note that no wall function was used for the wall treatment due to the low y^+ value. Results for the foils with no defect and 0.5 mm defect are shown in Fig. 4.12. The numerical solutions at angle of attack of 1.25° were affected by turbulence models. The results with $k - \varepsilon$ are different from those by other three turbulence models. Note that the $k - \omega$ model, which is the one recommended as best practice for 2-D simulations, was then used in the following simulations.

According to the convergence studies, the best-practice settings are recommended and summarized in Table 4.2. The numbers of grids for the foils with and without defects are summarized in Table 4.3.

Table 4.2: Best-practice settings for 3-D simulations with foil of 1 m span

Items	Variable	Recommended setting	Value
Domain size	L_{out}	≥ 3.0 m	3.0 m
First-grid spacing	y^+	[0.5, 1.0]	1.0
Grid aspect ratio near LE	AR_L	≤ 16	16
Span of foil		1.0 m	1.0 m
Turbulence model		$k-\omega$ SST $k-\omega$	$k-\omega$

Table 4.3: Number of grids for the foils with and without defects with best-practice settings

Item	No defect	0.1 mm defect	0.25 mm defect	0.5 mm defect
Number of grids over the span	100	100	100	100
Number of grids on suction side	289	289	302	298
Number of grids on pressure side	253	253	253	260
Number of grids on defect	-	21	35	39
Total number of grids	34,956,800	34,956,800	35,721,200	35,897,600

4.5.2 Results with Best-Practice Settings

Using the best-practice settings of Table 4.2, studies were carried out for the foils with no defect, 0.1 mm defect, 0.25 mm defect and 0.5 mm defect at various angles of attack from −4.0 to 4.75 degrees. The cavitation buckets, residuals of simulations, minimum pressure coefficients and their locations on the foil surface, pressure distribution and reduction of cavitation inception speed are provided in the following subsections.

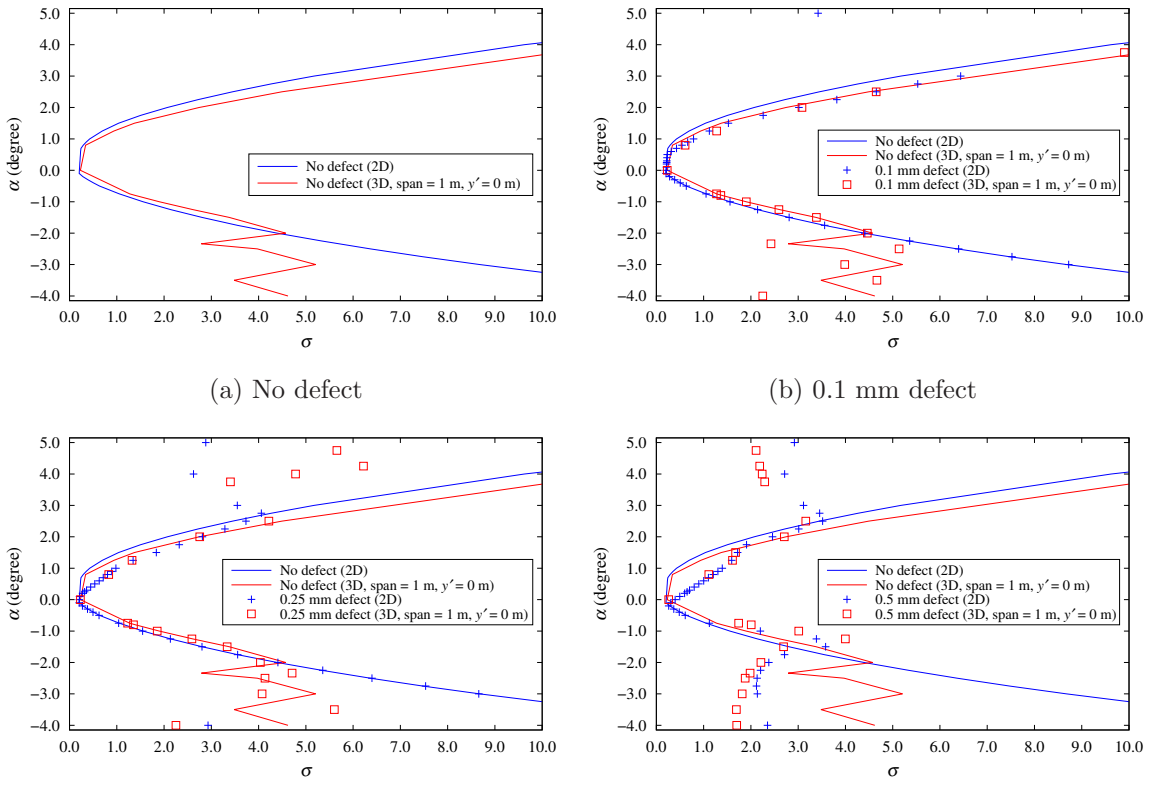

(a) No defect

(b) 0.1 mm defect

(c) 0.25 mm defect

(d) 0.5 mm defect

Figure 4.13: Cavitation buckets for the foils of 1 m span without and with LE defects

4.5.2.1 Cavitation Buckets

Cavitation buckets were compared for the foils without defect and with three different LE defects (0.5, 0.25 and 0.1 mm) at selected angles of attack in Fig. 4.13. The predicted cavitation buckets for foils of 1 m span are generally in good agreement with those from 2-D simulations. The cavitation buckets are narrowed by the LE defect in the region of typical propeller design, similar to the findings of 2-D studies, which means that the incipient cavitation speed is reduced by the LE defect.

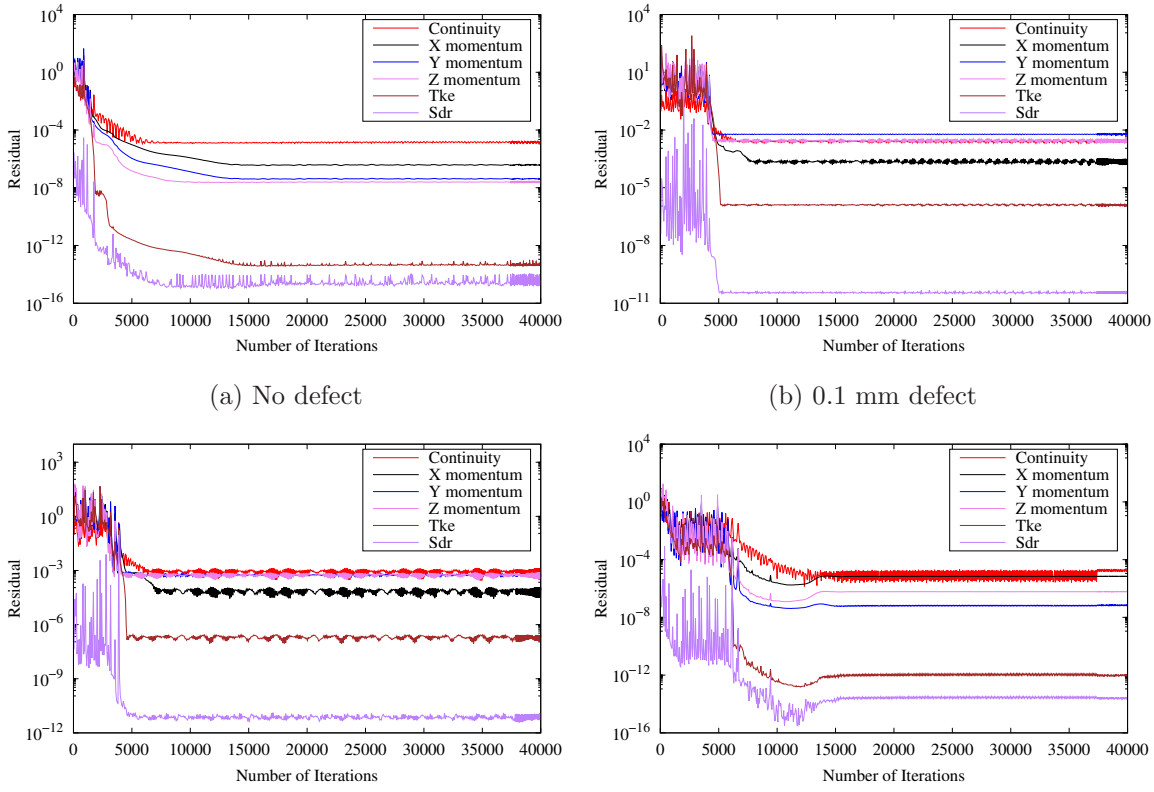

(a) No defect

(b) 0.1 mm defect

(c) 0.25 mm defect

(d) 0.5 mm defect

Figure 4.14: Simulation residuals for the foils of 1 m span without and with LE defects at $\alpha = 0.8°$

4.5.2.2 Residuals of Simulations

For example, the residuals of simulations for the foils with and without LE defects at $\alpha = 0.8°$ are provided in Fig. 4.14. It can be seen that three orders of magnitude reduction in residuals were achieved.

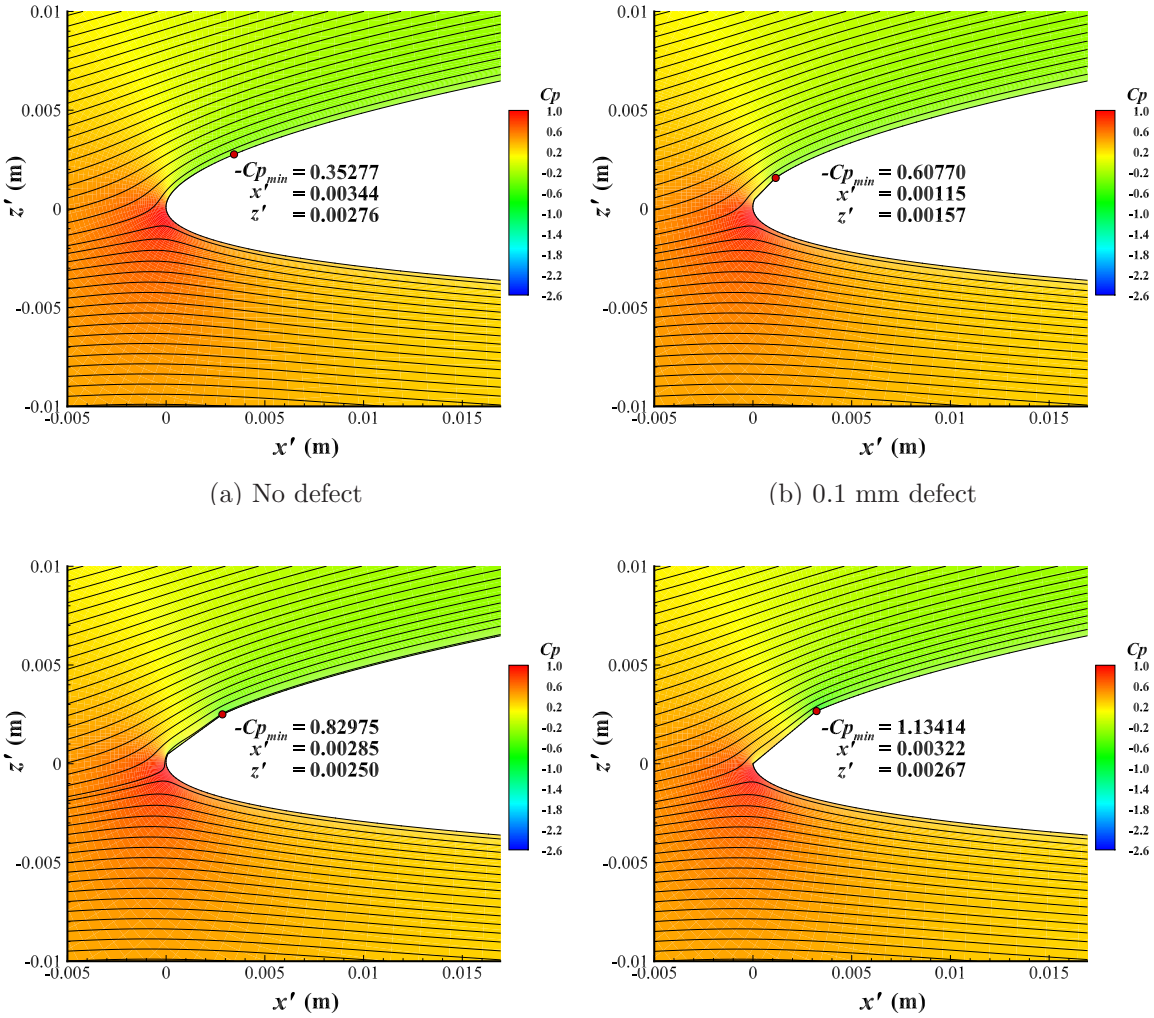

(a) No defect

(b) 0.1 mm defect

(c) 0.25 mm defect

(d) 0.5 mm defect

Figure 4.15: Pressure contours and streamlines for the foils of 1 m span without and with LE defects at $\alpha = 0.8°$

4.5.2.3 Pressure and Streamlines

As one example in the typical propeller design range, pressure contours and streamlines near LE at $\alpha = 0.8°$ are presented in Fig. 4.15. The minimum pressure coefficients and their locations on the foil surface are also given in these figures.

Figure 4.16 shows the pressure distributions near the LE on the face and the back for foils with and without defect at $\alpha = 0.8°$. It can be found that the differences in the pressure distributions from 2-D and 3-D simulations are generally insignificant. Table 4.4 summarizes the detailed minimum pressure and the corresponding location for the foils with and without defects at $\alpha = 0.8°$ along with relative errors between 2-D and 3-D solutions. The maximum relative error (17.6%) was obtained for the minimum pressure coefficient of the foil without defect.

Table 4.4: Minimum pressure coefficient and location for the foils of 1 m span with and without defects at $\alpha = 0.8°$

	Item	No defect	0.5 mm defect	0.25 mm defect	0.1 mm defect
2-D	$C_{p_{\min}}$	-0.29084	-1.20563	-0.8035	-0.54204
	x'	0.00401	0.00323	0.00287	0.00116
	z'	0.00299	0.00267	0.00251	0.00158
3-D	$C_{p_{\min}}$	-0.35277	-1.13414	-0.82975	-0.60770
	x'	0.00344	0.00322	0.00285	0.00115
	z'	0.00276	0.00267	0.00250	0.00157
Relative error	$C_{p_{\min}}$	17.6%	6.3%	3.2%	10.8%
	x'	16.6%	0.3%	0.7%	0.9%
	z'	8.3%	0.0%	0.4%	0.6%

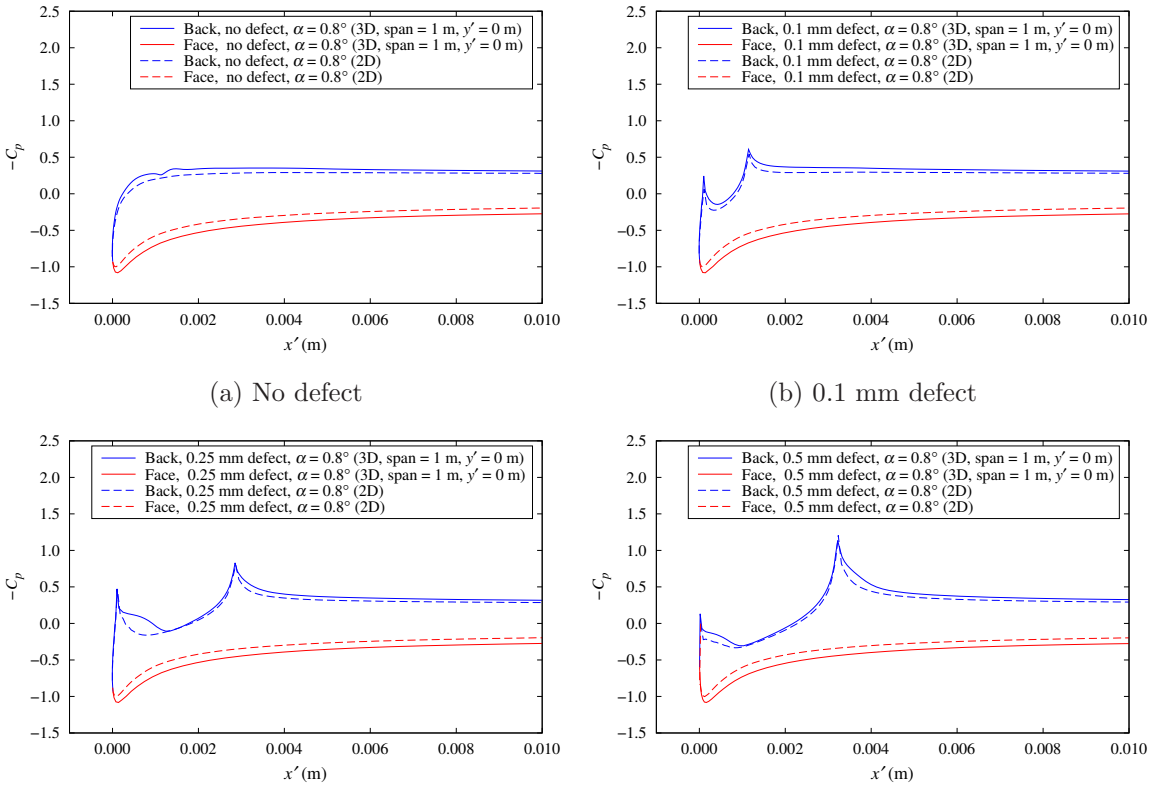

(a) No defect

(b) 0.1 mm defect

(c) 0.25 mm defect

(d) 0.5 mm defect

Figure 4.16: Pressure distributions on the foils of 1 m span without and with LE defects at $\alpha = 0.8°$

4.5.2.4 Effect of LE Defect on Cavitation Inception Speed

Figure 4.17 presents the comparison of reduction percentage in cavitation inception speed for the foils with LE defects in 2-D an 3-D simulations. The maximum reduction in inception speed can reach to 44% for the 0.5 mm defect at $\alpha = 0.8°$. From the cavitation buckets and the reduction of cavitation inception speed, the effect of LE defect is generally obvious. The differences in predictions of ISR from 2-D and 3-D simulations of 1 m span foils are insignificant for most angles of attack.

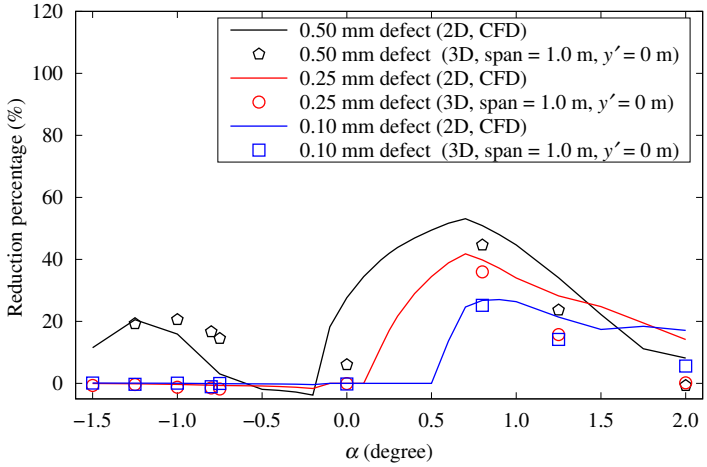

Figure 4.17: Comparison of the reduction percentage in cavitation inception speed for the foils with LE defects from 2-D and 3-D simulations of 1.0 m span

Chapter 5

3-D Simulations for the Foils of 0.525 m Span

Due to the limitation of the foil support mechanism of cavitation tunnel, the span of 0.525 m was applied to minimize the force and moment on the foil. This chapter presents an extension of previous studies on the effects of LE defects on cavitation performance of the modified NACA-66 ($a = 0.8$, $f/c = 0.014$, $t/c = 0.0416$) foils. For the foils of 0.525 m span tested in the cavitation tunnel, one foil was without defect and others had defects near the leading edge (LE). Extensive convergence studies were first carried out at angles of attack $\alpha = 0$, 1.25 and 4 degrees. Effects of RANS modelling parameters, such as domain size, grid aspect ratio, first-grid spacing, y^+, and turbulence model, on the solutions were carefully examined. The 3-D CFD simulations were performed with the steady RANS solver in Star-CCM+. Based on the results of convergence studies, the best-practice settings were proposed.

Using the proposed best-practice settings, 3-D simulations were carried out for

the foils of 0.525 m span with and without LE defects at various angles of attack in a cavitation tunnel. The cavitation buckets were presented and compared with those from 2-D RANS simulations and 3-D RANS studies on foils of 1 m span.

5.1 Geometry and Computational Domain

The test geometry is shown in Fig. 5.1, the end plates (green parts) were attached to the foil to reduce end effects, and four support arms (blue parts) were also installed to enable testing at different angles of attack. For the LE defects, their sizes are the same as those in Section 3.2.

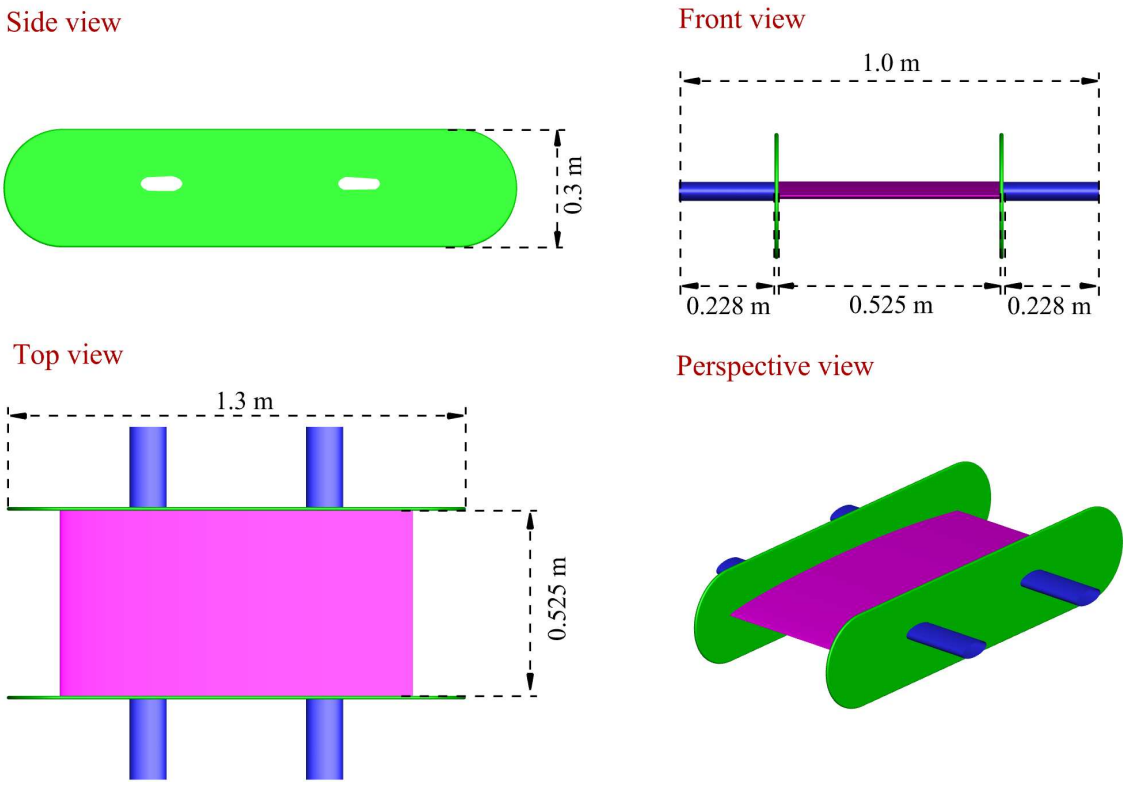

Figure 5.1: Foil of 0.525 m span with end plates and support arms

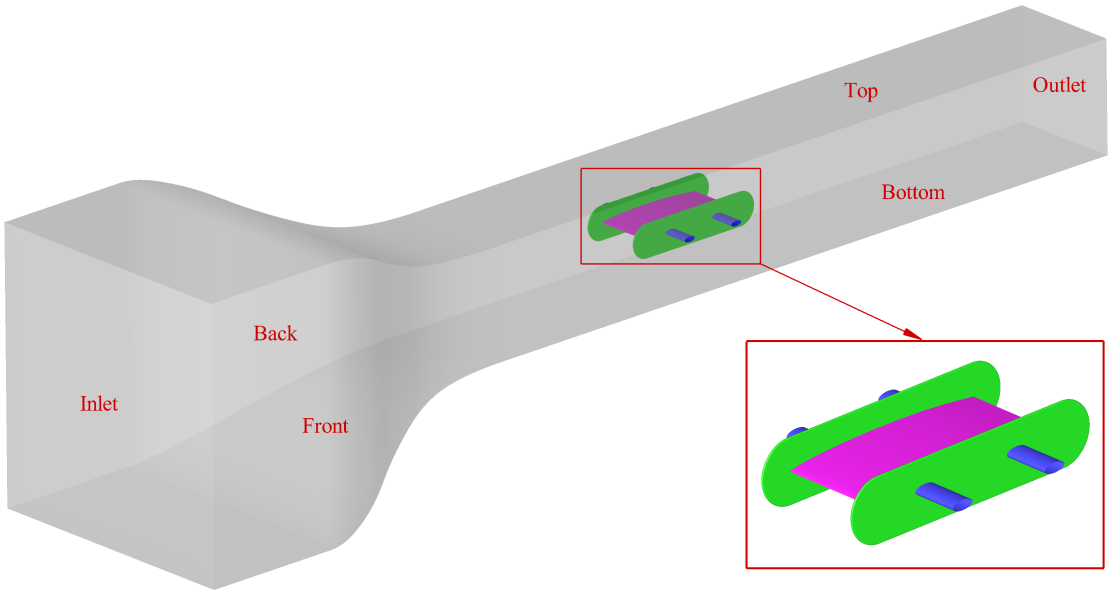

Figure 5.2: Geometry and computational domain of the cavitation tunnel

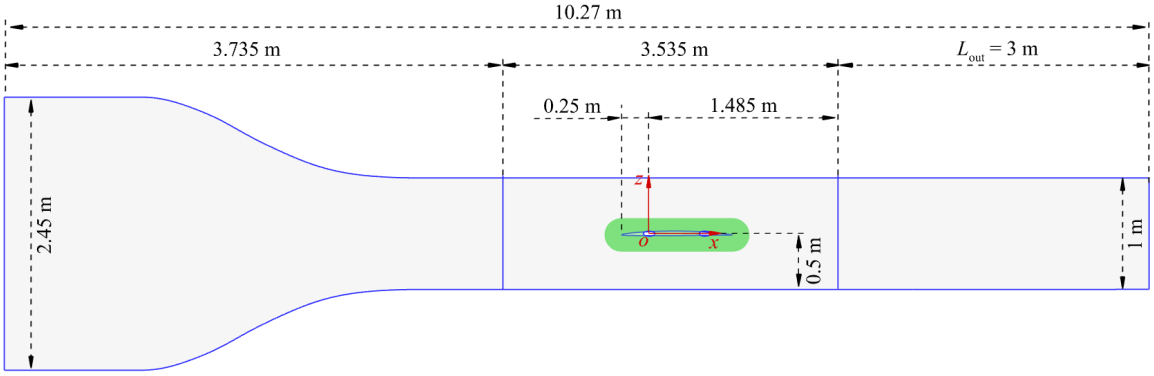

Figure 5.3: Domain sizes for 3-D simulations of the foil with 0.525 m span

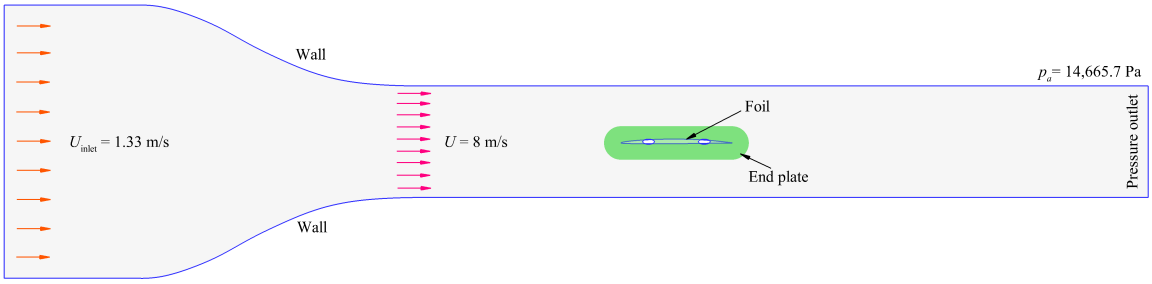

Figure 5.4: Boundary conditions for the the foil with 0.525 m span

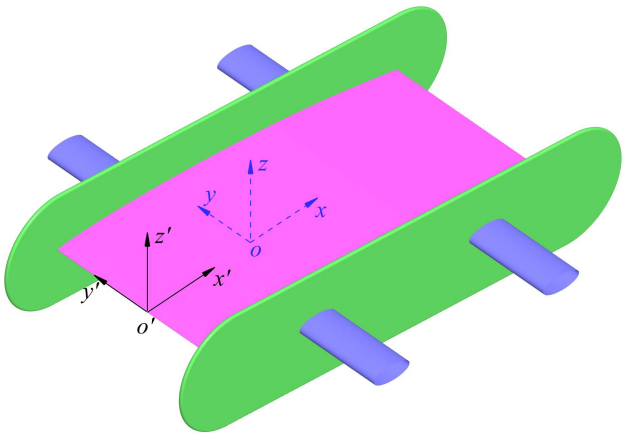

Figure 5.5: Coordinate system for 3-D simulations of the foil with 0.525 m span

As shown in Fig. 5.2, the computational domain covers a segment of the cavitation tunnel with square inlet and outlet sections. Figure 5.3 presents the domain size and the location of the foil inside the tunnel with the length of downstream $L_{\text{out}} = 3.0$ m. Following the dimensions of cavitation tunnel at the Brodarski Institut in Zagreb (Gospodnetic, 2022), the lengths of the inlet and outlet square's side are 2.45 m and 1.0 m, respectively.

The boundary conditions, as an example, for the convergence study is presented in Fig. 5.4. The pressure boundary condition with $p = p_a$ was specified on the outlet. A no-slip wall boundary condition was imposed on the surface of the foil. The Reynolds number in terms of the chord length of foil for all cases was $Re = 8.0 \times 10^6$. At the inlet boundary, a uniform velocity of $U_{\text{Inlet}} = 1.33$ m/s was specified. This leads to the inflow velocity of $U = 8.0$ m/s on the inlet of the test segment. Note that the angle of attack, α, is 0° in Figs. 5.3 and 5.4.

The origin is located at the center of the support arm. The oy-axis is along the span direction. The origin of the coordinate system, o-xyz, used in the present 3D simulations was shifted to o' (−0.250 m, 0 m, −0.011 m), as shown in Fig. 5.5. In

this way, $o'x'z'$ is consistent with the coordinate system in 2-D studies, which allows for direct comparison of 2-D and 3-D results.

5.2 Grid Generation

Due to the complex geometry of end plates attached to the foil of 0.525 m span, a hybrid grid with structured meshes around the foil and unstructured meshes near the end plates was generated. Similar to the study of the foil with 1 m span, the meshing topology of Gauthier and Hally (2019) was also employed in this chapter.

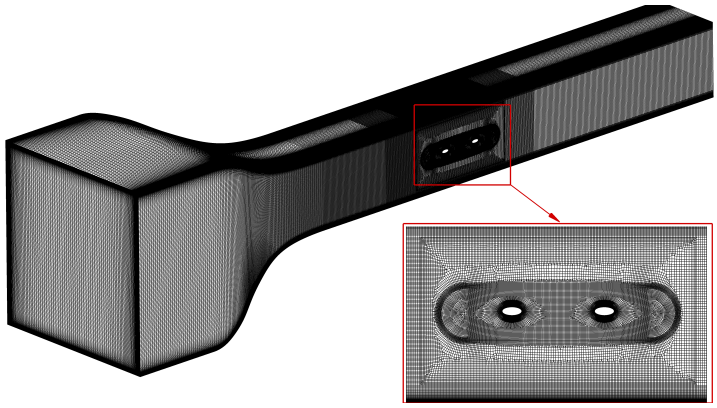

Figure 5.6: Grid for the foil with 0.5 mm defect at the angle of attack $\alpha = 0°$

A representative numerical grid for the foil of 0.525 m span with 0.5 mm defect at the angle of attack $\alpha = 0°$, as an example, is shown in Fig. 5.6. For this case, the first-grid spacing, y^+, is 1.0 and the length between the end of test segment and outlet, L_{out}, is 3 m. The total number of grids is 50,006,864. Note that 39 cells were distributed over the 0.5 mm defect to resolve the flow details. Meshes near the foil and the end plates are presented in Fig. 5.7 and Fig. 5.8, respectively, where the green part is end plate (150 mm long); the blue part denotes the support arms connecting

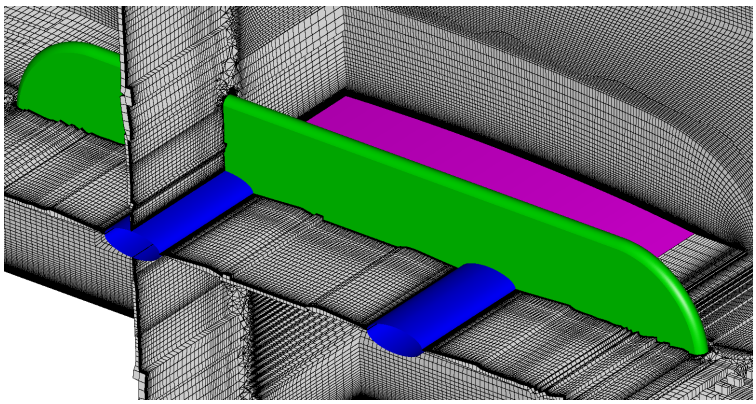

Figure 5.7: Meshes near foil and end plate

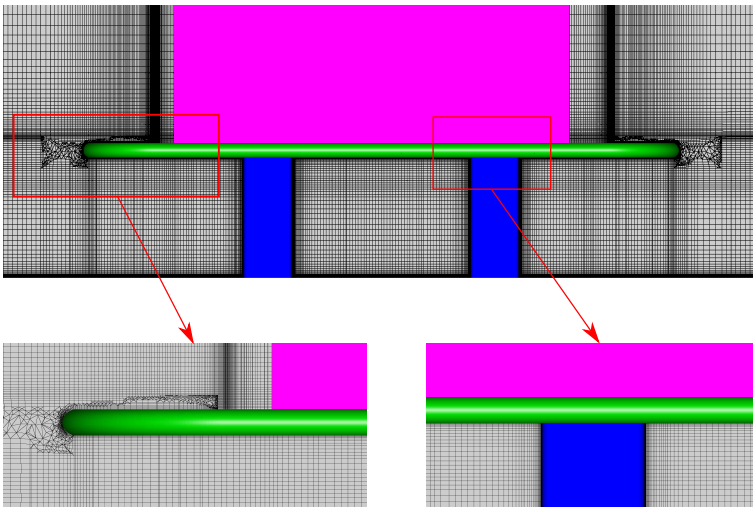

Figure 5.8: Views of local meshes

the foil to the tunnel walls; and the pink part represents for the surface of foil.

In present work, the number of grids in convergence studies ranges from 36,472,948 to 76,665,420. For instance, the number of grids for foils of 0.525 m span with and without defects at the angle of attack $\alpha = 4$ degrees are summarized in Table 5.1.

Table 5.1: Number of grids for foils of 0.525 m span with and without defects at the angle of attack $\alpha = 4°$

Item	No defect	0.1 mm defect	0.25 mm defect	0.5 mm defect
Number of grids over the span	100	100	100	100
Number of grids on suction side	289	289	302	298
Number of grids on pressure side	253	253	253	260
Number of grids on defect	-	21	35	39
Total number of grids	48,982,310	49,160,012	49,252,634	50,070,594

5.3 Simulation Parameters

Convergence studies on the domain size, grid aspect ratio, first-grid spacing, y^+, and turbulence model were first carried out. The foils of 0.525 m span with no defect and 0.5 mm defect at angles of attack $\alpha = 0°$, 1.25° and 4° were investigated. A summary of simulation parameters in convergence studies is provided below:

- Domain size in terms of L_{out}: 2.0, 3.0, 4.0, 5.0 and 6.0 m.
- Grid aspect ratio at LE, AR_L: 8.0, 16.0 and 32.0.
- First-grid spacing, y^+: 0.5, 0.707, 1.0, 1.414, 2.0, 2.828 and 4.0.
- Turbulence model: $k - \varepsilon$, $k - \omega$, SST $k - \omega$ and Spalart-Allmaras

Using the best-practice settings, studies were then carried out for the foils with no defect, 0.10 mm defect, 0.25 mm defect and 0.50 mm defect at various angles of attack between -4.0 and 5.0 degrees. The same convergence criteria as presented

in Section 4.3 was applied for the foils of 0.525 m span in this chapter. The initial turbulence intensity and turbulent viscosity ratio for the RANS models were set as 0.01 and 10, respectively. The detailed settings used in present 3-D simulations can be found in Table 3.6.

Furthermore, the preliminary validation studies for the foils of 0.525 m span with no defect and 0.5 mm defect were also carried out on the cavitation buckets. In the cavitation tests, inflow velocity at each angle of attack was varied (increased/decreased) until cavitation was observed. The same approach was applied in 3-D RANS simulations with the recommended best-practice settings. The cavitation bucket was obtained by examining the lowest pressure on the foil surface. When the lowest pressure equals to the vapour pressure, cavitation occurs. For each angle of attack, a variety of inflow velocities need to be simulated. The average values of detailed operating conditions, according to the experimental tests, are summarized below and presented in Tables 5.2 and 5.3, where t_w and p_v denote the temperature of water and vapour pressure of water, respectively.

- Geometry: No defect, 0.5 mm defect;
- Inflow velocity, U (m/s): 3.33 $\sim$ 7.85;
- Angle of attack, α (°): -0.75 $\sim$ 4.75.

Table 5.2: Operating conditions for the foil with no defect

α (deg)	U (m/s)	p_0 (Pa)	t_w (°C)	p_v (Pa)
4.75	6.12	11,748.00	19.70	2,290.45
4.50	6.28	11,900.50	19.70	2,290.45
4.25	6.26	11,051.20	19.70	2,290.45
4.00	6.85	10,908.25	19.80	2,304.74
3.75	6.81	10,198.50	19.73	2,295.22
-0.75	7.54	19,867.67	22.90	2,786.89
-1.00	6.60	18,013.11	22.72	2,757.20
-1.50	5.80	18,970.38	22.50	2,720.08
-2.00	5.28	21,638.57	21.80	2,618.43
-2.34	4.60	20,950.44	23.03	2,809.52
-2.50	3.76	16,221.00	17.10	1,946.05
-3.00	3.55	17,007.50	17.23	1,961.66
-3.50	3.69	17,493.07	17.43	1,987.69
-4.00	3.88	17,459.80	17.30	1,971.03

Table 5.3: Operating conditions for the foil with 0.5 mm defect

α (deg)	U (m/s)	p_0 (Pa)	t_w (°C)	p_v (Pa)
4.75	5.16	17,253.00	19.70	2,290.45
4.50	5.46	16,979.50	19.70	2,290.45
4.25	5.58	15,791.83	19.70	2,290.45
4.00	6.53	13,325.38	19.75	2,297.60
3.75	6.50	12,821.25	19.73	2,294.03
3.50	6.85	11,958.50	19.70	2,290.45
-0.75	7.83	15,016.67	22.90	2,786.89
-1.00	7.20	15,667.44	22.72	2,757.20
-1.50	6.10	17,320.88	22.50	2,720.08
-2.00	4.98	19,152.43	19.70	2,313.47
-2.34	4.48	22,310.09	23.06	2,814.66
-2.50	3.54	17,220.33	17.10	1,946.05
-3.00	3.33	18,027.91	17.24	1,963.08
-3.50	3.73	17,239.46	17.49	1,995.12
-4.00	3.81	17,715.50	17.10	1,946.05

5.4 Simulation Results

5.4.1 Results of Convergence Studies

A total of 114 cases were carried out in the convergence studies for the foils of 0.525 m span with 0.5 mm defect and no defect at angles of attack $\alpha = 0$, 1.25 and 4 degrees. Results on the mid-span sections of foils are presented and discussed in this section.

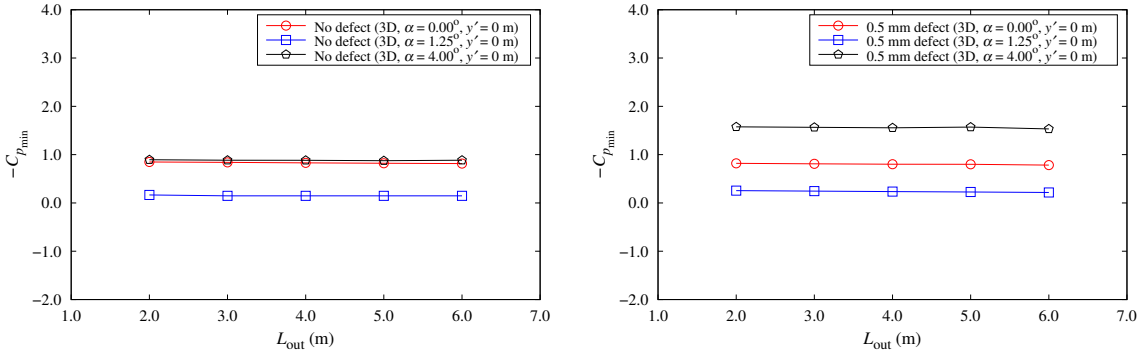

(a) No defect (b) 0.5 mm defect

Figure 5.9: Convergence of $-C_{p_{\min}}$ to L_{out} for the foils of 0.525 m span with no and 0.5 mm defects

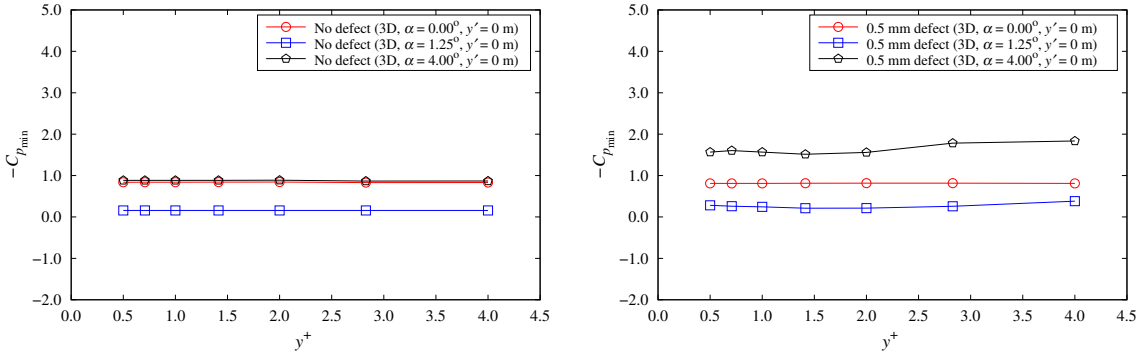

(a) No defect (b) 0.5 mm defect

Figure 5.10: Convergence of $-C_{p_{\min}}$ to y^+ for the foils of 0.525 m span with no and 0.5 mm defects

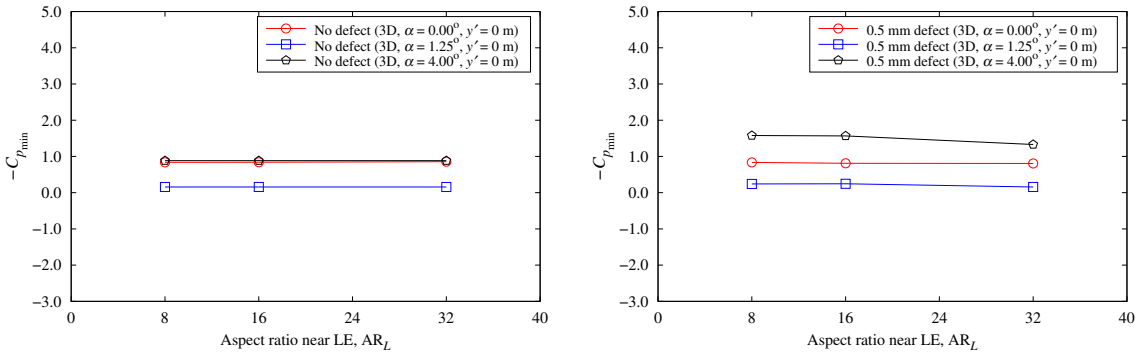

(a) No defect (b) 0.5 mm defect

Figure 5.11: Convergence of $-C_{p_{\min}}$ to AR_L for the foils of 0.525 m span with no and 0.5 mm defects

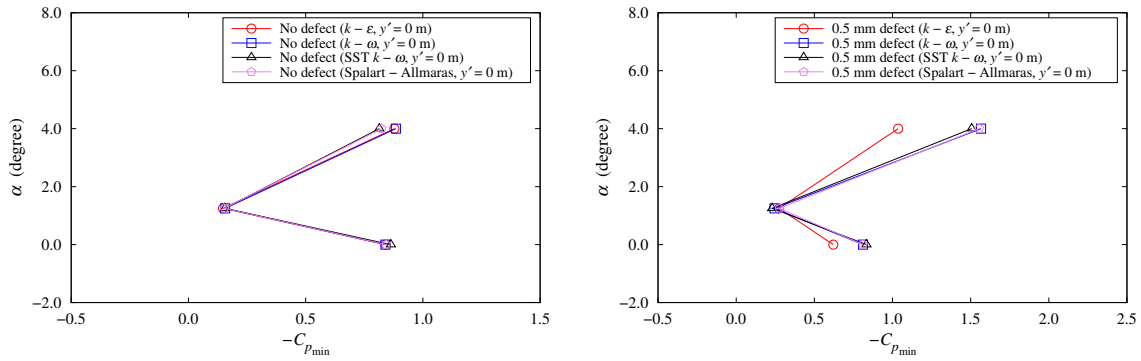

(a) No defect (b) 0.5 mm defect

Figure 5.12: Convergence of $-C_{p_{\min}}$ to turbulence model for the foils of 0.525 m span with no and 0.5 mm defects

Four domain sizes in terms of $L_{\text{out}} = 2.0$, 3.0, 4.0, 5.0 and 6.0 m were investigated. The convergence of negative minimum pressure coefficient to L_{out} is shown in Fig. 5.9. It can be seen that numerical results converged with the increase of the length of downstream. The negative minimum pressure coefficients, $-C_{p_{\min}}$, are insensitive to L_{out} at three angles of attack $\alpha = 0$, 1.25 and 4 degrees. In the following studies, $L_{\text{out}} = 3.0$ m was used.

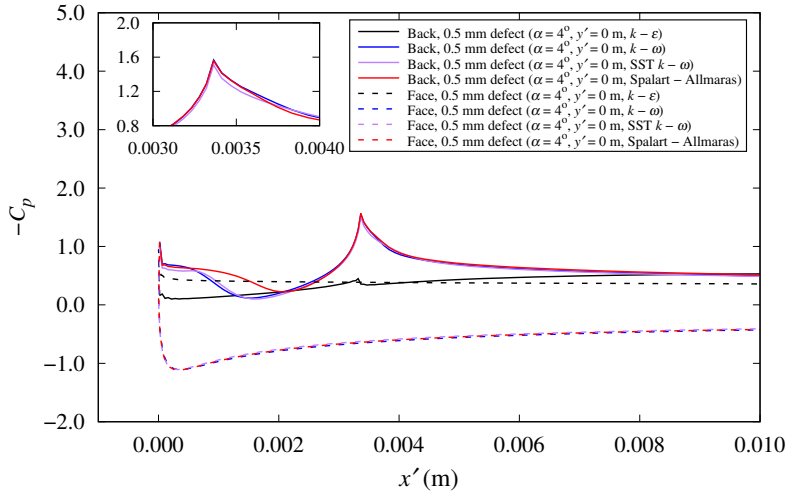

Figure 5.13: Convergence of pressure distributions near the LE on the face and back to turbulence model for the foil of 0.525 m span with 0.5 mm defect at $\alpha = 4°$

The effect of the first-grid spacing, y^+, for the foils with no defect and 0.5 mm defect was also investigated with $y^+ = 0.5$, 0.707, 1.0, 1.414, 2.0, 2.828 and 4.0. The negative minimum pressure coefficients with the $k - \omega$ model at angles of attack, $\alpha = 0°$, 1.25° and 4°, are presented in Fig. 5.10. It can be seen that the results at angle of attack $\alpha = 0°$ were insensitive to y^+. The predictions exhibited oscillations before converging as the y^+ decreased for the foil with 0.5 mm defect at $\alpha = 4°$. The first-grid spacing, $y^+ = 1.0$, was then employed.

Three aspect ratios for the near LE, $\text{AR}_L = 8$, 16, and 32, were used with $y^+ = 1.0$ to simulate the flow near the defect. The corresponding results at $\alpha = 0°$, 1.25° and 4° are presented in Fig. 5.11. The results indicated that the effect of grid aspect ratio on solutions with the $k - \omega$ was insignificant when $\text{AR}_L \leq 16$. The grid aspect ratio of 16 over the defect was then chosen.

Furthermore, various turbulence models, including the $k - \varepsilon$, $k - \omega$, SST $k - \omega$,

and Spalart-Allmaras models, were employed to examine their effects on the prediction of the minimum pressure coefficient at selected angles of attack. The aspect ratio of 16 over leading edge was employed. In the near-wall layers, the first-grid spacing was set as $y^+ = 1.0$. Results for the foils with no defect and 0.5 mm defect are shown in Fig. 5.12. For instance, the pressure distributions near LE on the face and back for the foil with 0.5 mm defect at angle of attack $\alpha = 4^\circ$ with different turbulence models are also presented in Fig. 5.13. The numerical solutions at angle of attack of 4° were affected significantly by turbulence models, especially for the cases with 0.5 mm defect. The results with $k - \varepsilon$ are different from those by other three turbulence models. As shown in Fig. 5.13, similar results were obtained with the $k - \omega$ and SST $k - \omega$ models. Note that the $k - \omega$ model, which is also the one recommended as best practice for 2-D simulations, was then recommended in the following simulations.

According to the convergence studies, the best-practice settings are recommended and summarized in Table 5.4.

Table 5.4: Best-practice settings for 3-D simulations with foil of 0.525 m span

Items	Variable	Recommended setting	Value
Domain size	L_{out}	≥ 3.0 m	3.0 m
First-grid spacing	y^+	[0.5, 1.0]	1.0
Grid aspect ratio near LE	AR_L	≤ 16	16
Turbulence model		$k - \omega$ SST $k - \omega$	$k - \omega$

5.4.2 Results with Best-Practice Settings

Using the best-practice settings, studies were carried out for the foils of 0.525 m span with no defect, 0.1 mm defect, 0.25 mm defect and 0.5 mm defect at various angles of attack range from -4.0 to 5.0 degrees. The cavitation buckets, minimum pressure coefficients and their locations on the foil surface, residuals of simulations, reduction of cavitation inception speed, as well as results of the preliminary validation study are provided in the following subsections.

5.4.2.1 Cavitation Buckets

Cavitation buckets, obtained using the mid-span section, are compared for the foils without and with three different LE defects (0.5 mm, 0.25 mm and 0.1 mm) in Fig. 5.14. The results of 2-D and 3-D with the foil of 1.0 m span are also included. The cavitation buckets are narrowed by the LE defects in the typical design range of angle of attack, $-1.5^\circ < \alpha < 2^\circ$, similar to the findings from 2-D results and 3-D solutions with 1.0 m span, which means that the incipient cavitation speed is reduced by the LE defect. However, the shapes of cavitation buckets are generally different with the reference data. This is mainly attributed to the effect of the attached end plates and support arms.

Figure 5.15 shows the second invariant of the velocity gradient tensor isosurfaces, $Q_c = 50\ \mathrm{s}^{-2}$, colored with horizontal velocity, u_1, while the solid surfaces of the foil, end plate and support arm are colored with gray. In STAR-CCM+, the value of Q_c can be determined with

$$Q_c = \frac{1}{2}\left((\nabla \cdot \mathbf{u})^2 + \|\mathbf{\Omega}\|_2^2 - \|\mathbf{S}\|_2^2\right) \tag{5.1}$$

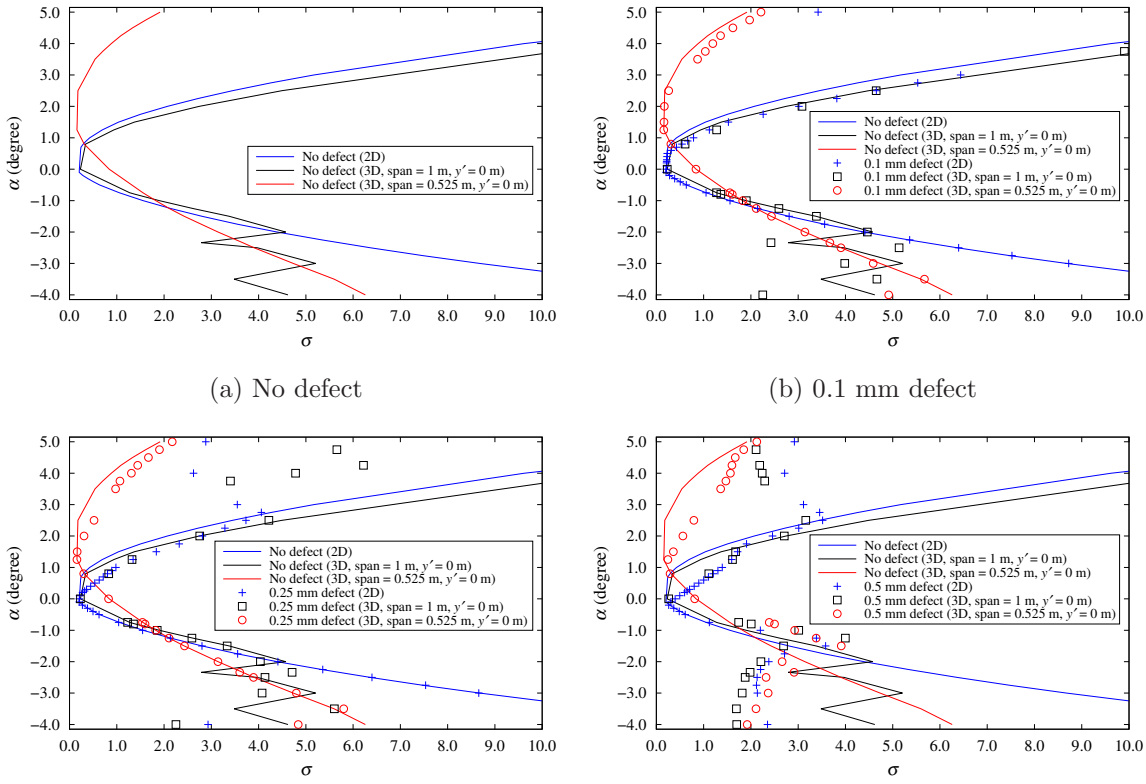

(a) No defect

(b) 0.1 mm defect

(c) 0.25 mm defect

(d) 0.5 mm defect

Figure 5.14: Cavitation buckets for the foils of 0.525 m span with and without LE defects using mid-span section

in which, $\mathbf{u}$ is the velocity vector, $\mathbf{S}$ is the strain rate tensor, and $\mathbf{\Omega}$ is the rotation rate tensor.

According to the definition, thresholding Q_c to positive values identifies rotation-dominated regions of the flow, or vortices. Similarly, negative values of Q_c are associated with straining regions of the flow (Banko and Eaton, 2019). As shown in Fig. 5.15, vortices are clearly identified in regions close to the wall and trailing edge of the foil for the results with 1.0 m span, while strong vortices can be observed after the support arms and the end plates in the solutions for the span of 0.525 m. It can also be seen that the LE defects have little impact on the vortex pattern in the

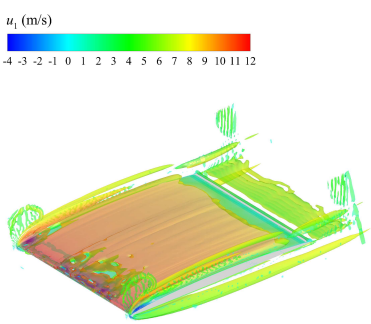

(a) No defect (span = 1.0 m)

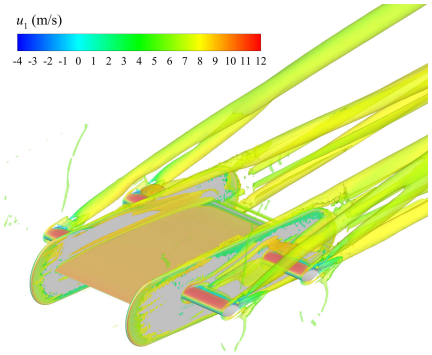

(b) No defect (span = 0.525 m)

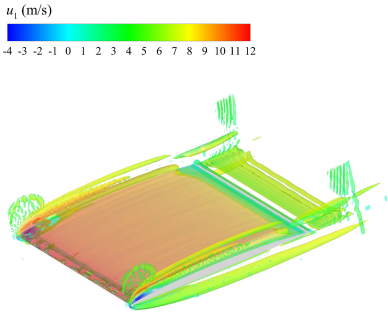

(c) 0.1 mm defect (span = 1.0 m)

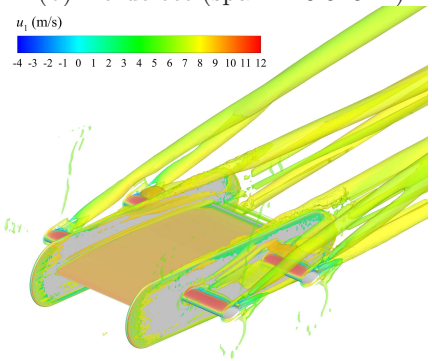

(d) 0.1 mm defect (span = 0.525 m)

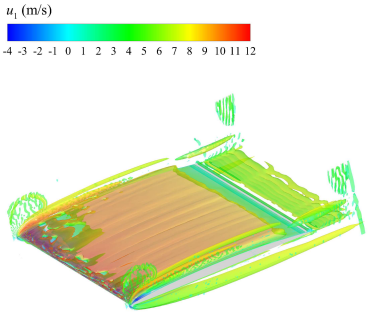

(e) 0.25 mm defect (span = 1.0 m)

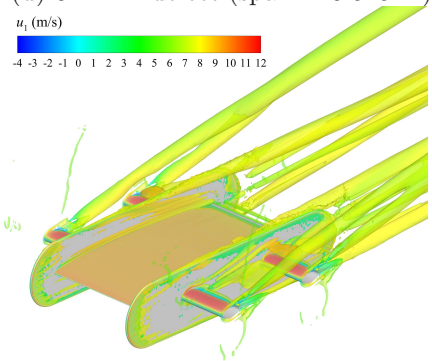

(f) 0.25 mm defect (span = 0.525 m)

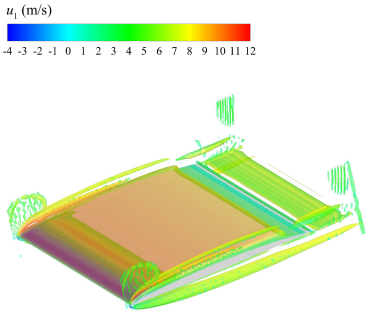

(g) 0.5 mm defect (span = 1.0 m)

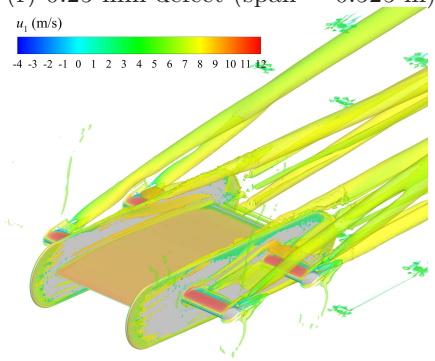

(h) 0.5 mm defect (span = 0.525 m)

Figure 5.15: Comparison of the isosurfaces of $Q_c = 50$ s^{-2} colored with horizontal velocity, u_1, for the foils with and without LE defects at $\alpha = 4°$

simulations for the 0.525 m span.

5.4.2.2 Pressure Contours and Streamlines

As one example, the comparison of pressure coefficient contours and streamlines near the LE at $\alpha = 2^\circ$ for the foils with no defect, 0.5 mm defect, 0.25 mm defect and 0.1 mm defect are presented in Fig. 5.16. The minimum pressure coefficients and their locations on the foil surface are also given in these figures. As expected, the defect led to lower pressure near the LE. It can be found that the differences in the pressure distributions from 2-D and 3-D simulations of 1 m span are generally insignificant. However, as a result of the significant vortices generated with the end plate and support shaft, the solutions with 0.525 m span are different from them. Table 5.5 shows minimum pressures and their locations for the foils with and without defects at $\alpha = 2^\circ$. Although locations of the minimum pressure depend on the size of a defect, they are generally located close to the ends of the flat defect. For example, the upper end point of the 0.5 mm defect is (0.00316 m, 0.0027 m) and the location of the minimum pressure for the span 0.525 m is at (0.00328 m, 0.00260 m) in Fig. 5.16.

Furthermore, the pressure distributions near the LE on the face and the back for foils with and without defect at $\alpha = 2^\circ$ of the mid-span section are presented in Fig. 5.17. It was found that the pressures on the back were significantly changed by the defect near LE. The effect of LE defect on pressure distribution is generally obvious, especially for the 0.5 mm defect.

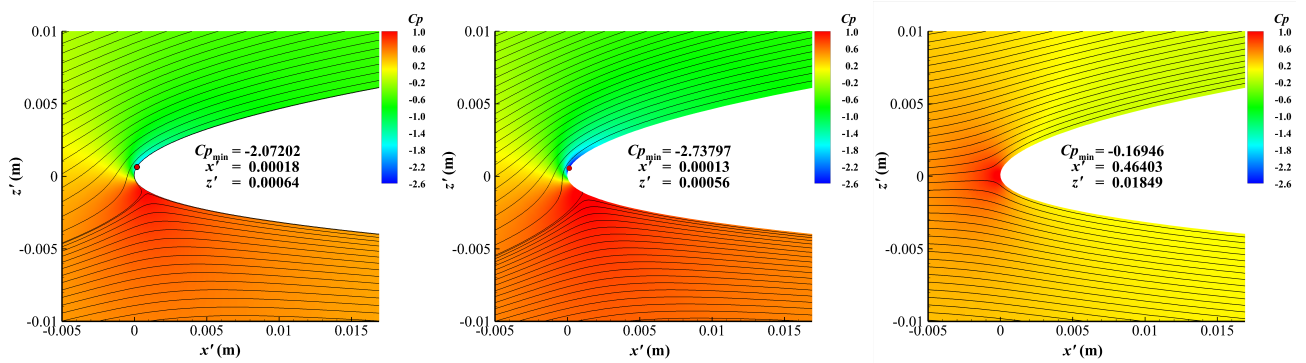

(a) No defect (2D)

(b) No defect (3D, span=1 m)

(c) No defect (3D, span=0.525 m)

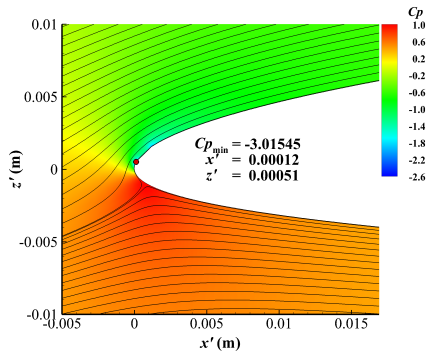

(d) 0.1 mm defect (2D)

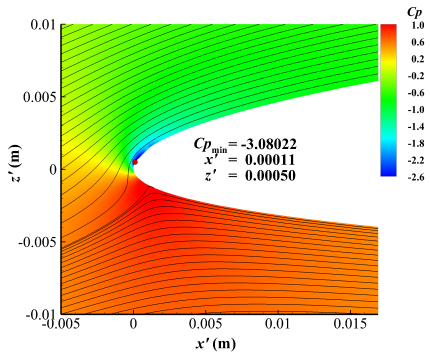

(e) 0.1 mm defect (3D, span=1 m)

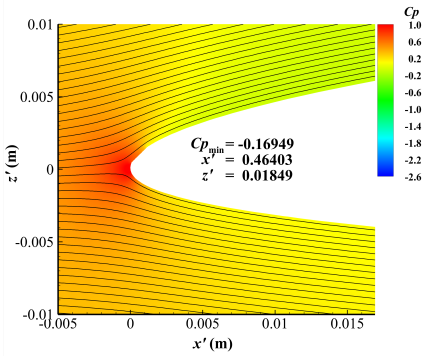

(f) 0.1 mm defect (3D, span=0.525 m)

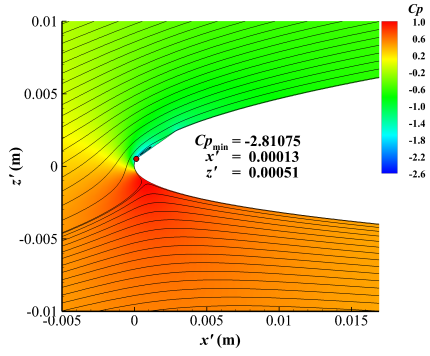

(g) 0.25 mm defect (2D)

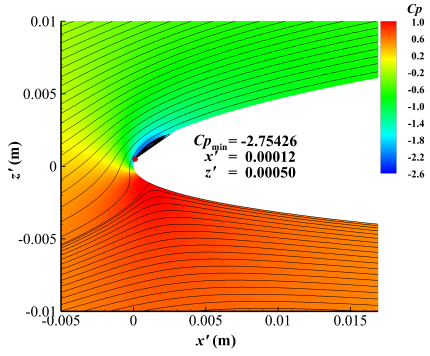

(h) 0.25 mm defect (3D, span=1 m)

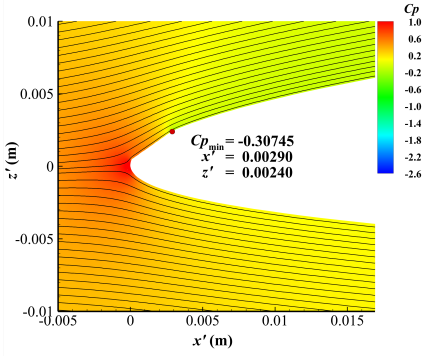

(i) 0.25 mm defect (3D, span=0.525 m)

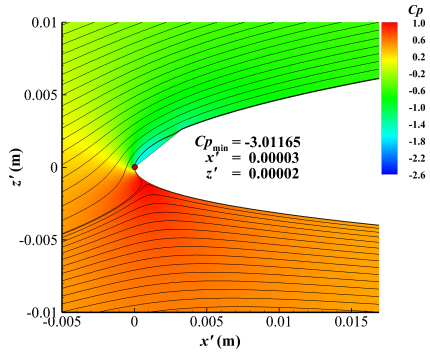

(j) 0.5 mm defect (2D)

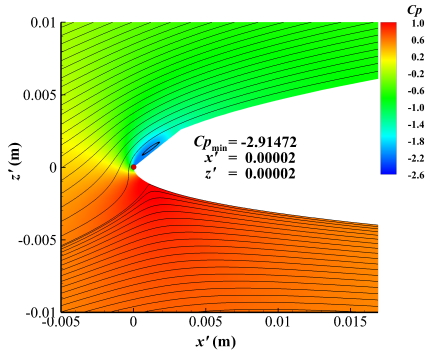

(k) 0.5 mm defect (3D, span=1 m)

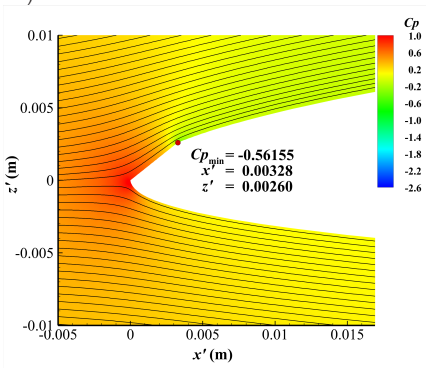

(l) 0.5 mm defect (3D, span=0.525 m)

Figure 5.16: Comparison of the pressure coefficient contours and streamlines for the foils with and without LE defects at $\alpha = 2^\circ$ of mid-span section

Table 5.5: Minimum pressure coefficients and their locations for the foils of 0.525 m span with and without LE defects at $\alpha = 2^\circ$

Simulation	Item	No defect	0.5 mm defect	0.25 mm defect	0.1 mm defect
2D	$-C_{p_{\min}}$	2.07202	3.01165	2.81075	3.01545
	x'	0.00018	0.00003	0.00013	0.00012
	z'	0.00064	0.00002	0.00051	0.00051
3D (Span = 1.0 m)	$-C_{p_{\min}}$	2.73797	2.91472	2.75426	3.08022
	x'	0.00013	0.00002	0.00012	0.00011
	z'	0.00056	0.00002	0.00050	0.00050
3D (Span = 0.525 m)	$-C_{p_{\min}}$	0.16946	0.56155	0.30745	0.16949
	x'	0.46403	0.00328	0.00290	0.46403
	z'	0.01849	0.00260	0.00240	0.01849

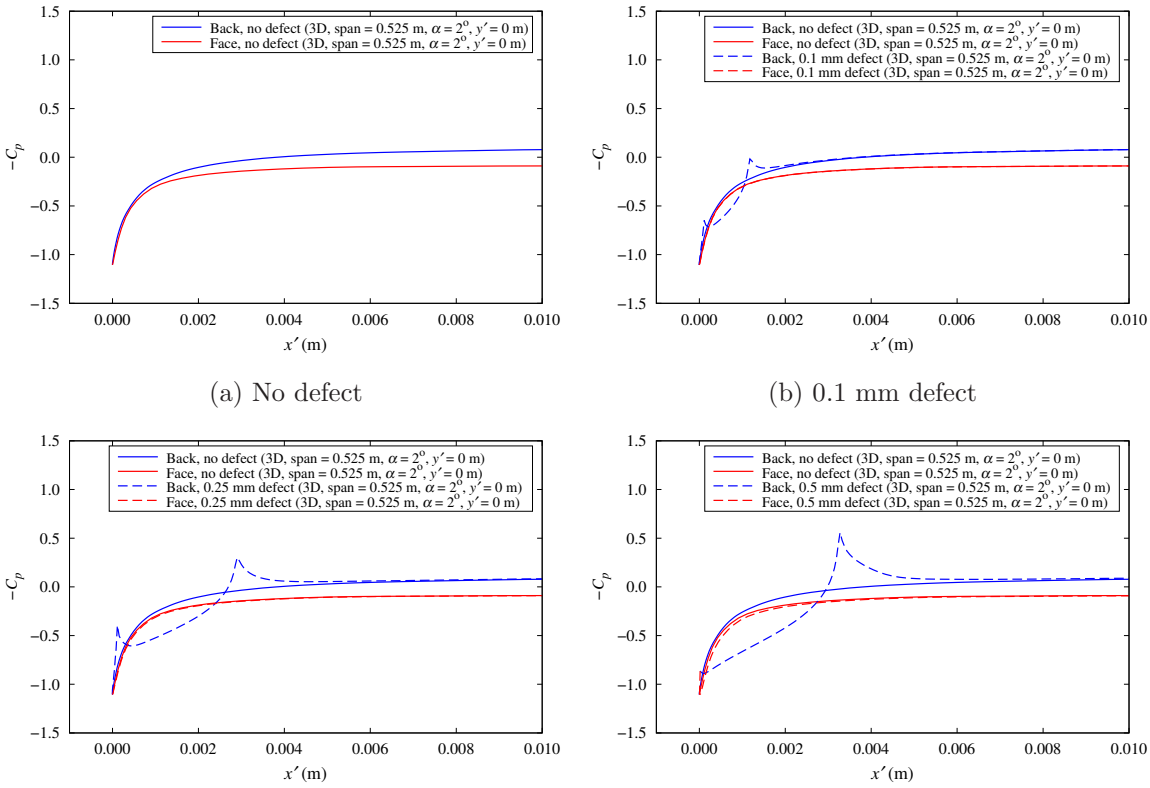

(a) No defect

(b) 0.1 mm defect

(c) 0.25 mm defect

(d) 0.5 mm defect

Figure 5.17: Comparison of the pressure distributions for the foils of 0.525 m span with and without LE defects at $\alpha = 2^\circ$ of mid-span section

5.4.2.3 Residuals of Simulations

Residuals of simulations for the four foils of 0.525 m span with no defect, 0.5 mm defect, 0.25 mm defect and 0.1 mm defect at $\alpha = 4°$ are shown in Fig. 5.18, as one example. Three orders of magnitude reduction in residuals were achieved.

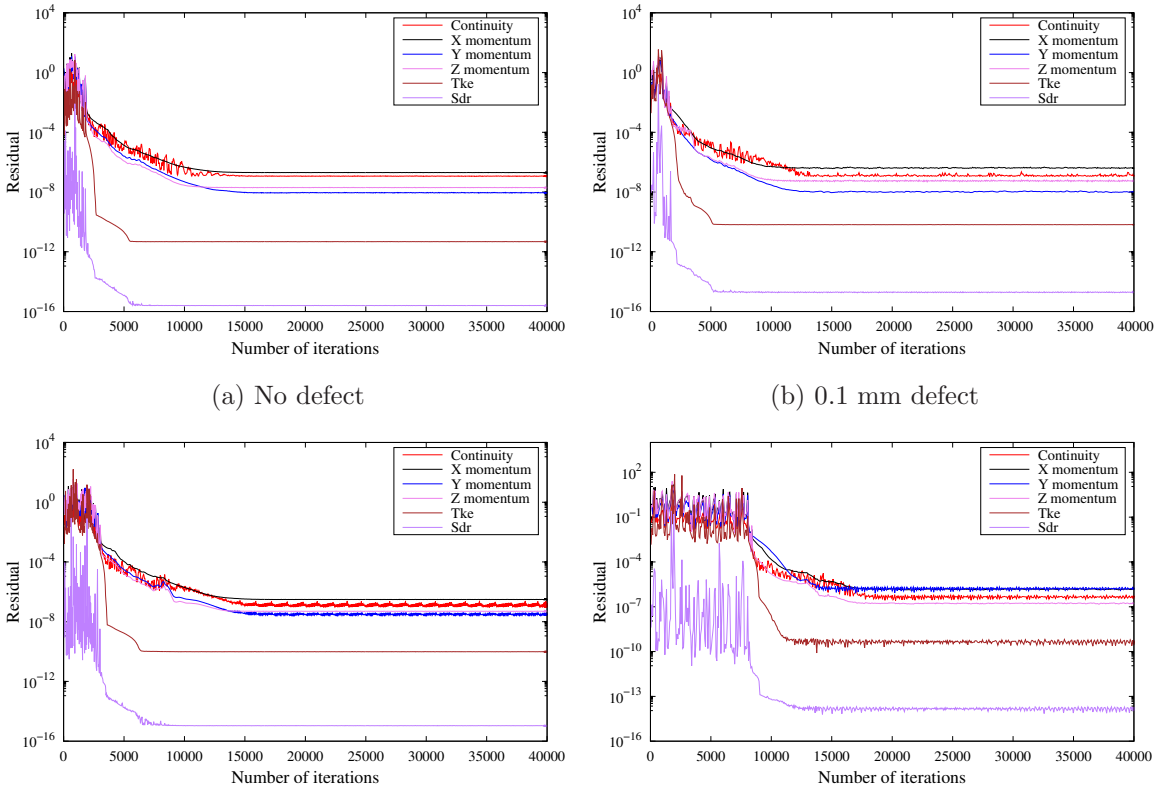

(a) No defect

(b) 0.1 mm defect

(c) 0.25 mm defect

(d) 0.5 mm defect

Figure 5.18: Residuals of simulations for the foils of 0.525 m span with and without LE defects at $\alpha = 4°$

5.4.2.4 Effect of LE Defect on Cavitation Inception Speed

Based on the cavitation buckets shown in Fig. 5.14, Fig. 5.19 presents the comparison of the percentage reduction in inception speed for the foils with LE defects in 2-D and 3-D simulations. The detailed calculation data for the foils with 0.525 m span is provided in Table 5.6. From the predicted cavitation buckets and reductions in cavitation inception speed, it can be observed that the LE defect has a significant effect on cavitation inception speed in the typical design range of angle of attack ($-1.5^\circ < \alpha < 2^\circ$) for a moderately loaded propeller.

The 2-D and 3-D simulations of 1.0 m span foils exhibit similar result patterns in the predicted ISR, with minor differences between them at most angles of attack. However, the 3-D simulations of 0.525 m span foils, which have end plates, show significant discrepancies in the ISR predictions, particularly when angles of attack are positive. Effects of end plate should be carefully examined and new designs will be used in the upcoming cavitation tunnel tests.

For the foils with 0.525 m span, the reduction in inception speed can reach to about 50% for the foil with 0.5 mm defect around $\alpha = 2^\circ$. Between $\alpha = 0.75^\circ$ and $\alpha = 2^\circ$, the reduction increases with the size of LE defect.

In summary, the LE defects significantly reduce the cavitation inception speeds at the normal range of angles of attack.

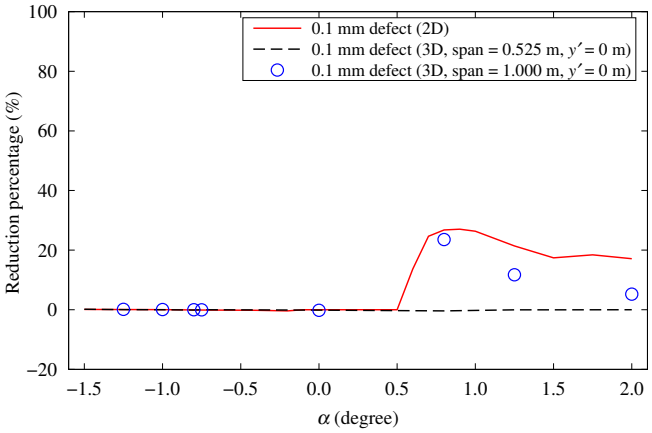

(a) 0.1 mm defect

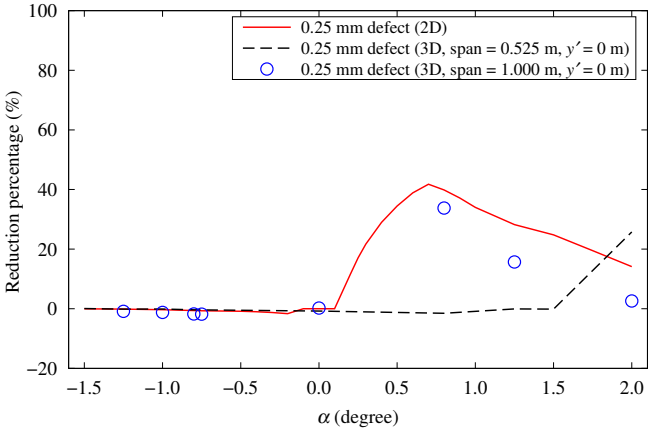

(b) 0.25 mm defect

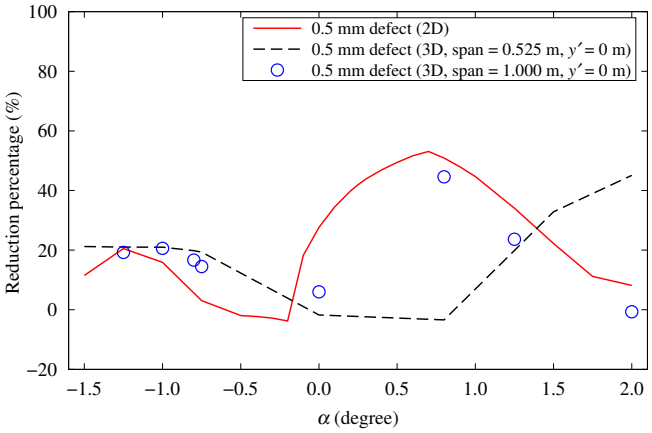

(c) 0.5 mm defect

Figure 5.19: Comparison of the reduction percentage in cavitation inception speed for the foils with LE defects from 2-D and 3-D simulations

Table 5.6: The percentage reduction in cavitation inception speed (mid-span section) for the foils of 0.525 m span in typical design range

α (°)	$-C_{p_{\min}}$				Percentage reduction in inception speed (%)		
	No defect	0.5 mm defect	0.25 mm defect	0.1 mm defect	0.5 mm defect	0.25 mm defect	0.1 mm defect
-1.50	2.42764	3.91201	2.43149	2.43518	21.22	0.08	0.16
-1.25	2.10927	3.38035	2.10404	2.11158	21.01	-0.12	0.05
-1.00	1.82577	2.92505	1.82201	1.82592	20.99	-0.10	0.00
-0.80	1.60850	2.50083	1.59688	1.60595	19.80	-0.36	-0.08
-0.75	1.55378	2.38821	1.54231	1.55410	19.34	-0.37	0.01
0.00	0.83970	0.81110	0.82688	0.83739	-1.75	-0.77	-0.14
0.80	0.30993	0.28992	0.30069	0.30756	-3.39	-1.53	-0.38
1.25	0.15698	0.24457	0.15683	0.15686	19.88	-0.05	-0.04
1.50	0.16200	0.35951	0.16160	0.16187	32.87	-0.12	-0.04
2.00	0.16946	0.56155	0.30745	0.16949	45.07	25.76	0.01

5.4.2.5 Preliminary Validation Study

Preliminary tests had been carried out by Gospodnetic (2022) in the cavitation tunnel at the Brodarski Institut in Zagreb, Croatia. As shown in Fig 5.20, the working section of the cavitation tunnel is 3.5 m long with a cross-section of 1 m by 1 m. Figures 5.21 and 5.22 present the experimental set-up in the cavitation tunnel. Four flanges were used to mount and secure the foil model in the cavitation tunnel. Flanges were bolted into recessed slots on the sides of the foil. Locations of flanges were at 25% of the chord length from the leading-edge. The end plates, fabricated with 10 mm thick Lexan, were bolted on each side of the foil.

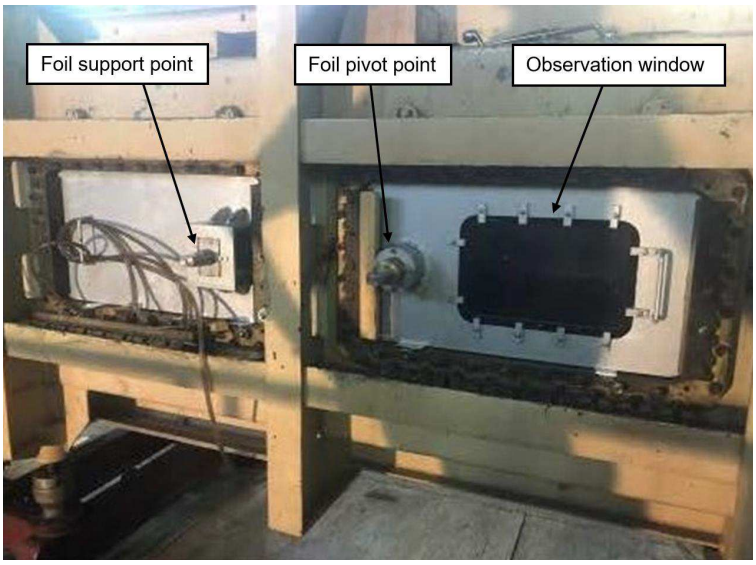

Figure 5.20: Measurement section of the cavitation tunnel (Gospodnetic, 2022)

The preliminary validation studies for the foils of 0.525 m span with no defect and 0.5 mm defect were conducted using the recommended settings. The cavitation buckets, obtained using the mid-span section of the foils with no defect and 0.5 mm defect, at angles of attack from $\alpha = -4^\circ$ to $\alpha = 4.75^\circ$ are shown in Fig. 5.23. It

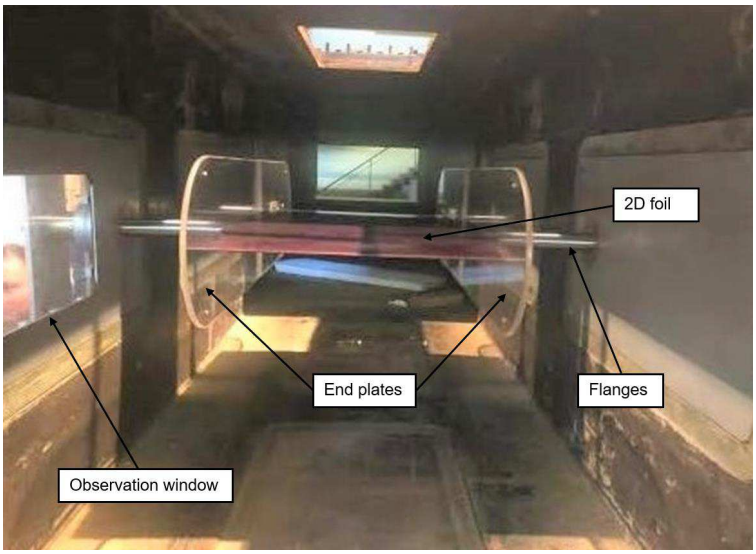

Figure 5.21: View from the LE for the foil model in the cavitation tunnel (Gospodnetic, 2022)

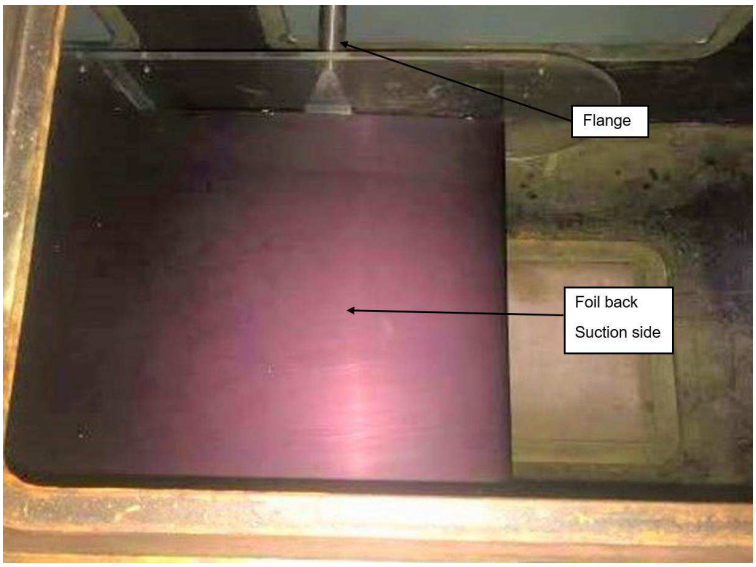

Figure 5.22: View from the top window for the foil model in the cavitation tunnel (Gospodnetic, 2022)

can be seen that the shapes of cavitation buckets are generally similar to those of the experimental ones. For the foils at positive angles of attack, the results indicate that the LE defect narrowed the cavitation bucket in comparison to the foil with no defect.

Note that the experimental cavitation buckets were based on observation during the tests while the numerical ones were determined from a single point where the pressure was equal to the vapour pressure. It took some time for a cavity to develop and become visible in the tests. This was not considered in the numerical simulations with the steady RANS solver. In future studies, the unsteady solver with a cavitation model should be used to simulate the development of cavitation in the tests.

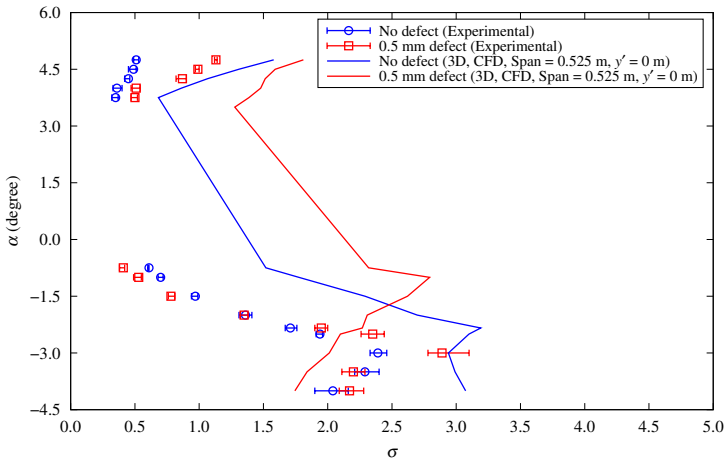

Figure 5.23: Comparison of experimental cavitation buckets and those from 3-D simulations using mid-span section

Chapter 6

3-D Simulations for a Full-Scale Propeller

This chapter extended 3-D RANS studies on the foils in a cavitation tunnel to full-scale propellers with and without LE defects. The DTMB 5168 propeller model from the study of Chesnakas and Jessup (1998) was used for the geometry of full-scale propellers. With the steady RANS solver in Star-CCM+, thorough convergence studies were carried out for the open-water simulations of the model-scale propeller first and then for the full-scale propellers without defect and with 0.5 mm defect at the advance ratio of $J = 1.102$. Effects of RANS modelling parameters, such as domain size, grid size, stretch ratio, first-grid spacing, y^+, and turbulence model, on the solutions were carefully examined. Numerical uncertainties due to spatial discretization were quantified with the least square root (LSR) method (Eça and Hoekstra, 2014). Based on the results of convergence studies, the best-practice settings for open-water propeller simulations with the steady RANS solver in Star-CCM+ were summarized.

Using the recommended best-practice settings, validation studies were first carried out for the model-scale propeller. Numerical results of downstream velocities, open-water and cavitation performance were compared with the experimental data of Chesnakas and Jessup (1998).

Open-water simulations were then extended to the full-scale propellers without and with LE defects. Effects of LE defects on cavitation inception speed were examined at various advance ratios from 0.921 to 1.205.

6.1 Geometry and Computational Domain

Simulations were carried out for propellers that have the same geometry as the five-bladed fixed-pitch propeller model, DTMB 5168. The geometry and principal particulars of the DTMB 5168 propeller in model and full scales are presented in Fig. 6.1 and Table 6.1, respectively. The Cartesian coordinate system is also shown in Fig. 6.1, where the origin is located at the center of propeller plane disk, the positive direction of X-axis is from upstream to downstream, and the positive direction of Z-axis is upward. For geometric simplification, a cylinder with constant radius (blue part) with a cap (red part) was used to model the hub, and the root fillets were ignored. The geometry of the cap was described by

$$\frac{(\mathrm{X}+0.3R)^2}{(0.65R)^2}+\frac{\mathrm{Y}^2}{(0.2819R)^2}+\frac{\mathrm{Z}^2}{(0.2819R)^2}=1 \tag{6.1}$$

where the value of X is within the range of $-0.95\ R$ to $-0.30\ R$.

As shown in Fig. 6.2, the computational domain is composed of two cylindrical regions: a rotating part containing the propeller and a static part for the rest of

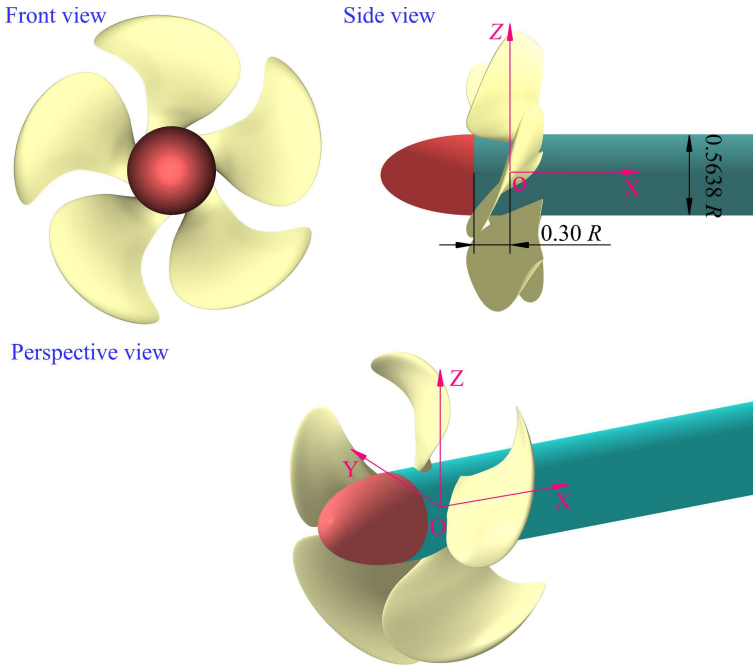

Figure 6.1: Geometry of the DTMB 5168 propeller

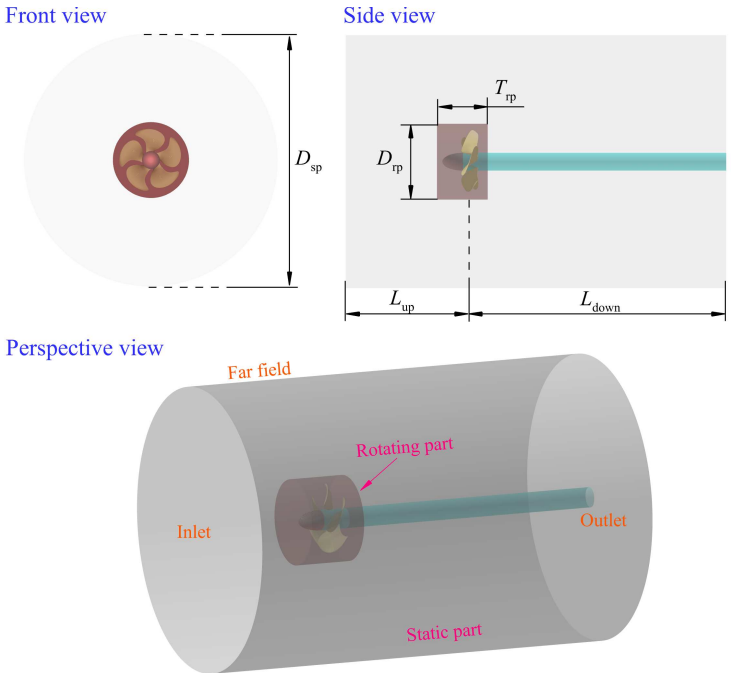

Figure 6.2: Computational domain

Table 6.1: Particulars for the five-bladed DTMB 5168 propeller (scale ratio = 5.71)

Item	Model	Full-scale
Diameter of propeller, D, (m)	0.4027	2.2989
Radius of propeller, R, (m)	0.2013	1.1494
Diameter of hub, D_{h}, (m)	0.1135	0.6481
Chord length at 0.70 R, $c_{0.7}$, (m)	0.1752	1.0000

the domain. The length of upstream is represented by L_{up}, L_{down} is the length of downstream, T_{rp} denotes the thickness of the rotating part, and D_{sp} and D_{rp} are the diameters of the static and the rotating parts, respectively. To simulate the rotating part, the multiple reference frame (MRF) technique was employed. In terms of boundary conditions, velocity boundary conditions were imposed on the inlet while the pressure boundary conditions were specified at the outlet. The far field was defined as a slip wall, and a no-slip wall condition was imposed on the surfaces of the propeller and other solid bodies in the domain.

6.2 Leading-Edge Manufacturing Defects

In this chapter, all the LE defects considered for full-scale propellers are also within Class S. Details on the definition of the LE defect can be found in the previous Chapter. It should also be noted that LE defects cannot be modeled in simulations of the model-scale propeller since they are very small.

Figure 6.3 shows the full-scale propellers with no and 0.50 mm defects, respectively.

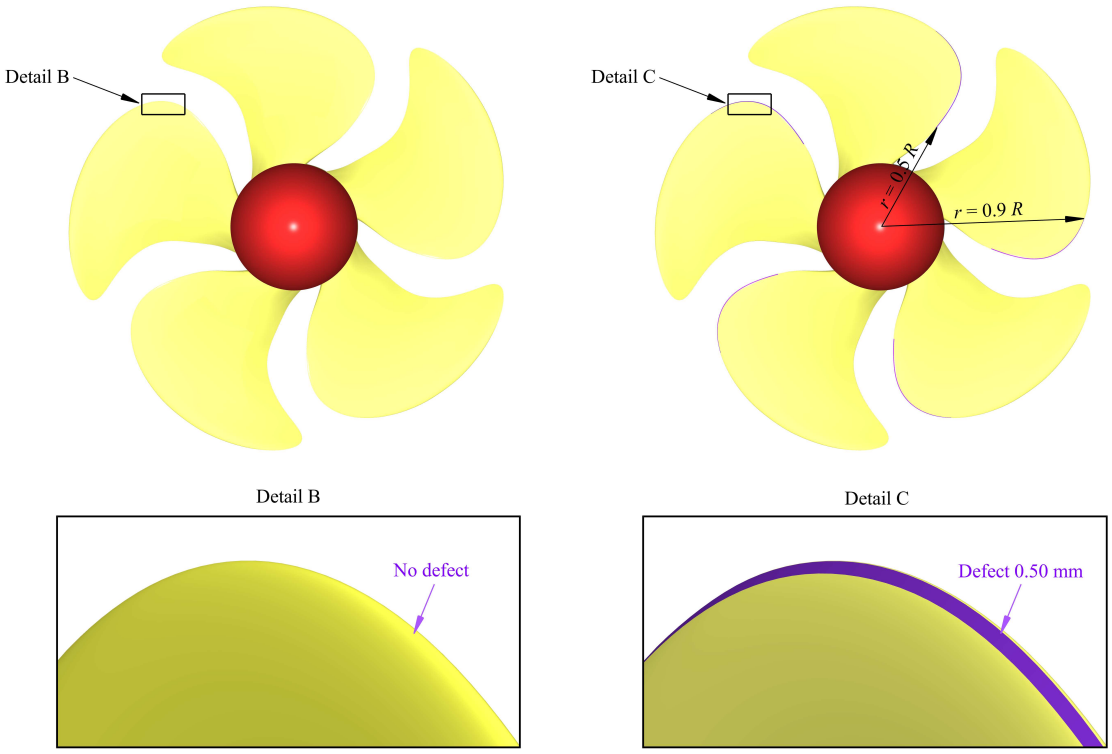

(a) No defect

(b) 0.50 mm defect

Figure 6.3: Full-scale propeller with no defect

In present study, the defects (purple parts) were distributed along the leading-edge between the blade sections of $r/R = 0.5$ and $r/R = 0.9$. As an example, details of the LE geometry for the full-scale propellers with and without defects on the blade section of $r/R = 0.7$ are shown in Fig. 6.4. Note that the 3-D blade sections have been expanded into a local 2-D coordinate system, oxy, in which the origin is located at the leading edge. Dimensions of the LE defects are given in Table 6.2.

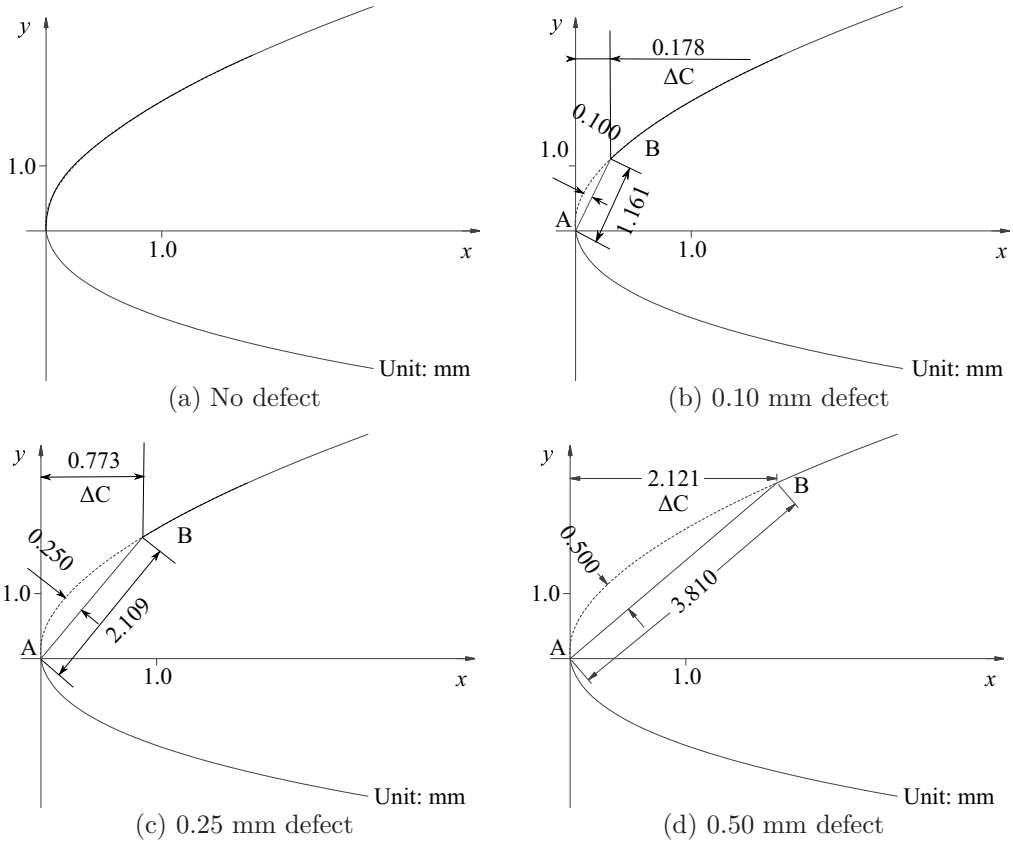

(a) No defect (b) 0.10 mm defect

(c) 0.25 mm defect (d) 0.50 mm defect

Figure 6.4: LE geometries for the full-scale propellers with and without LE defects on the blade section of $r/R = 0.7$

Table 6.2: Dimensions of LE defects on the blade section of $r/R = 0.7$ (unit: mm)

Defect	Length	ΔC	Point A		Point B	
			x	y	x	y
0.100	1.161	0.178	0.000	0.000	0.178	1.147
0.250	2.109	0.773	0.000	0.000	0.773	1.962
0.500	3.810	2.121	0.000	0.000	2.121	3.164

6.3 Grid Generation

Structured grid was distributed on the blade surface, and the same number of grids was applied on both the pressure and suction sides. The hexahedron grids in the prism layer were then generated by extruding the surface meshes along the wall's normal direction.

The first-grid spacing in terms of y^+ is estimated by

$$\Delta S = \frac{2y^+ c_{0.7}}{Re\sqrt{0.5C_f}} \tag{6.2}$$

in which, the Reynolds number, Re, is determined by

$$Re = \frac{c_{0.7}U_{0.7}}{\nu} = \frac{c_{0.7}\sqrt{{U_\infty}^2 + (0.7n\pi D)^2}}{\nu} \tag{6.3}$$

where $c_{0.7}$ and $U_{0.7}$ represent the chord length and the combined velocity of the blade section at 0.7 R, respectively, U_∞ is the incoming flow velocity in the open-water simulation, ν is the kinematic viscosity of water, n is the revolution speed, and D is diameter of the propeller.

The friction coefficient, C_f, is estimated using the ITTC 1957 formula (ITTC, 2021):

$$C_f = \frac{0.075}{(\log Re - 2)^2} \tag{6.4}$$

The thickness of boundary layer, δ, is estimated by

$$\delta = 0.37\frac{c_{0.7}}{Re^{1/5}} \tag{6.5}$$

As an example, the grids of full-scale propeller with 0.5 mm defect at the advance ratio of $J = 1.102$ are shown in Figs. 6.5, 6.6 and 6.7. In this case, the target value of y^+ was 1.0 and 39 grids were applied on the LE defect. Figure 6.5 presents

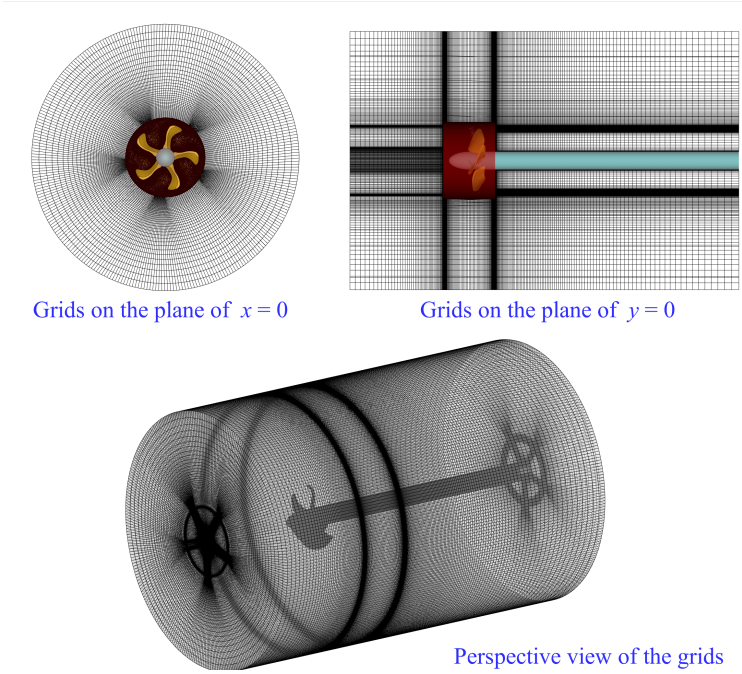

Figure 6.5: The grids on the planes of $X = 0$ and $Y = 0$ as well as whole domain for the full-scale propeller with 0.5 mm defect at $J = 1.102$

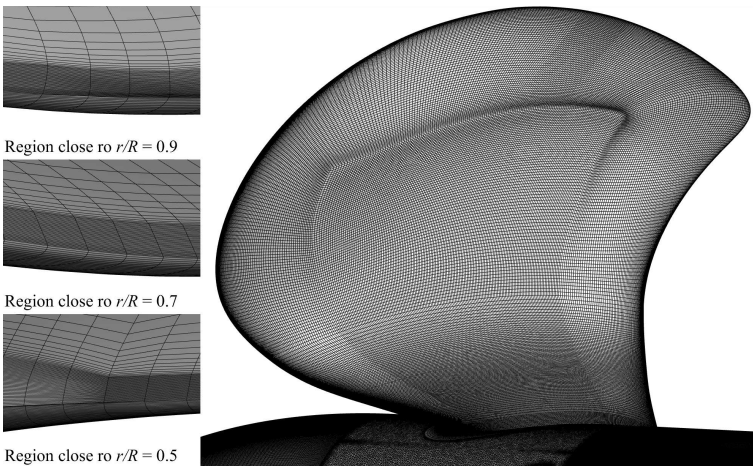

Figure 6.6: The blade surface mesh for the full-scale propeller with 0.5 mm defect at $J = 1.102$

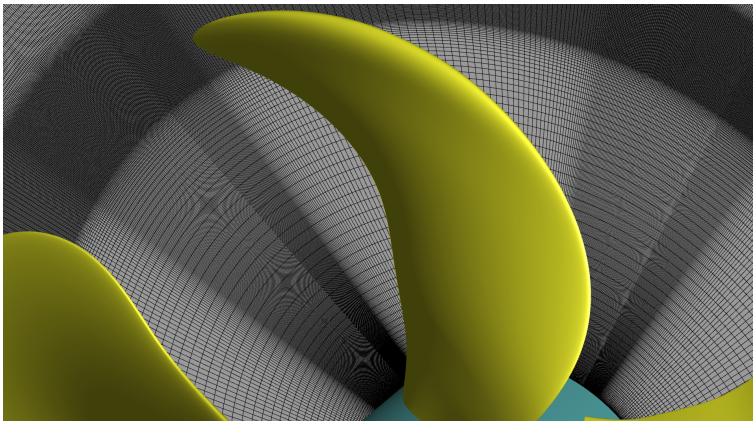

Figure 6.7: The grids on the downstream section of $X/R = 0.2386$ for the full-scale propeller with 0.5 mm defect at $J = 1.102$

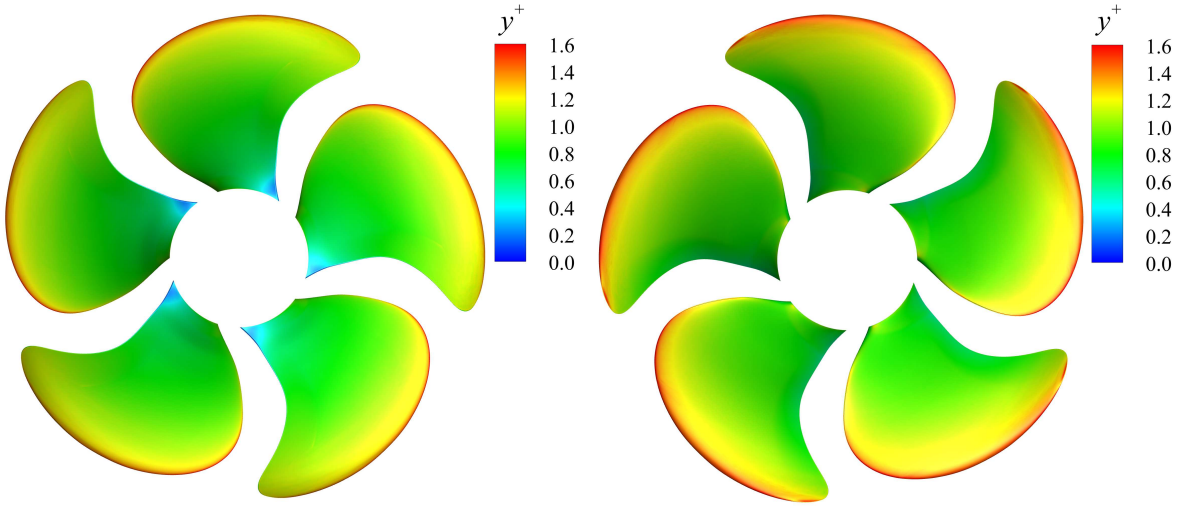

(a) Pressure side

(b) Suction side

Figure 6.8: The distribution of y^+ on the pressure and suction sides of the propeller with 0.5 mm defect at $J = 1.102$

the grids on the planes of $X = 0$ and $Y = 0$, along with an overview of the entire computational domain. The static domain was discretized with structured grids. To capture the downstream wake, a refinement of the grids in the region between 0.8 R and 1.1 R was implemented. Furthermore, the surface mesh of one blade of the full-scale propeller with 0.5 mm defect is shown in Fig. 6.6. Due to the complex flow-structure interactions near the leading and trailing edges as well as the tip region, grids were therefore refined in these regions. Following the previous study of Jin et al. (2021), the aspect ratio at the trailing edges was set as 32. The domain between blades is filled with unstructured cells. The blade surface grids in the regions close to the blade sections ($r/R = 0.5$, 0.7 and 0.9) are also shown in Fig. 6.6. Since the large gradients of the velocity field within the tip vortices, a high grid resolution is required to accurately capture these tip vortices over a distance. Figure 6.7 shows the grids on the downstream section of $X/R = 0.2386$. The grids were refined between the 0.9 R and 1.1 R in order to capture the tip vortices downstream. The mean cell size in the vortex refinement zone in terms of $\Delta x/D$ is 8.787E-4 in this figure.

In addition, Fig. 6.8 presents the distribution of y^+ on the suction and pressure sides of the full-scale propeller with 0.5 mm defect at $J = 1.102$. It is evident that the achieved y^+ values vary from the root to the tip. For example, the targeted y^+ was 1.0 at the blade section of 0.7 R, and the average y^+ values achieved on the suction and pressure sides are 0.94 and 1.01, respectively.

The number of grids for convergence studies ranges from 12,160,613 to 190,248,803 in this study. As an example, the typical number of grids for the propellers without and with 0.10 mm, 0.25 mm, 0.50 mm defects at the advance ratio of $J = 1.102$ are summarized in Table 6.3. In these cases, the targeted value of y^+ is 1.0.

Table 6.3: Typical number of grids for the full-scale propellers with no, 0.10 mm, 0.25 mm and 0.50 mm defects at the advance ratio of $J = 1.102$

Defect	Number of grids on defect	Total number of grids
No defect	-	135,861,672
0.10 mm defect	16	138,889,872
0.25 mm defect	25	144,303,623
0.50 mm defect	39	146,230,155

To assess the grid quality, the volume ratio, $\eta_{\Delta \mathrm{V}}$, the equiangle skewness, Q_{EAS}, and the mesh non-orthogonality were calculated. Figure 6.9 shows the grid quality for typical grids of the propellers without and with 0.10 mm, 0.25 mm, 0.50 mm defects at the advance ratio of $J = 1.102$. Note that the y-axis is on a logarithmic scale.

The volume ratio of the i-th grid is computed by

$$\eta_{\Delta \mathrm{V}i} = \max \left[\frac{\Delta V_i}{\min(\Delta V_j)}, \frac{\max(\Delta V_j)}{\Delta V_i} \right] \tag{6.6}$$

where ΔV_i and ΔV_j are the volumes of the cell i and its corresponding adjacent cell j, respectively. As illustrated in Fig. 6.9a, it can be observed that the volume ratios for the majority of grids are less than 5.0.

The equiangle skewness, Q_{EAS}, is expressed as the maximum ratio of the cell's included angle to the angle of an equilateral element and can be computed by

$$Q_{\mathrm{EAS}} = \max \left[\frac{\theta_{\max} - \theta_e}{180 - \theta_e}, \frac{\theta_e - \theta_{\min}}{\theta_e} \right] \tag{6.7}$$

where θ_e represents the angle for an equilateral element (i.e., 60° for a triangle, 90° for a quad), and $\theta_{\max}$ and $\theta_{\min}$ are the largest and smallest angles in cell, respectively.

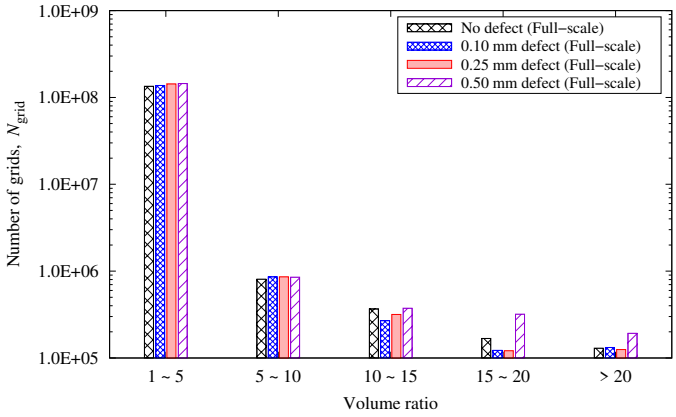

(a) Volume ratio, $\eta_{\Delta V}$

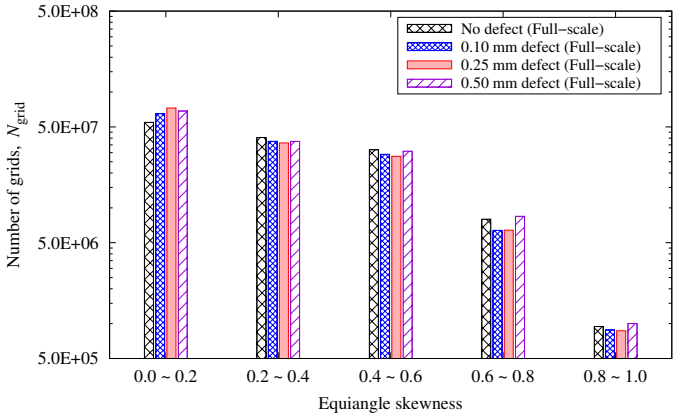

(b) Equiangle skewness, Q_{EAS}

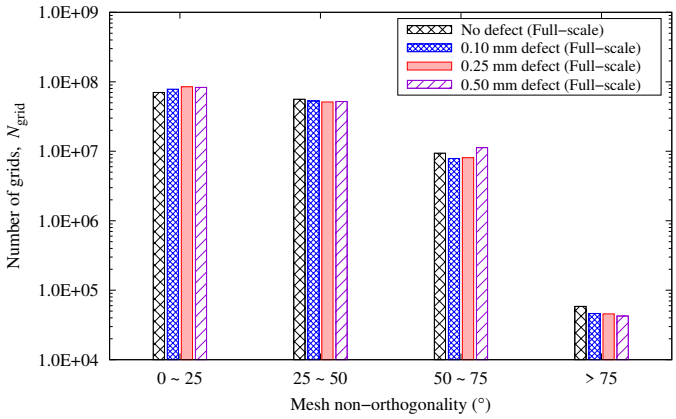

(c) Mesh non-orthogonality, θ_{NOR}

Figure 6.9: The grid quality of typical meshes for the full-scale propellers with no, 0.10 mm, 0.25 mm and 0.50 mm defects at the advance ratio of $J = 1.102$

The angle skewness varies between 0 and 1. It is recommended to keep this skewness measure below 0.8 for a good grid, and values below 0.9 are generally acceptable, depending on the solver. In Fig. 6.9b, it is evident for each case that only small portions of the grid, about 900,000 cells, exhibit skewness values greater than 0.8.

The non-orthogonality of a mesh is defined as the angle formed by the vector connecting two neighboring cell centers across their shared face and the face normal. For each cell, the maximum value of this measure is reported, considering all faces of that grid. Figure 6.9c shows the mesh non-orthogonality of these typical grids of full-scale propellers with and without LE defects. The number of cells with non-orthogonality greater than 75° for the full-scale propellers with no, 0.1 mm, 0.25 mm and 0.5 mm defects are 58,606, 46,040, 45,642 and 42,398, respectively. In summary, all the grids were generated with good quality.

6.4 Convergence Criteria

The maximum number of iterations was set as 40,000 for all simulations. The parameters including the residuals, pressure, thrust and torque coefficient were checked for the simulations of propeller. Three orders of magnitude reduction in residuals are considered as an acceptable level. Note that residuals are not the only measure for convergence. For the convergence of pressure, thrust, torque coefficients, the changes between their values at the present and previous iterations are used as indicators. The acceptable value is in the order of 10^{-4}.

6.5 Non-dimensionalization and Definition of Variables

The relationships between the axial, tangential, and radial velocities (U_x, U_t and U_r) in the stationary frame and those in the rotating frame are given by:

$$\begin{aligned} V_x &= U_x \\ V_t &= U_t - 2\pi n r \\ V_r &= U_r \end{aligned} \tag{6.8}$$

where n is the propeller revolution speed, V_x, V_t and V_r are the axial, tangential, and radial velocities in the rotating frame, respectively. These velocities are all normalized by the incoming flow velocity, U_∞.

In order to provide a more detailed description of the tip vortex structure, a primary/secondary coordinate system, as illustrated in Fig. 6.10, is introduced. In this coordinate system, the primary velocity, V_s, is defined in the axial-tangential ($x - t$) plane at the propeller pitch angle, φ. The tangential velocity, V_c, and the radial velocity, V_r, are then defined on the secondary-flow plane ($r - c$ plane), which is perpendicular to the primary velocity. Note that the pitch angle varies with the radius of a section, and the coordinate systems are different at different radii. The relations for velocity components are given below:

$$\begin{aligned} V_s &= V_x \sin(\varphi) + V_t \cos(\varphi) \\ V_c &= V_t \sin(\varphi) - V_x \cos(\varphi) \\ V_r &= V_r \end{aligned} \tag{6.9}$$

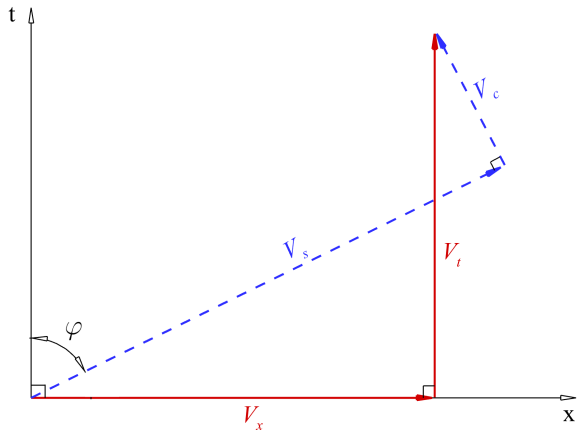

Figure 6.10: Primary and secondary coordinate system

The propeller thrust coefficient, K_{T}, and the torque coefficient, K_{Q}, are defined as follows,

$$K_{\mathrm{T}} = \frac{T}{\rho n^2 D^4} \quad \text{and} \quad K_{\mathrm{Q}} = \frac{Q}{\rho n^2 D^5} \tag{6.10}$$

where T and Q are the thrust and torque, respectively.

The propeller open-water efficiency, η_0, is given by

$$\eta_0 = \frac{J}{2\pi} \cdot \frac{K_{\mathrm{T}}}{K_{\mathrm{Q}}} \tag{6.11}$$

where $J = U_a/(nD)$ is the advance coefficient, and the advance speed, U_a, is equal to the incoming flow velocity, U_∞, in the open-water tests and simulations.

6.6 Simulation Parameters

Convergence studies on the domain size, grid size, grid stretching ratio, first-grid spacing, y^+, and turbulence model were first carried out for the model-scale propeller and then for the full-scale propellers with no and 0.5 mm defects at $J = 1.102$. A summary of simulation parameters in convergence studies is provided below:

- Length of upstream, L_{up}/D: 2.0, 3.0 and 4.0.
- Length of downstream, L_{down}/D: 4.0, 6.0, 8.0 and 10.0.
- Diameter of static domain, D_{sp}/D: 4.0, 6.0, 8.0 and 10.0.
- Radius of rotating domain, R_{rp}/R: 1.2, 1.3 and 1.4.
- Thickness of rotating domain, T_{rp}/D: 0.8, 1.0 and 1.2.
- Gird size in terms of the cell size in the vortex refinement zone, $\Delta x/D$: 1.757E-3, 1.242E-3, 8.787E-4, 6.212E-4 and 4.393E-4.
- Grid stretch ratio, SR: 1.1, 1.2, 1.3 and 1.4.
- First-grid spacing, y^+: 0.5, 0.707, 1.0, 1.414, 2.0, 2.828 and 4.0.
- Turbulence models: $k-\varepsilon$, $k-\omega$, SST $k-\omega$, Spalart-Allmaras and elliptic blending Reynolds stress models

The best-practice settings were proposed for model-scale simulations by comparing the solutions with the model test results. The best-practice non-dimensional settings for full-scale simulations were also proposed, which are very similar to those for the model-scale simulations.

Using the model-scale best practices, validation studies were first carried out for the propeller model by following the test matrices in the work of Chesnakas and Jessup (1998).

Simulations were then performed for the full-scale propellers with no, 0.10 mm, 0.25 mm and 0.50 mm defects. In the full-scale cases, simulations were carried out

Table 6.4: The simulation matrix for suction-side tip vortex with $p_0 = 22.0$ psi

J	U_∞	n (rps)		Experimental (model scale)			
	(m/s)	Model-scale	Full-scale	K_T	$10K_\mathrm{Q}$	η_0	σ
0.921	6.557	17.680	3.097	0.392	0.926	0.620	6.940
0.983	7.850	19.830	3.474	0.364	0.876	0.651	4.800
0.992	8.461	21.180	3.710	0.364	0.871	0.660	4.140
1.034	9.244	22.200	3.889	0.344	0.845	0.671	3.510
1.055	9.865	23.220	4.068	0.332	0.818	0.682	3.070
1.062	9.977	23.330	4.087	0.327	0.805	0.685	3.010
1.066	10.882	25.350	4.441	0.329	0.813	0.686	2.530
1.082	11.185	25.670	4.497	0.315	0.787	0.690	2.390
1.102	12.128	27.330	4.788	0.305	0.770	0.695	2.020
1.103	11.482	25.850	4.528	0.302	0.765	0.693	2.270
1.116	12.058	26.830	4.700	0.300	0.754	0.707	2.060
1.117	13.135	29.200	5.115	0.304	0.757	0.714	1.720
1.130	12.969	28.500	4.992	0.296	0.747	0.712	1.780
1.134	13.554	29.680	5.199	0.291	0.737	0.713	1.610
1.155	15.368	33.040	5.788	0.280	0.716	0.719	1.250
1.191	15.861	33.070	5.793	0.259	0.675	0.728	1.170

Table 6.5: The simulation matrix for suction-side tip vortex with $p_0 = 16.5$ psi

J	U_∞	n (rps)		Experimental (model scale)			
	(m/s)	Model-scale	Full-scale	K_T	$10K_\mathrm{Q}$	η_0	σ
1.004	7.621	18.850	3.302	0.349	0.852	0.654	3.860
1.059	9.608	22.530	3.947	0.322	0.806	0.674	2.430
1.115	10.709	23.850	4.178	0.299	0.755	0.703	1.950
1.136	11.816	25.830	4.525	0.290	0.736	0.714	1.600
1.159	13.166	28.210	4.942	0.278	0.710	0.722	1.290
1.205	15.480	31.900	5.588	0.241	0.653	0.707	0.930

with the same advance ratios and cavitation numbers as those in the experimental cases. The detailed simulation parameters, such as the advance ratio, J, the propeller revolution speed, n, the incoming flow velocity, U_∞, and the static pressure, p_0, were summarized in Tables 6.4 and 6.5. Two static pressure conditions ($p_0 = 16.5$ psi and 22.0 psi) were simulated. Note that the static pressure, p_0, was measured at the same level of the centre of propeller shaft on the outlet. The model test results of K_T, $10K_\mathrm{Q}$, η_0 and σ by Chesnakas and Jessup (1998) are also included in the tables.

Other default settings used in the simulations with the steady RANS solver can be found in Table 3.6.

6.7 Numerical Results

The convergence studies were conducted for both the model-scale propeller and the full-scale propellers with no and 0.50 mm defects at the advance ratio of $J = 1.102$. Based on the results of the convergence studies, the best-practice settings were summarized. With the recommended best practices, validation studies were first carried out the model-scale propeller at various advance ratios ranging from 0.921 to 1.205. Numerical simulations were then performed for the full-scale propellers using the geometry of DTMB 5168 propeller without and with LE defects. Note that the LE defects were only applied to the full-scale propellers, while the propeller model does not have any LE defects since they are too small in model scale. In this section, results of velocity field, cavitation buckets, pressure distribution, and residuals are presented for model- and full-scale propellers. The effect of LE defects on cavitation inception speed are also discussed for the full-scale propeller.

The model experimental results of Chesnakas and Jessup (1998) were used to validate the numerical solutions of the model-scale propeller. The experimental setup involved a hybrid LDV system, which combined lens-optic and fiber-optic assemblies. The lens-optic system measured two components of velocity, while the fiber-optic assembly measured a single component of velocity. Each system was traversed independently, leading to challenges in maintaining precise coincidence of all three measurements. Due to the uncertainties in probe positions and the coincident mode of the hybrid LDV system, along with the inherent precision errors of measurement instruments, experimental uncertainties should be considered in the comparison between numerical and experimental data. For cavitation inception, it was noted when three

of the five blades exhibited intermittent tip vortices. Another source of uncertainty in the cavitation number resulted from precision errors. The calculated uncertainties for the quantities measured in the test are summarized in Table 6.6, where the velocities were obtained in the tip vortex region. Significant uncertainties can be observed in the axial and radial velocities, reaching up to 19% of the incoming flow velocity (U_∞). The uncertainty in σ was estimated to be 0.4.

Table 6.6: The calculated uncertainties of experimental data from Chesnakas and Jessup (1998)

Item	Reference	Uncertainty
Advance coefficient, J	-	0.006
Cavitation number, σ	-	0.400
Axial velocity in stationary frame, U_x	U_∞	0.190
Tangential velocity in stationary frame, U_t	U_∞	0.075
Radial velocity in stationary frame, U_r	U_∞	0.190
Axial velocity in rotating frame, V_x	U_∞	0.190
Tangential velocity in rotating frame, V_t	U_∞	0.075
Radial velocity in rotating frame, V_r	U_∞	0.190
Primary velocity in rotating frame, V_s	U_∞	0.110

As the Reynolds numbers of the model- and full-scale propeller are not identical, it is not feasible to use the model experimental data to directly assess the accuracy of the numerical results for the full-scale propellers. However, since the unavailability of

sea-trial data of the full-scale propeller, the numerical and experimental data for the propeller model were included in the analysis of the full-scale predictions to provide the readers with some references.

6.7.1 Simulations for the Model-Scale Propeller

6.7.1.1 Convergence Studies

The five-bladed DTMB 5168 propeller model generates five tip vortices on a downstream section. As an example, the non-dimensional primary velocity contour at $X/R = 0.2386$ and $J = 1.102$ for the propeller model is shown in Fig. 6.11, where the primary velocity is normalized with inflow velocity in the rotating frame ($V_\infty = \sqrt{U_\infty^2 + 2\pi rn}$). In this case, $y^+ = 1$, the SST $k - \omega$ model and SR = 1.2 were used. Note that the vortex was numbered according to Chesnakas and Jessup (1998).

Figure 6.12 presents the non-dimensional axial, tangential and radial velocities, V_x/U_∞, V_t/U_∞ and V_r/U_∞, across these five vortex cores of the model-scale propeller at $X/R = 0.1756$ and 0.2386. Note that the axial location X is measured from the propeller mid-span section and R is the propeller radius. In this work, the position of the vortex center is specified at $\theta = 0$, where the minimum pressure occurs within the tip vortex. To provide a comprehensive comparison, the experimental data from Chesnakas and Jessup (1998), as well as the numerical results obtained using the $k-\omega$ model in the study of Peng et al. (2013), are also included. In these figures, the first valley, starting from the left, corresponds to the wake, and the second valley is associated with the tip vortex.

To quantify the differences between present predictions and the experimental data

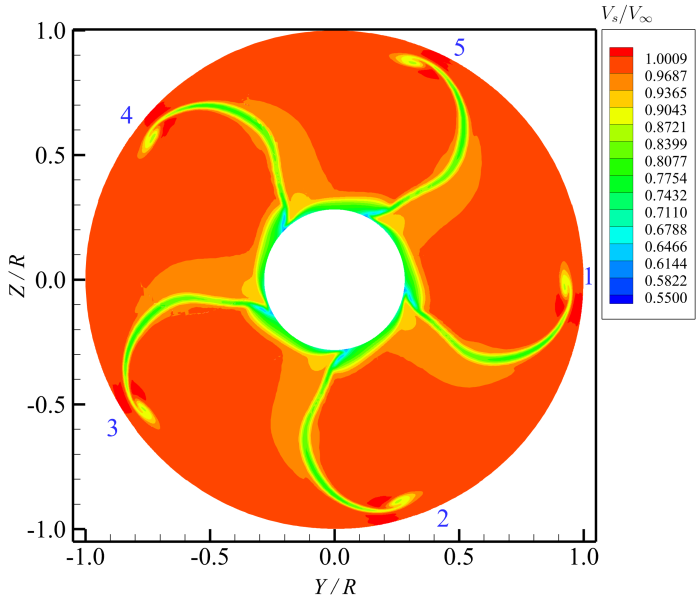

Figure 6.11: The contour of non-dimensional primary velocity, V_s/V_∞, at $X/R = 0.2386$ and $J = 1.102$ for the propeller model

by Chesnakas and Jessup (1998), the root mean square (RMS) errors as follows were calculated for V_x/U_∞, V_t/U_∞ and V_r/U_∞ across the vortex core:

$$\text{RMS} = \sqrt{\frac{\int_{\theta_1}^{\theta_2} (\text{Numerical} - \text{Experimental})^2 \ \mathrm{d}\theta}{\theta_2 - \theta_1}} \tag{6.12}$$

where θ_1 and θ_2 are -0.50 and 0.50 radians, respectively. Table 6.7 provides the RMS errors for the non-dimensional axial, tangential, and radial velocities across different vortex cores. It can be found that the RMS errors for the predicted radial velocity at both $X/R = 0.1756$ and 0.2386 are lower than those reported by Peng et al. (2013). In addition, the predicted axial velocity at $X/R = 0.1756$ shows slight improvement compared to the numerical result in Peng et al. (2013), while the axial velocity at $X/R = 0.2386$ is less accurate. On the other hand, the overall differences between the vortices are relatively small. Therefore, the averaged velocities across the five

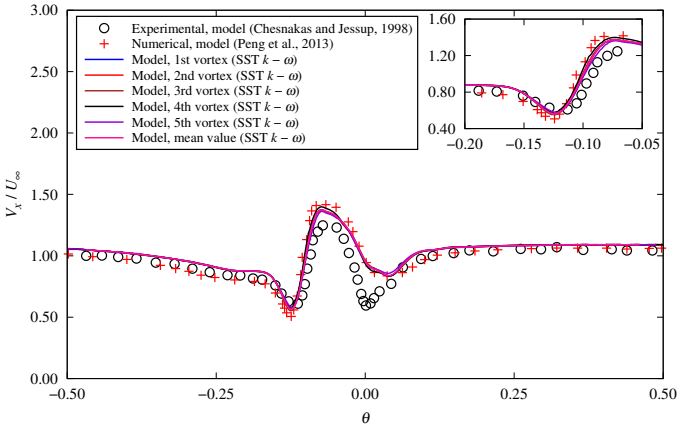

(a) V_x/U_∞ $(X/R = 0.1756)$

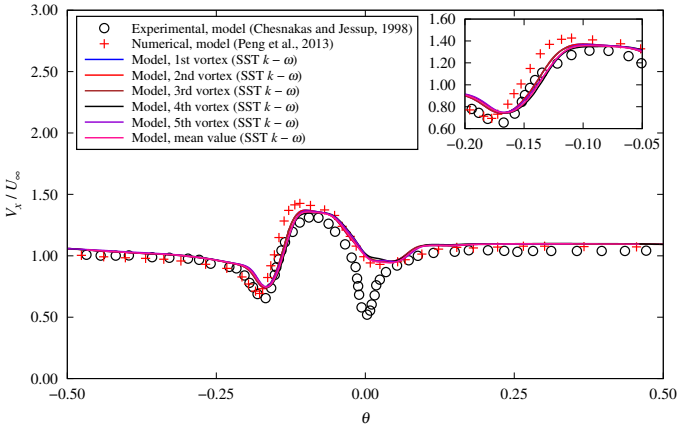

(b) V_x/U_∞ $(X/R = 0.2386)$

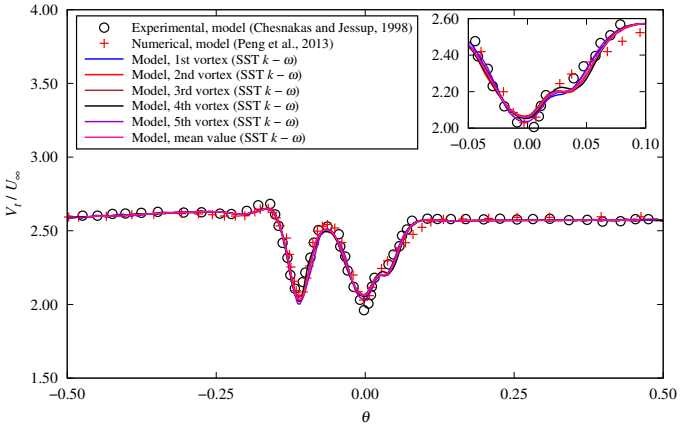

(c) V_t/U_∞ $(X/R = 0.1756)$

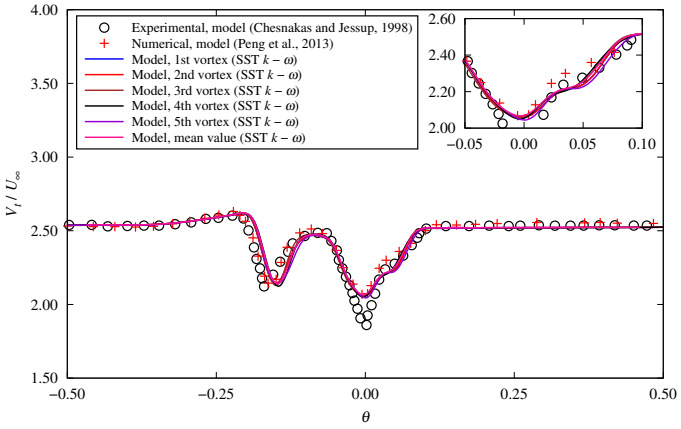

(d) V_t/U_∞ $(X/R = 0.2386)$

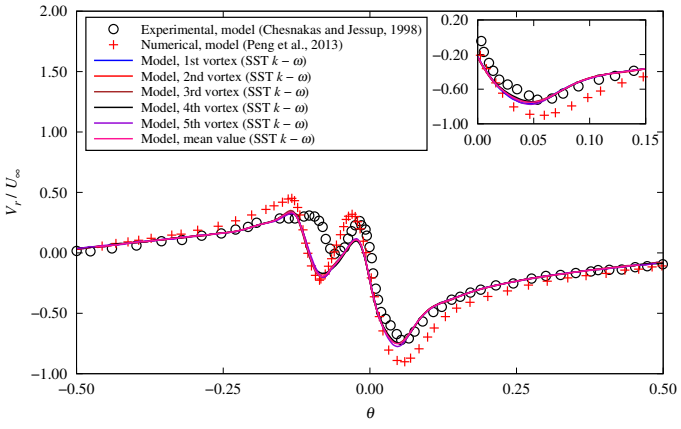

(e) V_r/U_∞ $(X/R = 0.1756)$

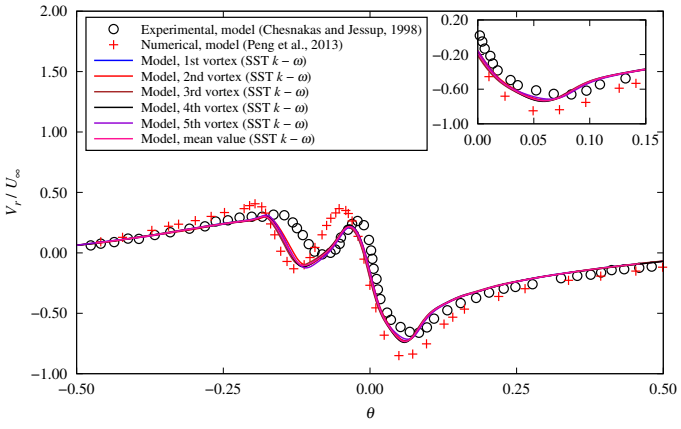

(f) V_r/U_∞ $(X/R = 0.2386)$

Figure 6.12: Non-dimensional velocities across different vortex cores at $X/R = 0.1756$ and $X/R = 0.2386$ for the propeller model with $J = 1.102$

Table 6.7: The RMS errors of the non-dimensional axial, tangential and radial velocities across different vortex cores for the propeller model at $J = 1.102$

Section	Item	V_x/U_∞ (10^{-2})	V_t/U_∞ (10^{-2})	V_r/U_∞ (10^{-2})
$X/R = 0.1756$	1st vortex	8.710	3.143	9.354
	2nd vortex	8.638	2.975	9.135
	3rd vortex	8.606	3.043	9.402
	4th vortex	8.762	2.826	9.073
	5th vortex	8.405	3.093	9.039
	Mean value	8.624	3.016	9.200
	Peng et al. (2013)	9.618	3.439	12.105
$X/R = 0.2386$	1st vortex	9.599	4.785	8.582
	2nd vortex	9.816	4.554	8.307
	3rd vortex	9.849	4.924	8.878
	4th vortex	10.242	5.479	8.175
	5th vortex	10.516	5.622	8.175
	Mean value	10.005	5.073	8.423
	Peng et al. (2013)	9.851	3.965	13.149

vortex cores were used in the following comparisons.

Cavitation occurs when the negative minimum pressure coefficient, $-C_{p_{\min}}$, on the five blades is equal to the cavitation number, σ. For instance, cavitation numbers obtained on the suction side in the tip region ($r/R \geq 0.95$) of blades for the model-scale

Table 6.8: The comparison of cavitation number on the suction side in the tip region ($r/R \geq 0.95$) for the propeller model at $J = 1.102$

Item	Numerical	Experimental		Relative error (%)	
Advance ratio	1.102	1.102	1.103	1.102	1.103
1st blade	2.522	2.020	2.270	24.84	11.09
2nd blade	2.591	2.020	2.270	28.25	14.13
3rd blade	2.593	2.020	2.270	28.36	14.22
4th blade	2.561	2.020	2.270	26.76	12.80
5th blade	2.523	2.020	2.270	24.90	11.15
Maximum value	2.593	2.020	2.270	28.36	14.22
Minimum value	2.522	2.020	2.270	24.84	11.09
Mean value	2.558	2.020	2.270	26.62	12.68

propeller are shown in Table 6.8. The maximum, minimum and mean results are also included. The minimum relative error is 11.09% for the 1st blade compared to the experimental data obtained at $J = 1.103$. Note that there were some geometrical deviations in the area near the tip, i.e., on the blade section of $r/R = 0.97$, between the design and the tested model in the experiment by Chesnakas and Jessup (1998). This likely contributed to the relative error. Furthermore, the uncertainty in the experimental data is another source of error. For instance, approximately 10% difference was observed between the experimental results at $J = 1.102$ and 1.103, indicating the uncertainty in the measurement. It is worth noting that no significant difference was

found in the predicted cavitation numbers on various blades. Therefore, the mean value will be used in subsequent sections, unless otherwise specified.

In summary, comprehensive convergence studies were conducted for the model-scale propeller, involving a total of 81 simulations. The simulation parameters including the domain size, grid size, grid stretching ratio, y^+ and turbulence model were examined carefully for the base case at the advance ratio of $J = 1.102$.

As examples, Figs. 6.13, 6.14 and 6.15 present the sensitivities of the non-dimensional velocities across the vortex core at $X/R = 0.2386$ to L_{up}, L_{down} and D_{sp}, respectively. These simulations were carried out using $y^+ = 1.0$ and SR $= 1.2$, along with the $k - \omega$ model. The results indicate that the predicted velocity at $X/R = 0.2386$ are generally insensitive to the lengths of upstream and downstream as well as the diameter of the static domain; $L_{\text{up}} = 2.0\ D$, $L_{\text{down}} = 4.0\ D$ and $D_{\text{sp}} = 6.0\ D$ were then employed in the following simulations for the propeller model.

The sensitivities of the non-dimensional velocities across the vortex core at $X/R = 0.2386$ to y^+ for the model-scale propeller using the $k - \varepsilon$ and $k - \omega$ models are presented in Fig. 6.16, in which the predicted velocities are showed to be sensitive to y^+ with the $k - \varepsilon$ model, and they do not converge as y^+ decreased. For the $k - \omega$ model, only slight differences were observed in the results obtained with $y^+ = 2.828$ and 4.000. In the region of $\theta \in [-0.15, -0.10]$, the predicted axial velocities using $y^+ = 2.828$ and 4.000 were greater than those obtained with other y^+ values. The recommended value of y^+ should be in the range of $[0.5, 2.0]$.

Twenty five cases were conducted for the model-scale propeller with various grid sizes in terms of $\Delta x/D =$ 1.757E-3, 1.242E-3, 8.787E-4, 6.212E-4 and 4.393E-4. Four turbulence models, including the $k - \varepsilon$, $k - \omega$, SST $k - \omega$, Spalart-Allmaras and

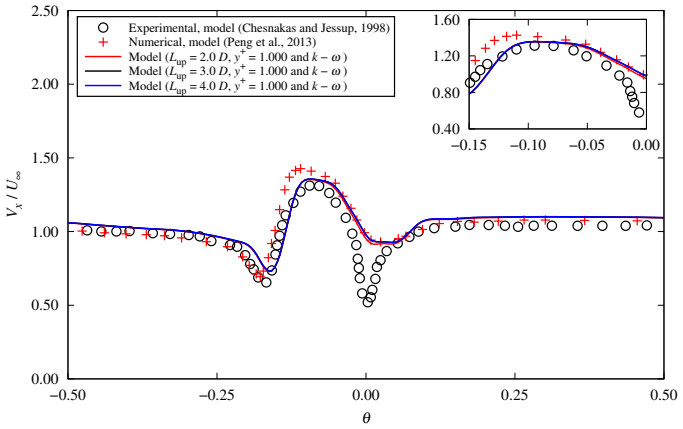

(a) Non-dimensional axial velocity, V_x/U_∞

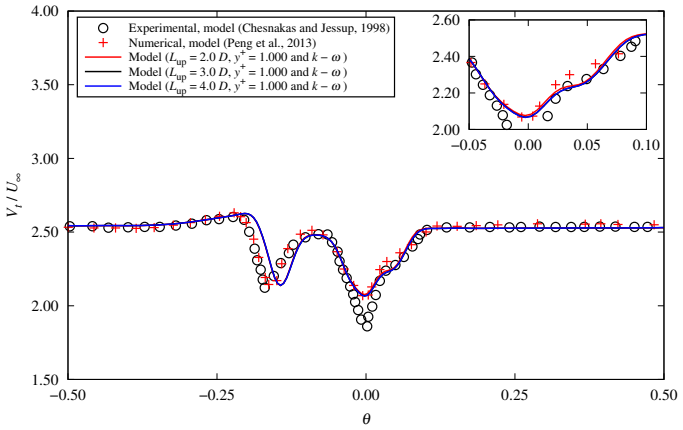

(b) Non-dimensional tangential velocity, V_t/U_∞

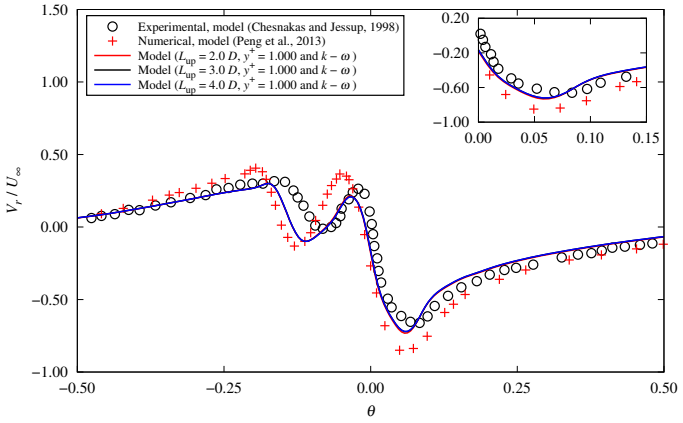

(c) Non-dimensional radial velocity, V_r/U_∞

Figure 6.13: Sensitivity of non-dimensional velocities across the vortex core at $X/R = 0.2386$ to L_{up} for the propeller model

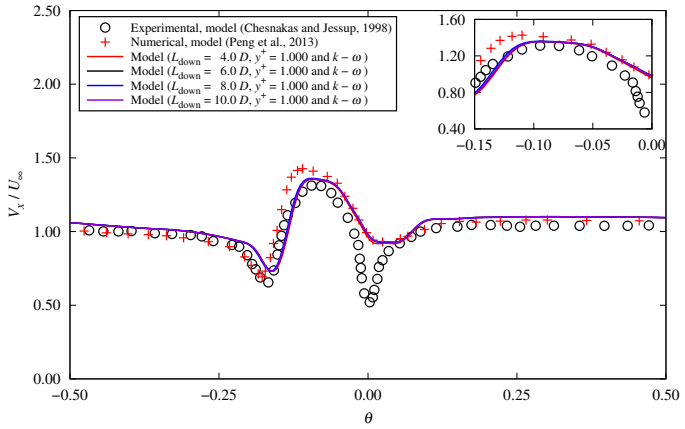

(a) Non-dimensional axial velocity, V_x/U_∞

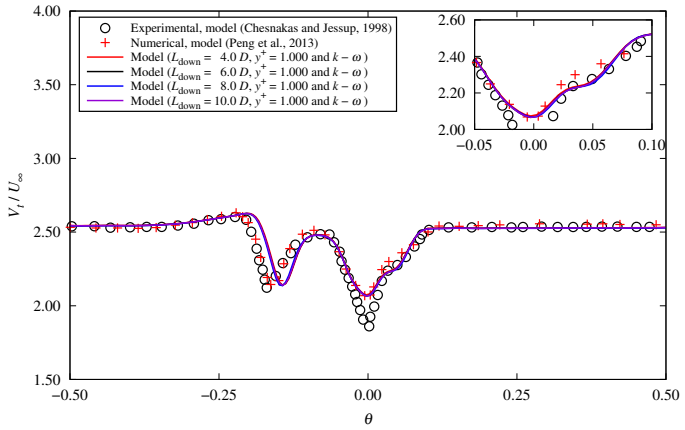

(b) Non-dimensional tangential velocity, V_t/U_∞

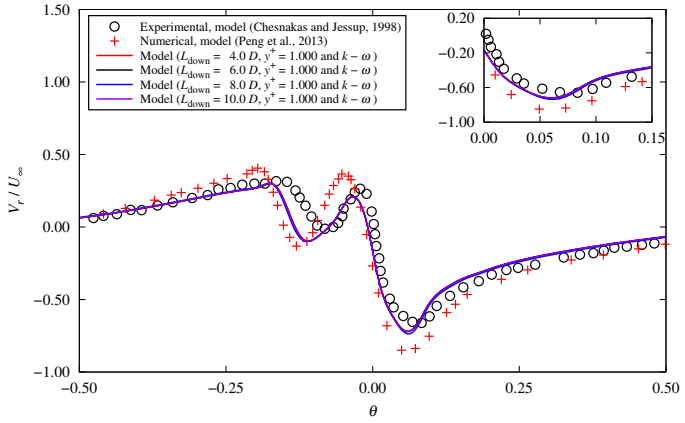

(c) Non-dimensional radial velocity, V_r/U_∞

Figure 6.14: Sensitivity of non-dimensional velocities across the vortex core at $X/R = 0.2386$ to L_{down} for the propeller model

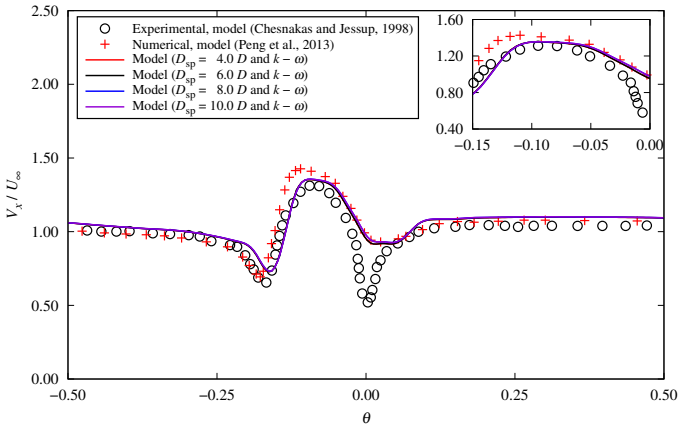

(a) Non-dimensional axial velocity, V_x/U_∞

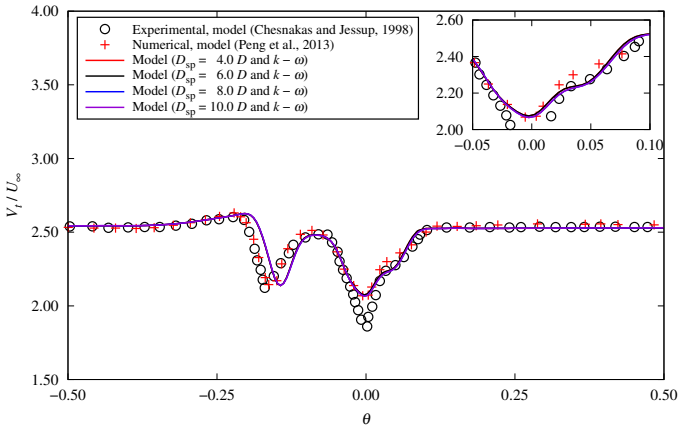

(b) Non-dimensional tangential velocity, V_t/U_∞

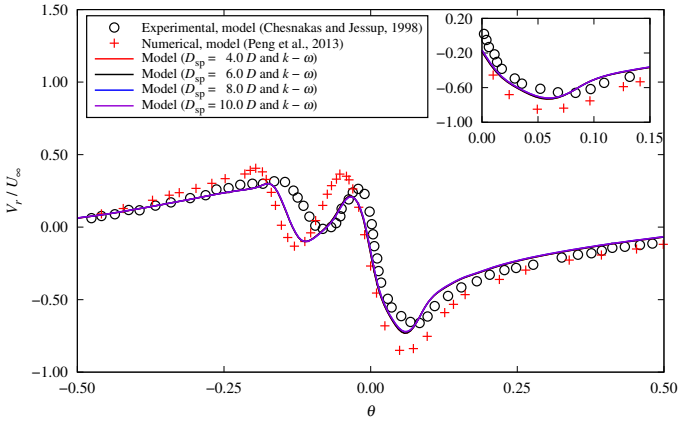

(c) Non-dimensional radial velocity, V_r/U_∞

Figure 6.15: Sensitivity of non-dimensional velocities across the vortex core at $X/R = 0.2386$ to D_{sp} for the propeller model

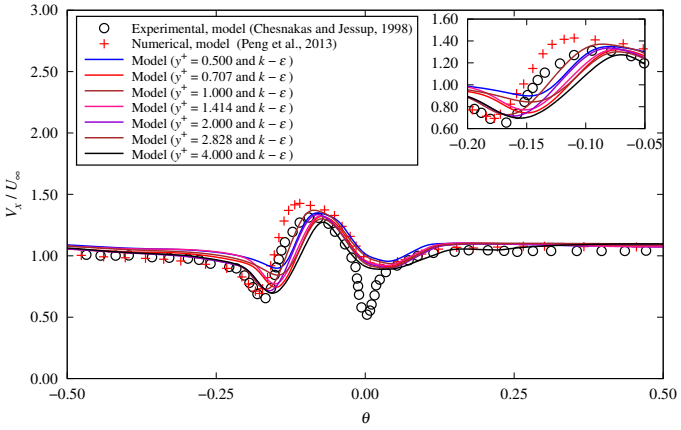

(a) V_x/U_∞ ($k - \varepsilon$ model)

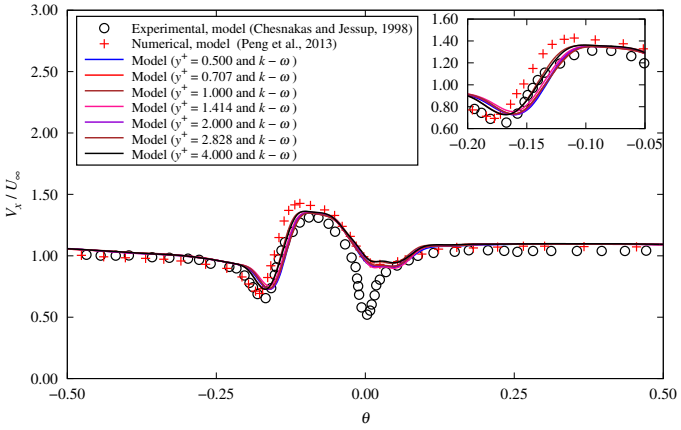

(b) V_x/U_∞ ($k - \omega$ model)

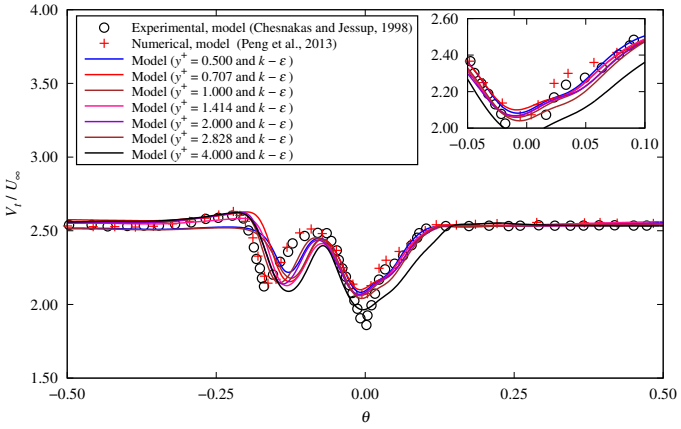

(c) V_t/U_∞ ($k - \varepsilon$ model)

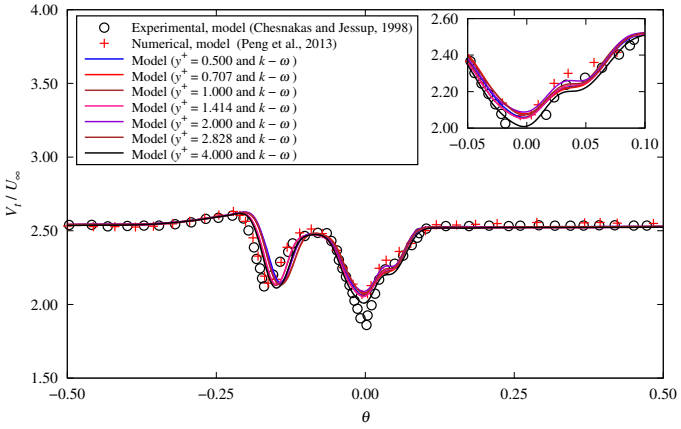

(d) V_t/U_∞ ($k - \omega$ model)

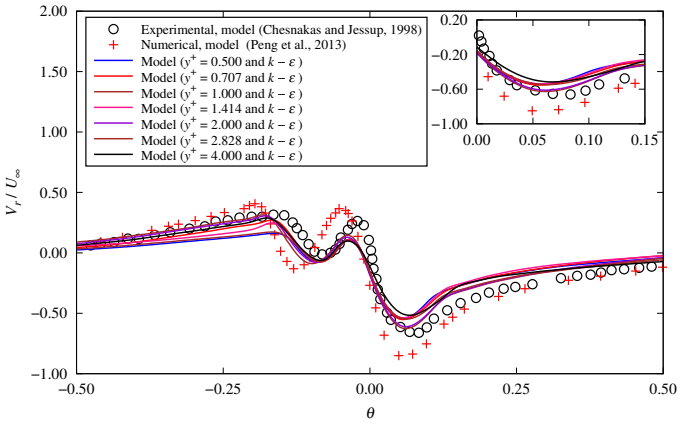

(e) V_r/U_∞ ($k - \varepsilon$ model)

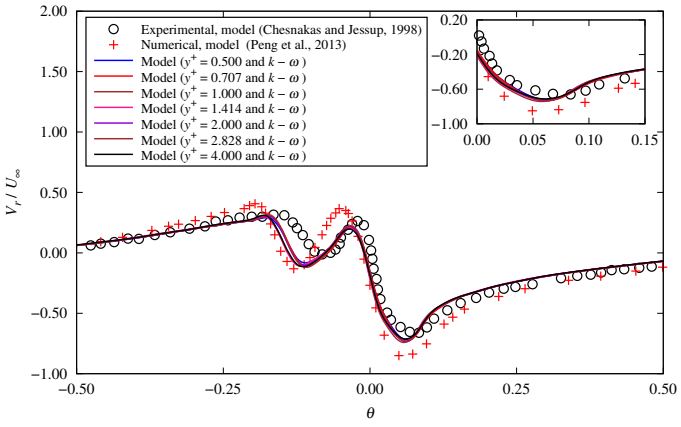

(f) V_r/U_∞ ($k - \omega$ model)

Figure 6.16: Sensitivity of non-dimensional velocities across the vortex core at $X/R = 0.2386$ to y^+ for the model-scale propeller using the $k - \varepsilon$ and $k - \omega$ models

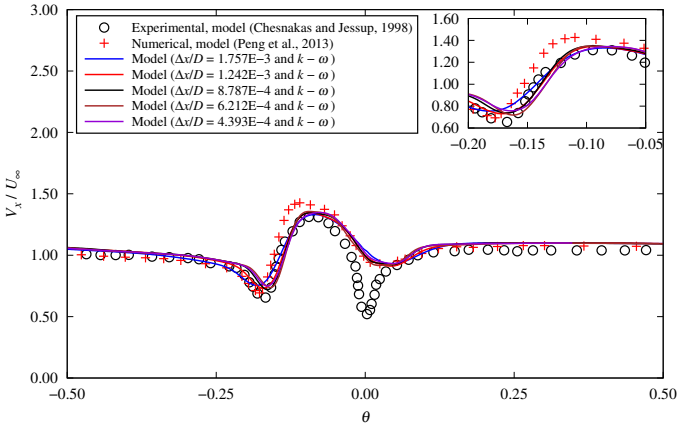

(a) V_x/U_∞ ($k\ -\ \omega$ model)

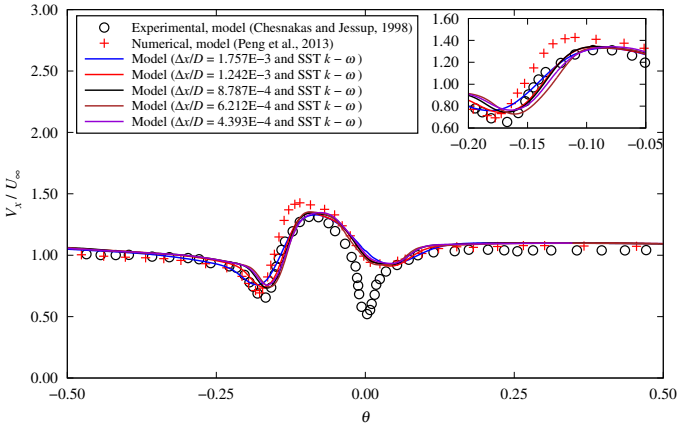

(b) V_x/U_∞ (SST $k\ -\ \omega$ model)

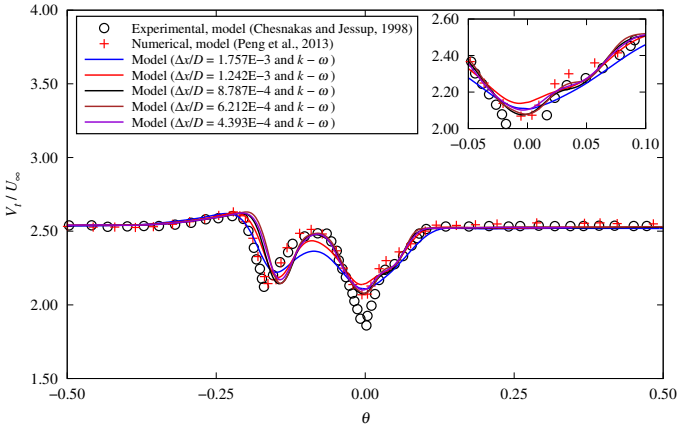

(c) V_t/U_∞ ($k\ -\ \omega$ model)

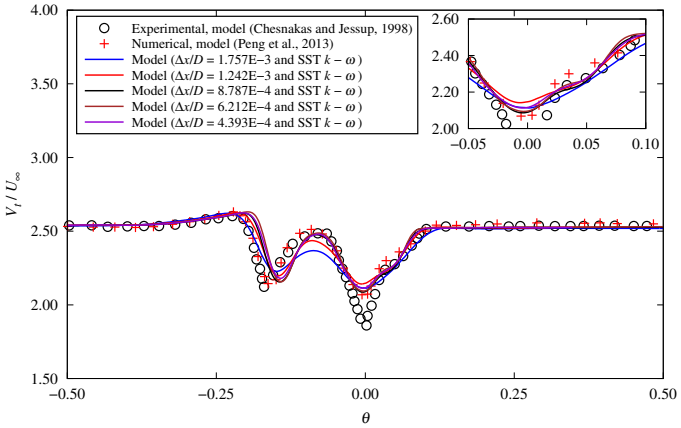

(d) V_t/U_∞ (SST $k\ -\ \omega$ model)

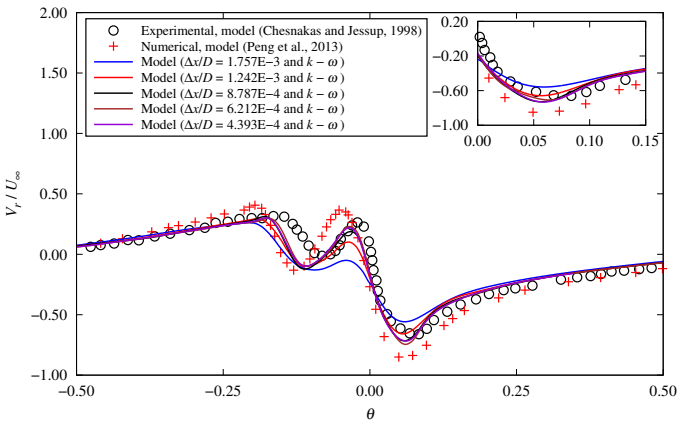

(e) V_r/U_∞ ($k\ -\ \omega$ model)

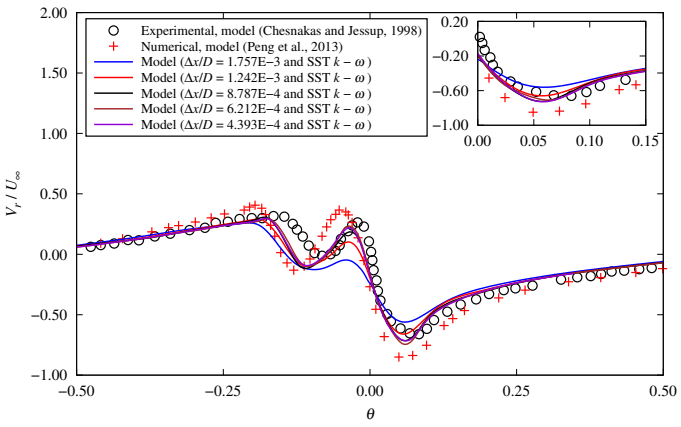

(f) V_r/U_∞ (SST $k\ -\ \omega$ model)

Figure 6.17: Sensitivity of non-dimensional velocities across the vortex core at $X/R = 0.2386$ to the grid resolution (Δx) for the model-scale propeller using the $k\ -\ \omega$ and SST $k\ -\ \omega$ models

elliptic blending Reynolds stress models, were applied. The value of y^+ was set as 1.0, and SR was 1.2 in these cases. As examples, non-dimensional velocities across the vortex core at $X/R = 0.2386$ for the model-scale propeller using the $k - \omega$ and SST $k - \omega$ models are shown in Fig. 6.17. It can be found that the results based on the $k - \omega$ and SST $k - \omega$ models converged with grid refinement. For the propeller model, the tangential and radial velocities are more sensitive to the grid size than the axial velocity. Compared with the model experimental data (Chesnakas and Jessup, 1998), significant difference can be seen in the predicted tangential and radial velocities with the grid sizes of $\Delta x/D = 1.757$E-3 and 1.242E-3.

Table 6.9 and 6.10 provide detailed RMS errors of V_x/U_∞, V_t/U_∞ and V_r/U_∞ with the advance ratio of $J = 1.102$ for the model-scale propeller using various turbulence models and grid sizes at $X/R = 0.1756$ and 0.2386, respectively. It can be observed that the RMS errors of downstream velocity generally decrease as the grid size decreases. The largest RMS error (15.739×10^{-2}) can be seen in the axial velocity at $X/R = 0.1756$ with $\Delta x/D = 1.757$E-3 using the EB-RSM model. And the minimum RMS error (5.397×10^{-2}) was achieved in the tangential velocity at $X/R = 0.1756$ with the medium grid size of $\Delta x/D = 8.787$E-4 using the Spalart-Allmaras model. The RMS errors for V_x/U_∞, V_t/U_∞ and V_r/U_∞ across the tip vortex core predicted by the eddy viscosity models were found to be slightly smaller than those of the Reynolds stress model. This observation is consistent with the findings reported by Peng et al. (2013).

Results of K_T, K_Q and η_0 for the model-scale propeller, obtained using different turbulence models and grid sizes, are shown in Fig. 6.18. The $k - \varepsilon$ model exhibits sensitivity to the grid resolution with $y^+ = 1.0$, resulting in non-convergent

Table 6.9: RMS errors of V_x/U_∞, V_t/U_∞ and V_r/U_∞ across the vortex core at $X/R = 0.1756$ for the model-scale propeller with various turbulence models and grid sizes when $J = 1.102$

Item	Turbulence model	Grid size	$X/R = 0.1756$		
		$\Delta x/D$ (10^{-3})	V_x/U_∞ (10^{-2})	V_t/U_∞ (10^{-2})	V_r/U_∞ (10^{-2})
Model (Present)	$k - \varepsilon$	1.757	14.016	10.692	10.741
		1.242	9.192	5.904	9.413
		0.879	9.066	6.541	7.482
		0.621	8.978	5.579	8.193
		0.439	8.837	6.185	7.876
	$k - \omega$	1.757	10.030	8.724	11.038
		1.242	8.804	6.166	9.099
		0.879	9.440	6.228	7.646
		0.621	8.824	6.891	7.624
		0.439	9.339	6.199	7.408
	SST $k - \omega$	1.757	9.844	8.754	11.007
		1.242	8.781	6.230	8.979
		0.879	9.358	6.307	7.535
		0.621	8.800	7.035	7.604
		0.439	9.259	6.291	7.317
	Spalart-Allmaras	1.757	10.332	8.289	11.170
		1.242	8.849	5.782	9.173
		0.879	9.013	5.397	8.154
		0.621	8.728	6.355	7.443
		0.439	9.055	5.776	7.291
	EB-RSM	1.757	15.739	10.317	12.598
		1.242	9.079	6.943	9.692
		0.879	9.786	7.412	9.826
		0.621	9.801	7.173	9.450
		0.439	9.468	7.517	9.494
Model (Peng et al., 2013)	$k - \omega$	-	9.618	3.439	12.105

Table 6.10: RMS errors of V_x/U_∞, V_t/U_∞ and V_r/U_∞ across the vortex core at $X/R = 0.2386$ for the model-scale propeller with various turbulence models and grid sizes when $J = 1.102$

Item	Turbulence model	Grid size	$X/R = 0.2386$		
		$\Delta x/D$ (10^{-3})	V_x/U_∞ (10^{-2})	V_t/U_∞ (10^{-2})	V_r/U_∞ (10^{-2})
Model (Present)	$k - \varepsilon$	1.757	10.428	10.904	9.470
		1.242	10.567	7.903	11.071
		0.879	10.279	7.394	8.581
		0.621	10.032	7.699	8.506
		0.439	10.264	7.488	7.961
	$k - \omega$	1.757	10.222	9.610	9.979
		1.242	11.323	7.473	11.698
		0.879	9.053	7.634	8.560
		0.621	10.399	7.438	9.224
		0.439	10.468	7.536	8.715
	SST $k - \omega$	1.757	11.199	9.857	9.228
		1.242	11.917	7.584	11.121
		0.879	10.419	8.393	8.248
		0.621	10.290	8.469	8.490
		0.439	10.063	8.287	7.812
	Spalart-Allmaras	1.757	10.748	10.512	8.988
		1.242	11.875	7.598	10.961
		0.879	10.758	8.154	8.279
		0.621	10.431	8.554	8.284
		0.439	10.350	7.915	8.011
	EB-RSM	1.757	11.321	10.172	10.980
		1.242	11.506	8.019	11.591
		0.879	11.375	8.833	9.072
		0.621	11.253	8.964	8.762
		0.439	10.863	8.826	8.440
Model (Peng et al., 2013)	$k - \omega$	-	9.851	3.965	13.149

Table 6.11: The estimated exact values of K_T, $10K_Q$, η_0 and σ in the tip region on the suction side for the model-scale propeller using the LSR method

Turbulence model	Estimated exact values				Experimental (model)				Relative error (%)			
	$\Phi_0(K_T)$	$\Phi_0(10K_Q)$	$\Phi_0(\eta_0)$	$\Phi_0(\sigma)$	K_T	$10K_Q$	η_0	σ	K_T	$10K_Q$	η_0	σ
$k-\varepsilon$	-	-	-	2.41036	0.305	0.770	0.695	2.020	-	-	-	19.32
$k-\omega$	0.29567	0.75351	0.68929	2.65312	0.305	0.770	0.695	2.020	3.06	2.14	0.82	31.34
SST $k-\omega$	0.29697	0.75051	0.69408	2.67360	0.305	0.770	0.695	2.020	2.63	2.53	0.13	32.36
Spalart-Allmaras	0.28782	0.74504	0.67846	2.65484	0.305	0.770	0.695	2.020	5.63	3.24	2.38	31.43
EB-RSM	0.29615	0.76533	0.67807	2.60544	0.305	0.770	0.695	2.020	2.90	0.61	2.44	26.87

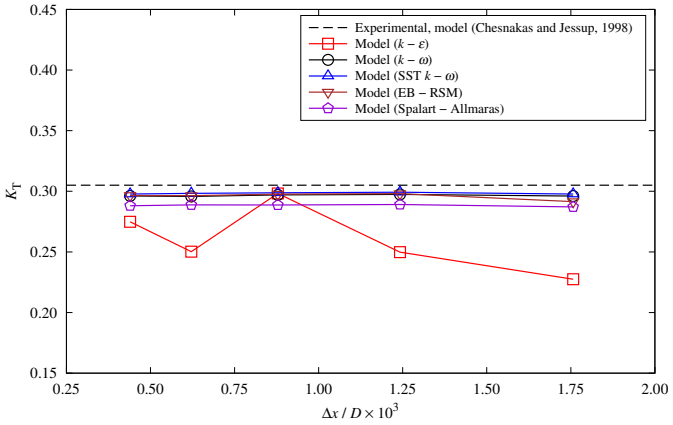

(a) Thrust coefficient, K_T

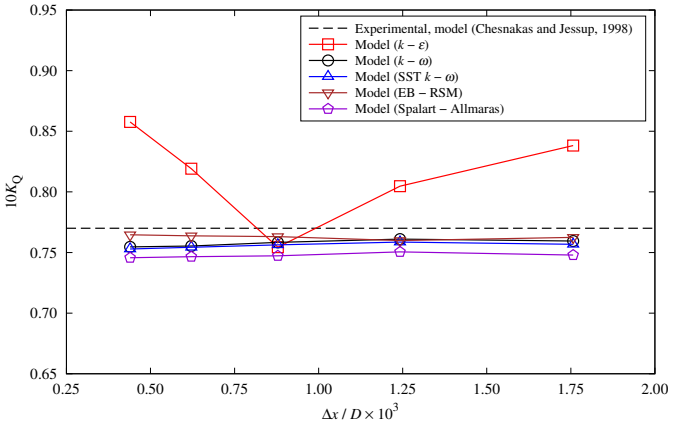

(b) Torque coefficient, K_Q

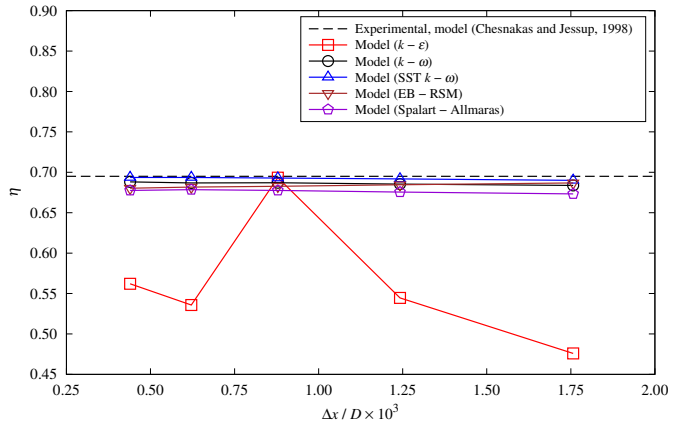

(c) Efficiency, η_0

Figure 6.18: Predicted open-water results for the model-scale propeller at $J = 1.102$ using different turbulence models and grid sizes

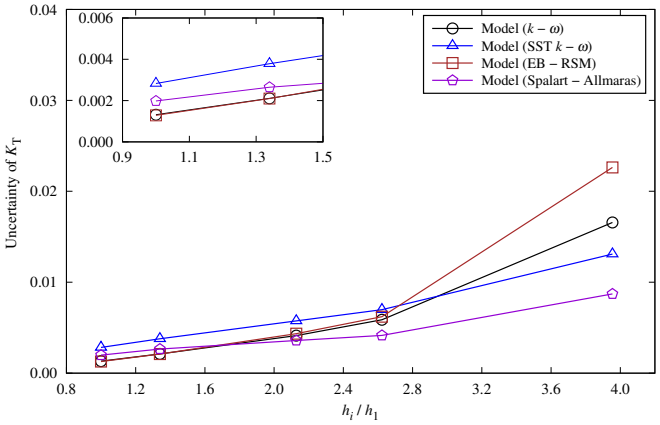

(a) Thrust coefficient, K_T

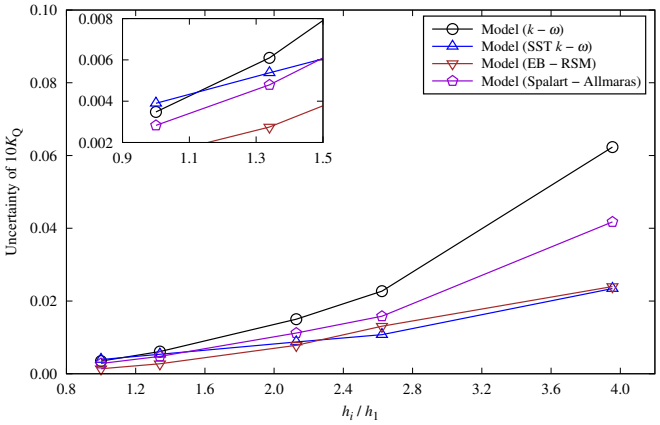

(b) Torque coefficient, K_Q

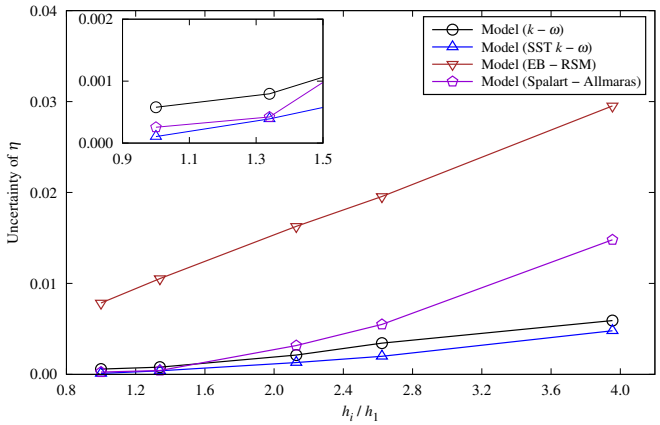

(c) Efficiency, η_0

Figure 6.19: Uncertainties of open-water results for the model-scale propeller at $J = 1.102$ using different turbulence models

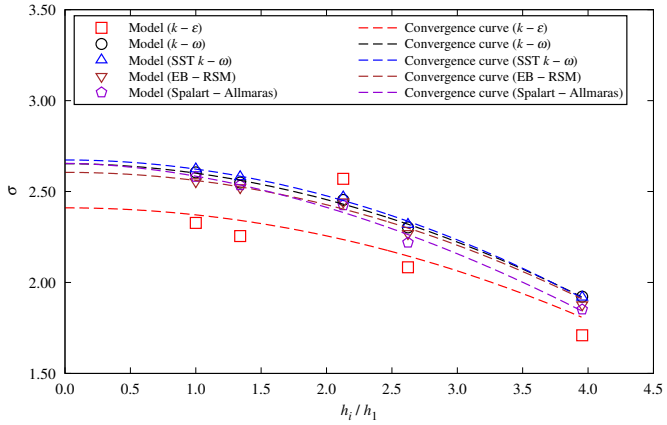

(a) Cavitation number

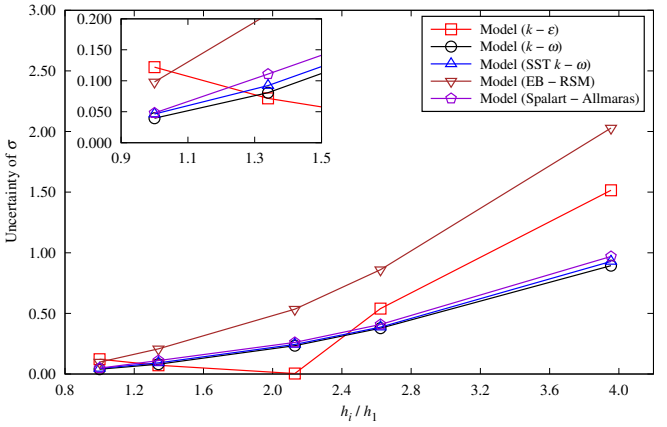

(b) Uncertainty

Figure 6.20: Predicted cavitation number on the suction side in the tip region and associated uncertainties for the model-scale propeller at $J = 1.102$ using different turbulence models

predictions as grid size decreases. The main reason for this phenomenon is that the standard $k - \varepsilon$ model is primarily suitable for turbulent core flows and is coupled with wall functions to connect with solution variables in the log-law region. Its accuracy is severely affected when the cells are resolved in the viscous sub-layer ($y^+ < 5$), as the log-law formulae cease to be valid (Salim and Cheah, 2009). The K_T, $10K_Q$, and η_0 values predicted by the $k - \omega$, SST $k - \omega$, Spalart-Allmaras and EB-RSM

models were found to be consistently under-predicted compared to the experimental data Chesnakas and Jessup (1998). There was no significant difference observed between the predictions with the $k - \omega$ and SST $k - \omega$ models.

Uncertainties due to spatial discretization, estimated using the LSR method, were presented in Fig. 6.19. Note that the uncertainties for the results by the $k - \varepsilon$ model were not calculated due to the divergence in its predictions. Figure 6.20 shows the predicted cavitation number on the suction side in the tip region and associated uncertainties for the model-scale propeller at $J = 1.102$ using different turbulence models. The convergence curves obtained by the LSR method (Eça and Hoekstra, 2014) were also presented in Fig. 6.20a. As expected, the uncertainties decreased as the grid size decreased. The uncertainties were small when the grid size of $\Delta x/D$ is not greater than 6.212E-4.

Table 6.11 presents the estimated exact values of K_{T}, $10K_{\mathrm{Q}}$, η_0 and σ in the tip region on the suction side. Compared with the experimental data (Chesnakas and Jessup, 1998), the relative errors of K_{T}, $10K_{\mathrm{Q}}$ and η_0 using the $k - \omega$, SST $k - \omega$ and EB-RSM models were found to be smaller than 3.50%. For η_0, the minimum relative error is 0.13% with the SST $k - \omega$ model. However, significant difference can be observed in the results of the cavitation number, with the SST$k - \omega$ model exhibiting the maximum relative error of 32.36%. The performance of the $k - \omega$, SST $k - \omega$ and Spalart-Allmaras models was similar, with all of their errors at around 30%. The EB-RSM model slightly outperforms them, yielding a relative error of 26.87%, while the $k - \varepsilon$ model attains the smallest relative error of 19.32%.

To explain these findings, two primary reasons are identified. Firstly, the present steady simulation does not account for the unsteady characteristics of the cavitat-

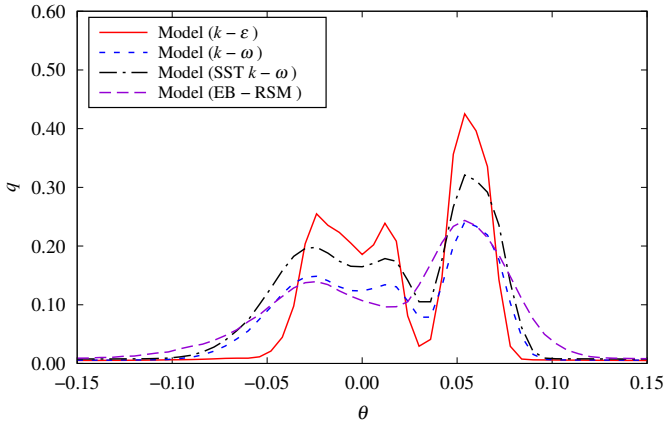

Figure 6.21: Comparison of predicted q at $r/R = 0.928$, $X/R = 0.2386$ and $J = 1.102$ using various turbulence models

ing procedure. Secondly, the cavitation model is not included, which would predict a higher value of the minimum pressure, indicating a lower cavitation number (Hanimann et al., 2016; Perić, 2022). It should be noted that the experimental data for σ at $J = 1.102$ and 1.103 are 2.02 and 2.27, respectively, with an uncertainty of 0.4. Despite these limitations, all presented predictions remain reasonable and fall within the range of experimental data (1.62, 2.67), considering the uncertainty. Based on the convergence studies, both the $k - \omega$ and SST $k - \omega$ models were recommended.

The turbulence predictions were examined by comparing the non-dimensional root mean square fluctuation of velocity, denoted as q, using various turbulence models in this study. The fluctuation of velocity, q, is directly related to the turbulent kinetic energy, k, expressed as $k = \frac{1}{2}(U_\infty q)^2$. Figure 6.21 presents the comparison of predicted q across the tip vortex at $X/R = 0.2386$ and $J = 1.102$. Notably, as both the results of fluctuation of velocity and turbulent kinetic energy were not saved in

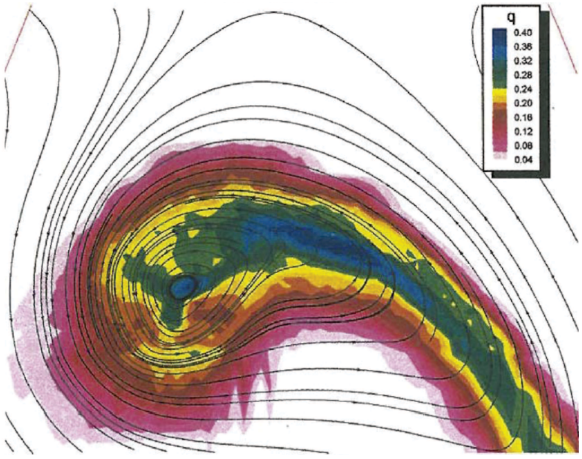

(a) Experimental (Chesnakas and Jessup, 1998)

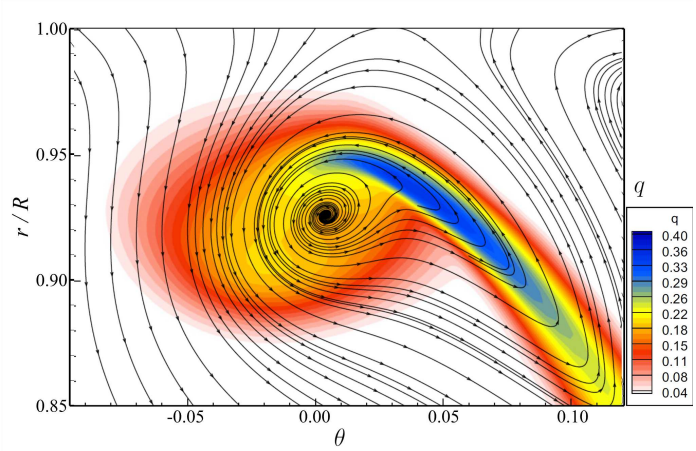

(b) SST $k - \omega$ (Peng et al., 2013)

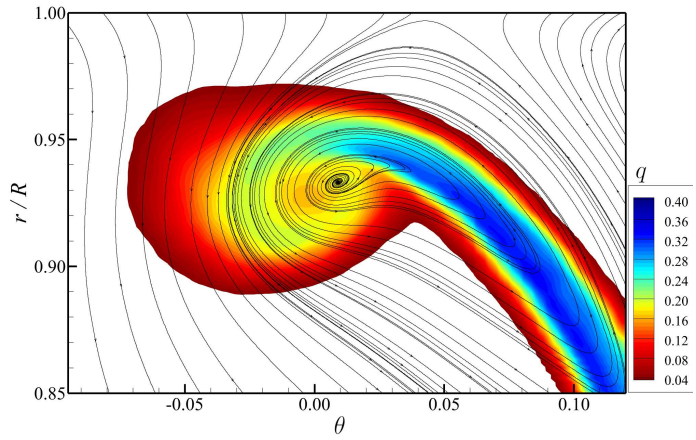

(c) SST $k - \omega$ (Present)

Figure 6.22: Comparison of predicted q contours at $X/R = 0.2386$ and $J = 1.102$ using the SST $k - \omega$ model with experimental data

the one-equation turbulence mode of Star-CCM+, the outcomes of Spalart-Allmaras model are not included in Fig. 6.21. As expected, the predicted non-dimensional root mean square fluctuation of velocity is large in the tip vortex region. Conversely, outside this region, i.e., $\theta \notin [-0.12, 0.12]$, are close to 0. The maximum values of q with various turbulence modes were in general observed at $\theta = 0.054$, with the $k - \varepsilon$ model yielding the highest value (0.43). The predictions of the $k - \omega$ and EB-RSM models were comparable, showing similar levels of q. The predicted q with SST $k - \omega$ is greater than that of the EB-RSM model, in agreement with the findings reported by Peng et al. (2013).

Furthermore, in Fig. 6.22, a comparison of predicted q contours at $X/R = 0.2386$ and $J = 1.102$ is presented using the SST $k - \omega$ model, along with experimental data (Chesnakas and Jessup, 1998) and numerical results from Peng et al. (2013). Note that both the experimental data (Chesnakas and Jessup, 1998) and numerical solutions from Peng et al. (2013) were obtained through screen capture, making it challenging to quantify the differences between them. The secondary streamlines are also included in these figures. It can be observed that the predicted secondary streamlines generally agree well with the reference data, although the values of q in the vortex core were underestimated by the present method. The non-dimensional root mean square fluctuation of velocity in the region of $\theta \in [0.70, 0.12]$ is larger in the present study compared to that of Peng et al. (2013).

According to the convergence studies for the model-scale propeller, the best-practice settings are recommended and summarized in Table 6.12

Table 6.12: Summary of the best-practice settings for the model-scale propeller

Item	Variable	Recommended setting	Value
Static domain	L_{up}/D	$\geq$ 2.0	2.0
	L_{down}/D	$\geq$ 4.0	4.0
	D_{sp}/D	$\geq$ 4.0	6.0
Rotating domain	R_{rp}/R	$\geq$ 1.2	1.2
	T_{rp}/D	$\geq$ 0.8	0.8
Mesh size	SR	[1.1, 1.3]	1.2
	y^+	[0.5, 2.0]	1.0
	$\Delta x/D$	$\leq$ 6.212E-4	6.212E-4
Turbulence model		$k - \omega$ SST $k - \omega$	$k - \omega$

6.7.1.2 Validation Studies for the Propeller Model with Best-Practice Settings

Using the recommended best-practice settings, validation studies were conducted for the model-scale propeller at various advance ratios ranging from 0.921 to 1.205. Two static pressures, p_0 = 16.5 psi and 22.0 psi, were applied. Compared with the experimental data from Chesnakas and Jessup (1998), the downstream velocities, open-water performance, and cavitation performance are discussed in this section.

Downstream velocities. To validate the prediction of tip vortex downstream, a close-up view of the tip vortex at $X/R = 0.2386$ and $J = 1.102$ is presented in Fig. 6.23. Compared with the experimental data from Chesnakas and Jessup (1998)

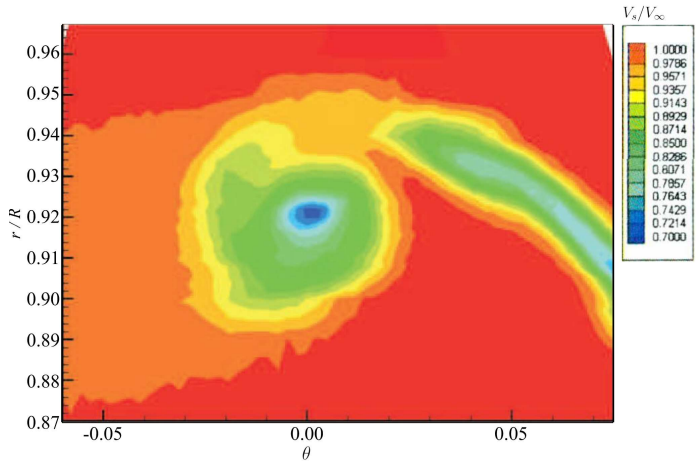

(a) Experimental (Chesnakas and Jessup, 1998)

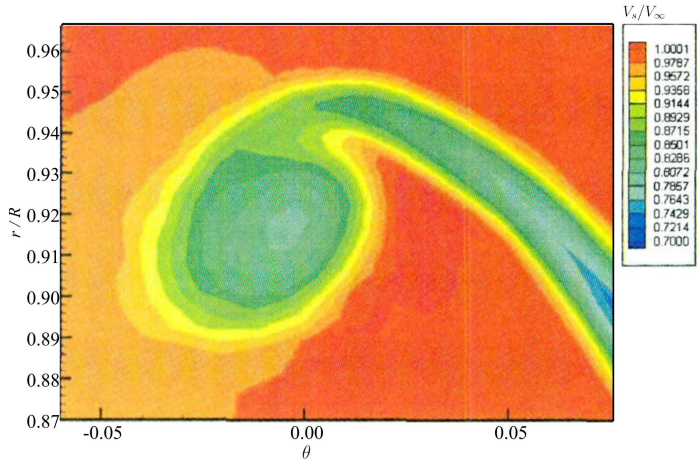

(b) Numerical (Hsiao and Pauley, 1999)

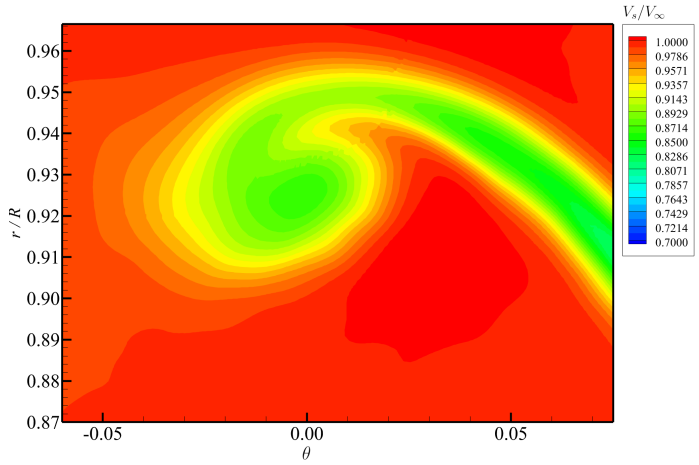

(c) Best-practice settings

Figure 6.23: Comparison of V_s/V_∞ in the tip vortex for the propeller model at $X/R = 0.2386$ and $J = 1.102$ using the best-practice settings

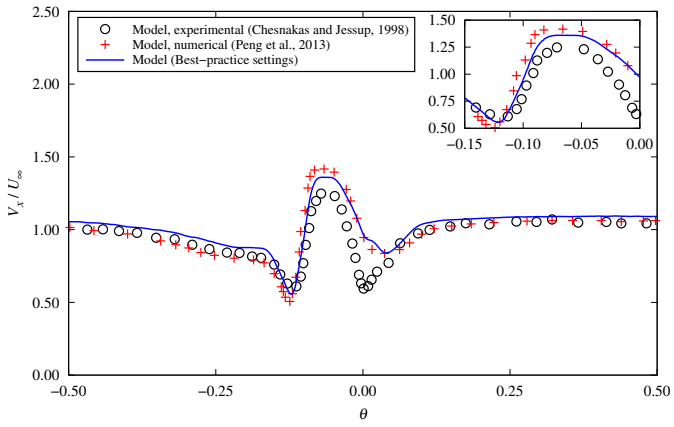

(a) V_x/U_∞ at $X/R = 0.1756$

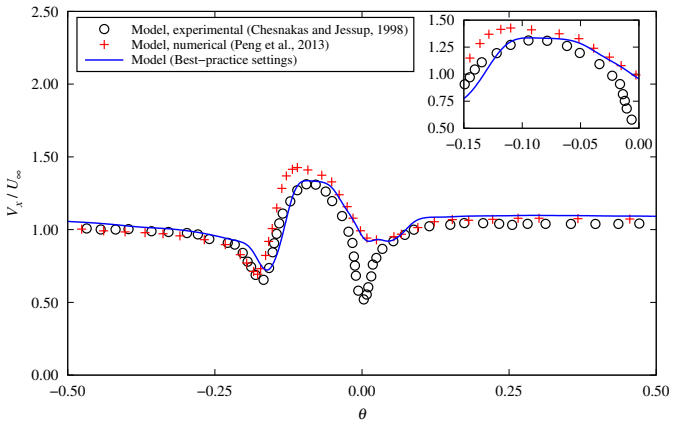

(b) V_x/U_∞ at $X/R = 0.2386$

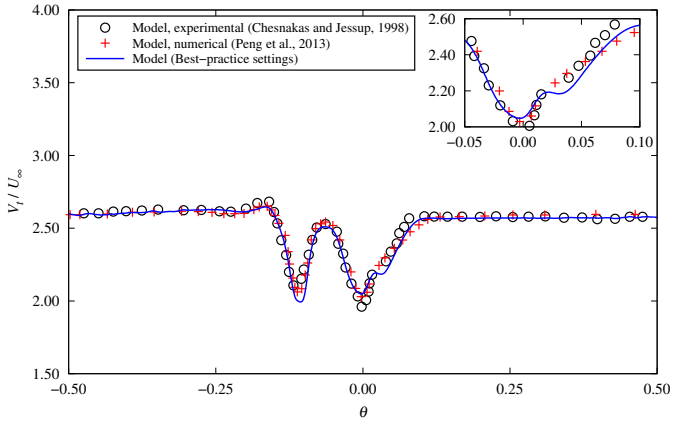

(c) V_t/U_∞ at $X/R = 0.1756$

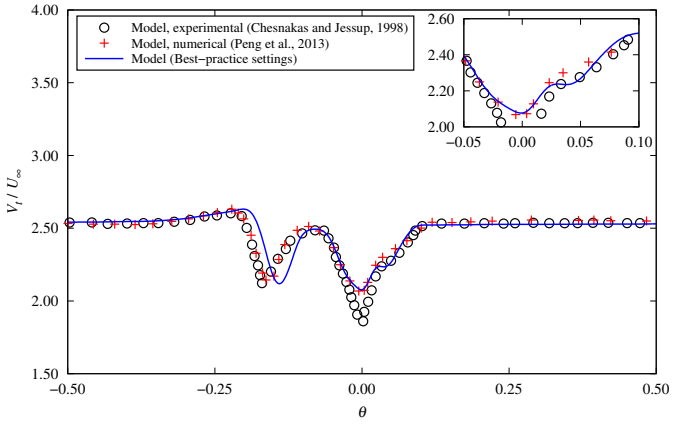

(d) V_t/U_∞ at $X/R = 0.2386$

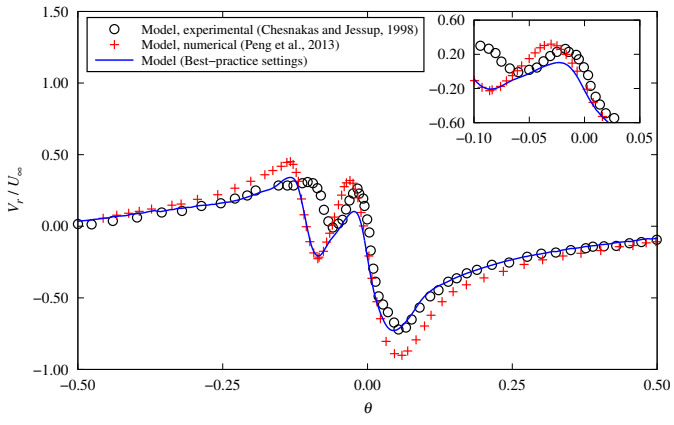

(e) V_r/U_∞ at $X/R = 0.1756$

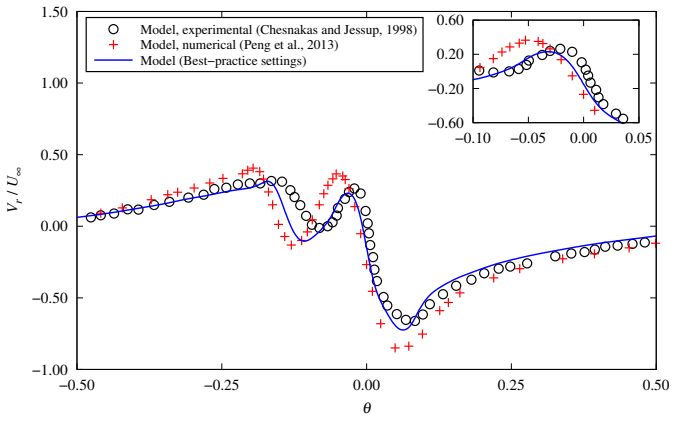

(f) V_r/U_∞ at $X/R = 0.2386$

Figure 6.24: Predicted V_x/U_∞, V_t/U_∞ and V_r/U_∞ across the cortex core for the propeller model at $X/R = 0.1756$ and 0.2386 using the best-practice settings when $J = 1.102$

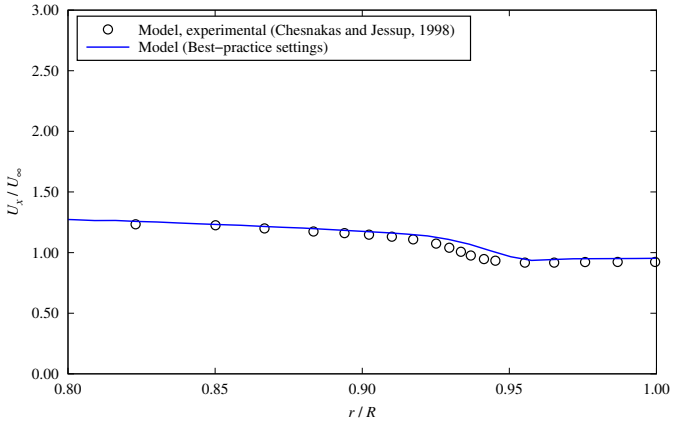

(a) Non-dimensional axial velocity, U_x/U_∞

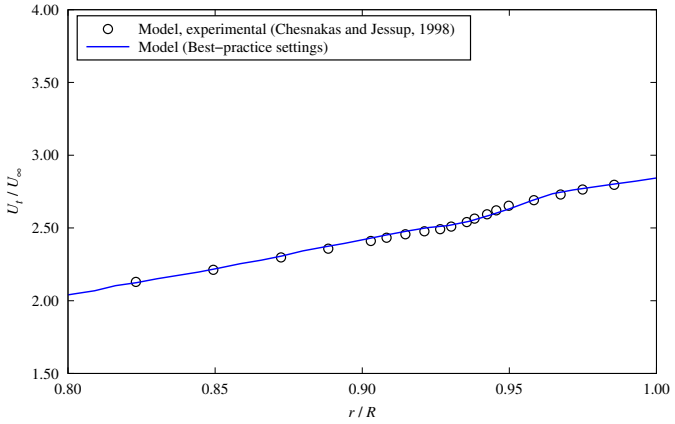

(b) Non-dimensional tangential velocity, U_t/U_∞

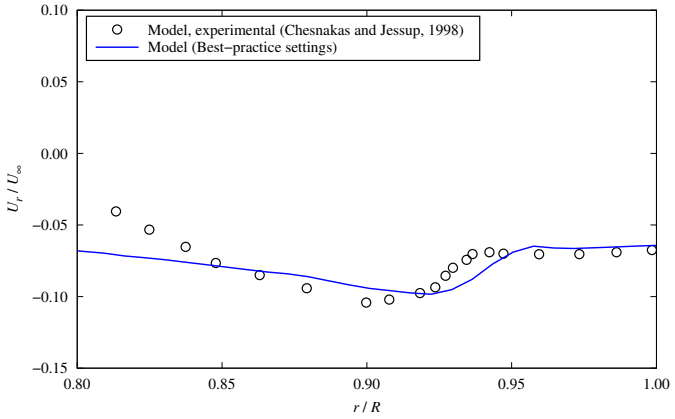

(c) Non-dimensional radial velocity, U_r/U_∞

Figure 6.25: Predicted circumferentially averaged U_x/U_∞, U_t/U_∞ and U_r/U_∞ for the propeller model at $X/R = 0.1756$ and $J = 1.102$ using the best-practice settings

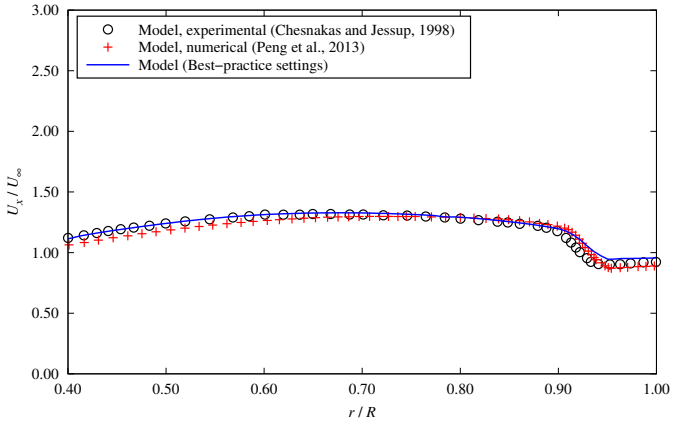

(a) Non-dimensional axial velocity, U_x/U_∞

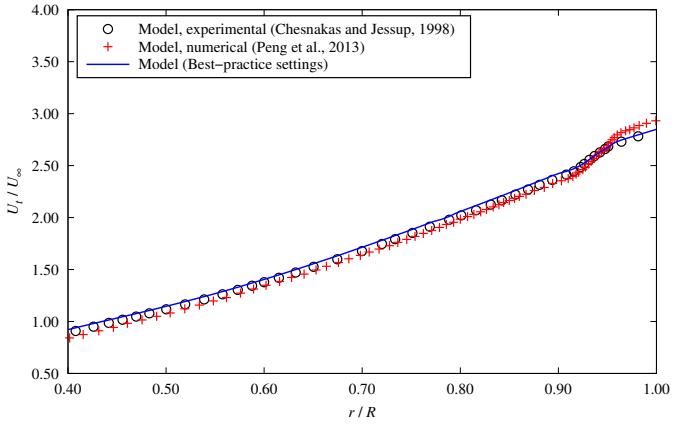

(b) Non-dimensional tangential velocity, U_t/U_∞

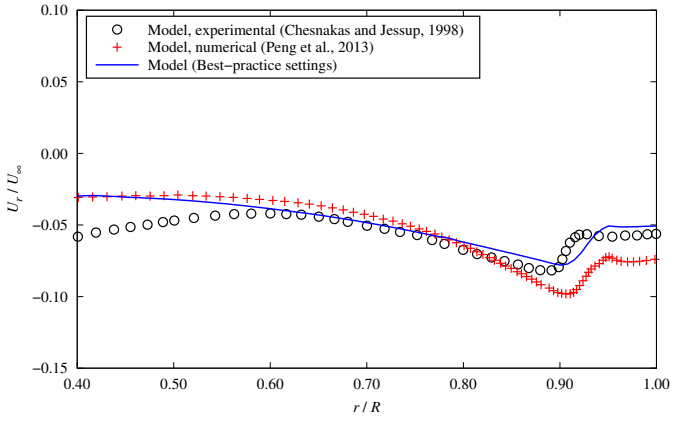

(c) Non-dimensional radial velocity, U_r/U_∞

Figure 6.26: Predicted circumferentially averaged U_x/U_∞, U_t/U_∞ and U_r/U_∞ for the propeller model at $X/R = 0.2386$ and $J = 1.102$ using the best-practice settings

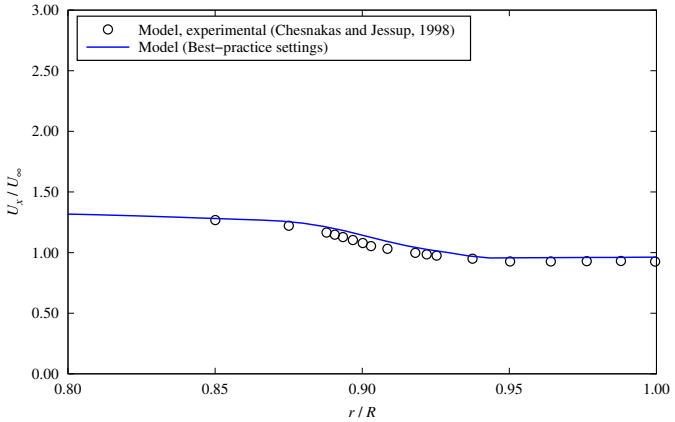

(a) Non-dimensional axial velocity, U_x/U_∞

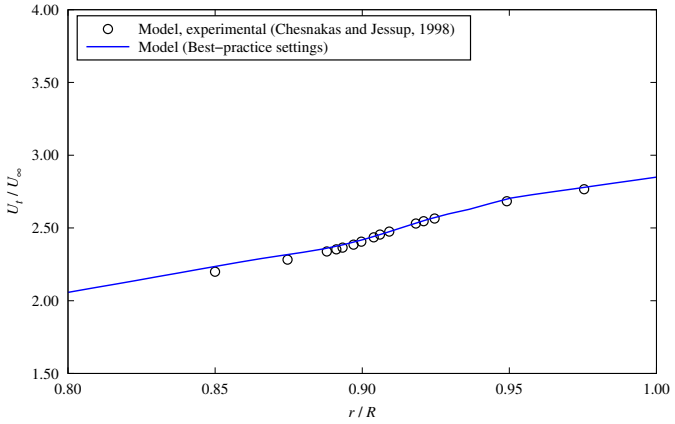

(b) Non-dimensional tangential velocity, U_t/U_∞

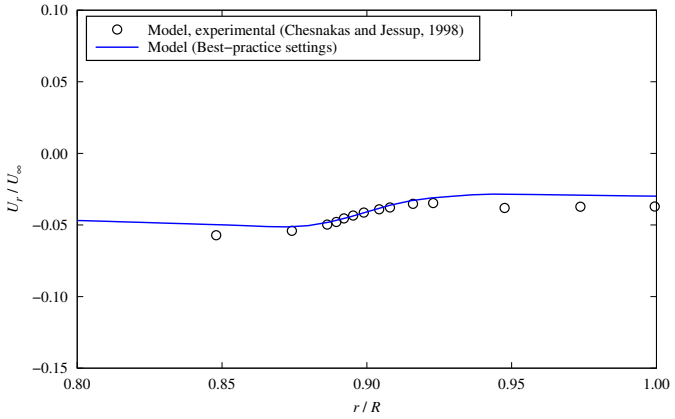

(c) Non-dimensional radial velocity, U_r/U_∞

Figure 6.27: Predicted circumferentially averaged U_x/U_∞, U_t/U_∞ and U_r/U_∞ for the propeller model at $X/R = 0.3963$ and $J = 1.102$ using the best-practice settings

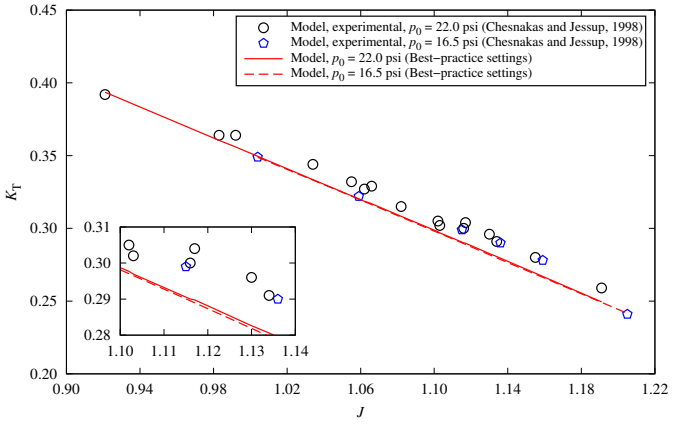

(a) Thrust coefficient, K_T

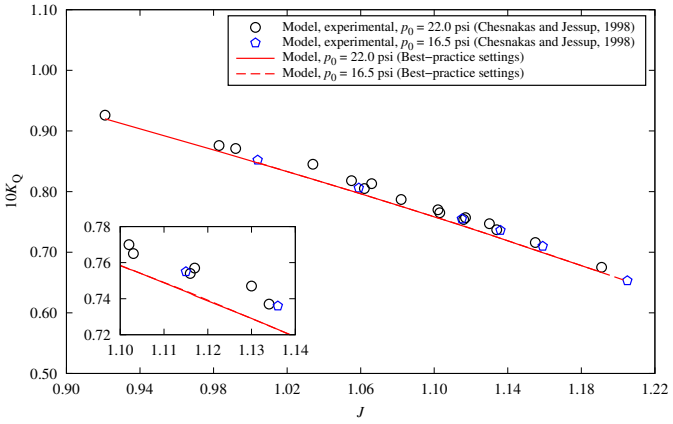

(b) Torque coefficient, K_Q

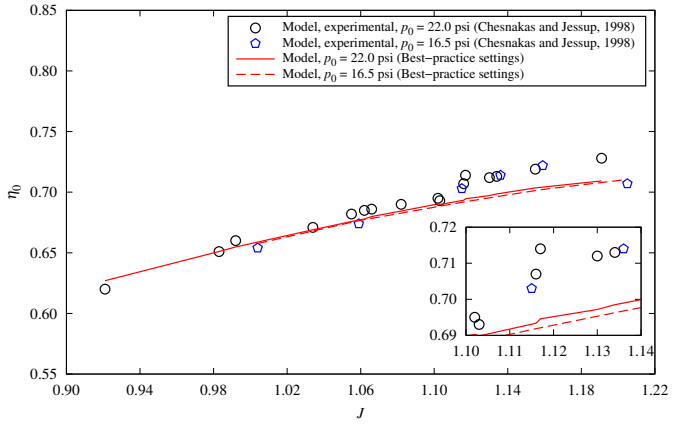

(c) Efficiency, η_0

Figure 6.28: Predicted open-water performance of the propeller model with different static pressures using the best-practice settings

and the numerical solution of Hsiao and Pauley (1999), the non-dimensional primary velocity, V_s/V_∞, in the tip vortex region was over-predicted. Note that the predicted tip vortex core was located at $r/R = 0.928$, while the observed location of the tip vortex core was at $r/R = 0.920$ in the experiment.

To further quantify the comparison between the numerical and experimental results, the non-dimensional axial, tangential and radial velocities (V_x/U_∞, V_t/U_∞ and V_r/U_∞) in the rotating frame at $X/R = 0.1756$ and 0.2386 are presented in Fig. 6.24. These figures also contain the numerical results of Peng et al. (2013). Table 6.13 summarizes the RMS errors of V_x/U_∞, V_t/U_∞ and V_r/U_∞ at $J = 1.102$. The predicted axial and radial velocities are in better agreement with experimental data compared to those by Peng et al. (2013), while the tangential velocity was better predicted in the work of Peng et al. (2013). In the present work, the minimum RMS error is 3.713×10^{-2} for the tangential velocity, V_t/U_∞, at $X/R = 0.1756$.

Figures 6.25, 6.26 and 6.27 present the circumferentially averaged axial, tangential and radial velocities (U_x/U_∞, U_t/U_∞ and U_r/U_∞) in the stationary frame at different downstream sections of $X/R = 0.1756$, 0.2386 and 0.3963, respectively. It can be found that the circumferentially averaged axial and tangential velocities are in good agreement with the corresponding experimental data (Chesnakas and Jessup, 1998), with only minor differences in the tip vortex region ($r/R \in [0.91, 0.95]$). For the circumferentially averaged radial velocity, large differences can be seen not only in the tip vortex region but also in the region of $r/R \leq 0.85$ on the $X/R = 0.1756$ section. On the section of $X/R = 0.2386$, the predicted radial velocities in the tip vortex region are in better agreement with experimental data than those from Peng et al. (2013). The circumferentially averaged radial velocities in this work and Peng et al.

Table 6.13: RMS errors of the non-dimensional axial, tangential and radial velocities in the rotating frame at $J = 1.102$ for the propeller model with the best-practice settings

Item	$X/R = 0.1576$			$X/R = 0.2386$		
	V_x/U_∞ (10^{-2})	V_t/U_∞ (10^{-2})	V_r/U_∞ (10^{-2})	V_x/U_∞ (10^{-2})	V_t/U_∞ (10^{-2})	V_r/U_∞ (10^{-2})
Present work	8.201	3.713	8.830	9.283	6.705	7.649
Peng et al. (2013)	9.618	3.439	12.105	9.851	3.965	13.149

Table 6.14: RMS errors of the circumferentially averaged axial, tangential and radial velocities in the stationary frame at $J = 1.102$ for the propeller model with the best-practice settings

Item	$X/R = 0.1576$			$X/R = 0.2386$			$X/R = 0.3963$		
	U_x/U_∞ (10^{-2})	U_t/U_∞ (10^{-2})	U_r/U_∞ (10^{-2})	U_x/U_∞ (10^{-2})	U_t/U_∞ (10^{-2})	U_r/U_∞ (10^{-2})	U_x/U_∞ (10^{-2})	U_t/U_∞ (10^{-2})	U_r/U_∞ (10^{-2})
Present work	3.602	1.313	1.347	2.731	3.132	1.041	3.330	2.479	0.649
Peng et al. (2013)	-	-	-	4.232	4.804	1.509	-	-	-

(2013) are over-predicted at $r/R \leq 0.55$, as shown in Fig. 6.26c.

Table 6.14 present the following RMS errors in predictions related to the experimental data for the circumferentially averaged velocities.

$$\text{RMS} = \sqrt{\frac{\int_{r_1}^{r_2} (\text{Numerical} - \text{Experimental})^2 \ \mathrm{d}r}{r_2 - r_1}} \tag{6.13}$$

where r_1 and r_2 are 0.8 R and 1.0 R, respectively, for $X/R = 0.1756$ and 0.3963 and they are 0.4 R and 1.0 R., respectively, for $X/R = 0.2386$. The maximum and minimum RMS errors are 3.602×10^{-2} and 0.649×10^{-2} for the circumferentially averaged axial and radial velocities, respectively.

Open-water performance. The predicted open-water results for the model-scale propeller using the best-practice settings with different static pressures, $p_0 =$ 22.0 psi and 16.5 psi, are presented in Fig. 6.28. As shown, the numerical solutions agree well with the experiment data (Chesnakas and Jessup, 1998) and the open-water performance is independent of the static pressure. The relative errors with respect to the experimental data from Chesnakas and Jessup (1998) are presented in Table 6.15. The maximum and minimum relative errors of the predicted thrust coefficient are 4.68% and 0.04%.

Cavitation performance. The comparison of the cavitation number in the tip region ($r/R \geq 0.95$) on the suction side for the propeller model with two static pressures, $p_0 = 16.5$ and 22.0 psi is shown in Fig. 6.29, and the relative errors are summarized in Table 6.16. Overall, the predicted cavitation numbers at the tip region on the suction side are basically the same under two different static pressures in the tunnel, and they in general agree well with the experimental data (Chesnakas and Jessup, 1998). The minimum relative error is 4.16% for the case of $J = 1.116$ with the static

Table 6.15: Relative Errors in predicted open-water performance for the model-scale propeller with the best-practice settings

p_0 (psi)	J	Numerical			Experimental			Relative error (%)		
		K_T	$10K_Q$	η_0	K_T	$10K_Q$	η_0	K_T	$10K_Q$	η_0
22.0	0.921	0.39353	0.92006	0.62697	0.392	0.926	0.620	0.39	0.64	1.12
	0.983	0.36046	0.86620	0.65105	0.364	0.876	0.651	0.97	1.12	0.01
	0.992	0.35592	0.85812	0.65484	0.364	0.871	0.660	2.22	1.48	0.78
	1.034	0.33351	0.82040	0.66899	0.344	0.845	0.671	3.05	2.91	0.30
	1.055	0.32241	0.80109	0.67576	0.332	0.818	0.682	2.89	2.07	0.91
	1.062	0.31865	0.79460	0.67782	0.327	0.805	0.685	2.55	1.29	1.05
	1.066	0.31689	0.79074	0.67992	0.329	0.813	0.686	3.68	2.74	0.89
	1.082	0.30829	0.77568	0.68442	0.315	0.787	0.690	2.13	1.44	0.81
	1.102	0.29770	0.75642	0.69026	0.305	0.770	0.695	2.39	1.76	0.68
	1.103	0.29693	0.75563	0.68983	0.302	0.765	0.693	1.68	1.22	0.46
	1.116	0.29002	0.74294	0.69335	0.300	0.754	0.707	3.33	1.47	1.93
	1.117	0.28979	0.74171	0.69457	0.304	0.757	0.714	4.68	2.02	2.72
	1.130	0.28262	0.72906	0.69717	0.296	0.747	0.712	4.52	2.40	2.08
	1.134	0.28059	0.72501	0.69850	0.291	0.737	0.713	3.58	1.63	2.03
	1.155	0.26918	0.70333	0.70352	0.280	0.716	0.719	3.87	1.77	2.15
	1.191	0.24944	0.66662	0.70927	0.259	0.675	0.728	3.69	1.24	2.57
16.5	1.004	0.34887	0.84769	0.65762	0.349	0.852	0.654	0.04	0.51	0.55
	1.059	0.32009	0.79743	0.67655	0.322	0.806	0.674	0.59	1.06	0.38
	1.115	0.29006	0.74425	0.69161	0.299	0.755	0.703	2.99	1.42	1.62
	1.136	0.27859	0.72288	0.69678	0.290	0.736	0.714	3.94	1.78	2.41
	1.159	0.26637	0.69967	0.70226	0.278	0.710	0.722	4.18	1.46	2.73
	1.205	0.24159	0.65212	0.71050	0.241	0.653	0.707	0.25	0.13	0.49

Table 6.16: Comparison of cavitation number in the tip region ($r/R \geq 0.95$) on the suction side for the model-scale propeller

p_0 (psi)	J	Experimental	Numerical	Relative error (%)
22.0	0.921	6.940	8.417	21.28
	0.983	4.800	5.644	17.57
	0.992	4.140	5.386	30.09
	1.034	3.510	4.124	17.48
	1.055	3.070	3.541	15.33
	1.062	3.010	3.352	11.36
	1.066	2.530	3.271	29.31
	1.082	2.390	2.859	19.64
	1.102	2.020	2.430	20.31
	1.103	2.270	2.397	5.62
	1.116	2.060	2.146	4.16
	1.117	1.720	2.149	24.92
	1.130	1.780	1.968	10.54
	1.134	1.610	1.925	19.55
	1.155	1.250	1.700	35.99
	1.191	1.170	1.311	12.08
16.5	1.004	3.860	4.916	27.35
	1.059	2.430	3.420	40.76
	1.115	1.950	2.140	9.75
	1.136	1.600	1.871	16.94
	1.159	1.290	1.623	25.83
	1.205	0.930	1.174	26.21

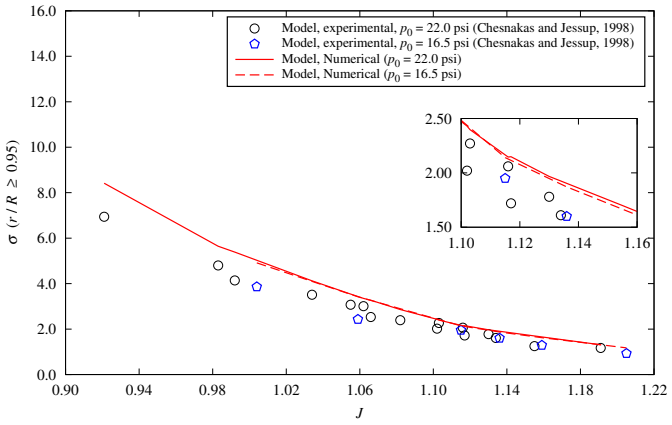

Figure 6.29: Cavitation numbers in the tip region ($r/R \geq 0.95$) on the suction side for the propeller model

pressure of 22.0 psi, and the maximum relative error is 40.76% at $J = 1.059$ with the static pressure of 16.5 psi.

6.7.2 Simulations for the Full-Scale Propellers with and without Defects

After the validation studies for the propeller model, simulations were extended to full-scale propellers (with and without LE defects) that have the same geometry as that of the propeller model. The best-practice settings were first developed in a similar way for the propeller model, and then applied to investigate the effects of LE defects on the open-water propeller performance.

6.7.2.1 Convergence Studies

A total of 172 cases were carried out in the convergence studies for the full-scale propellers using the geometry of DTMB 5168 propeller with no and 0.50 mm LE defects.

The predicted non-dimensional axial, tangential and radial velocities, V_x/U_∞, V_t/U_∞ and V_r/U_∞, across the vortex core at $X/R = 0.2386$ are presented and discussed.

Since there is no sea trial data available for the full-scale propeller, experimental data for the propeller model (Chesnakas and Jessup, 1998) are included in following figures as references.

Convergence studies for the full-scale propellers on domain size were first performed with three upstream length in terms of $L_{\text{up}} = 2.0$, 3.0 and 4.0 D. In these cases, the downstream length was set to 10.0 D, and the diameter of static domain was also 10.0 D. The rotating domain had a radius of 1.2 R and a thickness of 0.8 D. The value of y^+ was set to 1.0, and the $k - \omega$ model was employed. Figure 6.30 shows the sensitivities of non-dimensional velocities across the vortex core at $X/R = 0.2386$ to the length of upstream for the full-scale propeller with no and 0.50 mm defects. It can be seen that the results were independent of the length of upstream. The upstream with $L_{\text{up}} = 2.0$ D is then recommended.

Four downstream length in terms of $L_{\text{down}} = 4.0$, 6.0, 8.0 and 10.0 D were investigated. The diameter of static domain was set as 10.0 D. The radius and thickness of the rotating domain were 1.2 R and 0.8 D, respectively. These convergence studies were simulated with $y^+ = 1.0$ and the $k - \omega$ model. The convergence of non-dimensional velocities across the vortex core at $X/R = 0.2386$ with respect to the length of downstream for the full-scale propeller with no and 0.50 mm defects are shown in Fig. 6.31. The results indicate that the length of downstream has small influence on the downstream velocity. Therefore, a length of $L_{\text{down}} = 4.0$ D was used in the following studies.

Convergence studies were then conducted for different diameters of the static

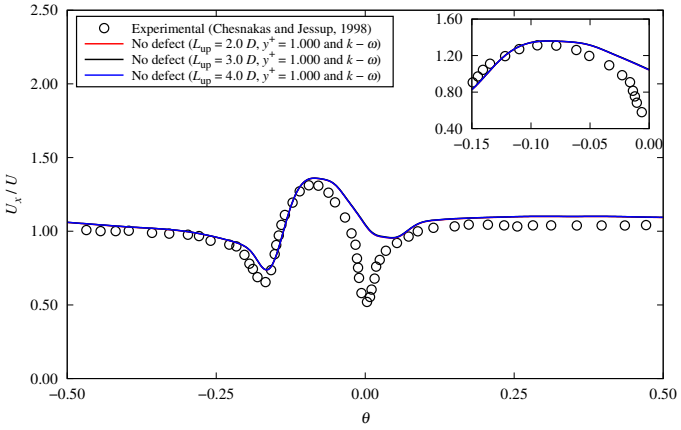

(a) V_x/U_∞ (no defect)

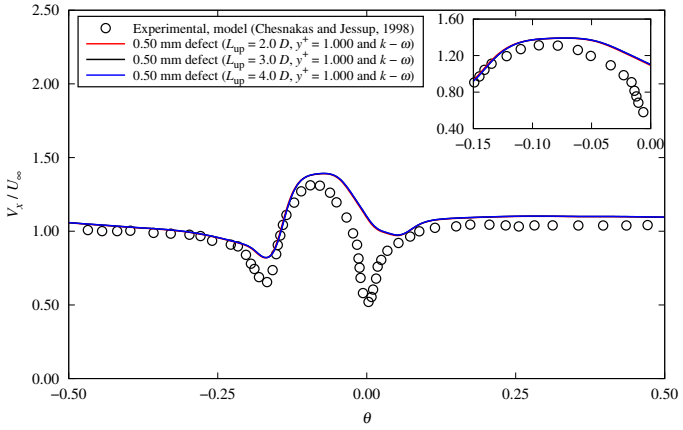

(b) V_x/U_∞ (0.5 mm defect)

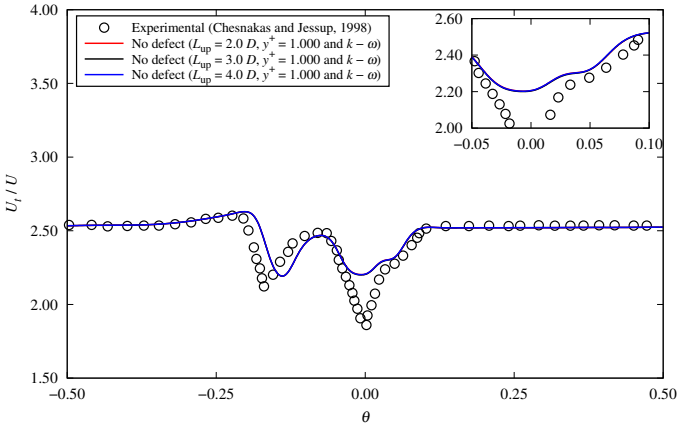

(c) V_t/U_∞ (no defect)

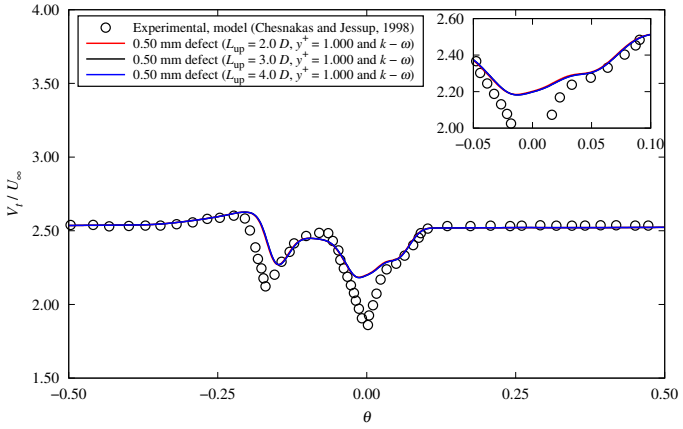

(d) V_t/U_∞ (0.5 mm defect)

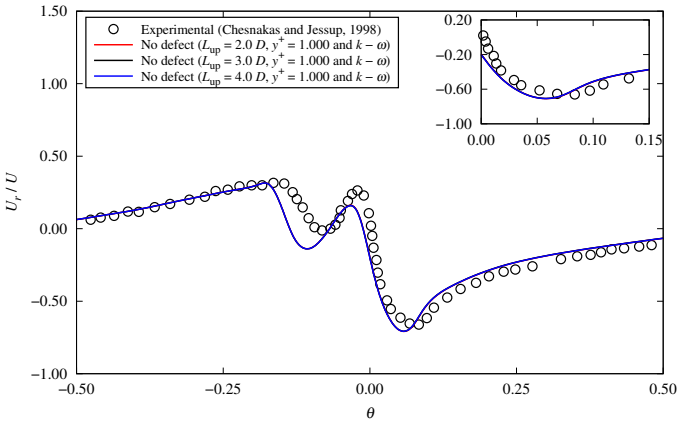

(e) V_r/U_∞ (no defect)

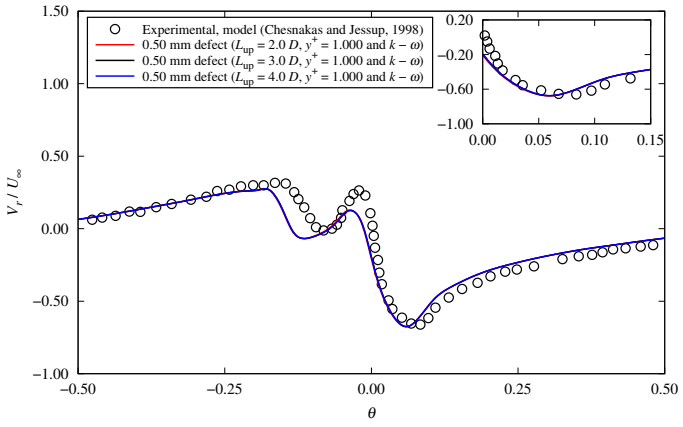

(f) V_r/U_∞ (0.5 mm defect)

Figure 6.30: Sensitivity of non-dimensional velocities across the vortex core at $X/R = 0.2386$ to L_{up} for the full-scale propellers with no and 0.5 mm defects

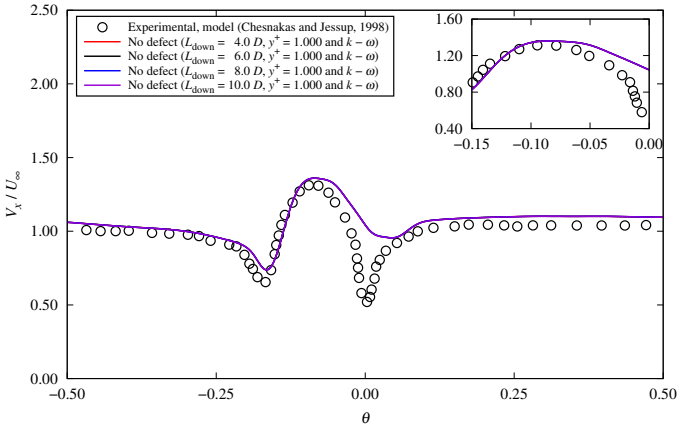

(a) V_x/U_∞ (no defect)

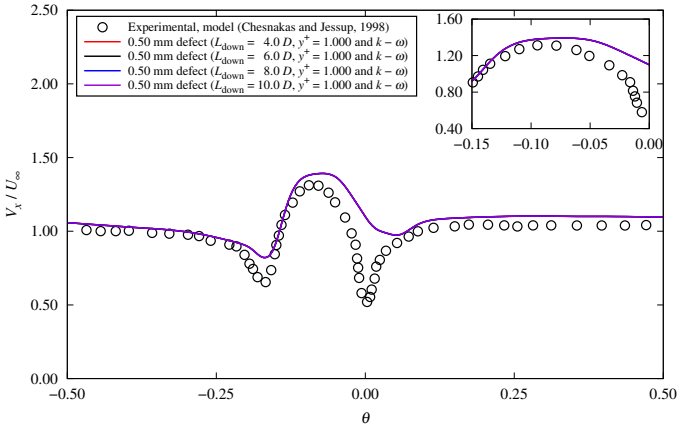

(b) V_x/U_∞ (0.5 mm defect)

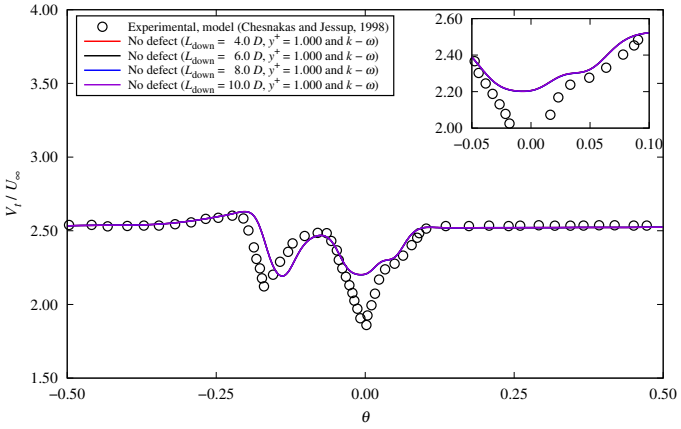

(c) V_t/U_∞ (no defect)

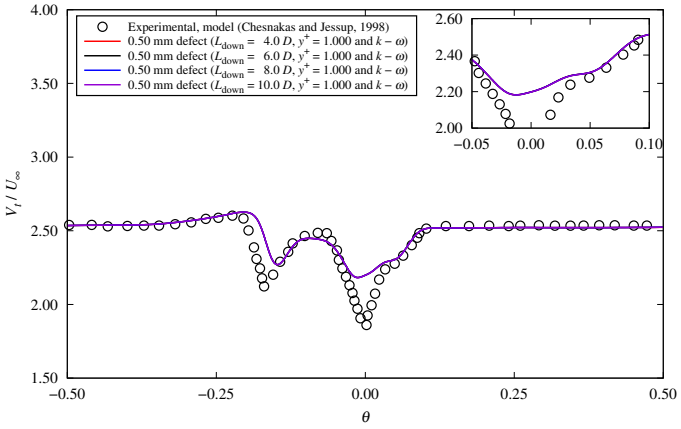

(d) V_t/U_∞ (0.5 mm defect)

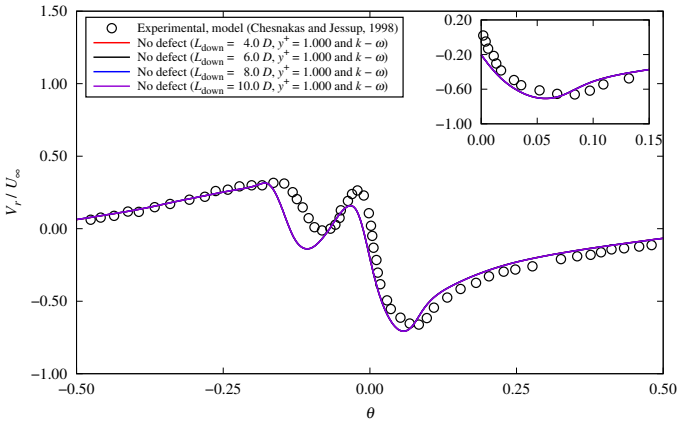

(e) V_r/U_∞ (no defect)

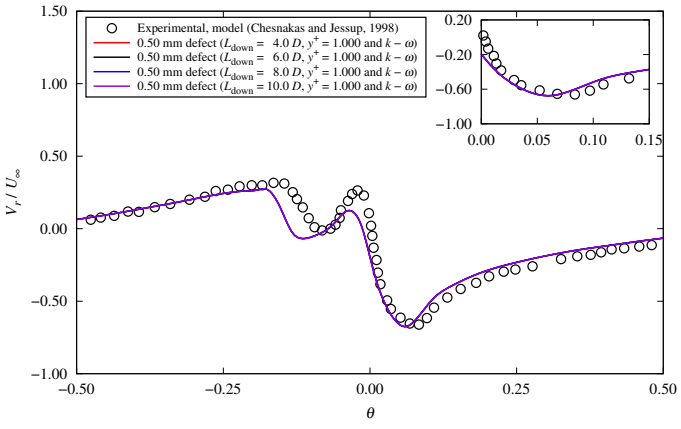

(f) V_r/U_∞ (0.5 mm defect)

Figure 6.31: Sensitivity of non-dimensional velocities across the vortex core at $X/R = 0.2386$ to L_{down} for the full-scale propellers with no and 0.5 mm defects

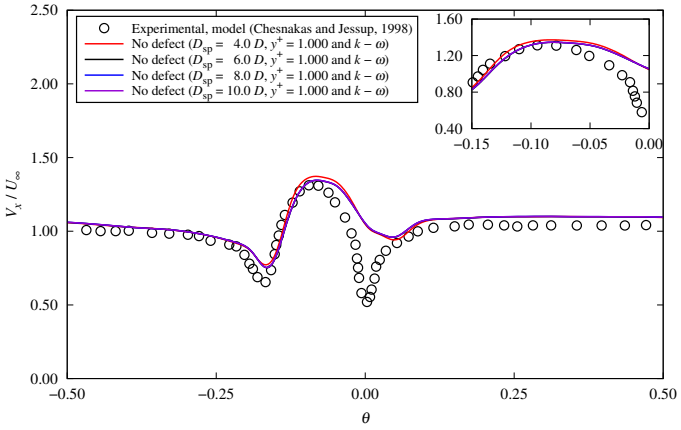

(a) V_x/U_∞ (no defect)

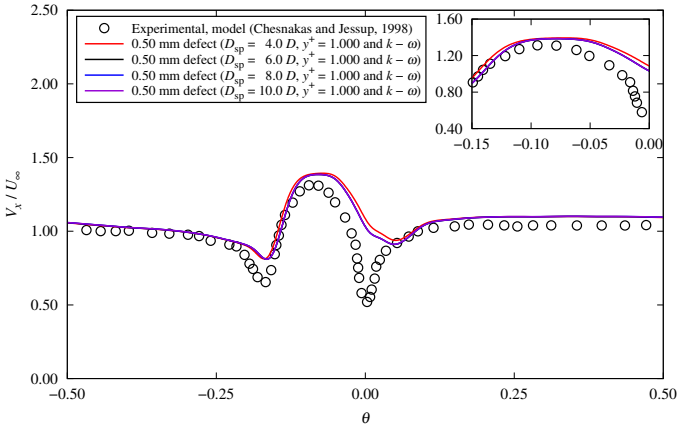

(b) V_x/U_∞ (0.5 mm defect)

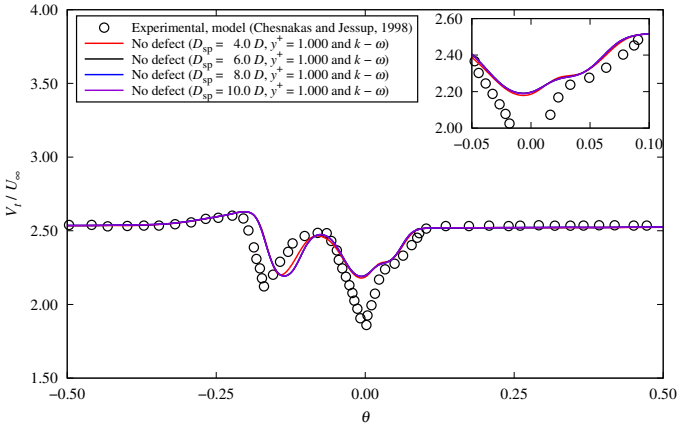

(c) V_t/U_∞ (no defect)

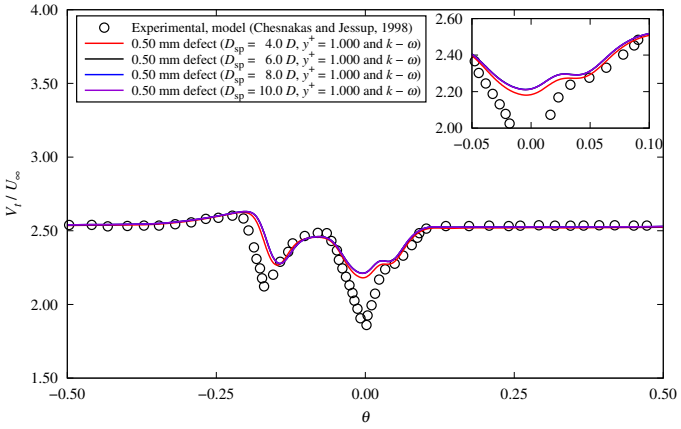

(d) V_t/U_∞ (0.5 mm defect)

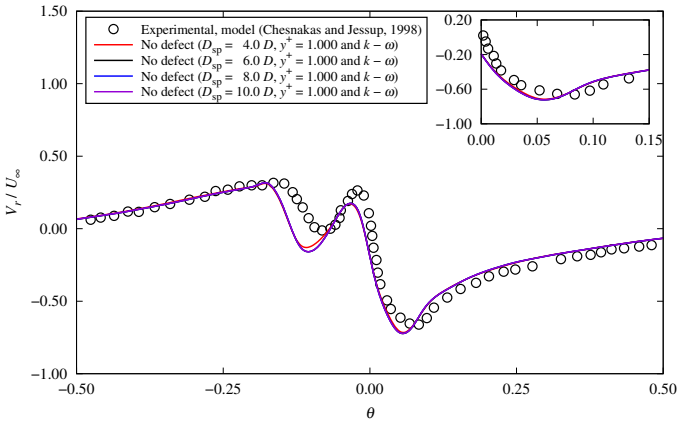

(e) V_r/U_∞ (no defect)

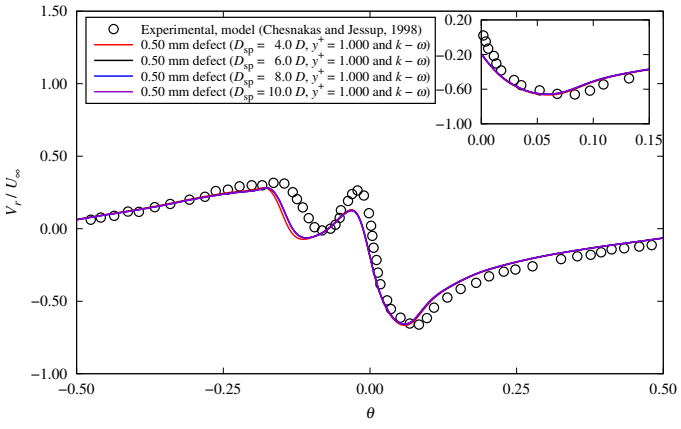

(f) V_r/U_∞ (0.5 mm defect)

Figure 6.32: Sensitivity of non-dimensional velocities across the vortex core at $X/R = 0.2386$ to D_{sp} for the full-scale propellers with no and 0.5 mm defects

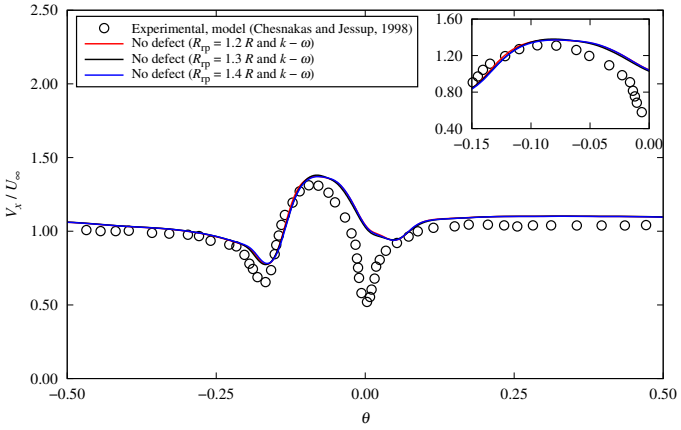

(a) V_x/U_∞ (no defect)

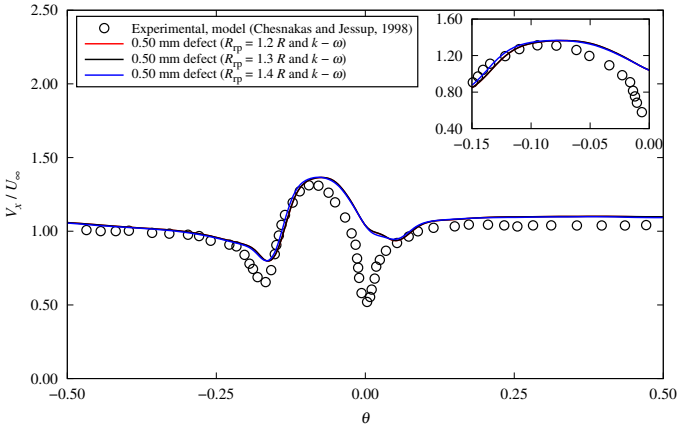

(b) V_x/U_∞ (0.5 mm defect)

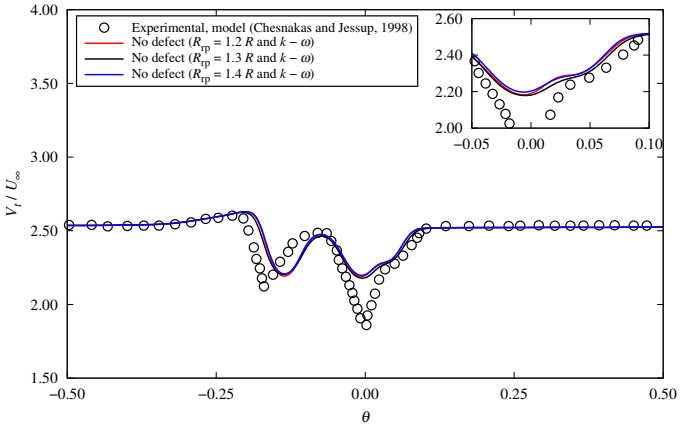

(c) V_t/U_∞ (no defect)

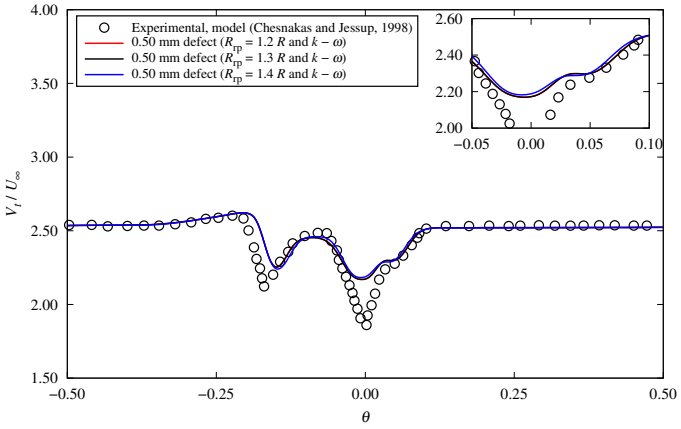

(d) V_t/U_∞ (0.5 mm defect)

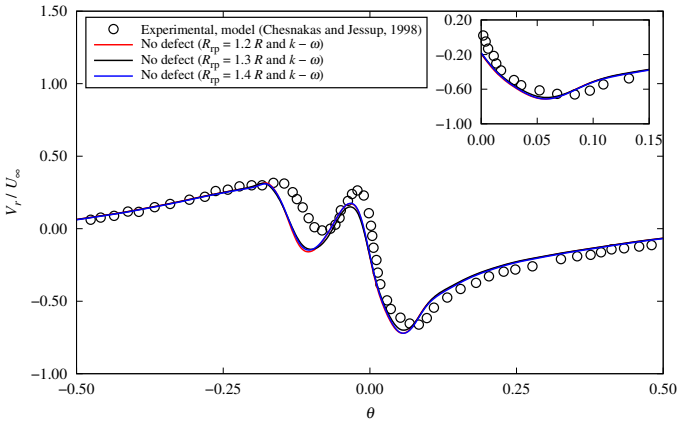

(e) V_r/U_∞ (no defect)

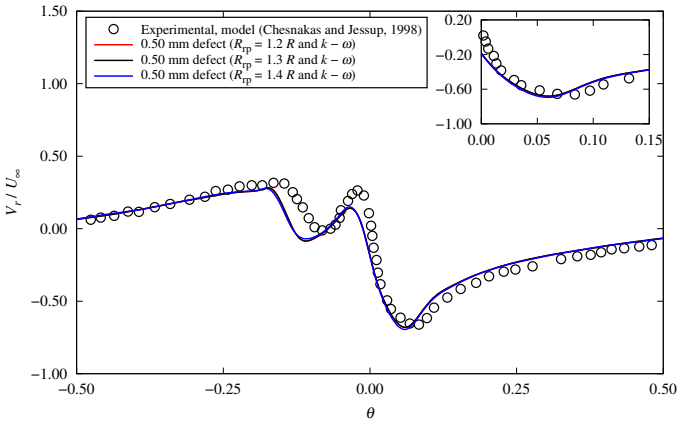

(f) V_r/U_∞ (0.5 mm defect)

Figure 6.33: Sensitivity of non-dimensional velocities across the vortex core at $X/R = 0.2386$ to R_{rp} for the full-scale propellers with no and 0.5 mm defects

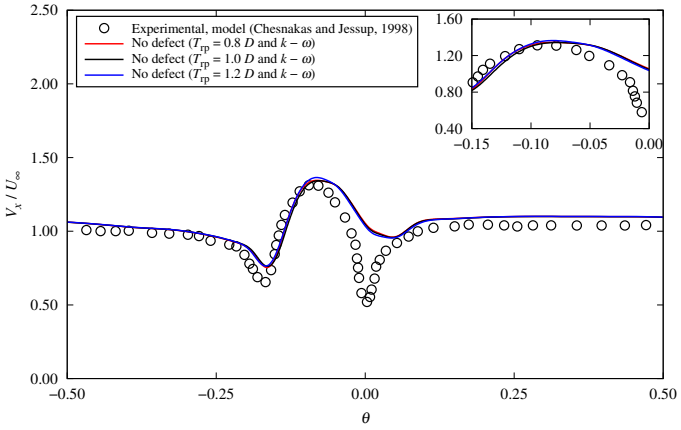

(a) V_x/U_∞ (no defect)

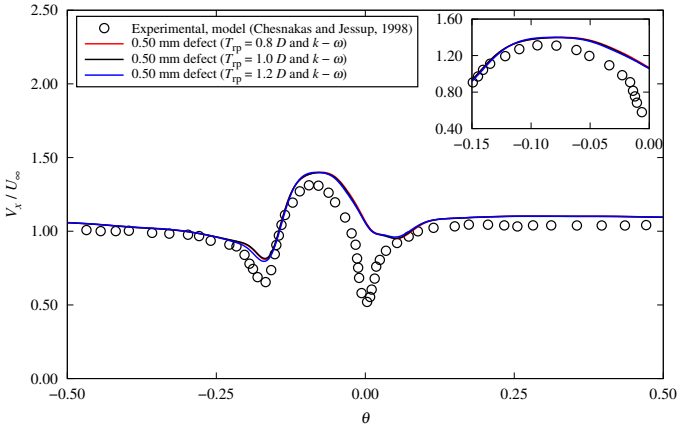

(b) V_x/U_∞ (0.5 mm defect)

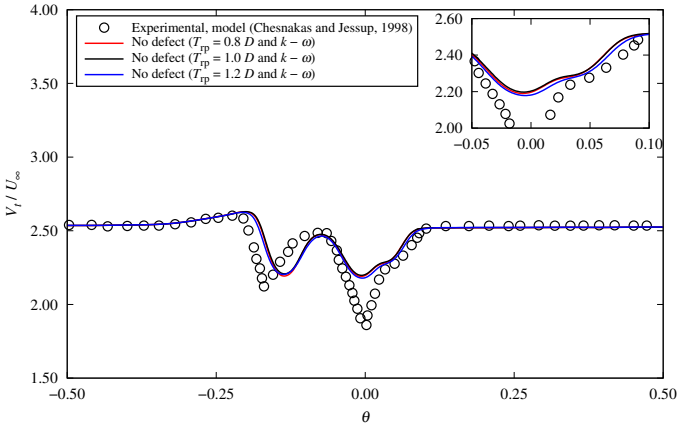

(c) V_t/U_∞ (no defect)

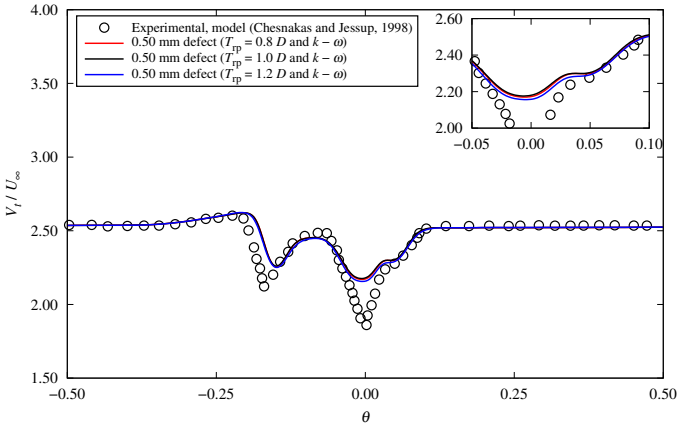

(d) V_t/U_∞ (0.5 mm defect)

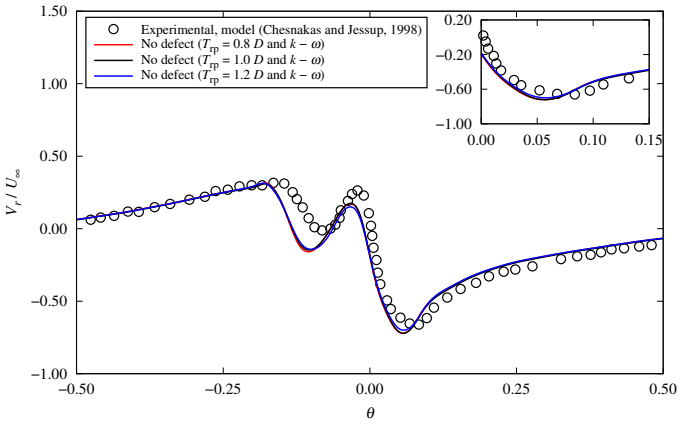

(e) V_r/U_∞ (no defect)

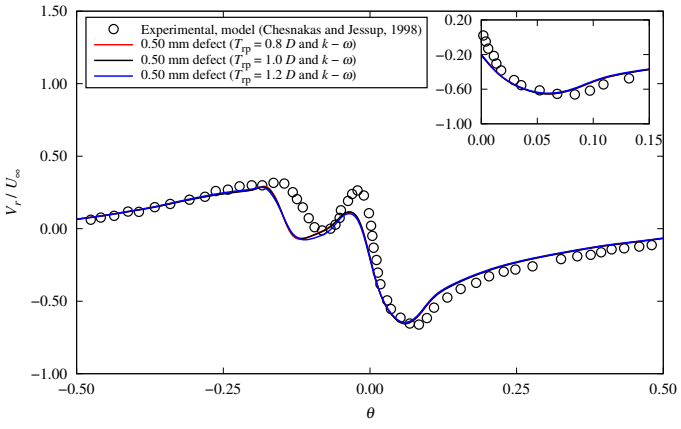

(f) V_r/U_∞ (0.5 mm defect)

Figure 6.34: Sensitivity of non-dimensional velocities across the vortex core at $X/R = 0.2386$ to R_{rp} for the full-scale propellers with no and 0.5 mm defects

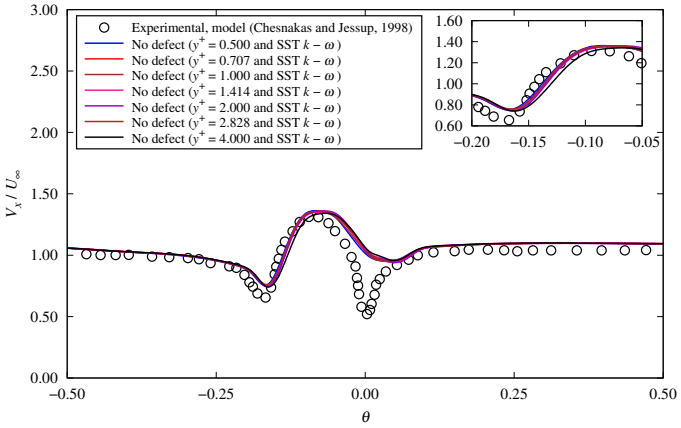

(a) V_x/U_∞ (no defect)

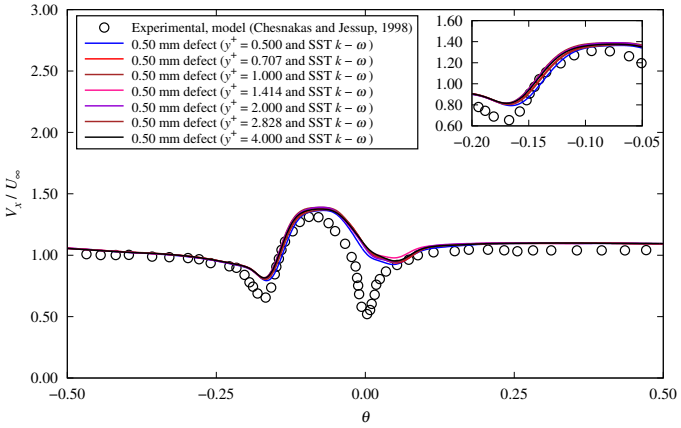

(b) V_x/U_∞ (0.5 mm defect)

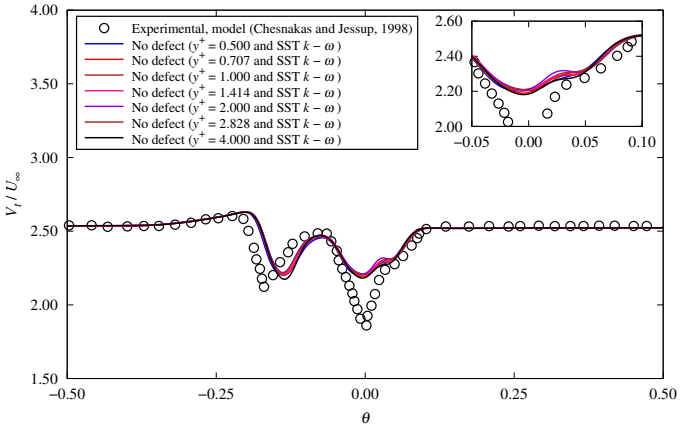

(c) V_t/U_∞ (no defect)

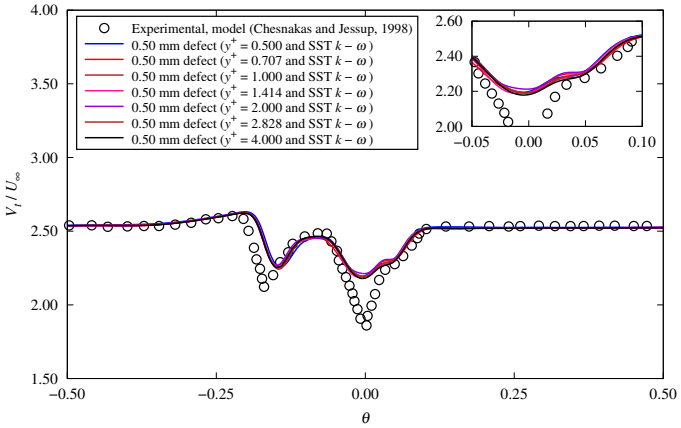

(d) V_t/U_∞ (0.5 mm defect)

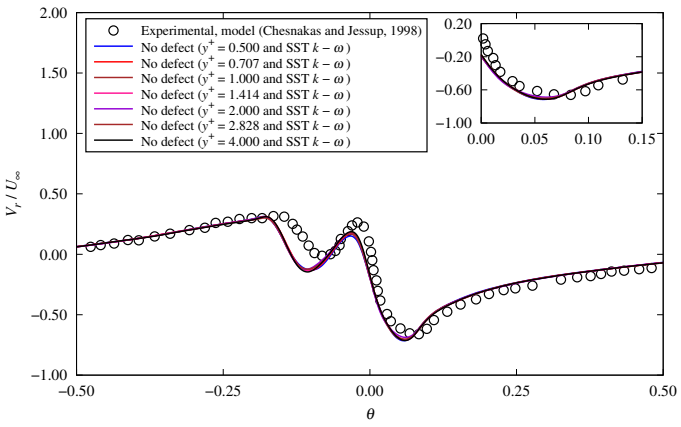

(e) V_r/U_∞ (no defect)

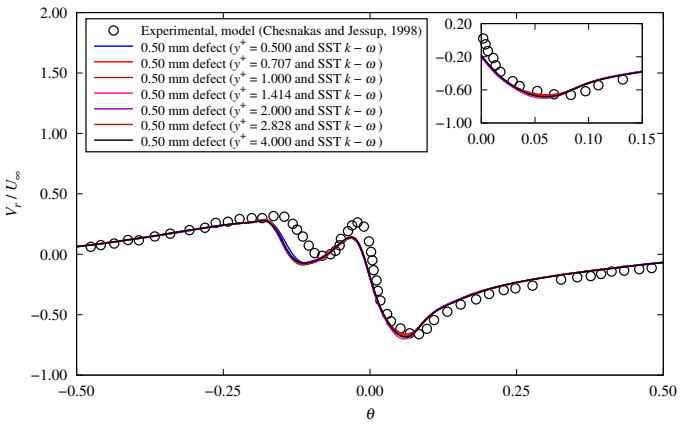

(f) V_r/U_∞ (0.5 mm defect)

Figure 6.35: Sensitivity of non-dimensional velocities across the vortex core at $X/R = 0.2386$ to y^+ for the full-scale propellers with no and 0.5 mm defects using the SST $k - \omega$ model

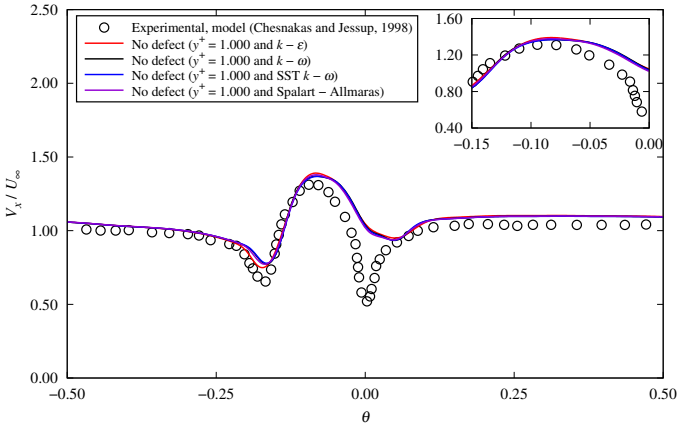

(a) V_x/U_∞ (no defect)

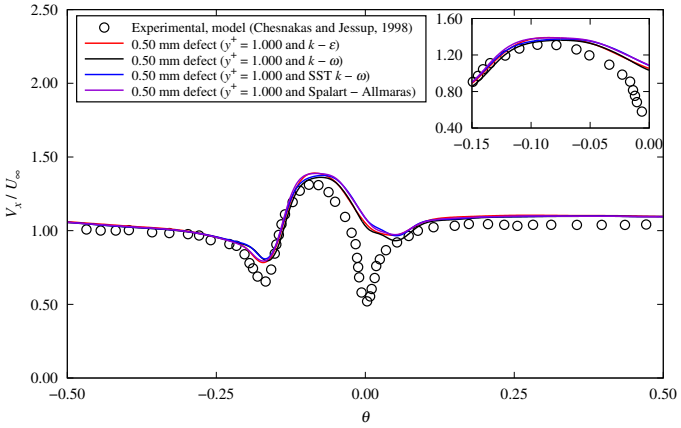

(b) V_x/U_∞ (0.5 mm defect)

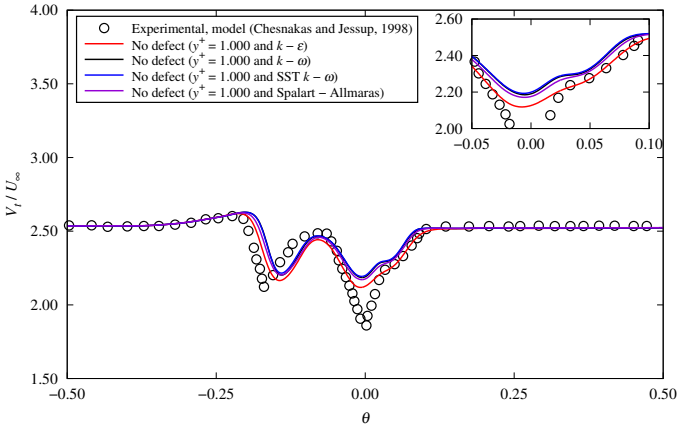

(c) V_t/U_∞ (no defect)

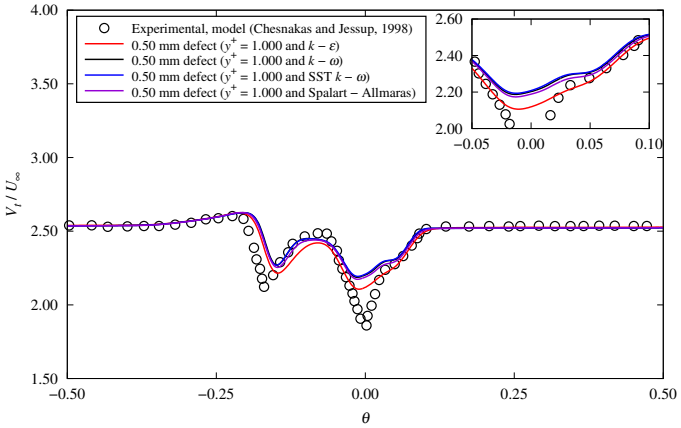

(d) V_t/U_∞ (0.5 mm defect)

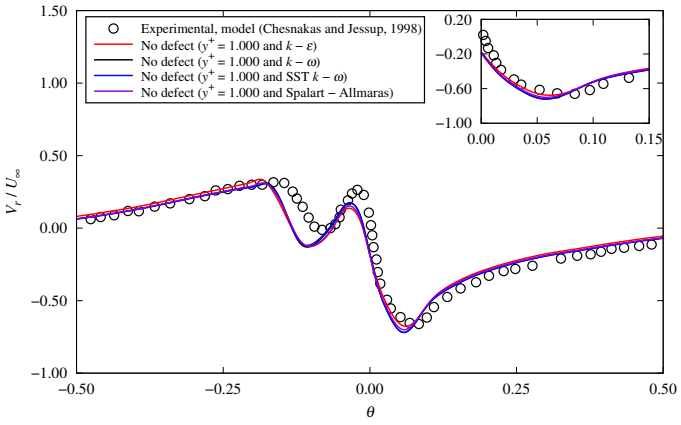

(e) V_r/U_∞ (no defect)

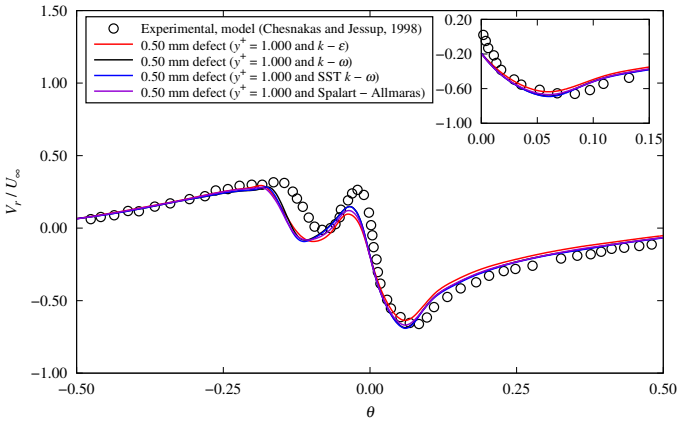

(f) V_r/U_∞ (0.5 mm defect)

Figure 6.36: The non-dimensional velocities across the vortex core at $X/R = 0.2386$ for full-scale propellers with no and 0.5 mm defects using different turbulence models and $y^+ = 1.0$

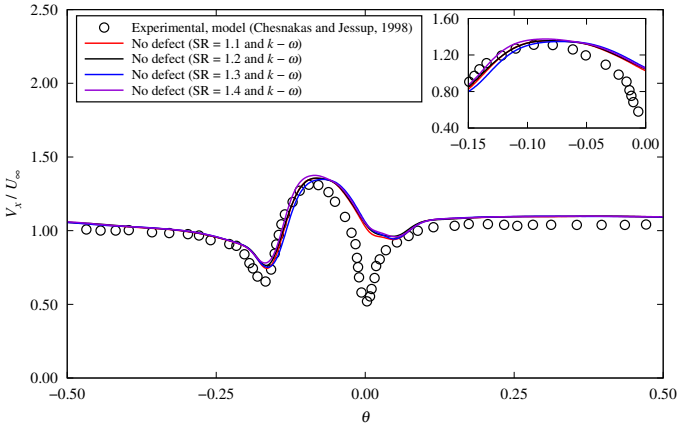

(a) V_x/U_∞ (no defect)

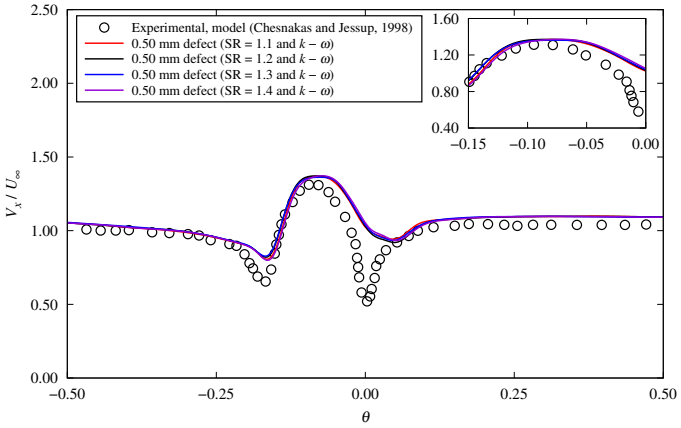

(b) V_x/U_∞ (0.5 mm defect)

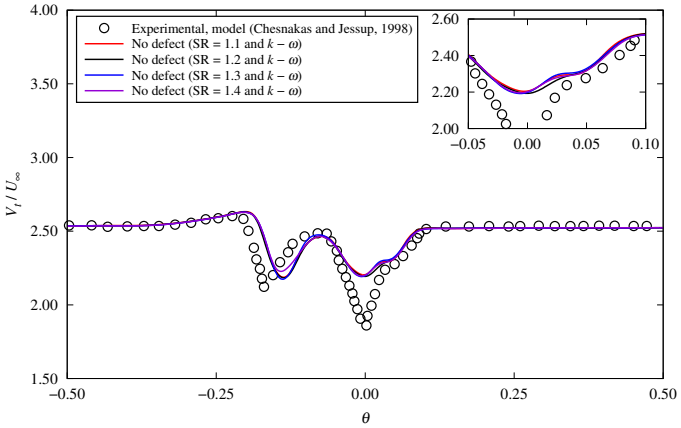

(c) V_t/U_∞ (no defect)

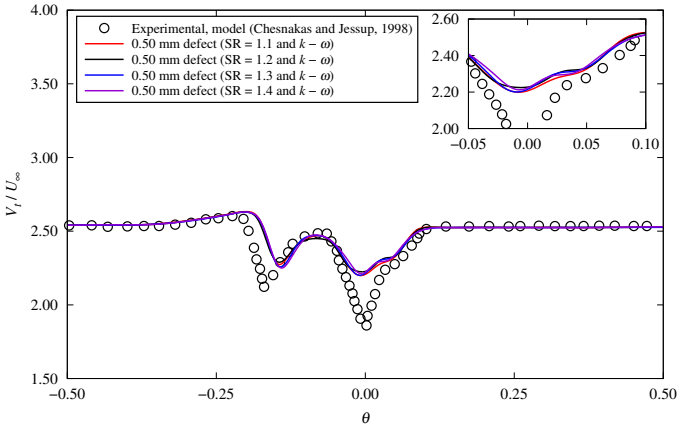

(d) V_t/U_∞ (0.5 mm defect)

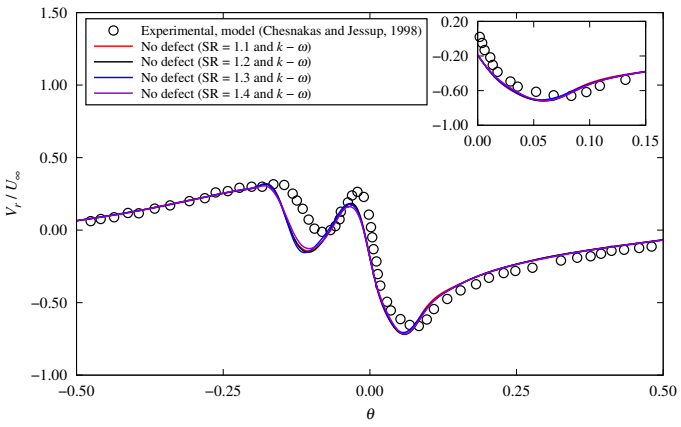

(e) V_r/U_∞ (no defect)

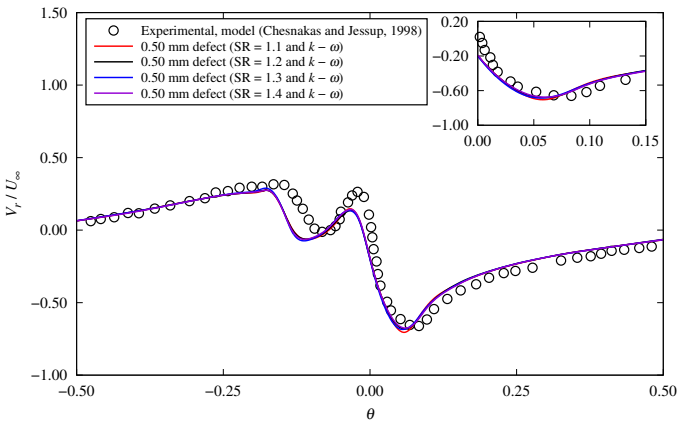

(f) V_r/U_∞ (0.5 mm defect)

Figure 6.37: Sensitivity of non-dimensional velocities across the vortex core at $X/R = 0.2386$ to SR for the full-scale propellers with no and 0.5 mm defects using the $k-\omega$ model

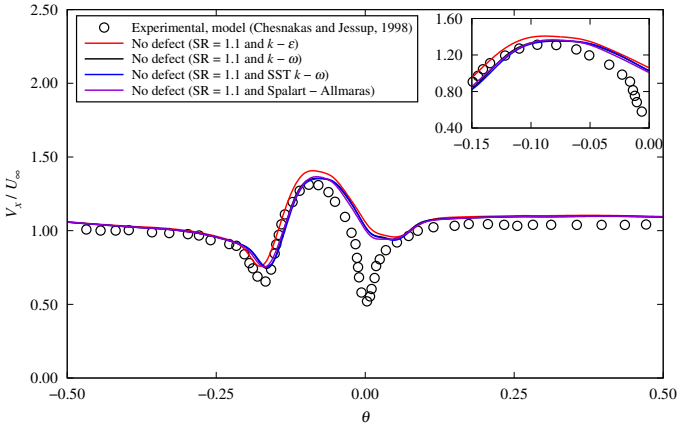

(a) V_x/U_∞ (no defect)

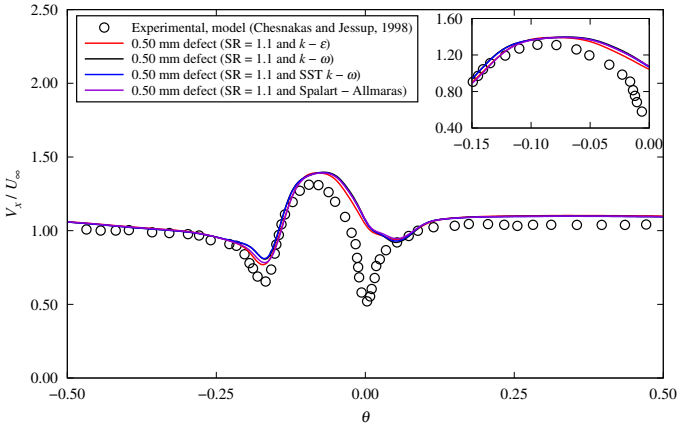

(b) V_x/U_∞ (0.5 mm defect)

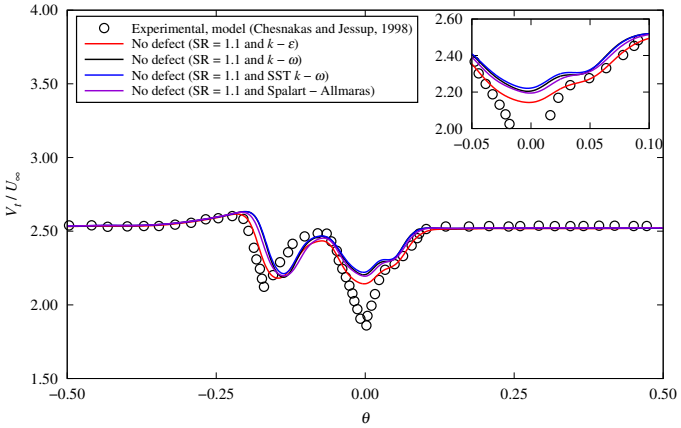

(c) V_t/U_∞ (no defect)

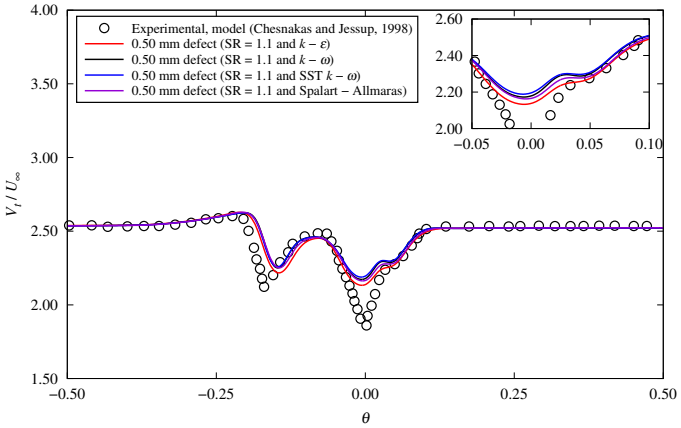

(d) V_t/U_∞ (0.5 mm defect)

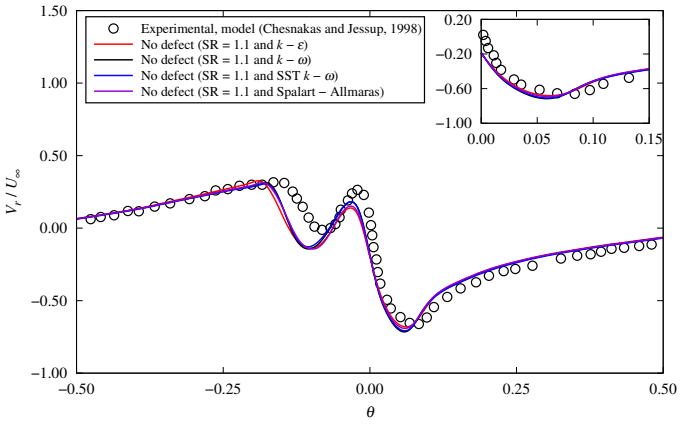

(e) V_r/U_∞ (no defect)

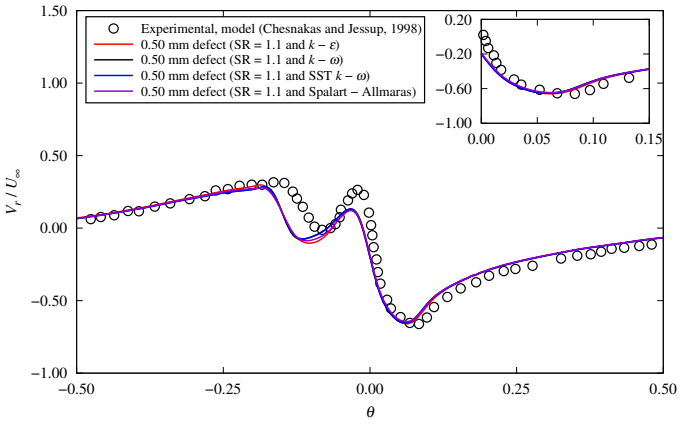

(f) V_r/U_∞ (0.5 mm defect)

Figure 6.38: The non-dimensional velocities across the vortex core at $X/R = 0.2386$ for full-scale propellers with no and 0.5 mm defects using different turbulence models and SR = 1.1

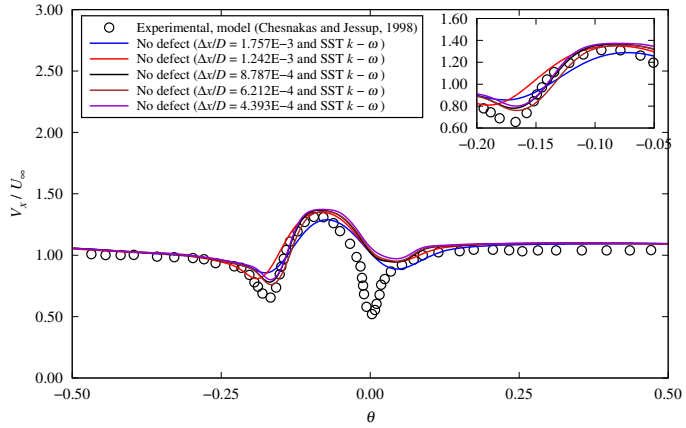

(a) V_x/U_∞ (no defect)

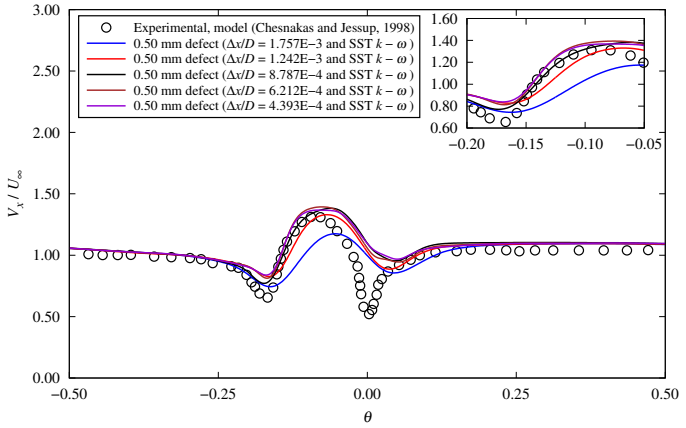

(b) V_x/U_∞ (0.5 mm defect)

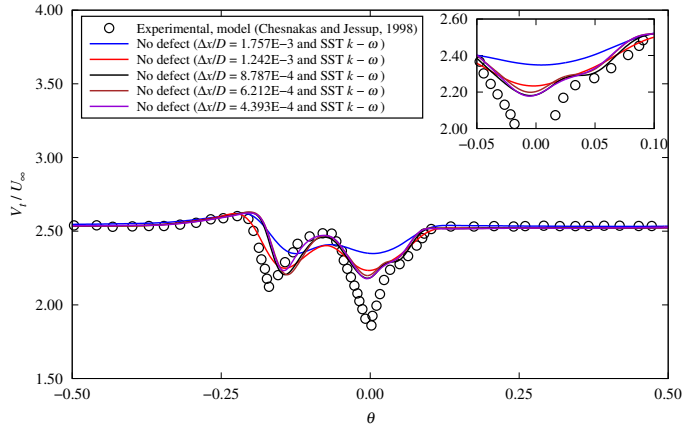

(c) V_t/U_∞ (no defect)

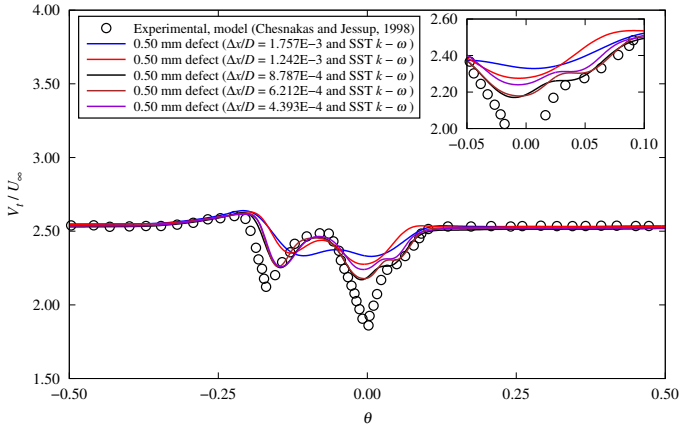

(d) V_t/U_∞ (0.5 mm defect)

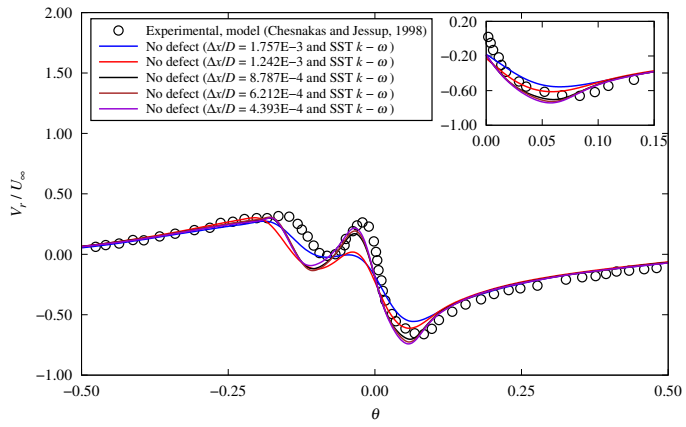

(e) V_r/U_∞ (no defect)

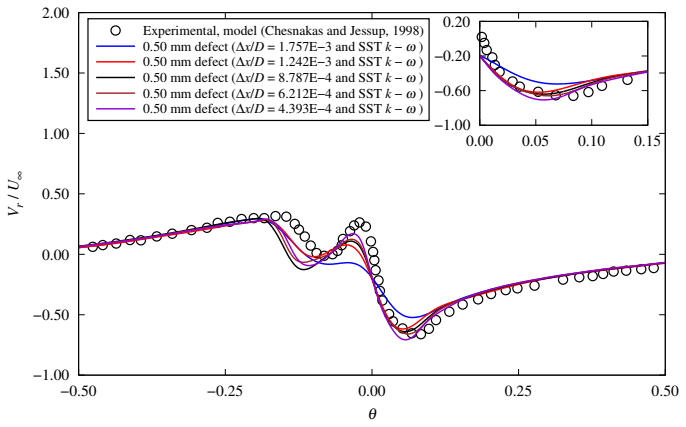

(f) V_r/U_∞ (0.5 mm defect)

Figure 6.39: Sensitivity of non-dimensional velocities across the vortex core at $X/R = 0.2386$ to the grid resolution (Δx) for the full-scale propellers with no and 0.5 mm defects using the SST $k - \omega$ model

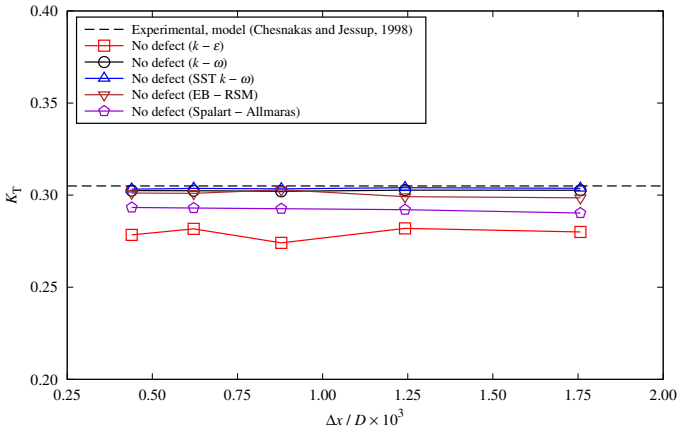

(a) Thrust coefficient, K_T (no defect)

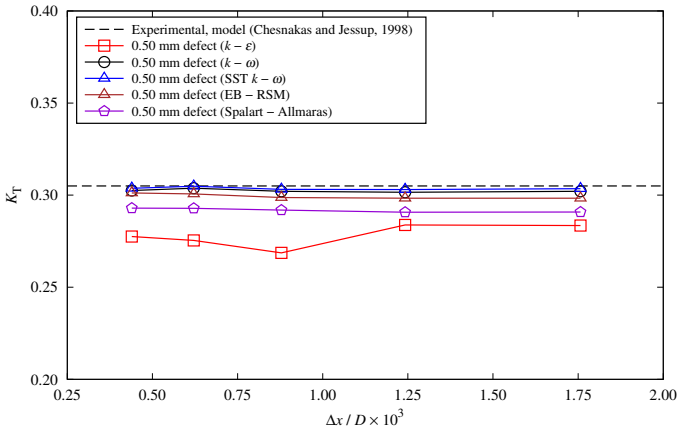

(b) Thrust coefficient, K_T (0.5 mm defect)

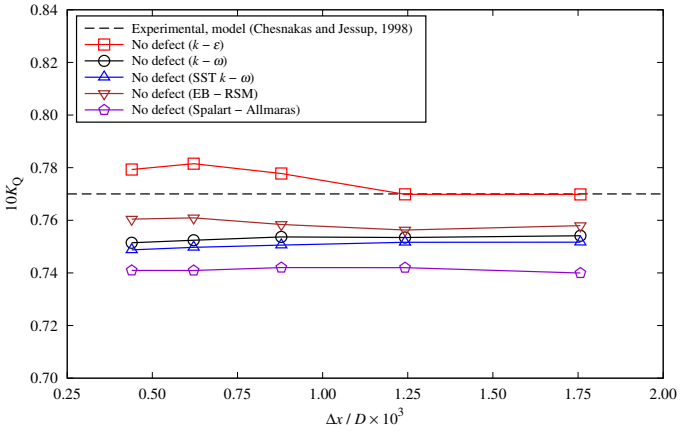

(c) Torque coefficient, K_Q (no defect)

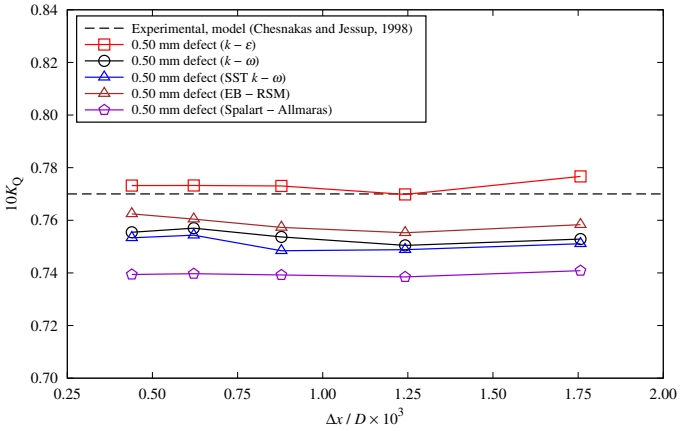

(d) Torque coefficient, K_Q (0.5 mm defect)

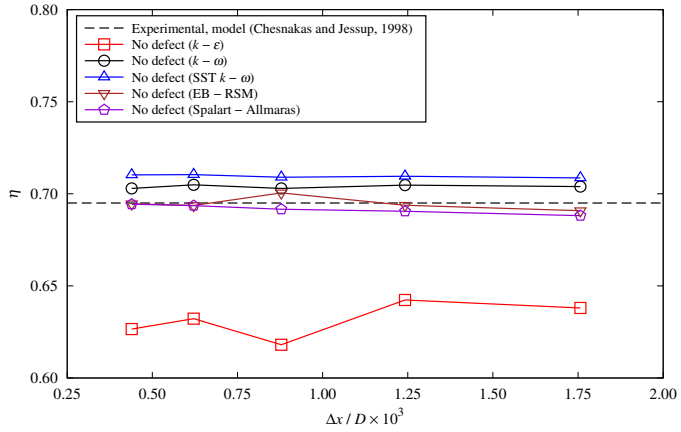

(e) Efficiency, η_0 (no defect)

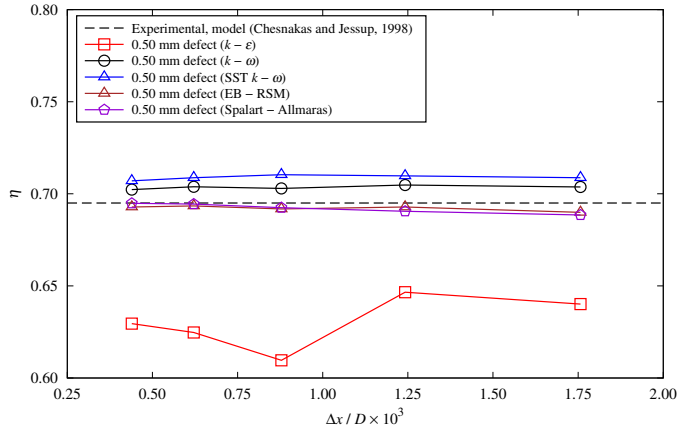

(f) Efficiency, η_0 (0.5 mm defect)

Figure 6.40: Open-water performance of the full-scale propellers with no and 0.50 mm defects at $J = 1.102$ using different turbulence models and grid sizes

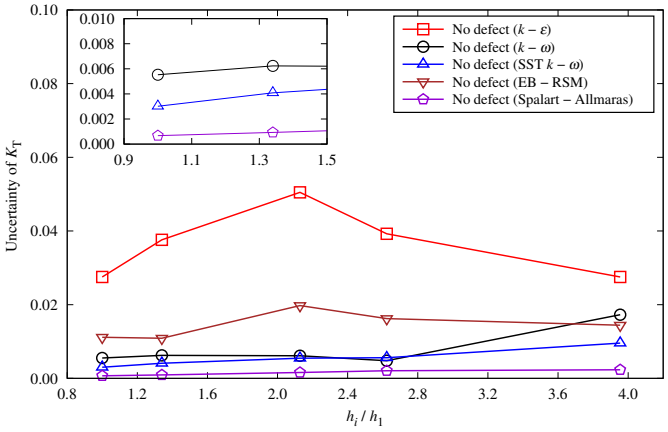

(a) Thrust coefficient, K_T (no defect)

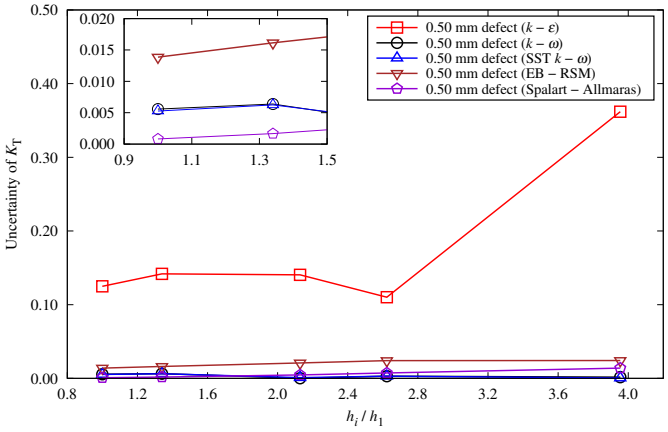

(b) Thrust coefficient, K_T (0.5 mm defect)

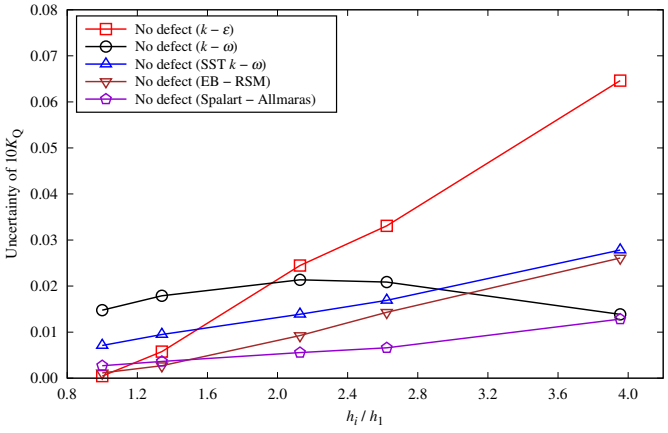

(c) Torque coefficient, K_Q (no defect)

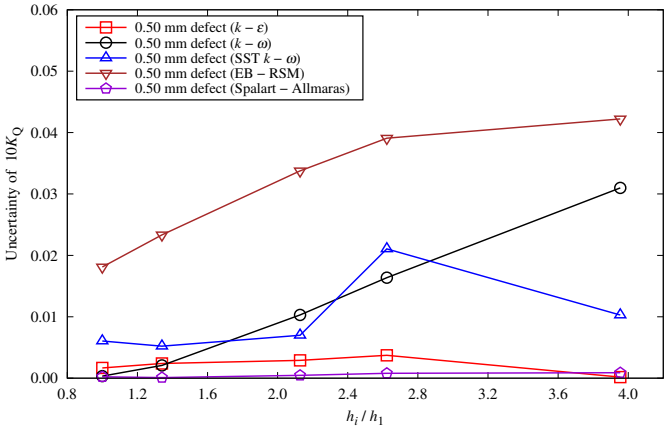

(d) Torque coefficient, K_Q (0.5 mm defect)

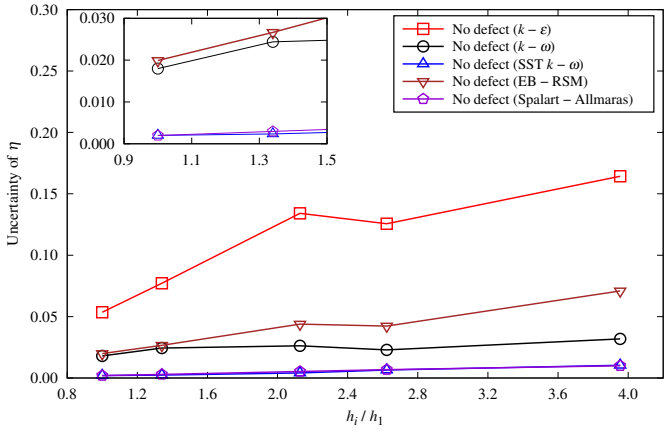

(e) Efficiency, η_0 (no defect)

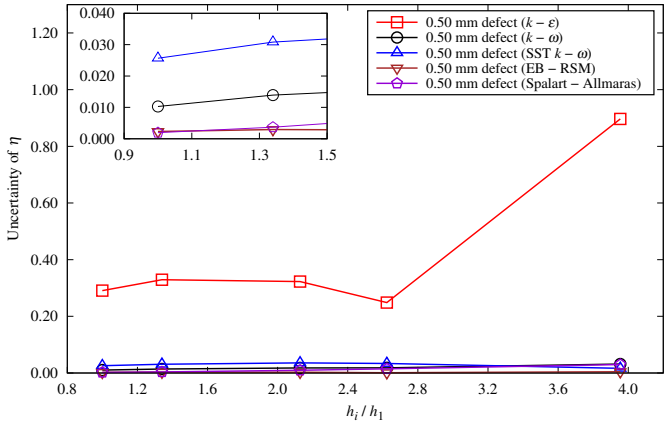

(f) Efficiency, η_0 (0.5 mm defect)

Figure 6.41: Uncertainties of predicted open-water results for the full-scale propellers with no and 0.5 mm defect at $J = 1.102$ using different turbulence models

domain, D_{sp} = 4.0, 6.0, 8.0, and 10.0 D. The radius of the rotating domain was 1.2 R, and the thickness was 0.8 D. The convergence of non-dimensional velocities across the vortex core at $X/R = 0.2386$ with respect to D_{sp} is presented in Fig. 6.32. The velocities across the vortex core at $X/R = 0.2386$ converge as the diameter of the static domain increases. As shown in Fig. 6.32, a small difference can be observed between $\theta = -0.15$ and -0.05 radians for the full-scale propeller without defect when using the smallest diameter of $D_{sp} = 4.0$ D. For the full-scale propeller with 0.50 mm defect, a slight discrepancy can be found between θ = -0.05 and $\theta = 0.05$ radians in the axial and tangential velocities with $D_{sp} = 4.0$ D, while the radial velocity shows differences in the region of $\theta \in (-0.20, -0.15)$ radians compared to the other cases. Based on these findings, it is recommended to use a diameter of $D_{sp} = 6.0$ D for the static domain in the subsequent cases.

As for the radius and thickness of the rotating domain, six cases with R_{sp} = 1.2, 1.3 and 1.4 R were examined for the full-scale propellers without defect and with 0.50 mm defect. The thickness of the rotating domain was 0.8 D. The simulations were performed with $y^+ = 1.0$ and the $k - \omega$ model. The sensitivities of the non-dimensional velocities across the vortex core at $X/R = 0.2386$ to the radius of the rotating domain, R_{rp}, for the full-scale propellers with no and 0.50 mm defects are presented in Fig. 6.33. The results indicate that the predicted axial and radial velocities are relatively insensitive to R_{rp}. Only slight oscillations can be observed in the second valley of the tangential velocity. Thus, the radius of rotating domain is recommended as $R_{sp} = 1.2$ R.

Similarly, the thickness of the rotating domain was examined to understand its impact on the simulation results. Six additional cases were simulated with three

different thickness, T_{sp} = 0.8, 1.0 and 1.2 D, for the full-scale propellers with no and 0.50 mm defects. As shown in Fig. 6.34, the non-dimensional velocities were independent of the thickness of the rotating domain. In the following studies, the thickness of the rotating domain with $T_{sp} = 0.8\ D$ was used.

The grid density on the propeller blade, especially with the boundary layer, must be sufficient so that the boundary layer can be well-predicted. To accurately resolve the flow in the boundary layer, seven values of y^+ less than 5, i.e., y^+ = 0.500, 0.707, 1.000, 1.414, 2.000, 2.828 and 4.000 were examined along with four turbulence models, $k - \varepsilon$, $k - \omega$, SST $k - \omega$ and Spalart-Allmaras. The prism layer stretching ratio was chosen as 1.2, and the gird size in terms of $\Delta x/D$ = 6.212E-4 was applied in these cases. As an example, the sensitivities of the non-dimensional velocities across the vortex core at X/R = 0.2386 to y^+ for the full-scale propellers with no and 0.50 mm defects using the SST $k - \omega$ model are shown in Fig. 6.35. The downstream velocities showed insensitivity to the value of y^+ when it was less than 4.0. Furthermore, the non-dimensional velocities across the vortex core at X/R = 0.2386 for full-scale propeller with 0.50 mm defect using different turbulence models and y^+ = 1.0 are shown in Fig. 6.36. It can be observed that the $k - \varepsilon$ model yields slight better results for the tangential velocity. The RMS errors of the other three turbulence models, i.e., $k - \omega$, SST $k - \omega$ and Spalart-Allmaras, are similar to each other. Based on the results, the value of y^+ = 1.0 was chosen for the following cases.

The effect of stretching ratio in the prism layer was investigated with SR = 1.1, 1.2, 1.3 and 1.4 for the full-scale propellers without defect and with 0.50 mm defect. The value of y^+ was set as 1.0, resulting in the first layer height of 2.103 $\times$ 10^{-6} m. The estimated thickness of the boundary layer was 1.211 $\times$ 10^{-2} m, and the numbers

of layers were 67, 39, 28 and 23 for SR = 1.1, 1.2, 1.3 and 1.4, respectively. Four turbulence models, $k-\varepsilon$, $k-\omega$, SST $k-\omega$ and Spalart-Allmaras, were applied in these simulations. For examples, Fig. 6.37 shows the sensitivity of non-dimensional velocities across the vortex core at $X/R = 0.2386$ to SR for the full-scale propeller with no and 0.50 mm defects using the $k-\omega$ model. It can be seen that the stretching ratio has no significant influence on the downstream velocity at $X/R = 0.2386$ for the full-scale propeller with 0.50 mm defect. However, for the full-scale propeller without defect, slight differences can be observed in the axial and tangential velocities between $\theta = -0.20$ and -0.10 radians when using a stretching ratio of SR = 1.4.

The non-dimensional velocities across the vortex core at $X/R = 0.2386$ with SR = 1.1 using various turbulence models are presented in Fig. 6.38. For the $k-\varepsilon$ model, the radial velocity aligns well with the predictions of other turbulence models, while smaller tangential velocity is noticeable in the tip vortex region. Furthermore, a slight larger axial velocity is observed in the predictions only with no defect. This deviation may be attributed to the large turbulence fluctuation velocity and numerical uncertainty associated with the fine grid near the wall when employing the $k-\varepsilon$ model (Salim and Cheah, 2009). The value of the prism layer stretching ratio less than 1.3 was recommended, and SR = 1.2 was used in the subsequent studies.

To examine the effect of grid size on the prediction of the downstream flow velocity, open-water and cavitation performance, convergence studies were performed using five grid resolutions in terms of $\Delta x/D$ = 1.757E-3, 1.242E-3, 8.787E-4, 6.212E-4 and 4.393E-4, along with five turbulence models, $k-\varepsilon$, $k-\omega$, SST $k-\omega$, Spalart-Allmaras and EB-RSM models. The value of y^+ was set to 1.0, and the stretching ratio of the prism layer was chosen as 1.2. In Fig. 6.39, as examples, the sensitivity

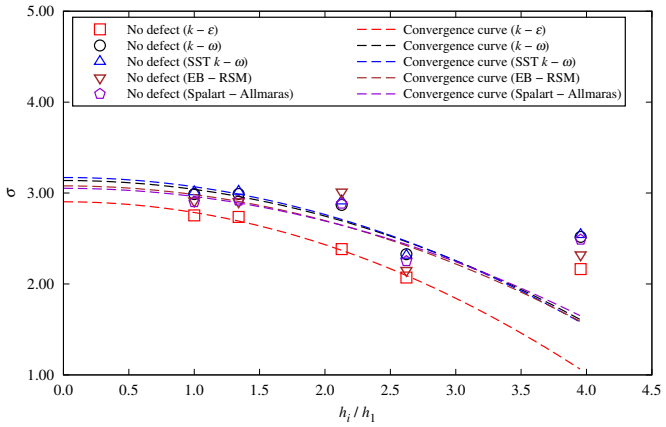

(a) No defect

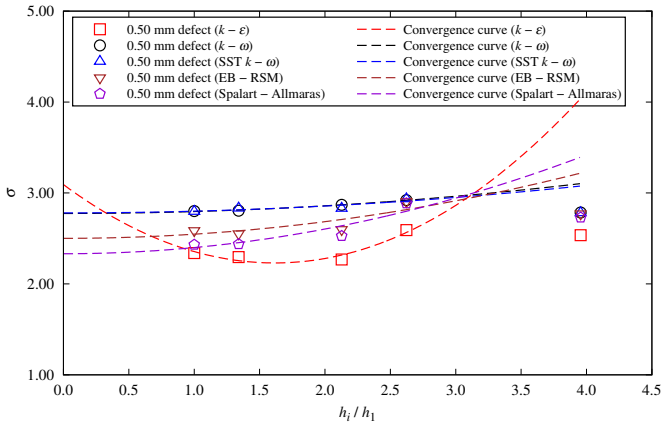

(b) 0.5 mm defect

Figure 6.42: Predicted cavitation numbers on the suction side in the tip region ($r/R \geq 0.95$) for the full-scale propellers with no and 0.5 mm defects at $J = 1.102$ using different turbulence models

of non-dimensional velocities across the vortex core at $X/R = 0.2386$ to grid size was shown by comparing results based on the SST $k - \omega$ model. It was clear that the velocities were not well predicted with the coarse grids with $\Delta x/D =$ 1.757E-3 and 1.242E-3 (the blue and red curves). However, as the grid size decreased, the numerical velocities across the vortex core at $X/R = 0.2386$ converged.

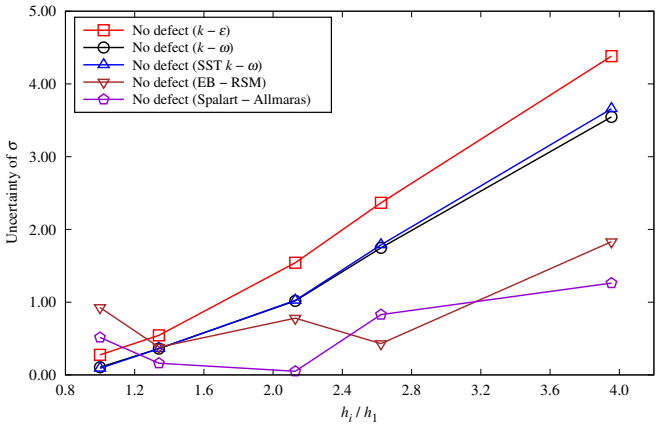

(a) No defect

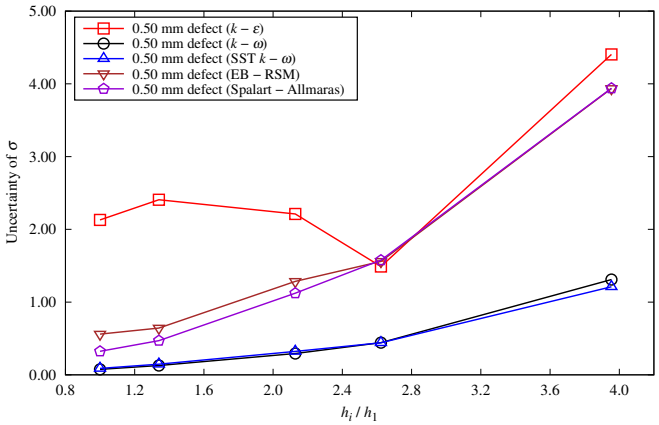

(b) 0.5 mm defect

Figure 6.43: Uncertainties of predicted cavitation numbers on the suction side in the tip region ($r/R \geq 0.95$) for the full-scale propellers with no and 0.5 mm defects at $J = 1.102$ using different turbulence models

For the open-water performance, the thrust and torque coefficients (K_{T} and K_{Q}), along with the open-water efficiency (η_0), for the full-scale propellers with no and 0.50 mm defects are shown in Fig. 6.40. These numerical solutions were obtained with the different turbulence models and grid sizes. For reference, the model experimental data of K_{T}, $10K_{\mathrm{Q}}$, and η_0 by Chesnakas and Jessup (1998) are also included in these

figures. It is important to note that the standard $k - \varepsilon$ model is primarily suitable for turbulent core flows and is coupled with wall functions to connect with solution variables in the log-law region. This model performs well when the wall-adjacent cells are in the log-law region, its accuracy is severely affected when the cells are resolved in the viscous sub-layer, as the log-law formulae cease to be valid (Salim and Cheah, 2009). On the contrary, the Spalart-Allmaras and $k - \omega$ models are designed to be applicable throughout the boundary layer, making them well-suited for fine grids when the first wall-adjacent cells are in the viscous sub-layer ($y^+ < 5$). To resolve the flow in the boundary layer, the first grid of all simulations in present work is located within the viscous sub-layer. As expected, the predicted open-water characteristics for the full-scale propellers using the $k - \omega$ and SST $k - \omega$ models showed insignificant differences, while large oscillations can be observed in the solutions with different grid resolutions using the $k - \varepsilon$ model.

To further evaluated the reliability of the predictions, uncertainties due to spatial discretization were calculated using the LSR method. The estimated exact values of open-water results, i.e.,$\Phi_0(K_\mathrm{T})$, $\Phi_0(10K_\mathrm{Q})$ and $\Phi_0(\eta_0)$, for the full-scale propellers with no and 0.50 mm defects are summarized in Table 6.17. The experimental data (Chesnakas and Jessup, 1998) of model-scale propeller was also included in the table as a reference. It can be found that the LE defect of 0.50 mm has no significant influence on the estimated exact open-water values using the $k - \omega$, SST $k - \omega$, Spalart-Allmaras and EB-RSM models.

Uncertainties of K_T, $10K_\mathrm{Q}$ and η_0 with different turbulence models and grid sizes estimated by the LSR method are presented in Fig. 6.41, in which h_i denotes the representative grid size of the i-th grid. As expected, the numerical uncertainties

decrease as the grids were refined. Significant differences can be observed in the results with the $k - \varepsilon$ model.

In terms of the cavitation performance, the cavitation numbers on the suction side in the tip region ($r/R \geq 0.95$) for the full-scale propellers with no and 0.50 mm defects using different turbulence models and grid sizes are presented in Fig. 6.42. The convergence curves based on the LSR method are also shown in the figure. It can be found that the cavitation number converged as the grid size decreased, and similar results were obtained with the $k - \omega$ and SST $k - \omega$ models. The numerical uncertainties of the cavitation numbers on the suction side in the tip region ($r/R \geq 0.95$) for the full-scale propellers with no and 0.50 mm defects using different turbulence models and grid sizes are presented in Fig. 6.43, and the corresponding estimated exact cavitation numbers, $\Phi_0(\sigma)$, are given in Table 6.17. It should be noted again that the experiments conducted by Chesnakas and Jessup (1998) were carried out using the DTMB 5168 propeller model, which did not have LE defect. Due to the scale effect and uncertainties in measurements, there are significant differences between the numerical results for the full-scale propellers and the experimental data (Chesnakas and Jessup, 1998) obtained with the model-scale propeller.

Considering both accuracy and computing efficiency, it is crucial to choose an appropriate grid size, especially in the vortex refinement zone. Based on the convergence analysis, the grid size with $\Delta x/D$ no greater than 6.212E-4 is recommended. Both the $k - \omega$ and SST $k - \omega$ models have shown good performance. Note that the $k - \omega$ model, which was recognized as the best-practice for 2-D simulations, was then used in the following simulations.

Based on the convergence studies, the best-practice settings for the full-scale pro-

Table 6.17: The estimated exact values of K_T, $10K_Q$, η_0 and σ using the LSR method

Item	Turbulence model	Estimated exact values				Experimental (model scale)			
		$\Phi_0(K_T)$	$\Phi_0(10K_Q)$	$\Phi_0(\eta_0)$	$\Phi_0(\sigma)$	K_T	$10K_Q$	η_0	σ
Full scale (no defect)	$k-\varepsilon$	0.27944	0.78755	0.62574	2.90405	0.305	0.770	0.695	2.020
	$k-\omega$	0.30408	0.74655	0.70305	3.13819	0.305	0.770	0.695	2.020
	SST $k-\omega$	0.30298	0.74634	0.71163	3.17099	0.305	0.770	0.695	2.020
	Spalart-Allmaras	0.29401	0.74009	0.69656	3.05194	0.305	0.770	0.695	2.020
	EB-RSM	0.30165	0.76163	0.69290	3.07871	0.305	0.770	0.695	2.020
Full scale (0.50 mm defect)	$k-\varepsilon$	0.31774	0.77635	0.72550	3.09263	0.305	0.770	0.695	2.020
	$k-\omega$	0.30328	0.75728	0.70158	2.77478	0.305	0.770	0.695	2.020
	SST $k-\omega$	0.30436	0.75559	0.69849	2.78077	0.305	0.770	0.695	2.020
	Spalart-Allmaras	0.29340	0.73995	0.69564	2.33176	0.305	0.770	0.695	2.020
	EB-RSM	0.30436	0.75559	0.69849	2.50110	0.305	0.770	0.695	2.020

pellers are presented in Table 6.18. In comparison to the recommended settings for the model-scale propeller, a slightly larger diameter of the static domain is recommended for the full-scale propeller. In addition, y^+ should be less than 2.0 for the model-scale propeller. However, a larger value of y^+ between 2.0 and 4.0 can be applied to full-scale propellers. The specific values used for full-scale propellers are also provided in Table 6.18.

Table 6.18: Summary of the best-practice settings for full-scale propellers

Item	Variable	Recommended setting	Value
Static domain	L_{up}/D	$\geq$ 2.0	2.0
	L_{down}/D	$\geq$ 4.0	4.0
	D_{sp}/D	$\geq$ 6.0	6.0
Rotating domain	R_{rp}/R	$\geq$ 1.2	1.2
	T_{rp}/D	$\geq$ 0.8	0.8
Mesh size	SR	[1.1, 1.3]	1.2
	y^+	[0.5, 4.0]	1.0
	$\Delta x/D$	$\leq$ 6.212E-4	6.212E-4
Turbulence model		$k - \omega$ SST $k - \omega$	$k - \omega$

6.7.2.2 Simulations for the Full-Scale Propellers with Best-Practice Settings

Using the best-practice settings provided in Table 6.18, simulations were conducted for the full-scale propellers with no defect, 0.10 mm defect, 0.25 mm defect and 0.50 mm defect at various advance ratios ranging from 0.921 to 1.205. Predicted velocities downstream, open-water performance, residuals of simulation, pressure coefficient, cavitation performance, and the reduction of cavitation inception speed, are presented and discussed in the following subsections. To offer a reference, the numerical results obtained for the model-scale propeller using the recommended settings from Table 6.12 are also included.

Downstream velocities. With the advance ratio of $J = 1.102$, the comparisons of three velocity components (V_x/U_∞, V_t/U_∞ and V_r/U_∞) for the full-scale propellers with and without LE defects at downstream section of $X/R = 0.2386$ are shown in Figs. 6.44 to 6.46. The results demonstrate that the tip vortex, wake, and blade-to-blade flow were well simulated using the present recommended best-practice settings from Table 6.18. The flow patterns for the full-scale propellers with and without leading-edge defects are similar.

In Fig. 6.44, the axial velocity was accelerated in the blade-to-blade region, with the maximum axial velocity observed in the tip vortex region. Regarding the tangential velocity at the downstream of $X/R = 0.2386$ (see Fig. 6.45), it was significantly reduced by the tip vortex. Nevertheless, due to the non-slip boundary condition applied to the propeller hub, the minimum value of V_t/U_∞ was found in the region close to the propeller hub. The tip vortex further exhibits a notable influence on the radial velocity, as shown in Fig. 6.46, resulting in a small radial velocity within the tip vortex region.

In addition, the primary velocity fields of the full-scale propellers with and without defects are given in Fig. 6.47. It also can be seen that the predicted primary velocity fields with different LE defects are visually similar to each other. As expected, the primary velocity remains relatively small in the region close to hub. The wakes are clearly visible as the curving green spokes in the plot of low primary velocity. Five tip vortices with the low primary velocity were also well captured.

For a thorough examination of the effects of the LE defects on the tip vortex structure, Fig. 6.48 present the computed non-dimensional axial, tangential and radial velocities (V_x/U_∞, V_t/U_∞ and V_r/U_∞) in the rotating frame across the tip vortex core

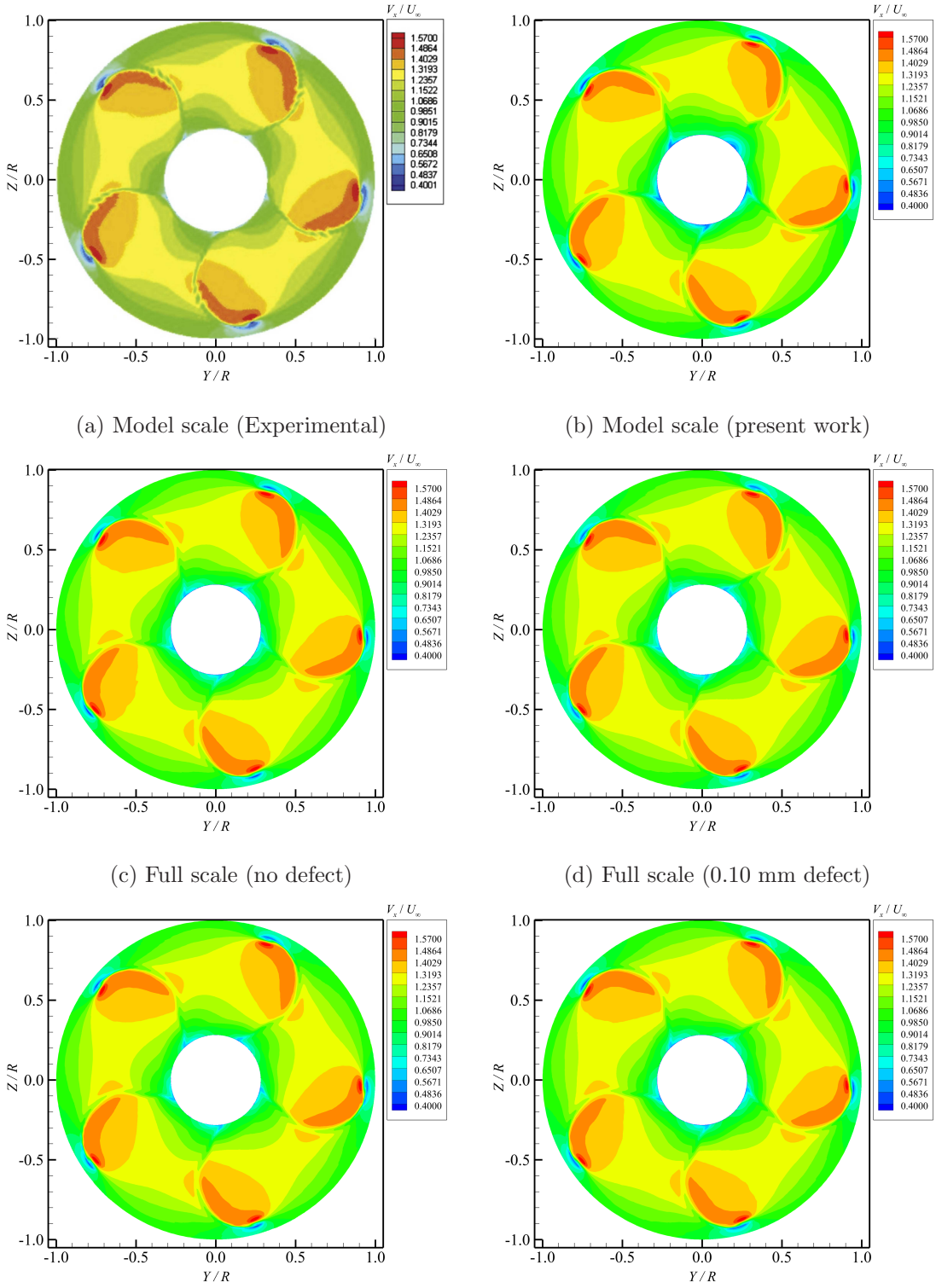

(a) Model scale (Experimental)

(b) Model scale (present work)

(c) Full scale (no defect)

(d) Full scale (0.10 mm defect)

(e) Full scale (0.25 mm defect)

(f) Full scale (0.50 mm defect)

Figure 6.44: Comparison of non-dimensional axial velocity, V_x/U_∞, contour at $X/R = 0.2386$ and $J = 1.102$ for full-scale propellers with and without defects

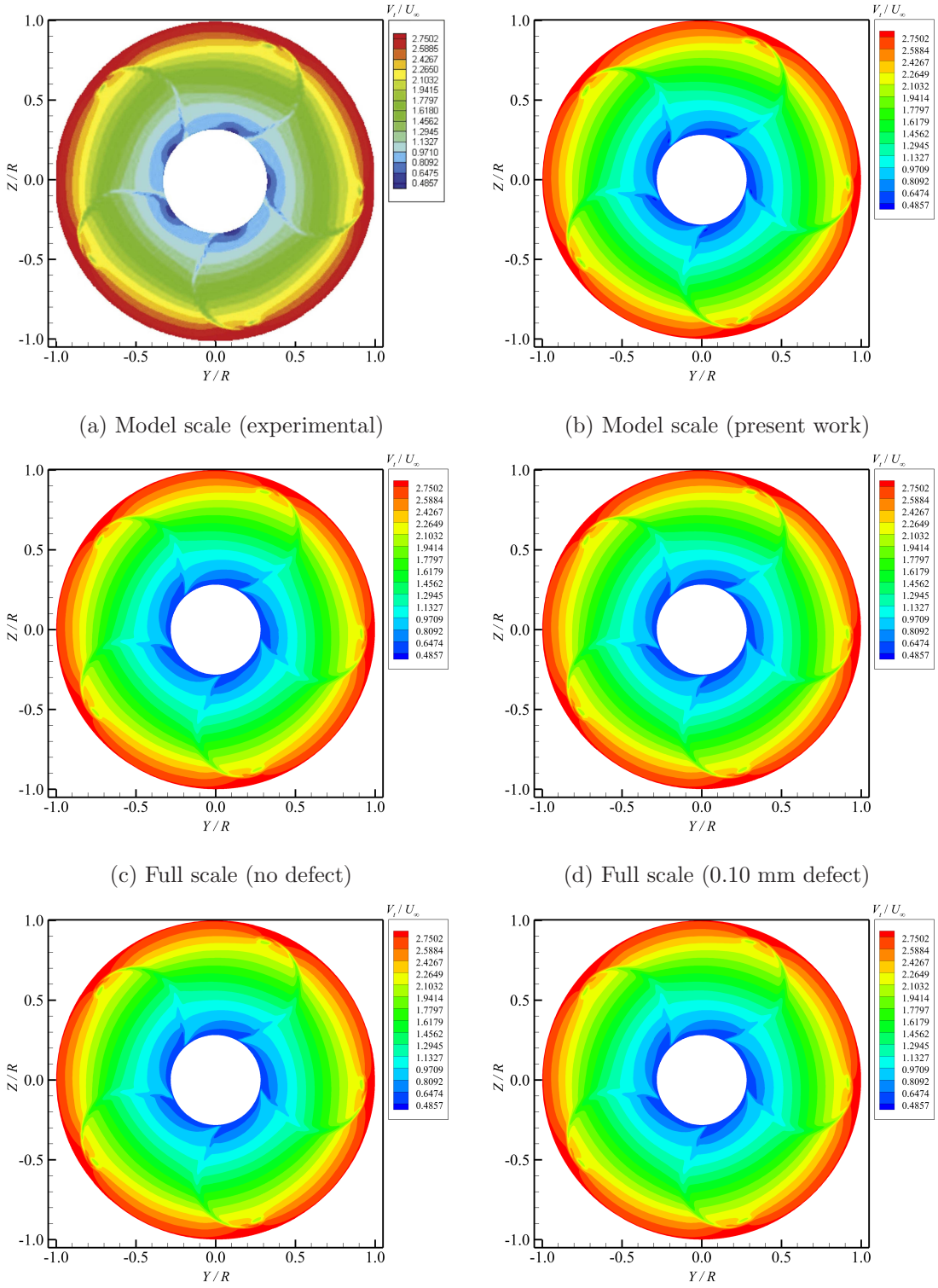

(a) Model scale (experimental)

(b) Model scale (present work)

(c) Full scale (no defect)

(d) Full scale (0.10 mm defect)

(e) Full scale (0.25 mm defect)

(f) Full scale (0.50 mm defect)

Figure 6.45: Comparison of non-dimensional tangential velocity, V_t/U_∞, contour at $X/R = 0.2386$ and $J = 1.102$ for the full-scale propellers with and without defects

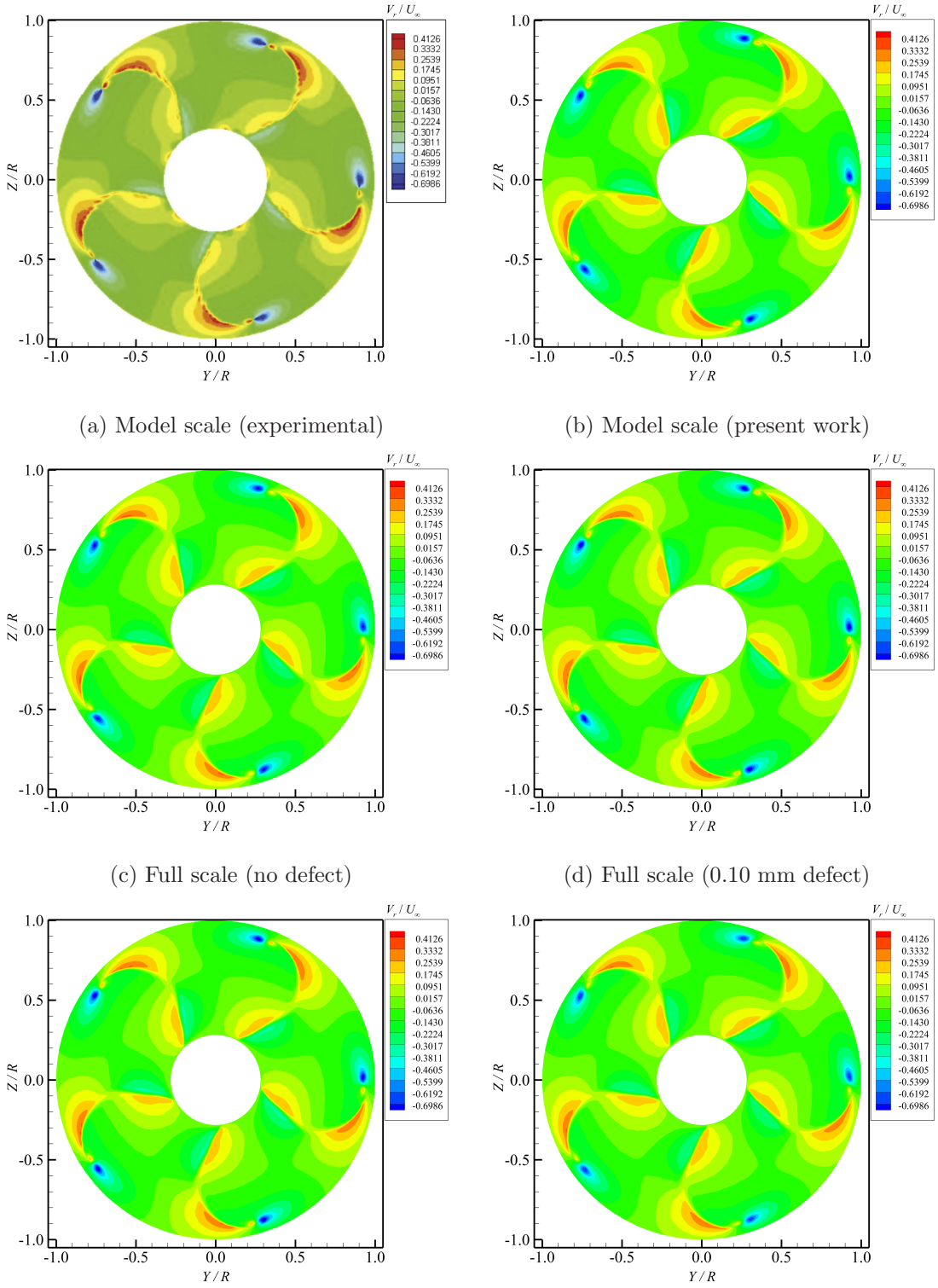

(a) Model scale (experimental)

(b) Model scale (present work)

(c) Full scale (no defect)

(d) Full scale (0.10 mm defect)

(e) Full scale (0.25 mm defect)

(f) Full scale (0.50 mm defect)

Figure 6.46: Comparison of non-dimensional radial velocity, V_r/U_∞, contour at $X/R = 0.2386$ and $J = 1.102$ for the full-scale propellers with and without defects

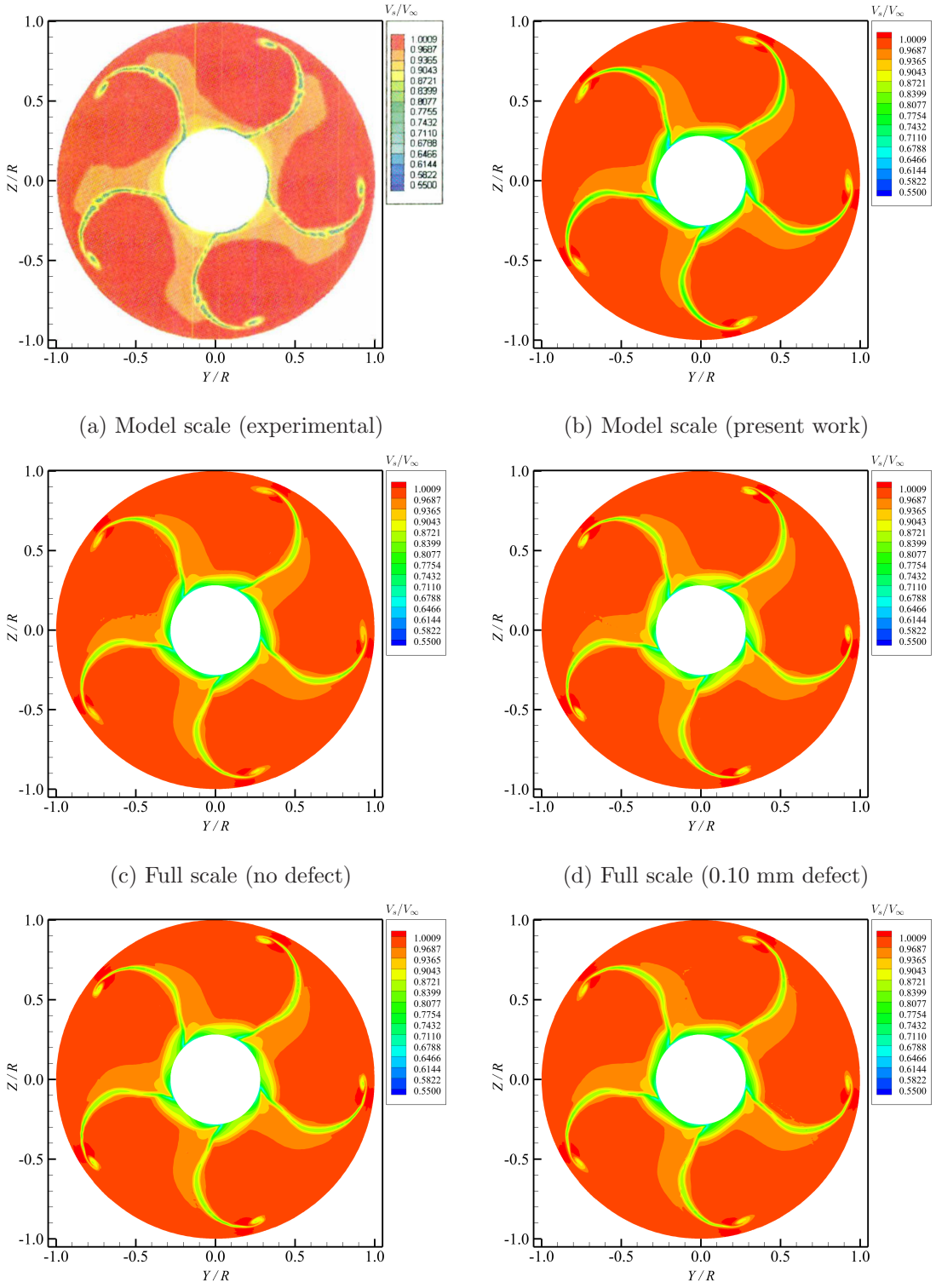

(a) Model scale (experimental)

(b) Model scale (present work)

(c) Full scale (no defect)

(d) Full scale (0.10 mm defect)

(e) Full scale (0.25 mm defect)

(f) Full scale (0.50 mm defect)

Figure 6.47: Comparison of non-dimensional primary velocity, V_s/V_∞, contour at $X/R = 0.2386$ and $J = 1.102$ for the propeller model and full-scale propellers with and without defects

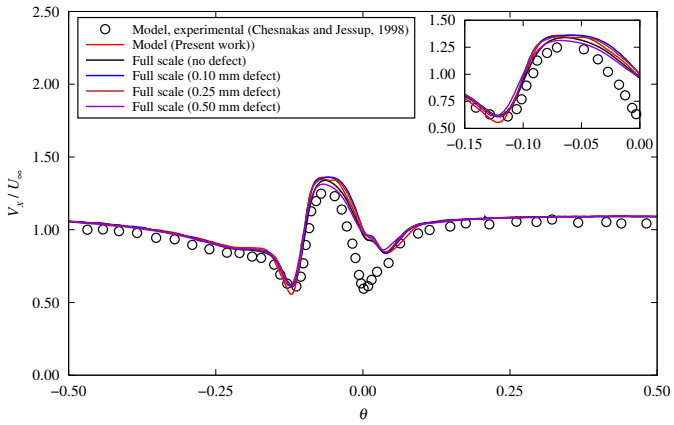

(a) V_x/U_∞ $(X/R = 0.1756)$

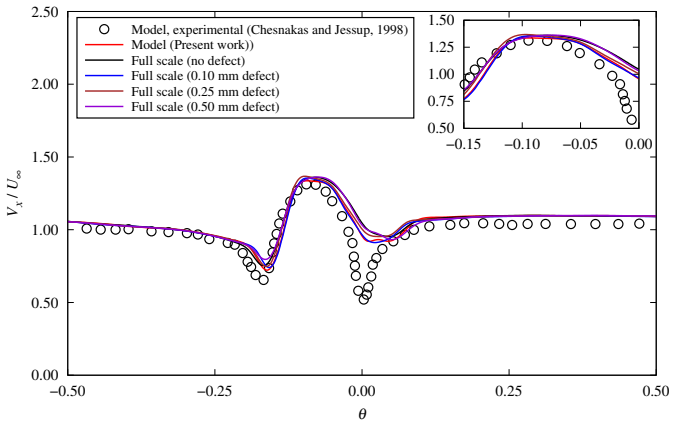

(b) V_x/U_∞ $(X/R = 0.2386)$

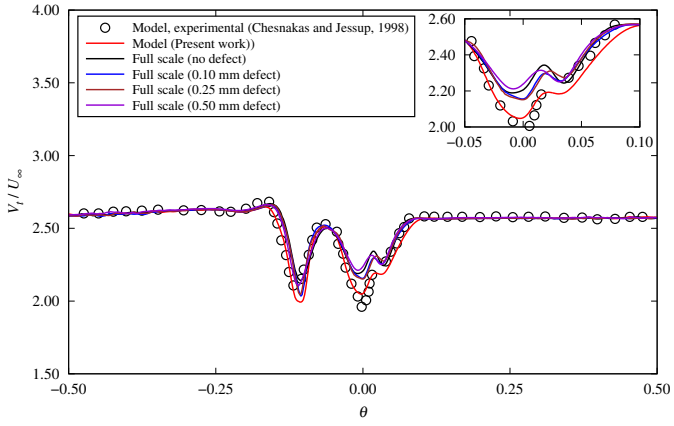

(c) V_t/U_∞ $(X/R = 0.1756)$

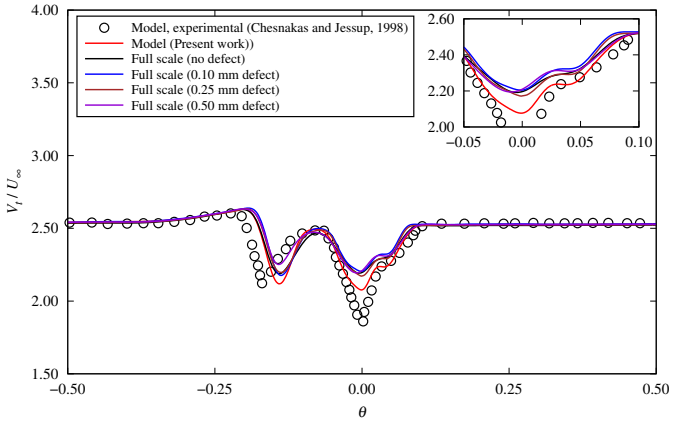

(d) V_t/U_∞ $(X/R = 0.2386)$

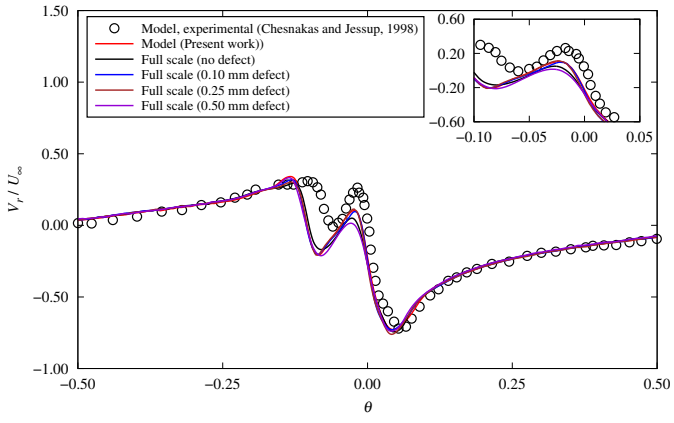

(e) V_r/U_∞ $(X/R = 0.1756)$

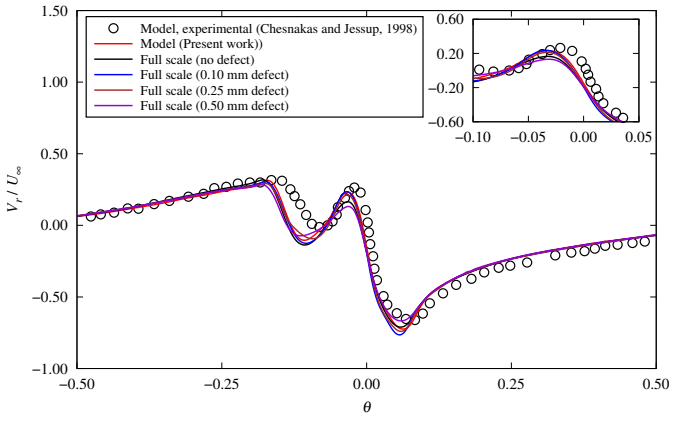

(f) V_r/U_∞ $(X/R = 0.2386)$

Figure 6.48: Predicted V_x/U_∞, V_t/U_∞ and V_r/U_∞ across the cortex core at $X/R = 0.1756$ and 0.2386 for $J = 1.102$ using the best-practice settings

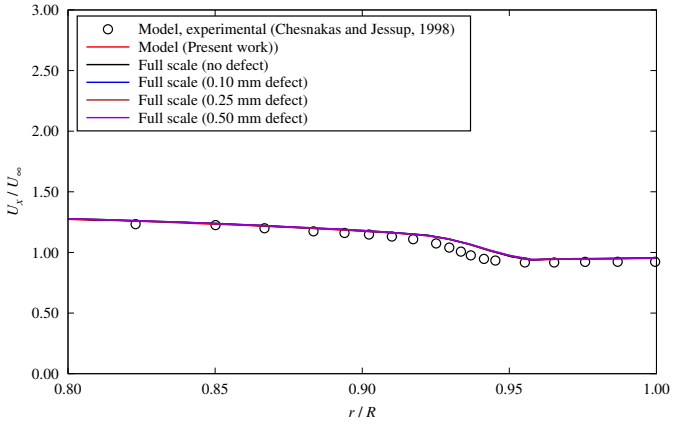

(a) Non-dimensional axial velocity, U_x/U_∞

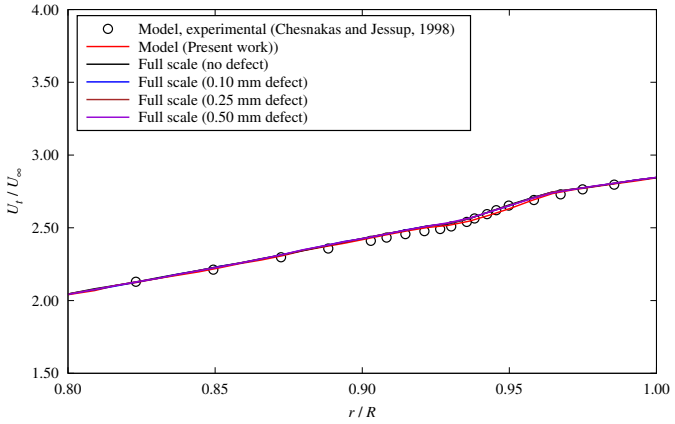

(b) Non-dimensional tangential velocity, U_t/U_∞

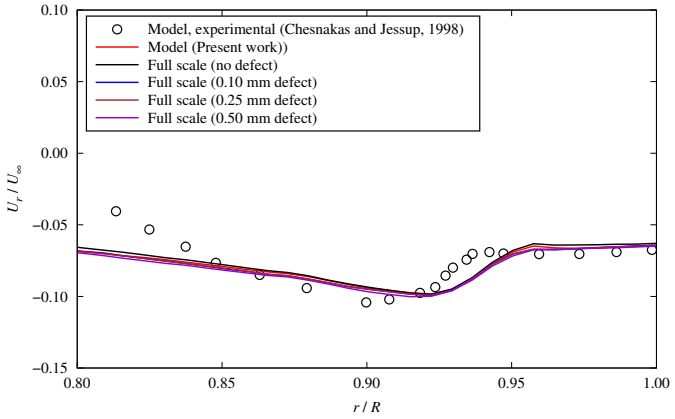

(c) Non-dimensional radial velocity, U_r/U_∞

Figure 6.49: Predicted circumferentially averaged U_x/U_∞, U_t/U_∞ and U_r/U_∞ at $X/R = 0.1756$ and $J = 1.102$ using the best-practice settings

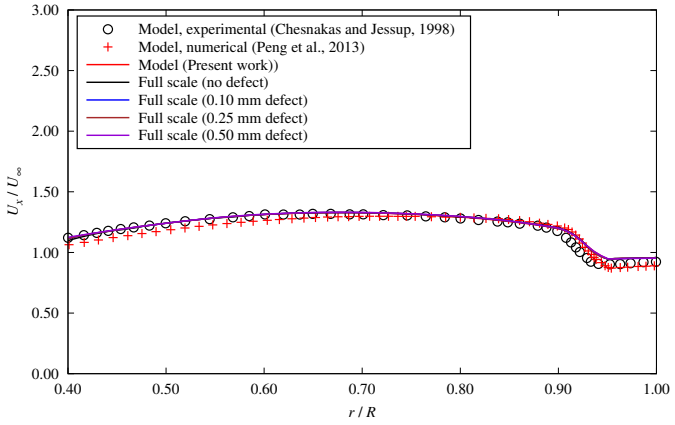

(a) Non-dimensional axial velocity, U_x/U_∞

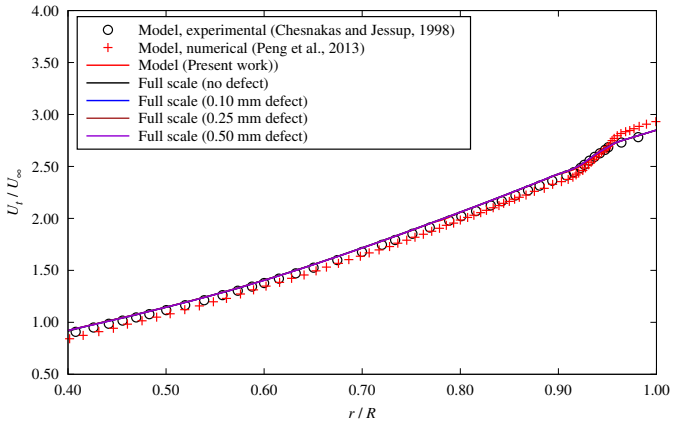

(b) Non-dimensional tangential velocity, U_t/U_∞

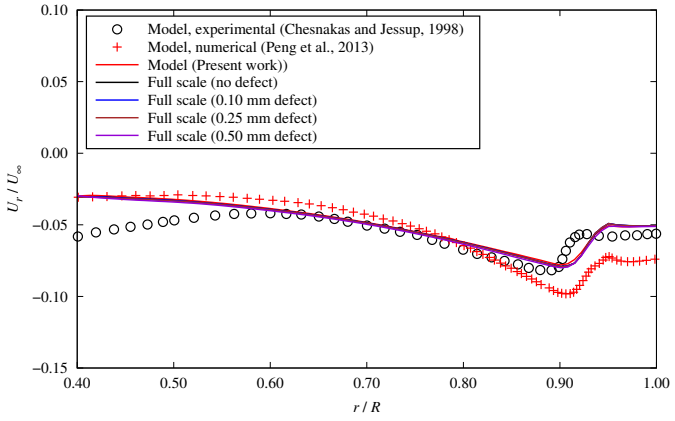

(c) Non-dimensional radial velocity, U_r/U_∞

Figure 6.50: Predicted circumferentially averaged U_x/U_∞, U_t/U_∞ and U_r/U_∞ at $X/R = 0.2386$ and $J = 1.102$ using the best-practice settings

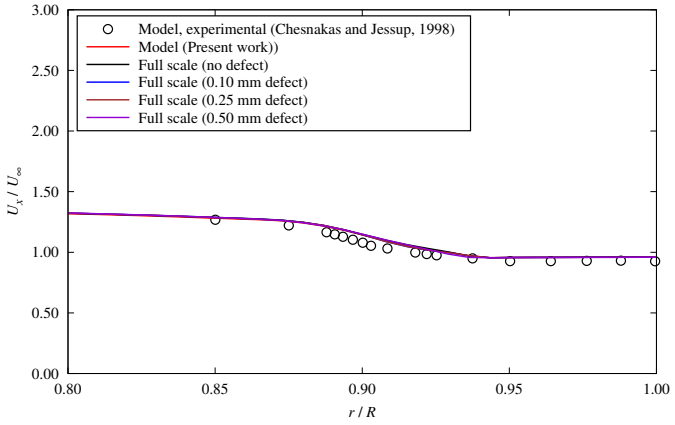

(a) Non-dimensional axial velocity, U_x/U_∞

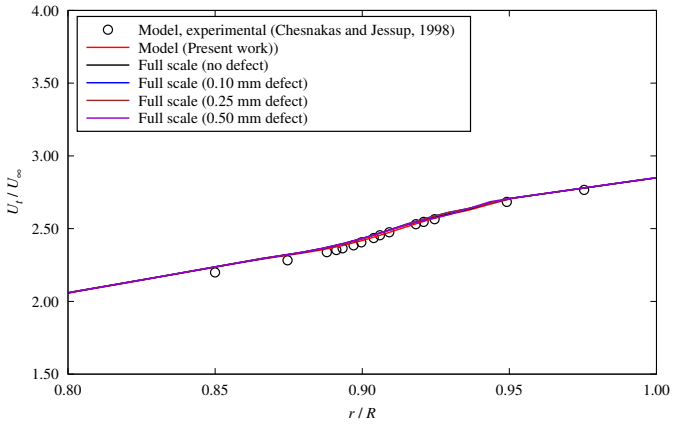

(b) Non-dimensional tangential velocity, U_t/U_∞

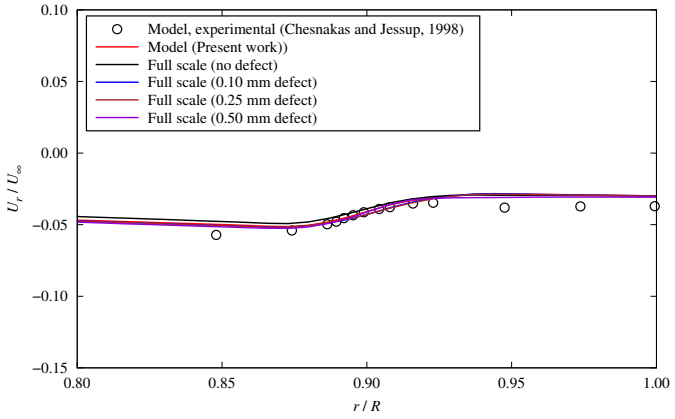

(c) Non-dimensional radial velocity, U_r/U_∞

Figure 6.51: Predicted circumferentially averaged U_x/U_∞, U_t/U_∞ and U_r/U_∞ at $X/R = 0.3963$ and $J = 1.102$ using the best-practice settings

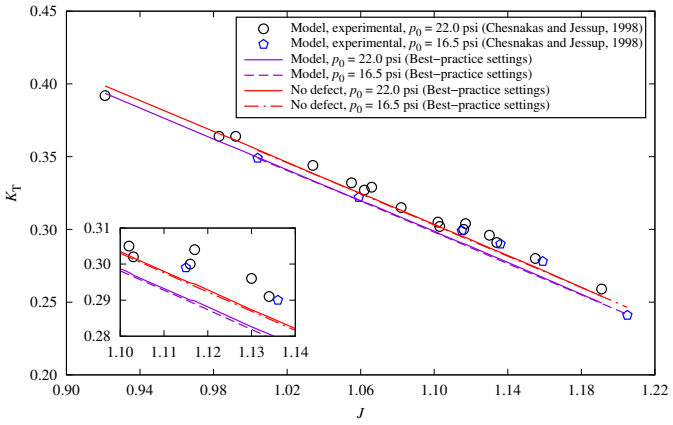

(a) Thrust coefficient, K_T (no defect)

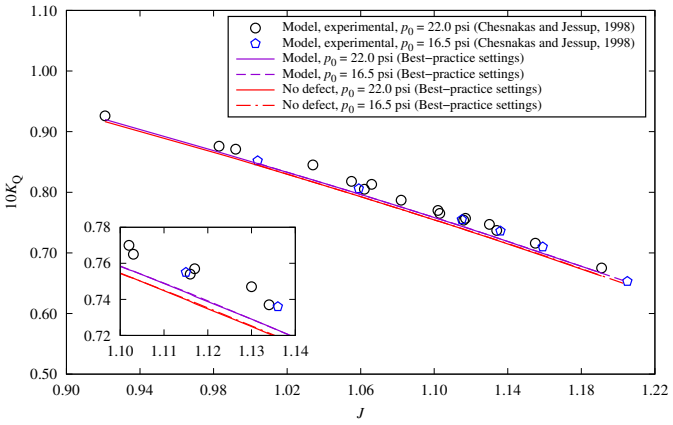

(b) Torque coefficient, K_Q (no defect)

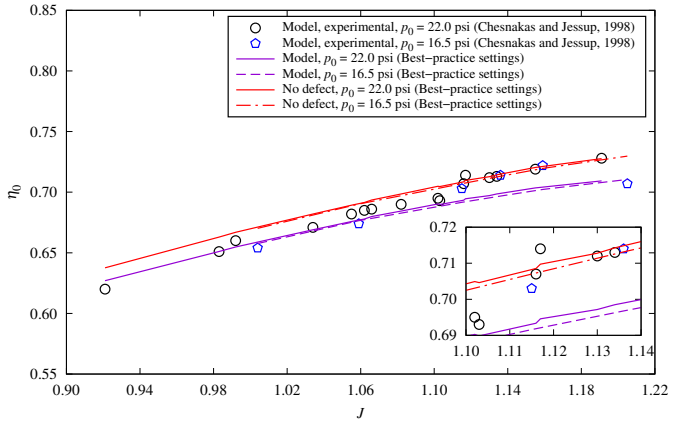

(c) Efficiency, η_0 (no defect)

Figure 6.52: Predicted open-water performance of the propeller model and full-scale propeller with no defect at different static pressures using the best-practice settings

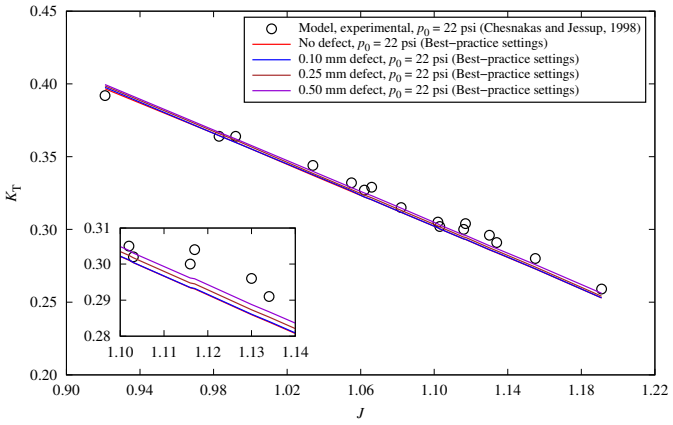

(a) Thrust coefficient, K_T

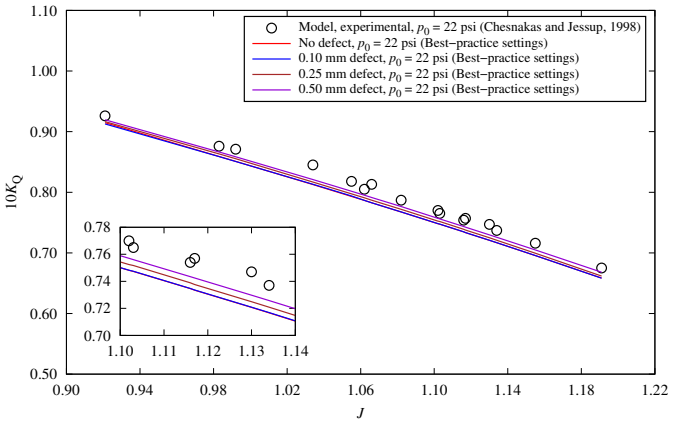

(b) Torque coefficient, K_Q

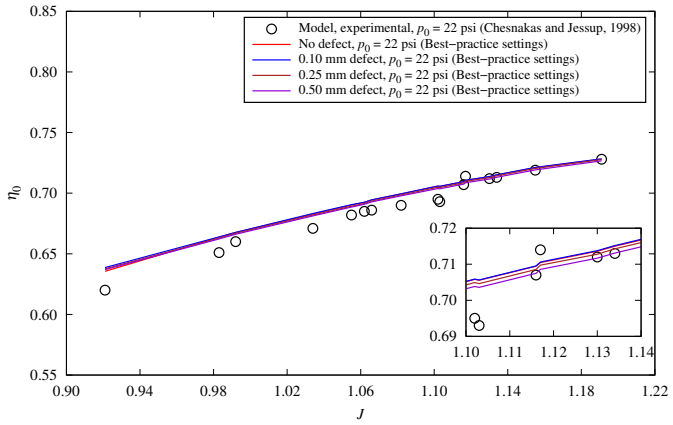

(c) Efficiency, η_0

Figure 6.53: Predicted open-water performance of the full-scale propellers without and with defects at $p_0 = 22.0$ psi using the best-practice settings

at two downstream sections, $X/R = 0.1756$ and 0.2386. Overall, the results showed that the LE defects had no significant influence on the velocities across the tip vortex core.

The flow outside the tip vortex region was evaluated by examining the circumferentially averaged axial, tangential, and radial velocities (U_x/U_∞, U_t/U_∞, and U_r/U_∞) in the stationary frame. The predicted circumferentially averaged U_x/U_∞, U_t/U_∞ and U_r/U_∞ at different sections of $X/R = 0.1756$, 0.2386 and 0.3963 are shown in Figs. 6.49 to 6.51. It can be observed that there was no significant difference between the predictions for the propeller model and full-scale propellers.

Open-water performance. The open-water performance of the full-scale propellers with and without LE defects was further examined at various advance ratios ranging from 0.921 to 1.205. Two static pressures, $p_0 = 16.5$ psi and 22.0 psi, were considered using the recommended settings. The predicted thrust coefficients (K_T), torque coefficients (K_Q), and open-water efficiencies (η_0) for the propeller model and the full-scale propeller without defects at different static pressures are shown in Fig. 6.52. The results indicate that the influence of static pressure on the open-water performance is insignificant. It is also observed that the numerical results for the propeller model are slightly smaller than those for the full-scale propeller without LE defect. The numerical results of the full-scale propellers without and with LE defects at $p_0 = 22.0$ psi are presented in Fig. 6.53. The results show that there is no significant difference in open-water performance for the propellers with and without LE defects at the range of advance ratios.

As an example, Fig. 6.54 shows the iteration histories of the thrust and torque coefficients, K_T and K_Q, for the full-scale propellers with and without defects at

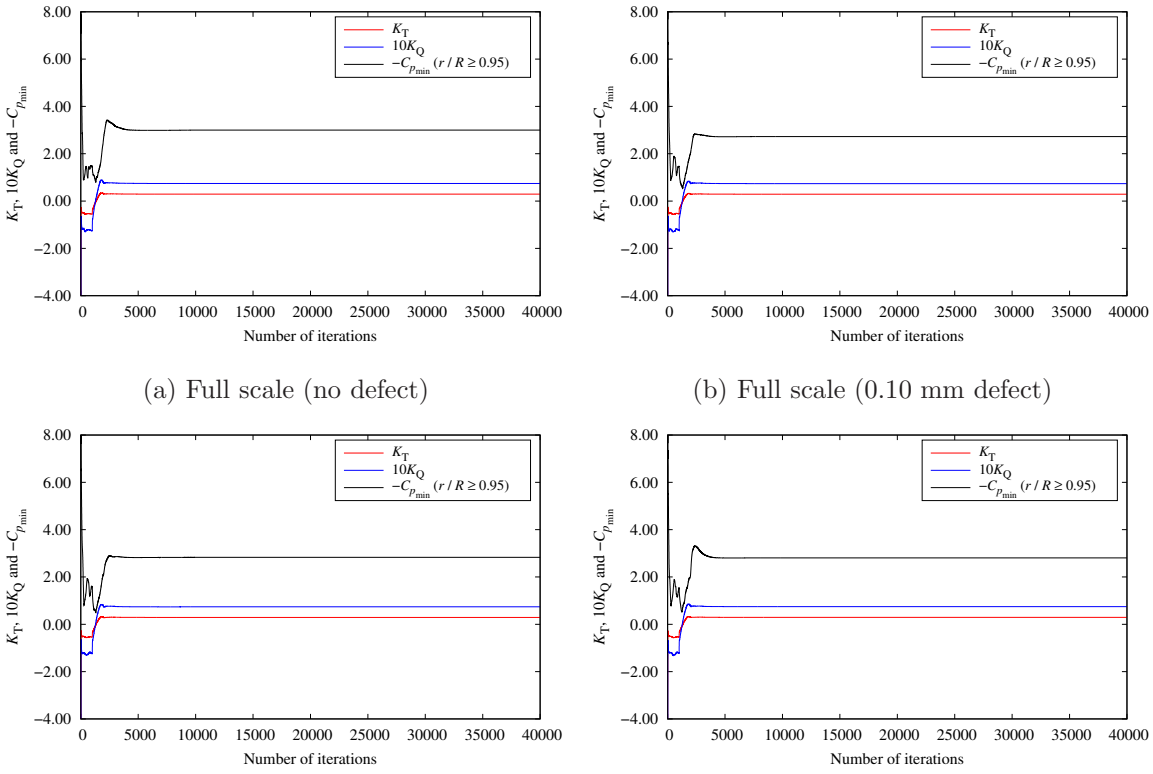

(a) Full scale (no defect)

(b) Full scale (0.10 mm defect)

(c) Full scale (0.25 mm defect)

(d) Full scale (0.50 mm defect)

Figure 6.54: Iteration histories of the thrust coefficient (K_T), torque coefficient (K_Q) and negative minimum pressure coefficient ($-C_{p_{min}}$) at $J = 1.102$

$J = 1.102$. The negative minimum pressure coefficient ($-C_{p_{min}}$) on suction side in tip region ($r/R \geq 0.95$) is also included. The figures show that the simulations reach convergence after approximately 10,000 iterations. Table 6.19 presents the final converged results of K_T, $10K_Q$, and $-C_{p_{min}}$, along with the corresponding changes in the last two iterations. It can be observed that all the changes are smaller than 10^{-4}, indicating that the convergence criteria is satisfied.

Residuals. The normalized root mean squared values of residuals for all cells are used to monitor the behavior of the solvers during each iteration. Figure 6.55 shows

Table 6.19: The thrust coefficient (K_{T}), torque coefficient (K_{Q}) and negative minimum pressure coefficient ($-C_{p_{\mathrm{min}}}$) on the suction side in tip region for the full-scale propellers with and without defects at $J = 1.102$

Item	No defect	0.1 mm defect	0.25 mm defect	0.5 mm defect
K_{T}	0.30228	0.30230	0.30241	0.30379
$10K_{\mathrm{Q}}$	0.74818	0.74827	0.75243	0.75702
$-C_{p_{\mathrm{min}}}$	2.86044	2.82213	2.82495	2.83143
Change in K_{T} between the last two iterations	7.1×10^{-8}	3.6×10^{-8}	3.0×10^{-8}	2.5×10^{-8}
Change in $10K_{\mathrm{Q}}$ between the last two iterations	1.3×10^{-7}	5.9×10^{-8}	5.3×10^{-8}	3.3×10^{-8}
Change in $-C_{p_{\mathrm{min}}}$ between the last two iterations	3.3×10^{-6}	1.4×10^{-6}	1.2×10^{-5}	1.1×10^{-6}

the residuals of simulations for the full-scale propellers with no defect, 0.10 mm defect, 0.25 mm defect, and 0.50 mm defect at $J = 1.102$ as an example. As seen in the figures, there is a three orders of magnitude reduction in all residuals except for that of "X momentum". It should be noted that while the residuals are indicative of convergence, they are not the only convergence criteria employed in this study, as the initial values can have a significant influence on the residuals.

Cavitation performance. Figure 6.56 shows the comparison of cavitation numbers in the tip region ($r/R \geq 0.95$) on the suction side for the propeller model and full-scale propeller with no defect at two static pressures, $p_0 = 16.5$ and 22.0 psi.

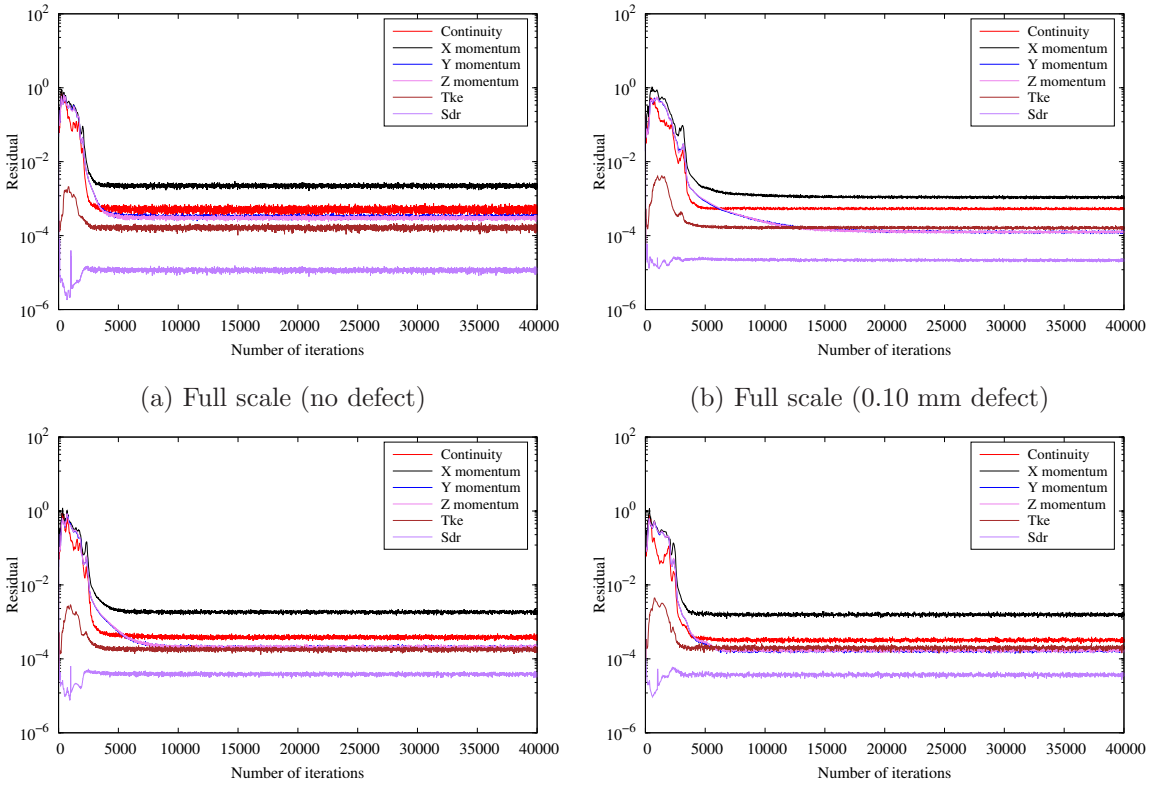

(a) Full scale (no defect)

(b) Full scale (0.10 mm defect)

(c) Full scale (0.25 mm defect)

(d) Full scale (0.50 mm defect)

Figure 6.55: Residuals of simulations for the full-scale propellers with and without defects at $J = 1.102$ using the best-practice settings

Slight differences are seen at two static pressures for the predicted cavitation numbers in the tip region on the suction side. The cavitation numbers for the full-scale propeller without defect are generally greater than those for the propeller model. As shown in Figs. 6.57 and 6.58, the results indicate that the 0.50 mm LE defect leads to an increase in cavitation numbers in the tip region, while there are no significant differences observed between the cases of no, 0.10 mm and 0.25 mm defects.

The cavitation numbers on the blade sections of $r/R \in [0.5, 0.9]$ for the full-scale propellers without and with defects are present in Fig. 6.59. As expected, similar

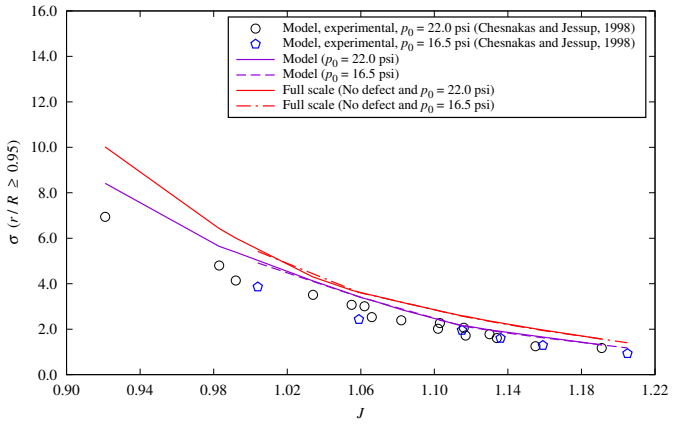

Figure 6.56: Cavitation numbers in the tip region ($r/R \geq 0.95$) on the suction side with difference static pressures

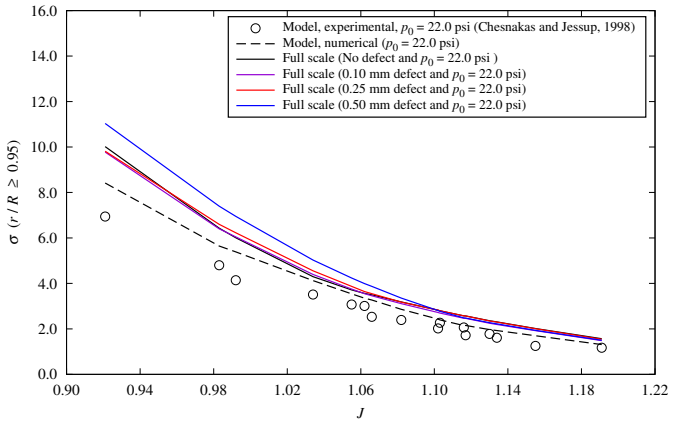

Figure 6.57: Cavitation numbers in the tip region ($r/R \geq 0.95$) on the suction side for the full-scale propellers without and with defects at $p_0 = 22.0$ psi

numerical results were obtained with different static pressures. Significant differences can be found between the full-scale propellers without defect and with 0.50 mm defect and the cavitation number decreases as the size of the defect decreases when J is smaller than 1.0.

Effect of LE defect on cavitation inception speed. Based on the predicted

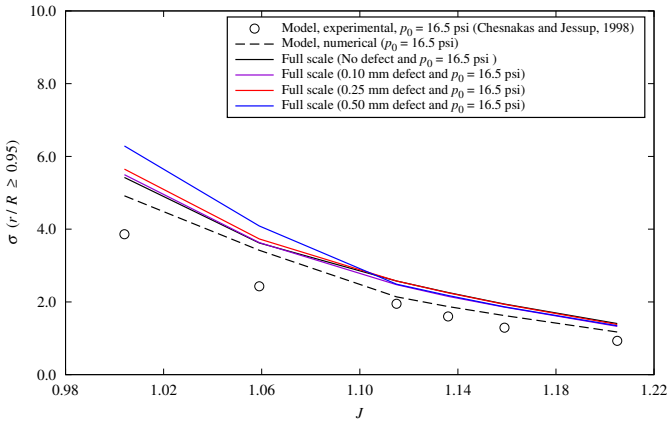

Figure 6.58: Cavitation numbers in the tip region ($r/R \geq 0.95$) on the suction side for the full-scale propellers without and with defects at $p_0 = 16.5$ psi

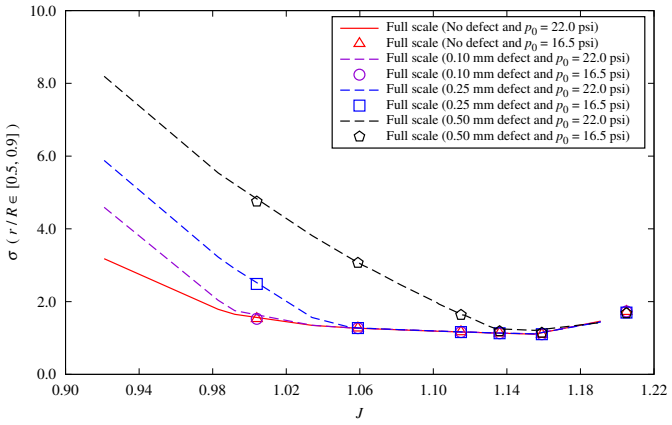

Figure 6.59: Cavitation numbers on the blade sections of $r/R \in [0.5, 0.9]$ for the full-scale propellers without and with defects

cavitation numbers shown in Fig. 6.59, Fig. 6.60 presents the comparison of the reduction percentages in cavitation inception speed on the blade sections of $r/R \in [0.5, 0.9]$ for the full-scale propellers with LE defects. The cavitation inception speed reduction ratios (ISR) are further provided in Table 6.20. From the predicted cavitation numbers and reductions in cavitation inception speed, it can be seen that the effect

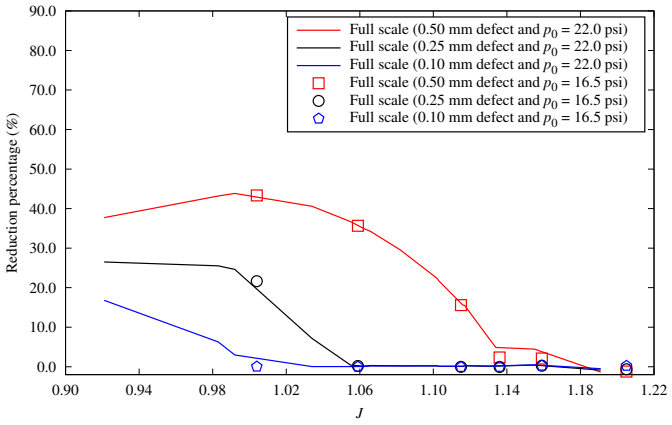

Figure 6.60: Cavitation inception speed reduction ratios (ISR) on the blade sections of $r/R \in [0.5, 0.9]$ for the full-scale propellers without and with defects

of LE defect is obvious on the blade sections of $r/R \in [0.5, 0.9]$.

For the full-scale propeller with 0.50 mm defect, the reduction in inception speed can reach to 43.83% at the advance ratio of $J = 0.992$ and at the static pressure of 22.0 psi. Within the advance ratio ranging from 0.921 to 1.034, the reduction increases with the size of LE defect. In summary, the LE defects significantly reduce the cavitation inception speeds at the investigated advance ratios. The maximum ISR is similar to that in the 2-D studies (Jin et al., 2020).

Pressure. The pressure distributions on the pressure side of the propeller at $J = 1.102$ are presented in Fig. 6.61. The numerical results of the propeller model by Hsiao and Pauley (1999). It can be observed that there is no significant difference in the results for the propeller model and the full-scale propellers. It can be observed that there is no significant difference in the results for the full-scale propellers with and without LE defects. The discrepancies between present results and the numerical model solutions from Hsiao and Pauley (1999), especially in the regions near the shaft

Table 6.20: Calculation details for the cavitation inception speed reduction ratios on the blade sections of $r/R \in [0.5, 0.9]$

p_0	J	$-C_{p_{\min}}$				Percentage reduction in inception speed (%)		
		No defect	0.50 mm defect	0.25 mm defect	0.10 mm defect	0.50 mm defect	0.25 mm defect	0.10 mm defect
22.0	0.921	3.17838	8.19507	5.88114	4.59189	37.72	26.49	16.80
	0.983	1.78741	5.53839	3.22336	2.03551	43.19	25.53	6.29
	0.992	1.64943	5.22728	2.90312	1.75188	43.83	24.62	2.97
	1.034	1.34725	3.81668	1.56310	1.34803	40.59	7.16	0.03
	1.055	1.27752	3.18967	1.28789	1.27850	36.71	0.40	0.04
	1.062	1.26266	2.98799	1.26695	1.26421	34.99	0.17	0.06
	1.066	1.25477	2.89689	1.26262	1.25959	34.19	0.31	0.19
	1.082	1.22304	2.46517	1.22898	1.22746	29.56	0.24	0.18
	1.102	1.18672	1.96892	1.19221	1.19182	22.36	0.23	0.21
	1.103	1.18463	1.93204	1.18753	1.18732	21.70	0.12	0.11
	1.116	1.16256	1.63286	1.16493	1.16578	15.62	0.10	0.14
	1.117	1.16137	1.62719	1.16694	1.16781	15.52	0.24	0.28
	1.130	1.14024	1.32749	1.14279	1.14437	7.32	0.11	0.18
	1.134	1.13419	1.25330	1.13755	1.13911	4.87	0.15	0.22
	1.155	1.10358	1.20934	1.11287	1.11441	4.47	0.42	0.49
	1.191	1.46267	1.42410	1.43789	1.44850	-1.35	-0.86	-0.49
16.5	1.004	1.52571	4.75178	2.48501	1.52730	43.34	21.64	0.05
	1.059	1.26878	3.06530	1.27329	1.26906	35.66	0.18	0.01
	1.115	1.16352	1.63348	1.16285	1.16235	15.60	-0.03	-0.05
	1.136	1.13031	1.18548	1.12924	1.12960	2.35	-0.05	-0.03
	1.159	1.09709	1.14435	1.10291	1.10322	2.09	0.26	0.28
	1.205	1.72058	1.67890	1.69874	1.72885	-1.23	-0.64	0.24

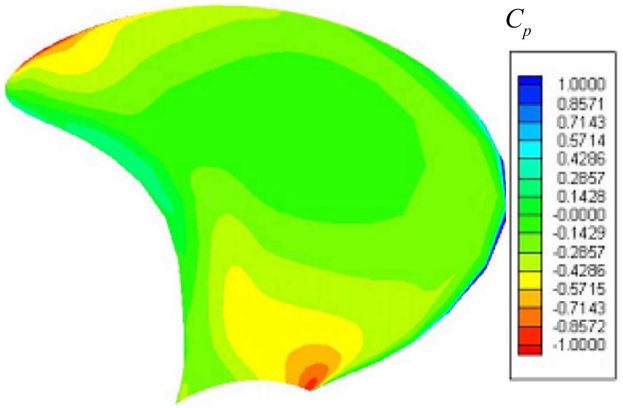

(a) Model scale (Hsiao and Pauley, 1999)

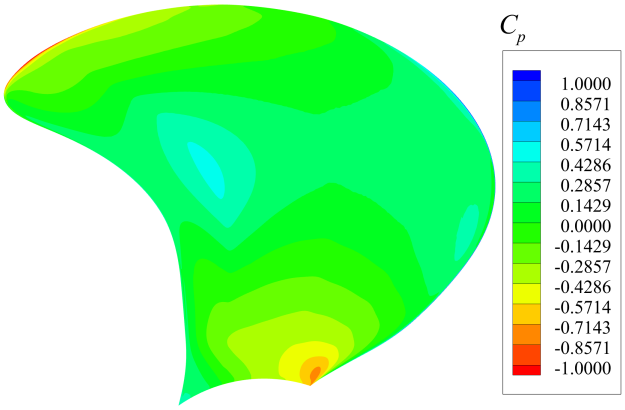

(b) Model scale (present work)

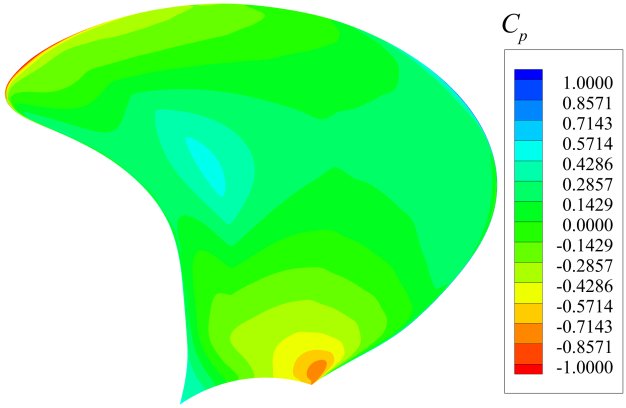

(c) Full scale (no defect)

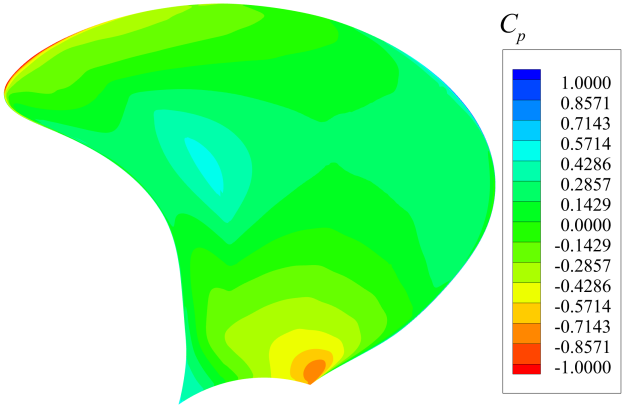

(d) Full scale (0.10 mm defect)

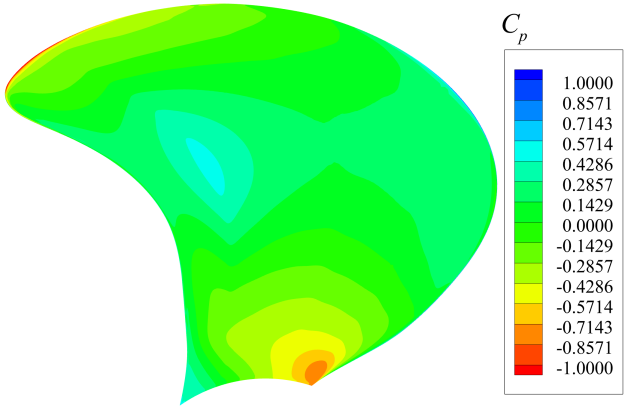

(e) Full scale (0.25 mm defect)

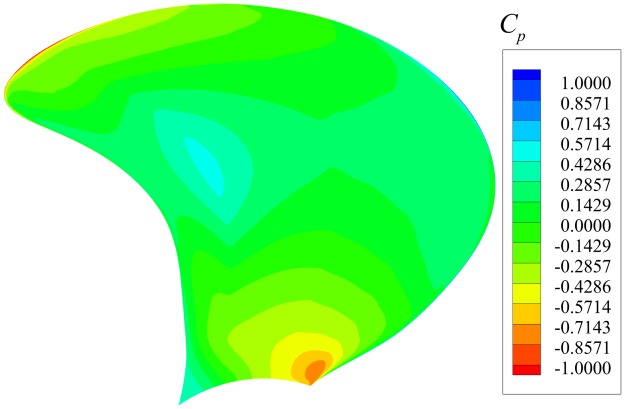

(f) Full scale (0.50 mm defect)

Figure 6.61: Comparison of C_p on the pressure side for the full-scale propellers without and with defects at $J = 1.102$

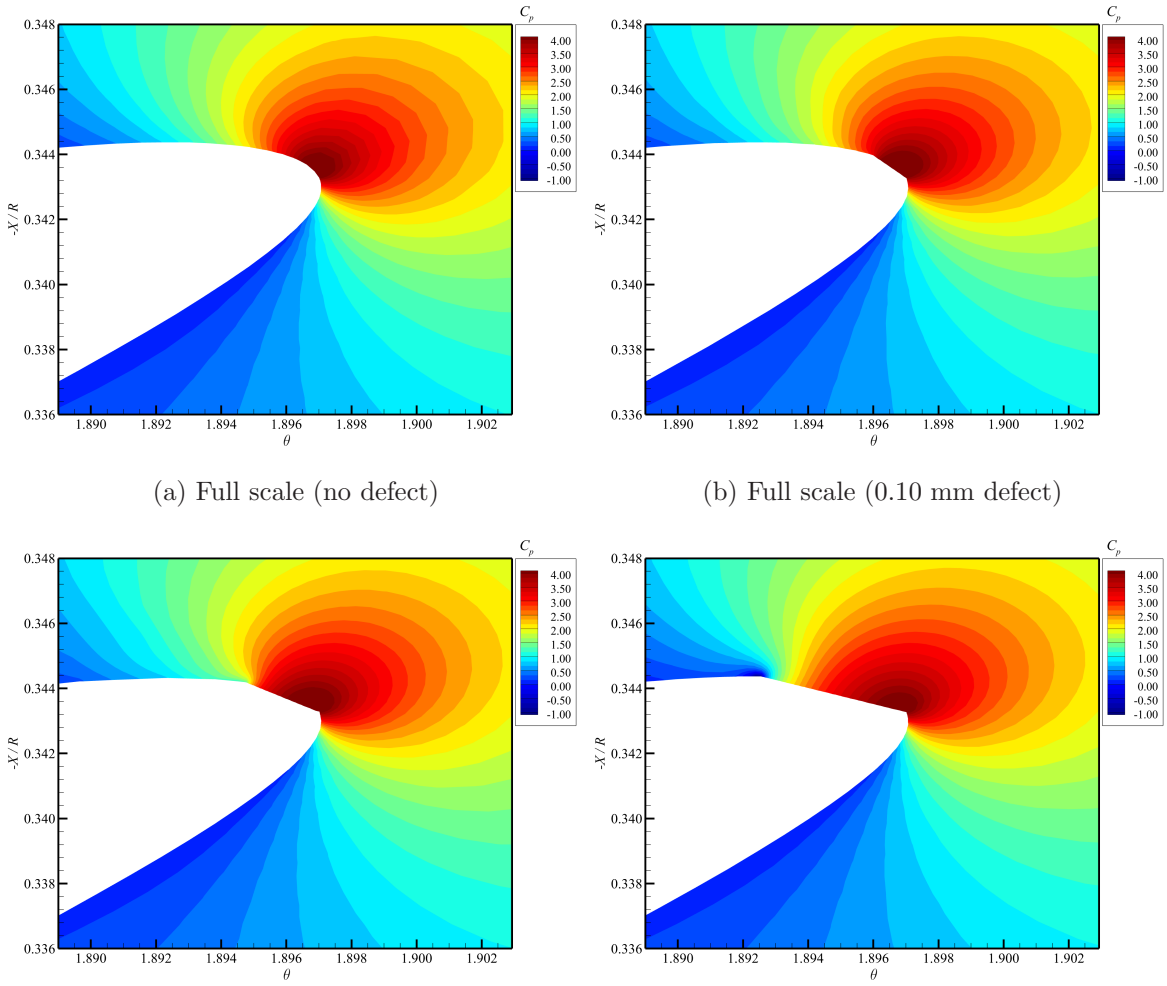

(a) Full scale (no defect)

(b) Full scale (0.10 mm defect)

(c) Full scale (0.25 mm defect)

(d) Full scale (0.50 mm defect)

Figure 6.62: Comparison of C_p close to the leading-edge on the section of $r = 0.70\ R$ for the propeller model and full-scale propellers without and with defects at $J = 1.102$

and tip, are likely due to the cap used in present work and the application of different turbulence models.

As an example, Figure 6.62 shows the pressure contours on the section of $r/R = 0.70$, near the leading-edge of the 5th blade, for the full-scale propellers with and without defects at $J = 1.102$. The maximum pressure was observed in the LE region. It is

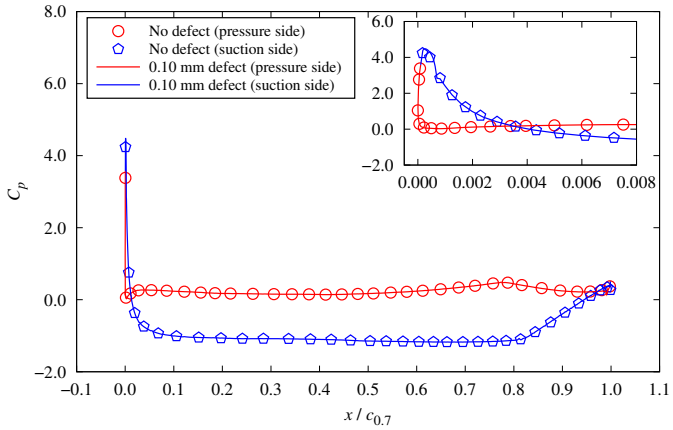

(a) Full scale (0.10 mm defect)

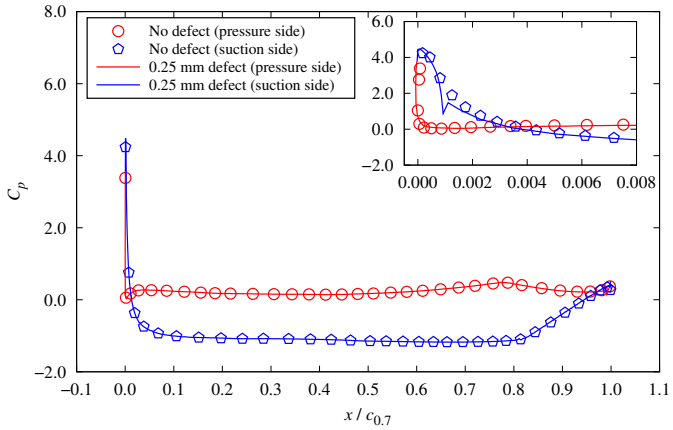

(b) Full scale (0.25 mm defect)

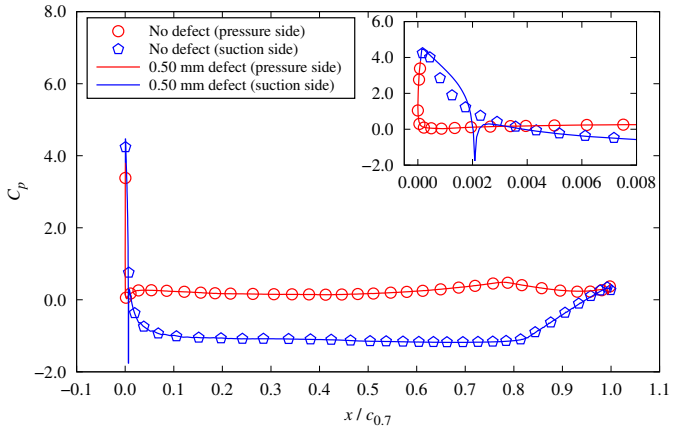

(c) Full scale (0.50 mm defect)

Figure 6.63: Comparison of C_p on the blade section of $r = 0.70\ R$ for the full-scale propellers without and with LE defects at $J = 1.102$

evident that the LE defects lower the pressure, particularly at the end of the 0.50 mm defect.

To further explain the mechanism of how LE defects affect the cavitation inception, their influence on the pressure distribution is given in Fig. 6.63, as an example, which shows the comparison of the predicted pressure coefficient, C_p, on the blade section of $r = 0.70\ R$ for the full-scale propellers without and with LE defects at $J = 1.102$. The blade sections have been expanded into a local 2-D coordinate system, xoy, with the origin located at the leading edge.

In Fig. 6.63a, the blade section with no defect exhibits a negative minimum pressure coefficient of $-C_{p_{\min}} = 1.177$ at $x/c_{0.7} = 0.68$ of the suction side. Note that the cavitation occurs when $-C_{p_{\min}} \geq \sigma$, and the condition of cavitation inception is $-C_{p_{\min}} = \sigma$. The location with the minimum pressure experiences cavitation first. It also can be observed that there was no significant difference in the pressure distribution between the sections no and 0.10 mm defects. The 0.25 mm defect slightly reduced pressure at its end, as shown in Fig. 6.63b, the negative minimum pressure coefficient, $-C_{p_{\min}} = 1.176$,occurs at a location similar to that of no defect.

Figure 6.63c shows a significant pressure reduction for the 0.50 mm defect. Compared to the results with no, 0.10 mm and 0.25 mm defects, a larger negative minimum pressure coefficient, $-C_{p_{\min}} = 1.765$, was obtained at the end of LE defect ($x/c_{0.7} = 0.00212$). It means that such a blade section with 0.50 mm defect would experience cavitation earlier than the others with no, 0.10 mm and 0.25 mm defects. The reduction in inception speed at the blade section of $r/R = 0.70$ can reach 18.33% with the advance ratio of $J = 1.102$. Detailed calculations for the reduction in cavitation inception speed on the blade section of $r/R = 0.70$ are summarized in

Table 6.21.

Table 6.21: Calculation details for the cavitation inception speed reduction ratios on the blade section of $r/R = 0.70$ at $J = 1.102$

Defect	$-C_{p_{\min}}$	Percentage reduction in inception speed (%)
No defect	1.177	–
0.10 mm	1.177	0.00
0.25 mm	1.176	-0.04
0.50 mm	1.765	18.33

Chapter 7

Conclusions and Future Work

7.1 Conclusions

A novel numerical simulation has been carried out to investigate the effects of leading-edge (LE) defect on marine propeller cavitation performance in this thesis. All the LE defects examined are within ISO 484 Class S tolerances. Simulations were performed with the steady RANS solver in Star-CCM+. Comprehensive convergence studies were carried out to examine the effects of RANS simulation parameters on results. The best-practice settings were recommended for both 2-D and 3-D simulations.

2-D simulations were first carried out for the DTMB modified NACA-66 $a = 0.8$ sections in 1 m chord length without and with LE defects using the structured grids. The 1 m chord length represents the chord length of a full-scale propeller at its 0.7 R section. Effects of the computational domain size, grid distribution, grid resolution, and turbulence model on the solutions were examined. Based on the results of convergence studies, best-practice settings were determined for simulations of 2-D foils

using Star-CCM+. With the best-practice settings for the 2-D simulations, studies were carried out to verify the minimum pressure coefficient envelops of the foil ($t/c = 0.2$, $f/c = 0.02$) without defect. Numerical results were generally in good agreement with potential-flow solutions by Brockett (1966) and the RANS solutions with ANSYS CFX and TRANSOM of Hally (2018).

CFD simulations using the best-practice settings were extended to the foils ($t/c = 0.0416$, $f/c = 0.014$) with three different sizes of defects near the LE, representing three levels of manufacturing tolerances within Class S. The predicted minimum pressure coefficients for the NACA-66 sections without and with LE defects were compared at various angles of attack. Comparative studies showed that the LE defects of various sizes within ISO Class S have large effects on the cavitation performance of 2-D foil sections in terms of reduced cavitation inception speed in the typical design range of angle of attack. As a consequence, such a defective section would experience cavitation at a lower speed than the design one. Smaller defects than Class S maximum deviation show a similar effect. The defects can also cause pressure drops at the furthest-forward edge of a LE defect.

To investigate the differences in 2-D and 3-D solutions and further quantify the effects of LE defect in future validation studies, 3-D RANS studies on the DTMB modified NACA-66 ($a = 0.8$, $f/c = 0.014$, $t/c = 0.0416$) foils of 1 m span with and without LE defect were conducted with the structured grids. The reason for choosing 1 m span is that the foils with and without LE defect were intended to be tested in a cavitation tunnel with 1 m by 1 m test section. Effects of RANS modelling parameters, such as domain size, grid aspect ratio, first-grid spacing, y^+, and turbulence model, on the solutions were carefully examined. Impact of foil span

on solution at the mid-span section was also investigated. Using the proposed best-practice settings for the foils of 1 m span, 3-D simulations were carried out for the foils in a cavitation tunnel without and with LE defects and at various angles of attack. The predicted cavitation buckets for foils of 1 m span were generally in good agreement with those from 2-D simulations. Both 2-D and 3-D simulations show that the effect of LE defect is generally obvious, especially for the 0.5 mm defect. The maximum reduction in inception speed can reach to 44%.

Due to the limitation of the foil support mechanism of cavitation tunnel, the span of 0.525 m was applied to minimize the force and moment on the foil. An extension of previous studies on the effects of LE defects on cavitation performance of the modified NACA-66 ($a = 0.8$, $f/c = 0.014$, $t/c = 0.0416$) foils were carried out in the cavitation tunnel. The dimensions of cavitation tunnel at Brodarski Institut in Zagreb (Gospodnetic, 2022) were applied. Due to the complex geometry of end plates attached to the foil of 0.525 m span, a hybrid grid with structured meshes around the foil and unstructured meshes near the end plates was generated. Convergence studies were necessary when using a hybrid grid. Similar to the study of the foil with 1 m span, effects of RANS modelling parameters, such as domain size, grid aspect ratio, first-grid spacing, y^+, and turbulence model, on the solutions were carefully examined. With the best-practice settings for the foil of 0.525 m span, the predicted cavitation buckets for foils without and with LE defects of 0.525 m span were obtained. It was found that the cavitation buckets were narrowed by the LE defects, especially for the 0.5 mm defect, which means that the incipient cavitation speed was reduced by the LE defect. However, the shapes of cavitation buckets were generally different with the 2-D and 3-D simulations of foil with 1 m span. As a result of the attached end

plates and support shafts, significant vortices can be observed in the downstream of the cavitation tunnel. For the foils with 0.525 m span, the reduction in inception speed can reach to about 50% for the foil with 0.5 mm defect around $\alpha = 2^{\circ}$.

Furthermore, the preliminary validation studies for the foils of 0.525 m span with no defect and 0.5 mm defect were also carried out on the cavitation buckets. In the cavitation tests (Gospodnetic, 2022), inflow velocity at each angle of attack was varied (increased/decreased) until cavitation was observed. The same approach was applied in 3-D RANS simulations with the recommended best-practice settings. The results show that the shapes of cavitation buckets are generally similar to those of the experimental ones (Gospodnetic, 2022). For the foils at positive angles of attack, the results indicate that the LE defect narrowed the cavitation bucket in comparison to the foil with no defect.

3-D RANS studies on the foils in a cavitation tunnel were then extended to the full-scale propellers with and without LE defects. The DTMB 5168 propeller model was used to for the geometry of full-scale propellers. By employing the steady RANS solver in Star-CCM+, thorough convergence studies were carried out for the open-water simulations of the model-scale propeller first and then for the full-scale propellers without defect and with 0.5 mm defect at the advance ratio of $J = 1.102$. Effects of RANS modelling parameters, such as domain size, grid size, stretch ratio, first-grid spacing, y^{+}, and turbulence model, on the solutions were carefully examined. Numerical uncertainties due to spatial discretization were quantified with the least square root (LSR) method of Eça and Hoekstra (2014). Based on the results of convergence studies, the best-practice settings for open-water propeller simulations with the steady RANS solver were summarized.

With the best-practice settings for the propeller, validation studies were first carried out for the model-scale propeller. The open-water simulations were then performed for the full-scale propellers with no, 0.10 mm, 0.25 mm and 0.50 mm defects. Two static pressure conditions (p_0 = 16.5 psi and 22.0 psi) were applied. In the model-scale validation studies, the predicted velocities across the tip vortex at $X/R = 0.1756$ and 0.2386 sections shown good agreement with the experimental ones (Chesnakas and Jessup, 1998). In the case of the full-scale propeller, it was found that the influence of the LE defect on the downstream velocity was insignificant.

In the validation studies of the propeller model, the computed thrust and torque coefficients, as well as open-water efficiency, are in good agreement with the experimental data (Chesnakas and Jessup, 1998). The static pressure had little impact on the open-water performance. The predictions for the propeller model were slightly smaller than those for the full-scale propeller with no defect. Furthermore, no significant differences were found between the open-water performance for the full-scale propellers with and without LE defects at various advance ratios.

The cavitation performance was also examined, focusing on the cavitation numbers in the tip region on the suction side of the blade for sections of $r/R \in [0.5, 0.9]$ with LE defects. Slight differences in the predicted cavitation numbers were seen at two static pressure conditions. The predicted cavitation numbers for the full-scale propeller without defects were generally greater than those for the propeller model. Numerical results showed that the full-scale propeller with 0.50 mm defect resulted in increased cavitation numbers in the tip region, while no significant differences were observed between the cases of no, 0.10 mm, and 0.25 mm defects. For the cavitation numbers on the blade sections of $r/R \in [0.5, 0.9]$, significant differences were found

between the full-scale propellers without defect and those with 0.50 mm defect. Particularly, the cavitation number decreased as the size of the defect decreased when J was smaller than 1.0. The cavitation buckets was narrowed by the LE defects that are within ISO 484 Class S tolerance.

Based on the predicted cavitation buckets, the reduction percentages in cavitation inception speed on the blade sections of $r/R \in [0.5, 0.9]$ were calculated for the full-scale propellers with LE defects. Larger leading-edge defect resulted in a greater increase in the cavitation number, indicating a higher reduction in the inception speed. The maximum reduction in inception speed (43.83%) was observed at $J = 0.992$ for the full-scale propeller with 0.50 mm defect. The effects of LE defect on ISR are in line with the findings in 2-D studies, in which the maximum reduction in inception speed for the foil of 1.0 m chord length with 0.50 mm LE defect was more than 40%.

The results demonstrate that the LE defects within the current ISO 484 Class S still have significant effect on cavitation performance. Note that propeller cavitation constitutes a major source of noise for ferries and cruise vessels at normal operating speeds. The noise levels from a ship jump substantially when propeller cavitation begins. To circumvent propeller noise and address the manufacturing defects, it is recommended to set the leading-edge defect tolerance within 0.10 mm for Class S to enhance the existing ISO 484 standards. Moreover, to minimize manufacturing tolerances, the adoption of more accurate CNC milling processes, capable of eliminating manual grinding of blade edges and tips, is recommended. This can help improve the precision and consistency of propeller manufacturing, ultimately enhancing performance and reducing noise emissions.

7.2 Novel Contributions

The novel contributions of this research are summarized as below:

1. Comprehensive numerical studies were carried out to understand the effects of LE defect on the cavitation performance of marine propeller. The studies showed that the LE defect within ISO 484 Class S tolerances would narrow the cavitation bucket. Larger LE defect resulted in a greater increase in the cavitation number, indicating a higher reduction in the inception speed. The maximum reduction in inception speed could reach to more than 40%.

2. Extensive convergence studies were conducted to assess the impacts of RANS simulation parameters on the predictions of the DTMB modified NACA-66 sections and DTMB 5168 propellers in model and full scales. The best-practice settings were proposed for both 2-D and 3-D simulations with the steady solver in Star-CCM+. Such recommendations can be applied for the other foils and propellers.

7.3 Recommendations for Future Work

The following aspects need to be addressed in future work.

7.3.1 Numerical Aspects

Simulations for other propeller manufacturing tolerances. This study focused on examining the effects of leading-edge defects on the cavitation performance of marine propeller. In the next phase, numerical simulations for the other propeller

manufacturing defects, such as those in thickness and camber distribution, will be carried out using the recommended best-practice settings.

Self-propulsion simulation considering LE defect. In this dissertation, the numerical simulations were performed with the uniform incoming flow. However, the full-scale ship propellers are generally working at the stern of the vessels. The effects of no-uniform wake field and propeller-hull-rudder interactions should be considered when predicting cavitation performance. In addition to the open-water simulation with non-uniform incoming flow, the self-propulsion simulation for the full-scale ship with the detailed propeller considering LE defect should be carried out in the future work.

Unsteady simulation. All the simulations were carried out with the steady RANS solver in present studies. It took some time for a cavity to develop and become visible in the tests. This was not considered in the numerical simulations with the steady RANS solver. In future studies, the unsteady solver is advisable for simulating real cavitation development.

Cavitation models. For a single-phase analysis, such as the open-water simulation conducted in this study, cavitation inception can be assessed by examining the minimum pressure. Note that the cavitation involves a phase change at the interface between the liquid and gas phases. The two-phase flow simulation with cavitation model could capture the dynamics at this liquid-gas interface, lead to a larger value of the minimum pressure than single-phase simulation (Hanimann et al., 2016; Perić, 2022). The accuracy of predicted cavitation number could then be improved by the application of cavitation model. It would be valuable to investigate the impact

of the LE defect using cavitation models, for example, the Full Rayleigh–Plesset model (Singhal et al., 2002) and the Schnerr-Sauer model (Sauer and Schnerr, 2001).

Cavitation inception criteria. In this study, cavitation is considered to occur when the cavitation number is equal to the negative minimum pressure at a single point. However, in future work, it may be worthwhile to investigate other cavitation inception criteria, such as a combination of the minimum pressure and the surface area of the foil over which the minimum pressure occurs. Comparisons between cavitation buckets generated using different cavitation inception criteria could provide valuable insights into the cavitation behavior.

Effect of end plate. Significant effects of the end plate on both cavitation bucket and cavitation inception speed were observed in the numerical results, further numerical studies should be carried out for different sizes of end plates.

7.3.2 Experimental Aspects

Quantification of experimental uncertainty. In the preliminary validation studies for the foils of 0.525 m span, the experimental cavitation buckets were based on observation. It is essential to quantify the experimental uncertainties. This will facilitate the development of improved best-practice settings.

Tests in the typical design range of angle of attack. The predictions indicated that the LE defect had a significant effect on cavitation inception speed in the typical design range of angle of attack ($-1.5^\circ < \alpha < 2^\circ$) for a moderately loaded propeller. However, the majority of experimental data from Gospodnetic (2022) fall outside

this range. Conducting further tests in the typical design range of angle of attack is recommended.

Sea trial. While the quality of CFD predictions has been confirmed through numerous comparisons with numerical and experimental data from propeller models, the accuracy of full-scale propeller simulations remains uncertain. The confidence in full-scale simulations could be improved with the availability of more data obtained from comprehensive full-scale measurements. All the LE defects considered for full-scale propellers in this thesis are within ISO 484 Class S. It should also be noted that such LE defects cannot be applied to the propeller model since they are very small. To gain a better understanding of the effects of LE defects on the cavitation performance of marine propellers, sea trials should be conducted.

Bibliography

Abbasi, A. A., Franzosi, G., Canepa, E., Gaggero, S., Villa, D., Viviani, M., and Tani, G. (2023). Experimental analysis of the flow field around a propeller with inclined shaft. *Ocean Engineering*, 285:115237.

Abdel-Maksoud, M. (2003). Numerical and experimental study of cavitation behaviour of a propeller. *Proceeding STG Sprechtag Cavitation, Hamburg, Germany*.

Ali, M. A., Peng, H., Qiu, W., and Bensow, R. (2017). Prediction of propeller tip vortex using OpenFOAM. In *Proceedings of the 36th International Conference on Ocean, Offshore and Arctic Engineering*, volume 57731, page V07AT06A005. American Society of Mechanical Engineers.

Alin, N., Chapuis, M., Fureby, C., Liefvendahl, M., Svennberg, U., and Troeng, C. (2010). A numerical study of submarine propeller-hull interactions. In *Proceedings of the 28th Symposium on Naval Hydrodynamics*. Pasadena, California.

Alves Pereira, F., Di Felice, F., and Salvatore, F. (2016). Propeller cavitation in non-uniform flow and correlation with the near pressure field. *Journal of Marine Science and Engineering*, 4(4):70.

Arndt, R. E. A. and George, W. K. (1979). Pressure fields and cavitation in turbulent shear flows. In *Proceedings of 12th Symposium on Naval Hydrodynamics*, pages 327–339. National Academy of Sciences.

Asnaghi, A. and Bensow, R. E. (2020). Impact of leading edge roughness in cavitation simulations around a twisted foil. *Fluids*, 5(4):243.

Asnaghi, A., Svennberg, U., Gustafsson, R., and Bensow, R. E. (2019). Roughness effects on the tip vortex strength and cavitation inception. In *Sixth International Symposium on Marine Propulsors: SMP19, Rome, Italy.*

Asnaghi, A., Svennberg, U., Gustafsson, R., and Bensow, R. E. (2021). Propeller tip vortex mitigation by roughness application. *Applied Ocean Research*, 106:102449.

Banko, A. and Eaton, J. (2019). A frame-invariant definition of the Q-Criterion. *Center for Turbulence Research Annual Research Briefs*, pages 181–194.

Barkmann, U., Heinke, H. J., and Lübke, L. (2011). Potsdam propeller test case (PPTC). In *Proceeding of the Second International Symposium on Marine Propulsors*, pages 36–38.

Barnaby, S. W. (1897). On the formation of cavities in water by screw propellers at high speeds. *Journal of the American Society for Naval Engineers*, 9(4):678–683.

Bertetta, D., Brizzolara, S., Canepa, E., Gaggero, S., and Viviani, M. (2012). EFD and CFD characterization of a CLT propeller. *International Journal of Rotating Machinery*, 2012.

Breslin, J. P. and Andersen, P. (1994). *Hydrodynamics of ship propellers*. Number 3. Cambridge University Press.

Brewer, W. H. and Kinnas, S. A. (1997). Experiment and viscous flow analysis on a partially cavitating hydrofoil. *Journal of Ship Research*, 41(3):161–171.

Brito Lopes, A. V., Emekwuru, N., and Abtahizadeh, E. (2022a). Flamelet generated manifold simulation of highly swirling spray combustion: adoption of a mixed homogeneous reactor and inclusion of liquid-flame heat transfer. *AIP Advances*, 12(11).

Brito Lopes, A. V., Emekwuru, N., Bonello, B., and Abtahizadeh, E. (2020). On the highly swirling flow through a confined bluff-body. *Physics of Fluids*, 32(5).

Brito Lopes, A. V., Emekwuru, N., and Joshi, K. (2022b). Are the available data from laboratory spray burners suitable for CFD modelling validations? a review. *Energy Conversion and Management: X*, page 100289.

Brockett, T. (1966). Minimum pressure envelopes for modified NACA-66 sections with NACA $a = 0.8$ camber and buships type 1 and type 2 sections. Technical report, David Taylor Model Basin Washington DC Hydromechanics Lab.

Burrill, L. C. (1951). Sir Charles Parsons and cavitation. *Transactions of Institute of Marine Engineers*, 63(8).

Chesnakas, C. J. and Jessup, S. D. (1998). Cavitation and 3-D LDV tip-flowfield measurements of propeller 5168. Technical report, Naval Surface Warfare Center Carderock Division Bethesda MD Hydromechanics Directorate.

Di Felice, F., Felli, M., Liefvendahl, M., and Svennberg, U. (2009). Numerical and experimental analysis of the wake behavior of a generic submarine propeller. In *Proceedings of the First International Symposium on Marine Propulsors*. Trondheim, Norway.

DNV (2010). Rules for classification of ships rules - new buildings - part 6: silent class notation.

Duan, J., Xu, R., Cui, L., and Li, R. (2023). Numerical study on prediction and discrimination methods of propeller tip vortex cavitation inception. *AIP Advances*, 13(5).

D'Agostino, D., Diez, M., Felli, M., and Serani, A. (2023). PIV snapshot clustering reveals the dual deterministic and chaotic nature of propeller wakes at macro-and micro-scales. *Journal of Marine Science and Engineering*, 11(6):1220.

Eça, L. and Hoekstra, M. (2014). A procedure for the estimation of the numerical uncertainty of CFD calculations based on grid refinement studies. *Journal of Computational Physics*, 262:104–130.

Felli, M. and Falchi, M. (2018). Propeller wake evolution mechanisms in oblique flow conditions. *Journal of Fluid Mechanics*, 845:520–559.

Fine, N. E. (1992). *Nonlinear analysis of cavitating propellers in nonuniform flow*. PhD thesis, Massachusetts institute of Technology.

Fine, N. E. and Kinnas, S. A. (1993). A boundary element method for the analysis of the flow around 3-d cavitating hydrofoils. *Journal of Ship Research*, 37(3):213–224.

Foeth, E. J., Van Doorne, C. W. H., Van Terwisga, T., and Wieneke, B. (2006). Time resolved PIV and flow visualization of 3D sheet cavitation. *Experiments in Fluids*, 40:503–513.

Franc, J. P. and Michel, J. M. (1985). Attached cavitation and the boundary layer: experimental investigation and numerical treatment. *Journal of Fluid Mechanics*, 154:63–90.

Gauthier, M. and Hally, D. (2019). Propeller defect study - part 1: effect of a leading edge defect on propeller performance. Technical report, DRDC Atlantic Centre, Canada.

Gibson, M. M. and Launder, B. E. (1978). Ground effects on pressure fluctuations in the atmospheric boundary layer. *Journal of Fluid Mechanics*, 86(3):491–511.

Gospodnetic, D. and Gospodnetic, S. (1996). Integrated propeller manufacturing system. In *12th Symposium on Theory and Practice of Shipbuilding*. Zagreb, Croatia, May.

Gospodnetic, S. (2013). CNC milling of monoblock propellers to final form and finish. In *Ottawa Marine Technical Symposium*. Ottawa, Canada, February.

Gospodnetic, S. (2015). CNC machining of propellers to better than class s tolerances. In *SNAME 14th Propeller & Shafting Symposium*. Norfolk, Virginia, USA.

Gospodnetic, S. (2022). Impact of manufacturing tolerances on propeller performance, investigation 1: 2D foil section in the rectilinear flow. Technical report, Transport Canada.

Hally, D. (2008). Preliminary CFD simulations of 2-D foils with defects. Technical report, DRDC Atlantic Centre, Canada.

Hally, D. (2018). Preliminary CFD simulations of 2-D foils with defects. DRDC Atlantic Centre, Canada.

Hanimann, L., Mangani, L., Casartelli, E., and Widmer, M. (2016). Cavitation modeling for steady-state CFD simulations. In *IOP Conference Series: Earth and Environmental Science*, volume 49, page 092005. IOP Publishing.

Heinke, H. J. (2011). Potsdam propeller test case (PPTC): open water tests with the model propeller VP1304.

Heinke, H. J. and Kröger, W. (2013). Potsdam propeller test case (PPTC): measurement of the cavitation nuclei in the tunnel water and cavitation observations with the model propeller VP1304.

Heinz, S. (2020). A review of hybrid RANS-LES methods for turbulent flows: concepts and applications. *Progress in Aerospace Sciences*, 114:100597.

Holl, J. W. (1960). The inception of cavitation on isolated surface irregularities. *Journal of Basic Engineering*, 82(1):169–183.

Hsiao, C. T. and Chahine, G. L. (2005). Scaling of tip vortex cavitation inception noise with a bubble dynamics model accounting for nuclei size distribution. *Journal of Fluids Engineering*, 127(1):55–65.

Hsiao, C. T. and Chahine, G. L. (2008). Scaling of tip vortex cavitation inception for

a marine open propeller. In *Proceedings of the 27th Symposium on Naval Hydrodynamics*, pages 5–10.

Hsiao, C. T. and Pauley, L. L. (1999). Numerical computation of tip vortex flow generated by a marine propeller. *Journal of Fluids Engineering*, 121(3):638–645.

Huang, T. T. (1986). The effects of turbulence stimulators on cavitation inception of axisymmetric headforms. *Journal of Fluids Engineering*, 108(2):261–268.

IMO (2014). Guidelines for the reduction of underwater noise from commercial shipping to address adverse impacts on marine life.

ISO (2005a). Shipbuilding - ship screw propellers - manufacturing tolerances - part 1: propellers of diameter greater than 2.5 m. ISO.

ISO (2005b). Shipbuilding - ship screw propellers - manufacturing tolerances - part 2: propellers of diameter between 0.80 and 2.5 m inclusive. ISO.

ITTC (2017). Recommended procedures and guidelines 7.5-03-02-03, practical guidelines for ship CFD applications. In *Proceedings of the 28th International Towing Tank Conference*. ITTC, Wuxi, China.

ITTC (2021). The specialist committee on hydrodynamic noise final report and recommendations to the 29th ITTC. In *Proceedings of the 29th International Towing Tank Conference*. ITTC, Virtual.

Janssen, A. and Leever, S. (2017). Propeller manufacture and tolerances. *Encyclopedia of Maritime and Offshore Engineering*, pages 1–13.

Jin, S., Zha, R., Peng, H., and Qiu, W. (2021). Comparison of 2-D and 3-D RANS studies on effects of leading-edge propeller manufacturing defects on cavitation performance. In *Proceedings of the 29th Annual Conference of the Computational Fluid Dynamics Society of Canada*. St. John's, Newfoundland and Labrador, Canada, July.

Jin, S., Zha, R., Peng, H., Qiu, W., and Gospodnetic, S. (2020). 2D CFD studies on effects of leading-edge propeller manufacturing defects on cavitation performance. In *SNAME Maritime Convention*. The Society of Naval Architects and Marine Engineers.

Johnsson, C.-A. and Rutgersson, O. (1991). Leading edge roughness-a way to improve propeller tip vortex cavitation. In *SNAME Propeller and Shafting Symposium*, page D021S002R002. SNAME.

Jones, E. A. (1980). Model scale effects on a 16-309 flapped hydrofoil section. Technical report, Defence Research Establishment Atlantic Dartmouth (Nova Scotia).

Jones, W. P. and Launder, B. E. (1972). The prediction of laminarization with a two-equation model of turbulence. *International Journal of Heat and Mass Transfer*, 15(2):301–314.

Kerwin, J., Kinnas, S., and Wilson, M. B. (1986). Experimental and analytical techniques for the study of unsteady propeller sheet cavitation. In *Proceedings of the 16th Symposium on Naval Hydrodynamics*.

Kerwin, J. E. and Lee, C. S. (1978). Prediction of steady and unsteady marine

propeller performance by numerical lifting-surface theory. *Transactions of SNAME*, 86:518–253.

Kethanur Balasubramaniam, S. V., Coutier-Delgosha, O., Fezzaa, K., and Clark, S. (2023). Understanding cavitation inception mechanisms through ultra-fast synchrotron X-ray imaging. *Bulletin of the American Physical Society*.

Kim, S. and Kinnas, S. A. (2022). Prediction of developed tip vortex cavitation and its induced hull pressure via a boundary element method. In *Proceedings of the 34th Symposium on Naval Hydrodynamics*.

Kinnas, S. A., Abdel-Maksoud, M., Barkmann, U., Lubke, L., and Tian, Y. (2015). The second workshop on cavitation and propeller performance. In *Proceedings of the Fourth International Symposium on Marine Propulsors*.

Kinnas, S. A. and Fine, N. E. (1992). A numerical nonlinear boundary element method for the analysis of unsteady propeller sheet cavitation. In *Proceedings of the 19th Symposium on Naval Hydrodynamics*, pages 717–733.

Korkut, E. and Atlar, M. (2002). On the importance of the effect of turbulence in cavitation inception tests of marine propellers. *Proceedings of the Royal Society of London. Series A: Mathematical, Physical and Engineering Sciences*, 458(2017):29–48.

Korkut, E., Atlar, M., and Odabasi, A. Y. (1999). On the viscous scale effects in cavitation inception of marine propellers. In *Proceedings of the 3rd ASME/JSME Joint Fluids Engineering Conference*.

Kuiper, G. (1978). Scale effects on propeller cavitation inception. In *Proceedings of 12th ONR Symposium on Naval Hydrodynamics*, pages 400–429.

Launder, B. and Spalding, D. (1974). The numerical computation of turbulent flows. *Computer Methods in Applied Mechanics and Engineering*, 3(2):269–289.

Lee, C. S. (1979). *Predicton of steady and unsteady performance of marine propellers with or without cavitation by numerical lifting-surface theory*. PhD thesis, Massachusetts Institute of Technology.

Lee, J. (1987). *A potential based panel method for the analysis of marine propellers in steady flow*. PhD thesis, Massachusetts Institute of Technology.

Lee, J. Y., Paik, B. G., and Lee, S. J. (2009). PIV measurements of hull wake behind a container ship model with varying loading condition. *Ocean Engineering*, 36(5):377–385.

Li, D. Q., Grekula, M., Lindell, P., and Hallander, J. (2012). Prediction of cavitation for the INSEAN propeller E779A operating in uniform flow and non-uniform wakes. In *Proceedings of the 8th International Symposium on Cavitation*.

Li, G., Chen, Q., and Liu, Y. (2020). Experimental study on dynamic structure of propeller tip vortex. *Polish Maritime Research*, (2):11–18.

Liefvendahl, M., Alin, N., Chapuis, M., Fureby, C., Svennberg, U., and Troëng, C. (2010). Ship and propulsor hydrodynamics. In *V European Conference on Computational Fluid Dynamics*. Lisbon, Portugal.

Lien, F. S. and Leschziner, M. A. (1994). Assessment of turbulence-transport models including non-linear rng eddy-viscosity formulation and second-moment closure for flow over a backward-facing step. *Computers & Fluids*, 23(8):983–1004.

Lloyd, T., Vaz, G., Rijpkema, D., and Schuiling, B. (2015). The potsdam propeller test case in oblique flow: prediction of propeller performance, cavitation patterns and pressure pulses. In *Proceedings of the Second International Workshop on Cavitating Propeller Performance*.

Lubke, L. (2015). Potsdam propeller test case (PPTC) cavitation in oblique flow case 2. In *Proceeding of the Fourth International Symposium on Marine Propulsors*.

Mach, K. P. (2011). Potsdam propeller test case (PPTC): LDV velocity measurements with the model propeller VP1304.

Manceau, R. and Hanjalić, K. (2002). Elliptic blending model: a new near-wall Reynolds-stress turbulence closure. *Physics of Fluids*, 14(2):744–754.

Menter, F. R. (1994). Two-equation eddy-viscosity turbulence models for engineering applications. *AIAA Journal*, 32(8):1598–1605.

NAVSEA (2004). Standard propeller drawing, No. 810-4435837, Rev. B. USA.

Newton, R. N. (1961). Performance data of propellers for high speed craft. *RINA Transactions*, 103(2):93–129.

Pan, Y. (2009). *A viscous/inviscid interactive approach and its application to wetted or cavitating hydrofoils and propellers with non-zero trailing edge thickness*. PhD thesis, University of Texas at Austin.

Parsons, C. (1897). The application of the compound steam turbine to the purpose of marine propulsion. *Journal of the American Society for Naval Engineers*, 9(2):374–384.

Peng, H. H., Qiu, W., and Ni, S. (2013). Effect of turbulence models on rans computation of propeller vortex flow. *Ocean Engineering*, 72:304–317.

Pereira, F., Salvatore, F., and Di Felice, F. (2004). Measurement and modeling of propeller cavitation in uniform inflow. *Journal of Fluids Engineering*, 126(4):671–679.

Perić, M. (2022). Prediction of cavitation on ships. *Brodogradnja: Teorija i Praksa Brodogradnje i Pomorske Tehnike*, 73(3):39–58.

Posa, A. and Balaras, E. (2018). Large-eddy simulations of a notional submarine in towed and self-propelled configurations. *Computers & Fluids*, 165:116–126.

Posa, A., Broglia, R., and Balaras, E. (2019). Les study of the wake features of a propeller in presence of an upstream rudder. *Computers & Fluids*, 192:104247.

Regener, P. B., Mirsadraee, Y., and Andersen, P. (2018). Nominal vs. effective wake fields and their influence on propeller cavitation performance. *Journal of Marine Science and Engineering*, 6(2):34.

Richardson, L. F. (1911). IX. The approximate arithmetical solution by finite differences of physical problems involving differential equations, with an application to the stresses in a masonry dam. *Philosophical Transactions of the Royal Society*

of London. Series A, Containing Papers of a Mathematical or Physical Character, 210(459-470):307–357.

Rizk, M. A., Belhenniche, S. E., Imine, O., and Kinaci, O. K. (2023). Cavitation predictions of E779A propeller by a RANSE-based CFD and its performance behind a generic hull. *Journal of Marine Science and Application*, 22(2):273–283.

Rutland, C. J. (2011). Large-eddy simulations for internal combustion engines–a review. *International Journal of Engine Research*, 12(5):421–451.

Salim, S. M. and Cheah, S. (2009). Wall y^+ strategy for dealing with wall-bounded turbulent flows. In *Proceedings of the International Multiconference of Engineers and Computer Scientists 2009*, volume 2, pages 2165–2170.

Salinas, R. (2015). AQUO Project No. 314227, WP 2: noise sources, impact of propeller noise on global URN, Task T2.5.

Salvatore, F., Pereira, F., Felli, M., Calcagni, D., and Di Felice, F. (2006). Description of the INSEAN E779A propeller experimental dataset. *Technical Report INSEAN 2006-085 INSEAN-Italian Ship Model Basin*.

Sauer, J. and Schnerr, G. H. (2001). Development of a new cavitation model based on bubble dynamics. *ZAMM - Journal of Applied Mathematics and Mechanics / Zeitschrift für Angewandte Mathematik und Mechanik*, 81(S3):561–562.

Sezen, S. and Atlar, M. (2022). Marine propeller underwater radiated noise prediction with the fwh acoustic analogy part 3: assessment of full-scale propeller hydroacoustic performance versus sea trial data. *Ocean Engineering*, 266:112712.

Sezen, S. and Atlar, M. (2023a). Marine propeller underwater radiated noise prediction with the FWH acoustic analogy part 1: assessment of model scale propeller hydroacoustic performance under uniform and inclined flow conditions. *Ocean Engineering*, 279:114552.

Sezen, S. and Atlar, M. (2023b). Marine propeller underwater radiated noise prediction with the FWH acoustic analogy part 2: assessment of model scale propeller hydroacoustic performance under non-uniform flow conditions. *Ocean Engineering*, 270:113443.

Sezen, S., Uzun, D., Ozyurt, R., Turan, O., and Atlar, M. (2021a). Effect of biofouling roughness on a marine propeller's performance including cavitation and underwater radiated noise (URN). *Applied Ocean Research*, 107:102491.

Sezen, S., Uzun, D., Turan, O., and Atlar, M. (2021b). Influence of roughness on propeller performance with a view to mitigating tip vortex cavitation. *Ocean Engineering*, 239:109703.

Shen, Y. T. (1985). Wing sections for hydrofoils - part 3: experimental verifications. *Journal of Ship Research*, 29(1):39–50.

Shen, Y. T., Gowing, S., and Jessup, S. (2009). Tip vortex cavitation inception scaling for high reynolds number applications. *Journal of Fluids Engineering*, 131(7):071301.

Singhal, A. K., Athavale, M. M., Li, H., and Jiang, Y. (2002). Mathematical basis and validation of the full cavitation model. *Journal of Fluids Engineering*, 124(3):617–624.

Southall, B. L., Scholik-Schlomer, A. R., Hatch, L., Bergmann, T., Jasny, M., Metcalf, K., Weilgart, L., and Wright, A. J. (2017). Underwater noise from large commercial ships-international collaboration for noise reduction. *Encyclopedia of Maritime and Offshore Engineering*, pages 1–9.

Spalart, P. and Allmaras, S. (1992). A one-equation turbulence model for aerodynamic flows. In *Proceedings of the 30th Aerospace Sciences Meeting and Exhibit*, page 439.

Spalart, P. R. and Rumsey, C. L. (2007). Effective inflow conditions for turbulence models in aerodynamic calculations. *AIAA Journal*, 45(10):2544–2553.

Spalart, P. R. and Venkatakrishnan, V. (2016). On the role and challenges of CFD in the aerospace industry. *The Aeronautical Journal*, 120(1223):209–232.

Sun, H. and Kinnas, S. A. (2006). Simulation of sheet cavitation on propulsor blades using a viscous/inviscid interactive method. In *Proceedings of the Sixth International Symposium on Cavitation*.

Tremblay, C. and Gospodnetic, S. (2017). Manufacturing propellers in the 21st century. *Maritime Engineering Journal*, 83:10–15.

Tucker, P. G. and Tyacke, J. C. (2016). Eddy resolving simulations in aerospace–invited paper (Numerical Fluid 2014). *Applied Mathematics and Computation*, 272:582–592.

Van Beek, T. and Janssen, A. (2000). An integrated design and production concept for ship propellers. In *Proceedings of the 34th WEGEMT School*, pages 2000–7. TUDelft, AULA, June.

Van Gent, W. (1994). Pressure field analysis of a propeller with unsteady loading and sheet cavitation. In *Proceedings of the 20th Symposium on Naval Hydrodynamics*, pages 355–367.

Versteeg, H. K. and Malalasekera, W. (2007). *An introduction to computational fluid dynamics: the finite volume method*. Pearson Education.

Watanabe, T., Kawamura, T., Takekoshi, Y., Maeda, M., and Rhee, S. H. (2003). Simulation of steady and unsteady cavitation on a marine propeller using a RANS CFD code. In *Proceedings of the Fifth International Symposium on Cavitation*.

Wilcox, D. C. (1998). *Turbulence modeling for CFD*, volume 2. DCW industries La Canada, CA.

Wilcox, D. C. (2008). Formulation of the $k - \omega$ turbulence model revisited. *AIAA Journal*, 46(11):2823–2838.

Yilmaz, N., Dong, X., Aktas, B., Yang, C., Atlar, M., and Fitzsimmons, P. A. (2020). Experimental and numerical investigations of tip vortex cavitation for the propeller of a research vessel, "The Princess Royal". *Ocean Engineering*, 215:107881.